



**HAL**  
open science

# Energy storage properties of iridium oxides : model materials for the study of anionic redox

Arnaud Perez

► **To cite this version:**

Arnaud Perez. Energy storage properties of iridium oxides : model materials for the study of anionic redox. Chemical engineering. Université Pierre et Marie Curie - Paris VI, 2017. English. NNT : 2017PA066323 . tel-01725130

**HAL Id: tel-01725130**

**<https://theses.hal.science/tel-01725130>**

Submitted on 7 Mar 2018

**HAL** is a multi-disciplinary open access archive for the deposit and dissemination of scientific research documents, whether they are published or not. The documents may come from teaching and research institutions in France or abroad, or from public or private research centers.

L'archive ouverte pluridisciplinaire **HAL**, est destinée au dépôt et à la diffusion de documents scientifiques de niveau recherche, publiés ou non, émanant des établissements d'enseignement et de recherche français ou étrangers, des laboratoires publics ou privés.

# Université Pierre et Marie Curie

ED 397 – Physique et Chimie des Matériaux

*Laboratoire de Chimie du Solide et Energie – Collège de France*

## **Energy storage properties of iridium oxides: model materials for the study of anionic redox**

By Arnaud Perez

PhD thesis in Chemistry

Directed by Gwenaëlle Rousse and Jean-Marie Tarascon

Presented and defended in public on December 19<sup>th</sup>, 2017

In front of the jury :

Dr. Valérie Pralong	Research Director, CRISMAT, Caen	Referee
Prof. Michel Pouchard	Professor Emeritus, ICMCB, Bordeaux	Referee
Prof. Artem M. Abakumov	Professor, Skoltech, Moscow	Examiner
Prof. Peter G. Bruce	Professor, Oxford University	Examiner
Dr. Damien Dambournet	Associate Professor, UPMC - Sorbonne University	Examiner
Dr. Gwenaëlle Rousse	Associate Professor, UPMC - Sorbonne University	Director
Prof. Jean-Marie Tarascon	Professor, Collège de France, Paris	Director





# Université Pierre et Marie Curie

ED 397 – Physique et Chimie des Matériaux

*Laboratoire de Chimie du Solide et Energie – Collège de France*

## **Propriétés de stockage de l'énergie dans les oxydes d'iridium : matériaux modèles pour l'étude du redox anionique**

Par Arnaud Perez

Thèse de doctorat en Chimie

Dirigée par Gwenaëlle Rousse et Jean-Marie Tarascon

Présentée et soutenue publiquement le 19 décembre 2017

Devant un jury composé de :

Dr. Valérie Pralong	Directeur de Recherche, CRISMAT, Caen	Rapporteur
Prof. Michel Pouchard	Professeur Emérite, ICMCB, Bordeaux	Rapporteur
Prof. Artem M. Abakumov	Professeur, Skoltech, Moscou	Examineur
Prof. Peter G. Bruce	Professeur, Oxford University	Examineur
Dr. Damien Dambournet	Maître de Conférences, UPMC - Sorbonne Universités	Examineur
Dr. Gwenaëlle Rousse	Maître de Conférences, UPMC - Sorbonne Universités	Directrice
Prof. Jean-Marie Tarascon	Professeur, Collège de France, Paris	Directeur





*A mon grand-père, électrochimiste malgré lui.*



## Acknowledgements

I had an amazing time during the three years I worked at Collège de France. Not because it is so cool to assemble Swagelok cells or grind powder or we had such a nice view of Paris from the rooftop (although this one does count), but because I knew every morning that I would spend the day with great people, maybe meet someone new, that I would learn something from them, that someone would try a crazy experiment that day, that I could share some results with them and always get interesting thoughts, and if I had an issue with anything, there would be plenty of people in the lab to help me figure it out. This is truly amazing.

Therefore, the first thing I want to do is thank Jean-Marie Tarascon for all the efforts he daily puts into making this lab what it is and for giving me the opportunity to work in such an amazing environment. I couldn't think of a more available and passionate supervisor and I hope I can give to others as much as he gave to everyone in the lab.

When I think about passion for science, I also think about Gwenaëlle Rousse, who has shown me how excellent you can become at something when you enjoy it. Thank you for everything I learned from you and for the continuous cheerful mind you bring to the lab!

Of course, I would like to thank all the members of the lab who shared these three years with me. I had a lot of pleasure to meet every one of them and spend some precious time together in and out of the lab. Thank you all for your enthusiasm, your advices, your openness and I wish you all the best for the future!

Finally, most of the work I will present here would not have been possible without the help and collaboration of many people that I warmly acknowledge. D. Batuk and A. Abakumov for TEM experiments, D. Foix (XPS), E. J. Berg (DEMS), E. Salager (NMR), H. Vezin (EPR), A. Iadecola (XAS), Z. Lin and P. Simon (pseudocaps), M. Saubanère and M.-L. Doublet (DFT). It was extremely motivating to learn from their respective fields and understand better the systems we were working on. I would also like to thank R. Beer who did a great work on the protonation of iridates during his internship, it was a pleasure to work with him on this topic. A large part of the data presented here was obtained in several synchrotron or neutron facilities thanks to the great help of dedicated beamline scientists: T. Hansen (ILL), V. Pomjakushin (PSI), S. Belin and V. Briois (SOLEIL).



# Table of Contents

<b>General introduction.....</b>	<b>1</b>
<b>Chapter I. State of the art .....</b>	<b>5</b>
<b>I.1. From intercalation chemistry to Li/Na-ion batteries .....</b>	<b>5</b>
I.1.a. Intercalation chemistry in low dimensionality solids .....	5
I.1.b. From Li batteries to Li-ion batteries.....	7
I.1.c. The more erratic development of Na-ion batteries.....	8
I.1.d. Post Li-ion technologies and their promises .....	9
<b>I.2. Increasing the capacity of cathode materials for Li-ion batteries.....</b>	<b>10</b>
I.2.a. Transition metal substitution .....	10
I.2.b. Li-rich materials with excess Li in the transition metal layers.....	12
I.2.c. The drawbacks of high energy density Li-rich cathode materials.....	13
<b>I.3. Anionic redox as a new paradigm for high capacity cathode materials.....</b>	<b>13</b>
I.3.a. Model materials based on Ru and Ir.....	13
I.3.b. A source of creativity for new material design.....	15
I.3.c. Anionic redox: current understanding of the electronic structure .....	16
<b>I.4. Conclusion .....</b>	<b>19</b>
<b>Chapter II. Anionic redox in Na-rich layered oxides: study of Na<sub>2</sub>IrO<sub>3</sub> .</b>	<b>21</b>
<b>II.1. Introduction.....</b>	<b>21</b>
<b>II.2. Synthesis and structure .....</b>	<b>22</b>
<b>II.3. Electrochemical properties .....</b>	<b>26</b>
<b>II.4. Structural evolution upon cycling .....</b>	<b>29</b>
II.4.a. <i>In situ</i> XRD study.....	29
II.4.b. O1'-NaIrO <sub>3</sub> .....	30
II.4.c. O1-Na <sub>0.5</sub> IrO <sub>3</sub> .....	32
II.4.d. Reversibility after a complete cycle .....	34
II.4.e. Minimization of cationic repulsions in the structure.....	34

---

<b>II.5. Participation of Ir and O to the redox.....</b>	<b>37</b>
II.5.a. X-ray photoemission spectroscopy study .....	37
II.5.b. X-ray Absorption Near-edge Spectroscopy (XANES) .....	38
II.5.c. Distortion of the IrO <sub>6</sub> octahedra.....	40
<b>II.6. Stability issues and long-term cycling .....</b>	<b>42</b>
II.6.a. Capacity decrease in Na half-cells .....	42
II.6.b. Long-term cycling in full cells.....	45
<b>II.7. Conclusion.....</b>	<b>47</b>
<b>Chapter III. Metastability of the Li-substituted Na(Li<sub>1/3</sub>Ir<sub>2/3</sub>)O<sub>2</sub> .....</b>	<b>49</b>
<b>III.1. Introduction .....</b>	<b>49</b>
<b>III.2. Synthesis and structure.....</b>	<b>49</b>
III.2.a. Phase diagram: solid-solution or not ?.....	49
III.2.b. Synchrotron X-ray diffraction: honeycomb stacking.....	50
III.2.c. Neutron diffraction: position of Li and Na .....	51
<b>III.3. Electrochemical properties.....</b>	<b>54</b>
III.3.a. Na(Li <sub>1/2</sub> Ir <sub>2/3</sub> )O <sub>2</sub> vs. Li .....	54
III.3.b. <i>In situ</i> and <i>ex situ</i> XRD study .....	56
III.3.c. Decomposition of the material.....	58
III.3.d. Na(Li <sub>1/2</sub> Ir <sub>2/3</sub> )O <sub>2</sub> vs. Na.....	59
<b>III.4. Conclusion.....</b>	<b>63</b>
<b>Chapter IV. Pushing to the limits of anionic redox with a new Li<sub>3</sub>IrO<sub>4</sub> phase .....</b>	<b>65</b>
<b>IV.1. Introduction .....</b>	<b>65</b>
<b>IV.2. Synthesis and structure.....</b>	<b>66</b>
<b>IV.3. Electrochemical properties.....</b>	<b>68</b>
IV.3.a. Galvanostatic cycling in Li cells.....	68
IV.3.b. Reversible Li <sup>+</sup> intercalation on reduction .....	70
IV.3.c. Amorphisation and oxygen loss on full oxidation .....	72
IV.3.d. Reversible cycling.....	77
<b>IV.4. Participation of oxygen and iridium to the redox .....</b>	<b>79</b>

---

IV.4.a. Extended X-ray Absorption Fine Structure at Ir L <sub>III</sub> -edge .....	80
IV.4.b. X-ray Absorption Near Edge Spectroscopy .....	83
IV.4.c. Electron paramagnetic resonance .....	86
<b>IV.5. Conclusion .....</b>	<b>87</b>
<b>Chapter V. Preparation of proton-based iridates and energy storage in H<sub>3+x</sub>IrO<sub>4</sub>.....</b>	<b>89</b>
<b>V.1. Introduction.....</b>	<b>89</b>
<b>V.2. Preparation and characterization of proton-based iridates .....</b>	<b>89</b>
V.2.a. Synthesis of the Li/Na-based precursor materials .....	89
V.2.b. Proton-exchange reaction in acidic media.....	90
<b>V.3. Electrochemical properties of H<sub>3.4</sub>IrO<sub>4</sub>.....</b>	<b>99</b>
V.3.a. Li intercalation cathode in organic electrolyte .....	99
V.3.b. Pseudocapacitive material in aqueous electrolyte .....	101
V.3.c. Proton positions .....	107
V.3.d. Charge compensation by Ir .....	109
<b>V.4. Conclusion .....</b>	<b>110</b>
<b>General conclusions.....</b>	<b>111</b>
<b>Annexes .....</b>	<b>115</b>
<b>A.1. Structural characterization.....</b>	<b>115</b>
A.1.a. Laboratory X-ray diffraction (XRD) .....	115
A.1.b. Synchrotron XRD .....	115
A.1.c. Neutron diffraction (ND).....	116
<b>A.2. Electrochemical characterization.....</b>	<b>117</b>
A.2.a. Electrode preparation.....	117
A.2.b. Electrochemical cells .....	117
A.2.c. Electrochemical cycling .....	120
<b>A.3. X-ray absorption spectroscopy .....</b>	<b>122</b>
A.3.a. Data collection and pre-treatment.....	122
A.3.b. Analysis of EXAFS data .....	122
A.3.c. Analysis of XANES data.....	123

<b>A.4. Additional experimental techniques .....</b>	<b>124</b>
A.4.a. Transmission electron microscopy (TEM) .....	124
A.4.b. X-ray photoemission spectroscopy (XPS) .....	124
A.4.c. Density Functional Theory (DFT) calculations .....	125
A.4.d. Thermogravimetric analysis - mass spectrometry (TGA-MS) .....	125
<b>A.5. Additional experimental results.....</b>	<b>126</b>
A.5.a. EXAFS fits.....	126
<b>References .....</b>	<b>129</b>
<b>List of figures .....</b>	<b>141</b>
<b>List of tables .....</b>	<b>145</b>

*The importance of models in science is often underestimated. Models represent more complex classes of related systems and contribute to the study of those classes by focusing research on particular, tractable problems. The development of useful, widely accepted models is a critical function of scientific research: many of the techniques (both experimental and analytical) and concepts of science are developed in terms of models; they are thoroughly ingrained in our system of research and analysis.*

*- George M. Whitesides -*



## General introduction

The production and consumption of energy at the beginning of the 21<sup>st</sup> century have reached levels with major environmental repercussions that calls for a paradigm shift in the way we produce, distribute and use energy. Short-term alternatives need to be found to fossil fuels, which have a large impact on climate change by producing greenhouse gases. To this extent, renewable energies from wind and solar sources, among others, are considered by many countries as a realistic solution to produce unlimited energy with low environmental impact. This will not only require a complete transformation of our energy infrastructures, to solve the intermittence issue of these energy sources, but also to adapt our current technology based on fossil fuels to electricity.

Improving energy storage therefore stands as a key challenge with the objectives of facilitating the transition to electric vehicles and renewable energy sources in the next years. To reach these goals, several technologies are being developed that try to meet the performances required for diverse applications. Among them, electrochemical energy storage means such as batteries, fuel cells and electrochemical capacitors currently stand as the winning combination to meet this challenge in the next years by covering a large range of energy and power densities.

A worldwide effort from the scientific community is currently attached to understanding and solving the different bottlenecks limiting the performance of these systems. In the case of batteries, a major challenge is to improve the maximum capacity stored by finding new materials for both the positive and negative electrodes. Since 1991 and the development of the first Li-ion batteries based on  $\text{LiCoO}_2$  and graphite, the capacity of the positive electrode has barely increased from 135 mAh/g for  $\text{LiCoO}_2$  to 200 mAh/g for today's best cathode materials, showing the difficulty to design new materials with high capacities. The most promising materials so far are the layered Li-rich "NMC", which hold to their promise of delivering up to 300 mAh/g, thus doubling the capacity of the cathode. This family presenting unexpectedly large capacity is struggling with different issues that prevent their implementation in commercial Li-ion batteries. To solve these issues, fundamental studies to understand the chemical origin of these properties were undertaken in our group through simple model materials based on Ru or Ir, leading to a new paradigm in the development of cathode materials, i.e. using the redox properties of oxygen instead of the transition metal

present in the material. This process, known as anionic redox, has triggered the discovery of a large number of materials with capacities exceeding 300 mAh/g, but still lacks fundamental understanding.

In this work, we studied the electrochemical properties of different iridate materials to progress in our understanding of anionic redox. Although iridium is a rare and expensive element that cannot be considered for applications, it appeared as an excellent model material for anionic redox due to its high structural stability under electrochemical stress. In this line, we could study a variety of iridates by changing the nature and amount of insertion cations ( $H^+$ ,  $Li^+$ ,  $Na^+$ ) in the structure and observe the effect on the redox properties of these materials.

This work is divided in five chapters:

The first chapter details more precisely the Li-ion and Na-ion battery technologies and summarizes the important developments to improve the capacity of these systems. The most recent results on anionic redox will be presented to clarify our current knowledge of this new process and the questions that remain unanswered at this point.

The second chapter focuses on the electrochemical properties of the Na-rich layered iridate  $Na_2IrO_3$ , which shows a combined cationic and anionic redox activity upon cycling and well-defined structural transitions when Na is removed from the structure.

The third chapter describes the results we obtained in our attempt to partially substitute Na with Li in the previous material to form  $Na(Li_{1/3}Ir_{2/3})O_2$  and modify the redox properties of the material. This material can be synthesized but shows an unexpected instability upon the first charge that limits its use.

In the fourth chapter, the amount of alkali metal in the material is increased at the expense of iridium to form a new layered phase  $Li_3IrO_4$ . The modification of the Li/Ir ratio in the structure has a strong impact on the balance between cationic and anionic redox. This new material shows a reversible intercalation of 3.5 Li for only one Ir, the largest capacity reported for cathode materials based on intercalation reactions.

The fifth chapter further explores the potential applications of the new  $Li_3IrO_4$  phase by treating it in acid to form the protonated phase  $H_3IrO_4$ . This new material conserves the

rich electrochemical properties of its parent phase by showing a large activity in both non-aqueous (vs. Li) and aqueous (vs. capacitive carbon) electrolytes. The large capacitance and fast kinetic observed in aqueous electrolyte open interesting opportunities to develop pseudocapacitive materials.

To conclude, the main results of this work will be summarized and their impact on the development of new materials with large capacity for energy storage will be discussed.



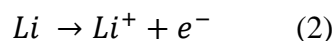
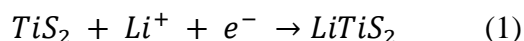
## Chapter I. State of the art

### I.1. From intercalation chemistry to Li/Na-ion batteries

#### I.1.a. Intercalation chemistry in low dimensionality solids

Primary and secondary (i.e. rechargeable), batteries based on electrochemical reactions have been used for a long time, but it is only with specific developments in solid-state chemistry that Li-ion batteries have been made possible.

In the 1970s, several research groups are interested in the synthesis of low dimensionality solids based on transition metal for their peculiar magnetic and electronic properties. Among these materials, sulfides readily form two-dimensional layered structures, e.g. layers of  $MS_2$  composition (M = transition metal) separated by a “van der Waals gap” (Figure I.1a). The stability of these structures resides in the equilibrium between strong ionocovalent interactions inside the  $MS_2$  layers and weak van der Waals forces between them. In 1975, Whittingham *et al.* reported on the intercalation of Li in these layered structures using a chemical reducing agent n-butyl lithium,<sup>1</sup> leading to the insertion of one Li per formula unit to form  $LiTiS_2$ . This work triggered the idea of an electrochemical system based on Li insertion in layered materials with the demonstration of the first Li battery (Figure I.1c), using  $Li_xTiS_2$  as a cathode and metallic Li as the anode according to the two reversible reactions (1) and (2),<sup>2</sup> and a similar system based on  $MoS_2$  was patented in 1980.<sup>3</sup>



In parallel, the synthesis of layered transition metal oxides was developed in the solid-state group of Bordeaux (France). Because of the high electronegativity of oxygen, layered phases with  $MO_2$  compositions cannot be formed directly due to the strong repulsion between oxygen from neighbouring layers. However, layered structures can be formed that already contain alkali cations such as  $LiMO_2$  or  $NaMO_2$  (Figure I.1b), as the positively charged alkali ions screen the repulsive interaction between adjacent oxygens. The difference in cation size between alkali and transition metal drives a segregation of the cations in alternating layers. The covalence of the  $M^{3+}-O^{2-}$  bond also competes with the more ionic interaction between  $Li^+$

and  $O^{2-}$ . Several layered phases were identified containing Mn, Co, Cr, with different stacking sequences depending on the nature (Li, Na, K) and content of alkali ions, leading to a nomenclature of layered transition metal oxides by Delmas *et al.*,<sup>4</sup> based on the coordination of the alkali (octahedral = O, prismatic = P, tetrahedral = T) and the number of  $MO_2$  slabs needed to describe the periodicity of the stacking sequence in the material (e.g. O3, P3, P2, T1...). In 1980, Mizushima *et al.* demonstrated the reversible electrochemical properties of  $LiCoO_2$  (Figure I.1d),<sup>5</sup> and proposed that Li-based layered oxides could be considered as high energy density cathode materials, with higher potential compared to sulfur-based compounds. Similar achievements were realized the same year by Braconnier *et al.* with the reversible cycling of Na in  $Na_xCoO_2$ .<sup>6</sup> These first successes were the starting point of a search for new oxides with Li/Na intercalation properties,<sup>7-13</sup> with notably the interesting behavior of the spinel material  $LiMn_2O_4$ <sup>14</sup>, and later extended to polyanionic materials containing  $(XO_4)^{n-}$  anionic groups ( $X = S, P, \dots$ ) with the discovery of the widely used olivine  $LiFePO_4$ .<sup>15</sup>

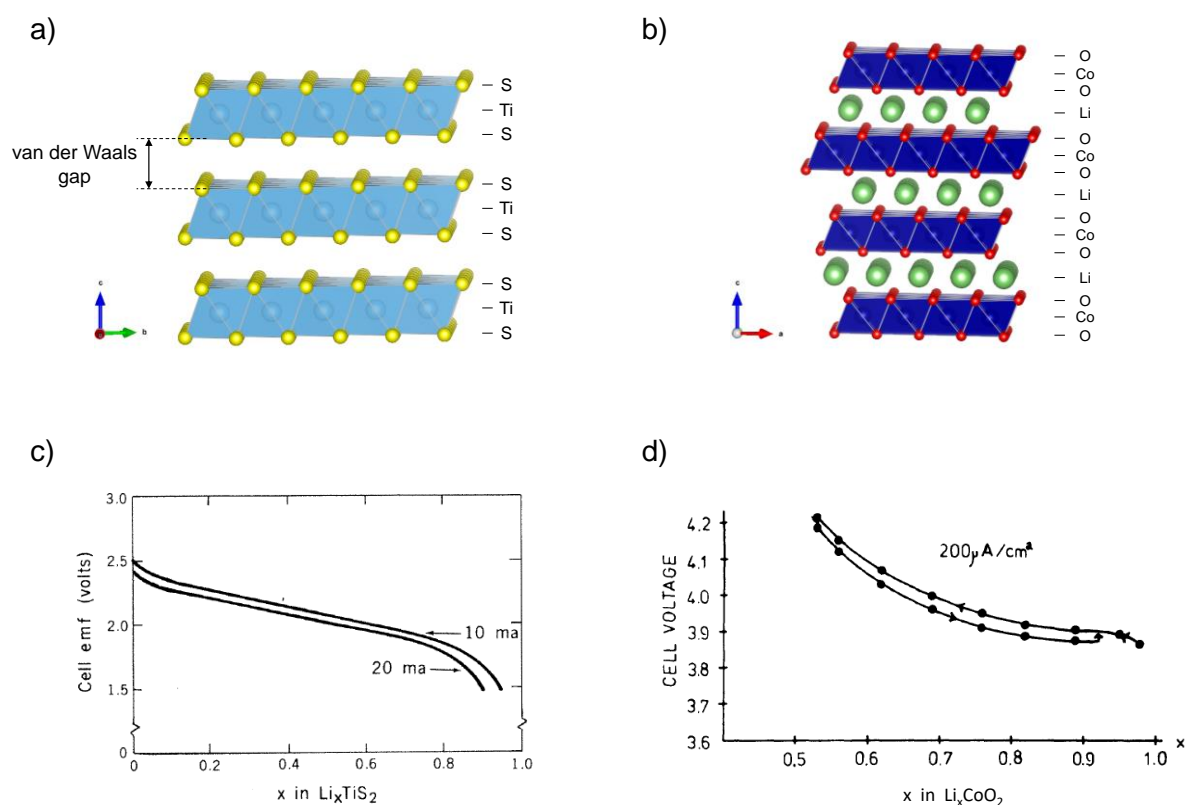


Figure I.1 : Intercalation in low dimensionality materials. Layered structures of  $TiS_2$  (a) and  $LiCoO_2$  (b). Li ions can be reversibly intercalated/deintercalated in or out of the van der Waals gap upon chemical or electrochemical reduction/oxidation (c and d). Adapted from Whittingham<sup>2</sup> and Mizushima *et al.*<sup>5</sup>

### I.1.b. From Li batteries to Li-ion batteries

At the end of the 1980s, despite the large progresses made in cathode materials for Li batteries, their commercial success was still impeded by unresolved safety issues, among which the reactivity of the organic electrolyte used with metallic Li and the dendritic growth of Li on the anode upon successive plating/stripping, eventually leading to short-circuits and a possible inflammation of the cell (Figure I.2a). Among the solutions proposed to solve these problems was the idea of M. Armand to replace the organic electrolyte by a polymer electrolyte (Figure I.2b),<sup>16</sup> which prevents the formation of dendrites, a strategy that is used nowadays in the Bluecars developed by the Bolloré group.<sup>17</sup> The second strategy consisted in replacing the metallic lithium by an intercalation material<sup>18</sup> with a Li insertion potential low enough to achieve decent cell voltages (Figure I.2c). This was made possible by the development of cokes, quickly replaced by graphite, that intercalate lithium at very low potentials, leading to the announcement by SONY in 1990 of a “rocking-chair” or lithium-ion battery based on  $\text{LiCoO}_2$  and carbon, in which  $\text{Li}^+$  ions transfer from one intercalation electrode to another upon successive charge and discharge, and are never present in the form of metallic lithium. This first announcement was closely followed by a  $\text{LiNiO}_2$ /carbon cell from Moly Energy<sup>19</sup> and a system based on the spinel  $\text{LiMn}_2\text{O}_4$ /carbon by BellCore.<sup>20</sup> The technology developed by SONY met an important success and started the widespread development of Li-ion batteries for portable electronics.

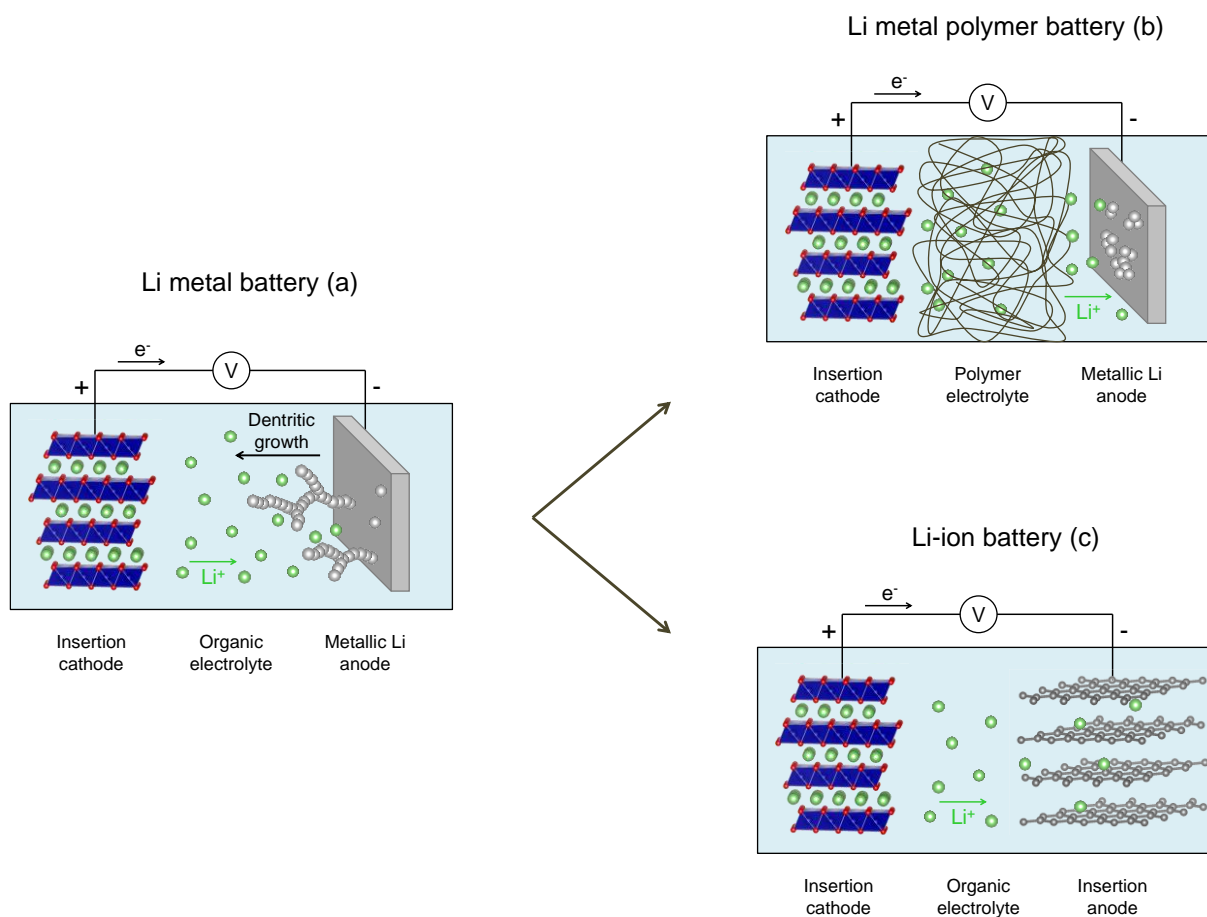


Figure I.2 : Schematic representation of Li batteries. The cathode (positive electrode) and anode (negative electrode) are separated by an electrolyte with good ionic conductivity. In batteries using metallic Li anodes (a), the dendritic growth of Li upon charge can short-circuit the battery, making it unsafe. Replacing the liquid organic electrolyte by a polymer electrolyte blocks the formation of dendrites and increases the safety of the cell (b). Metallic Li can also be replaced by anode materials which intercalate  $Li^+$  ions at low potentials such as graphite in Li-ion batteries (c).

### I.1.c. The more erratic development of Na-ion batteries

Due to the success of Li-ion batteries, the search for materials intercalating Na lost all interest for many years. In addition to the intrinsically lower performances compared to Li (higher weight, lower potential), several issues hindered their development, such as the moisture sensitivity of Na-based layered oxides and of metallic Na, the absence of a proper anode as graphite does not intercalate Na, and the higher solubility of Na salts compared to Li salts, preventing the formation of a stable solid electrolyte interphase (SEI), whose role is to limit electrolyte decomposition by passivating the highly reducing anode.

Since 2010, a renewed interest in Na-ion batteries has stemmed from the belief that lithium reserves could be insufficient to support the development of large scale storage systems and the expected transition from fuel to electric vehicles. Large progresses have been

made, with especially the development of hard carbons as suitable anode materials<sup>21</sup> and electrolyte additives<sup>22</sup> to form more stable SEI layers on the anode. An increasing number of potential cathode materials are reported, among which layered oxides and polyanionic compounds show the most interest. Although no commercial battery has reached the market yet, several prototypes have been announced, such as the first “18650” Na-ion prototype in 2015 by the French Network on Electrochemical Energy Storage.<sup>23</sup>

#### I.1.d. Post Li-ion technologies and their promises

The Na-ion battery is only one of the systems currently studied to replace or compete with Li-ion batteries. Several technologies have the potential to surpass the current Li-ion systems by increasing drastically the specific energy stored (Figure I.3). However, these technologies are still far from commercialization as they are struggling with several issues that require deep fundamental understanding to be overcome.

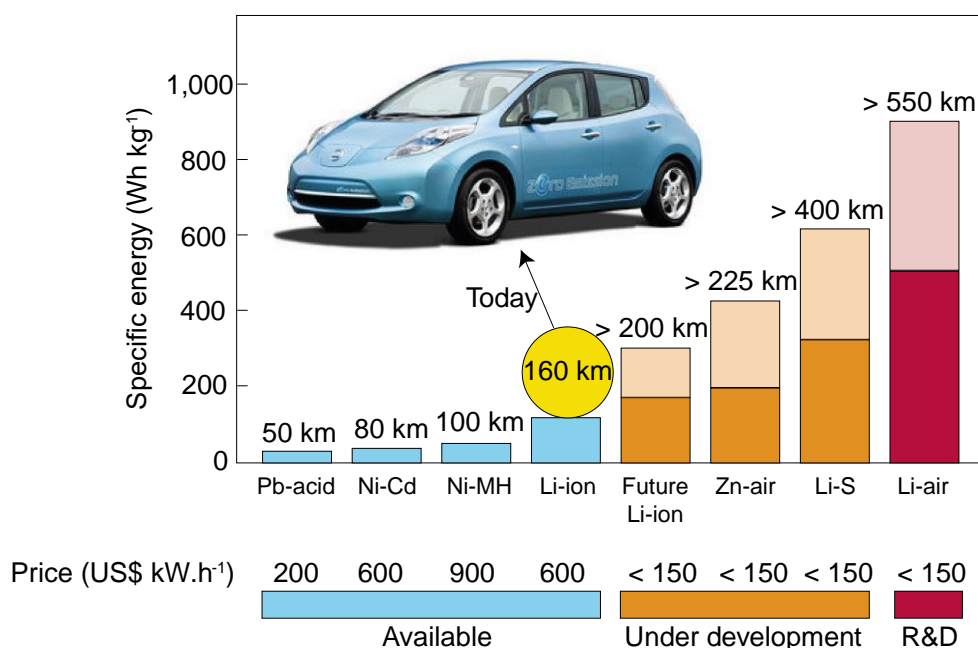


Figure I.3 : Specific energy, estimated driving range and cost of available battery technologies compared to systems under development. Adapted from Bruce *et al.*<sup>24</sup>

Li-O<sub>2</sub> batteries, also called Li-air batteries, rely on the plating/stripping of metallic Li on one side, and the reversible formation of Li<sub>2</sub>O<sub>2</sub> on the other side (Figure I.4a).<sup>24</sup> This technology could theoretically give energy densities 5 to 10 times higher than Li-ion batteries, but parasitic reactions, as well as high overpotentials, among other problems, limit its development.

Li-S batteries hold similar promises based on the reaction of Li with S (Figure I.4b).<sup>24</sup> However, one major issue is the solubility of intermediate polysulfides  $\text{Li}_2\text{S}_x$  formed that act as redox shuttles between the cathode and anode, leading to capacity fade.

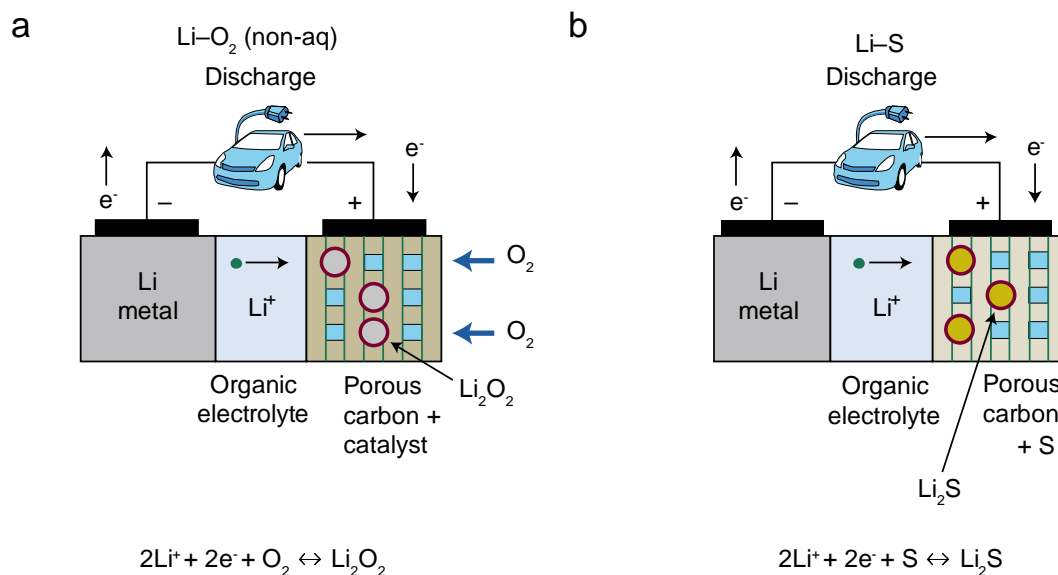


Figure I.4 : Schematic representations of Li- $\text{O}_2$  and Li-S batteries. Adapted from Bruce *et al.*<sup>24</sup>

An interesting characteristic of these systems is that they rely on the redox properties of species (O, S) that only play the role of ligand in materials for Li-ion battery in which they are considered to be electrochemically inactive.

Other systems are also studied based on the intercalation of multivalent cations ( $\text{Mg}^{2+}$ ,  $\text{Ca}^{2+}$ ) in host materials. Nevertheless, all these systems are far from achieving the degree of maturity and performance of the Li-ion system, which can also benefit from large improvements in term of capacity, voltage and cyclability.

## I.2. Increasing the capacity of cathode materials for Li-ion batteries

### I.2.a. Transition metal substitution

The development of the  $\text{LiCoO}_2/\text{C}$  lithium-ion battery started a race to improve the performances of the cell, notably by increasing the capacity of the cathode material. In  $\text{LiCoO}_2$ , only 0.5 Li can be removed reversibly for a capacity of 130 mAh/g. Further delithiation, in an attempt to achieve larger capacities was demonstrated by Amatucci *et al.* in 1996 by stabilizing the fully delithiated  $\text{CoO}_2$  phase with an O1 structure.<sup>25</sup> Although long-



## I.2.b. Li-rich materials with excess Li in the transition metal layers

As early as 1988, James and Goodenough investigated the electrochemical behavior of  $\text{Li}_2\text{MoO}_3$ ,<sup>12</sup> a layered oxide with a larger content of Li compared to the  $\text{LiMO}_2$  family.  $\text{LiMO}_2$  and  $\text{Li}_2\text{MO}_3$  type materials share similar structures, with the latter containing excess Li in the metallic layers, so that it can also be described as  $\text{Li}(\text{Li}_{1/3}\text{M}_{2/3})\text{O}_2$  (Figure I.6). A comparable study followed in 1996 by Kobayashi *et al.* using  $\text{Li}_2\text{RuO}_3$ <sup>36</sup> with, in both cases, more than 1 Li removed from the material.

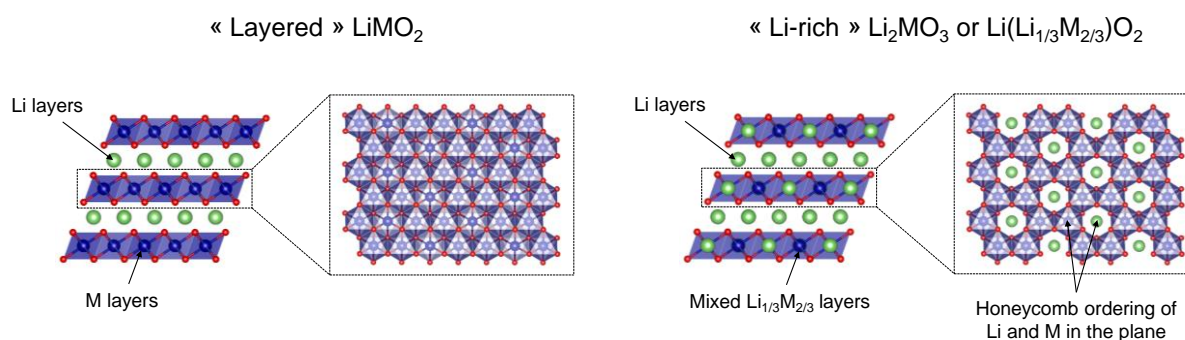


Figure I.6 : Structural difference between the classical layered  $\text{LiMO}_2$  phases and the Li-rich  $\text{Li}_2\text{MO}_3$  phases. In the  $\text{LiMO}_2$  structure (left), all octahedral sites in the metal layer are occupied by  $\text{M}^{3+}$  cations, whereas in the  $\text{Li}_2\text{MO}_3$  phases, one third of the sites is occupied by  $\text{Li}^+$  and two thirds by  $\text{M}^{4+}$  cations.

As 3d transition metals were preferred for applications, little interest was given to these Li-rich materials until Kalyani *et al.* showed that Li could be removed from  $\text{Li}_2\text{MnO}_3$  when charged above 4.5 V, that he attributed to the  $\text{Mn}^{4+}/\text{Mn}^{5+}$  redox couple.<sup>37</sup> This result was totally unexpected as Mn in octahedral coordination does not usually reach the +5 oxidation state. Several studies followed trying to activate further the electrochemical activity of  $\text{Li}_2\text{MnO}_3$ , notably to improve the reversibility of the process by acid-leaching,<sup>38,39</sup> and to find a more reasonable explanation to the redox activity. Among them the loss of oxygen together with  $\text{Li}^+$  removal, oxidation of the electrolyte and exchange of  $\text{Li}^+$  by protons were advanced.<sup>40</sup> Solid solutions between the Li-rich  $\text{Li}_2\text{MnO}_3$  and layered  $\text{LiMO}_2$  with  $\text{M} = \text{Cr}, \text{Ni}$  or  $\text{Co}$  were investigated by Dahn and coworkers, giving materials with large reversible capacities ( $> 200$  mAh/g) after a first activation cycle which was shown to correspond to oxygen loss upon Li removal.<sup>41</sup> Eventually, materials with Ni, Co, Mn and Li in excess, called “Li-rich NMC” were identified as particularly promising for Li-ion batteries (Figure I.5),<sup>42</sup> thus producing an abundant literature in the following years. Concurrent patents were registered based on different description of very similar materials, i.e. “solid-solution

$x \text{Li}(\text{Mn}_{1/2}\text{Ni}_{1/2})\text{O}_2 - y \text{LiCoO}_2 - z \text{Li}(\text{Li}_{1/2}\text{Mn}_{2/3})\text{O}_2$ <sup>43</sup> or “composite  $\text{Li}_2\text{MnO}_3\text{-LiMO}_2$  with nano-domains”<sup>44</sup>, depending on the synthesis method, overall leading to a lot of confusion about the nature of the materials and the mechanism responsible for their high capacity. Despite the large emulation created around these promising materials and several attempts to transfer them to the automotive industry, severe issues became apparent that still prevent their commercialization in Li-ion batteries.

### **I.2.c. The drawbacks of high energy density Li-rich cathode materials**

Li-rich NMC materials, whatever their composition, share the common feature that they need to be charged to high potential on the first cycle before showing a reversible cycling behavior on the next cycles. As the large capacity on the first cycle could not be fully attributed to the redox of metal cations, it was rapidly speculated to come from the release of oxygen from the material<sup>45</sup> and finally proved by measuring  $\text{O}_2$  gas release using differential electrochemical mass spectrometry (DEMS).<sup>46</sup> This oxygen loss is accompanied by a densification of the material at the surface in the case of  $\text{Li}_{1.2}\text{Mn}_{0.54}\text{Co}_{0.13}\text{Ni}_{0.13}\text{O}_2$ ,<sup>47</sup> but this mechanism cannot be applied to the bulk material, leaving some capacity unexplained by classical cationic redox mechanisms.<sup>48,49</sup>

After the first activation cycle, these materials were found to suffer from several problems such as generation of  $\text{CO}_2$  gas formed because of the high reactivity of these materials, especially Ni-rich materials, with carbonate-based electrolytes at high potentials.<sup>50</sup> However, the main issues found in Li-rich NMC materials are the voltage decay and hysteresis building upon cycling which complicate the battery management in electric vehicles.<sup>51-53</sup> The complexity of this family of materials, containing Ni, Mn and Co, with properties largely depending on synthesis conditions, prevented a simple rationalization of the mechanisms at stake and therefore the possibility to find appropriate solutions.

## **I.3. Anionic redox as a new paradigm for high capacity cathode materials**

### **I.3.a. Model materials based on Ru and Ir**

To overcome the complexity of Li-rich NMC and gain fundamental understanding on these unanswered questions, simplified model systems were used, in which Co, Ni and Mn

were replaced by only one electrochemically active element. Sathiya *et al.* reported the electrochemical behavior of the  $\text{Li}_2\text{Ru}_{1-y}\text{Sn}_y\text{O}_3$  solid solution,<sup>54</sup> which shows similar features as Li-rich NMC: activation through two plateaus on the first charge and a sloping charge/discharge behavior on the next cycles, resulting in reversible capacities higher than 200 mAh/g with good capacity retention and very little voltage decay. It was shown that Ru and O participate equally to the charge compensation, through the  $\text{Ru}^{4+}/\text{Ru}^{5+}$  redox couple and the formation of “peroxo-like”  $(\text{O}_2)^{n-}$  species whose signal was spotted both with XPS and EPR spectroscopy (Figure I.7). This first report with experimental evidence of oxygen redox reversibility in a Li-rich cathode material was the starting point for the search of new oxides with high capacity based on anionic redox. By changing the Sn substituent with Ti, it was also possible to reproduce the continuous voltage decay observed in Li-rich NMC, and to confirm its correlation with the trapping of small cations in tetrahedral sites.<sup>55</sup> Such a mechanism is in line with the progressive formation of rock-salt or spinel-like domains in Li-rich NMC upon cycling.<sup>51</sup> Additionally, the hysteresis which lowers the round-trip energy efficiency of Li-rich NMC was also studied with the model  $\text{Li}_2\text{Ru}_{0.75}\text{Sn}_{0.25}\text{O}_3$  compound and associated with the anionic redox activity in the material, suggesting a slower kinetic for anionic processes compared to cationic ones.<sup>56</sup>

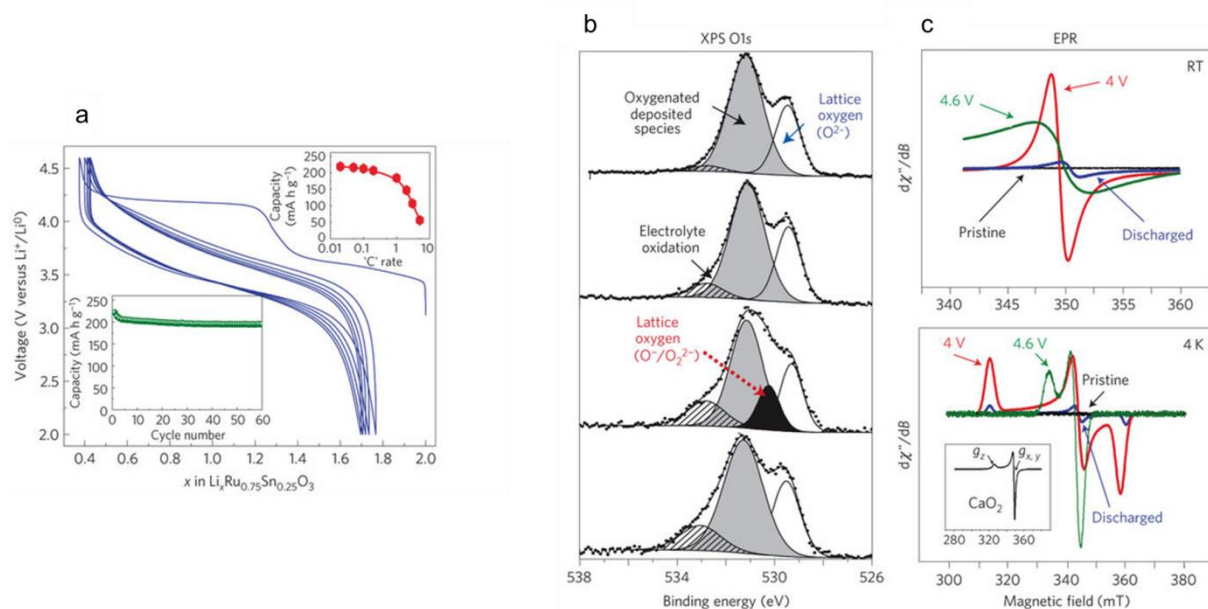


Figure I.7 : Electrochemical behavior of the model compound  $\text{Li}_2\text{Ru}_{0.75}\text{Sn}_{0.25}\text{O}_3$ . The material is activated upon the first charge with a staircase-like voltage profile, followed by a smooth curve on the next cycles which results in more than 200 mAh/g reversible capacity (a) This large capacity comes from the reversible oxidation of Ru and O, with the formation of peroxo-like species detected by XPS (b) and EPR spectroscopy (c). Adapted from Sathiya *et al.*<sup>54</sup>

Despite the large array of questions answered by Ru-based compounds, the massive cationic migrations in the material did not allow detailed structural studies of the anionic network during cycling. To clarify this issue, Ru was replaced by Ir, a 5d metal less prone to migrate from the metallic sites to the empty Li sites during cycling, as suggested by early reports from Kobayashi *et al.*<sup>57</sup> showing that the two-step voltage curve of  $\text{Li}_2\text{IrO}_3$  is maintained upon cycling, unlike Li-rich NMC and Ru-based compounds. The structural evolution of the layered  $\text{Li}_2\text{IrO}_3$  was reinvestigated,<sup>58</sup> indeed showing that Ir does not migrate and retain the layered structure up to  $\text{Li}_{0.5}\text{IrO}_3$ . To minimize the strain at low Li content, the  $\text{IrO}_3$  layers stacking changes from O3 to O1. This ideal situation, in which all layers are perfectly aligned on top of each other, made it possible to visualize by electron microscopy the projection of O-O peroxo-like dimers formed on oxidation (Figure I.8), further confirmed by neutron diffraction. O-O distances as short as 2.4 Å were found, a value still far from the 1.5 Å O-O distances in very ionic peroxides such as  $\text{Li}_2\text{O}_2$ . In addition to this discovery, Ir was found to be a promising platform to stabilize different structures upon strong electrochemical stress and study the chemistry of oxygen redox.

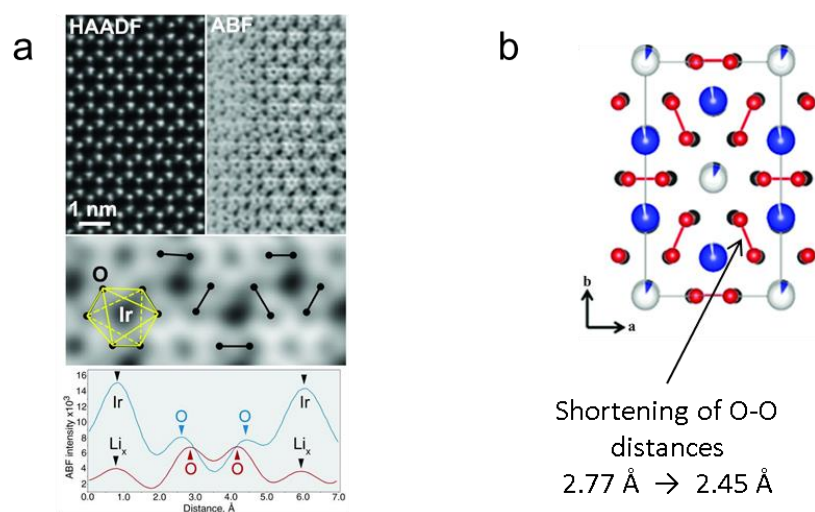


Figure I.8 : Visualization of short O-O distances in  $\text{Li}_{0.5}\text{IrO}_3$  by electron microscopy. The structural change from O3 to O1 upon Li deintercalation from  $\text{Li}_2\text{IrO}_3$  permits to observe the projection of the O columns in the material using annular bright field scanning transmission electron microscopy (ABF-STEM) imaging (a) Oxidation of oxygen leads to shortening of O-O bonds consistent with the formation of  $(\text{O}_2)^{n-}$  species (b). Adapted from McCalla *et al.*<sup>58</sup>

### I.3.b. A source of creativity for new material design

In the 4 years following the first evidence on oxygen activity in Li-rich oxides, an increasingly large number of new materials were designed to take advantage of the high capacities offered by anionic redox, and to bring new knowledge about this process. Among

them, it is worth mentioning the generalization of anionic redox to Na-rich layered oxides with the  $\text{Na}_2\text{Ru}_{1-y}\text{Sn}_y\text{O}_3$  phases.<sup>35</sup> The comparison between an ordered and disordered  $\text{Na}_2\text{RuO}_3$  materials suggested that honeycomb ordering in the metallic planes was necessary to activate anionic redox,<sup>59</sup> but this result is in contradiction with the fact that anionic redox can be triggered in a large family of Li-rich rocksalt oxides with disordered cation distribution.<sup>60–64</sup> In addition to layered and disordered rocksalts, a high temperature polymorph ( $\beta$ ) of the layered  $\text{Li}_2\text{IrO}_3$  ( $\alpha$ ),<sup>65</sup> with an ordered tridimensional distribution of Ir atoms, showed an increased stability upon complete delithation to  $\beta\text{-IrO}_3$ , with a large participation of oxygen to the redox activity. These reports largely open the path for the design of new high capacity materials based on anionic redox, thus requiring a good understanding of the oxygen redox chemistry.

### I.3.c. Anionic redox: current understanding of the electronic structure

At this point, it is pertinent to summarize our understanding of anionic redox chemistry, especially in terms of electronic structure. It is well known that O can adopt different formal oxidation states when associated to cations whose ionization energy is too high to give up another electron, such as  $\text{Li}^+$ ,  $\text{Na}^+$ ,  $\text{K}^+$ ,  $\text{Ca}^{2+}$ ,  $\text{Zn}^{2+}$  [...] to form molecular oxygen ions such as  $\text{O}_2^{2-}$  or  $\text{O}_2^-$ . However, it is less common in transition metal oxides, in which electrons are easily transferred from the metal nd orbitals to the low-lying oxygen 2p orbitals to form  $\text{O}^{2-}$ . Within the common approximation of a purely ionic crystal, oxygens are only considered as localized negative charges which interact with the transition metal orbitals through electrostatic stabilization (Figure I.9). Depending on the coordination of the transition metal, the crystal field lifts the degeneracy of the five d orbitals, e.g. in three  $t_{2g}$  orbitals ( $d_{xy}$ ,  $d_{yz}$ ,  $d_{xz}$ ) and two  $e_g$  orbitals ( $d_{x^2-y^2}$ ,  $d_{z^2}$ ) in the case of octahedral coordination. During electrochemical oxidation/reduction, the d levels just below/above the Fermi level are emptied or filled, respectively, explaining the established understanding of electrochemical activity in terms of cationic redox.

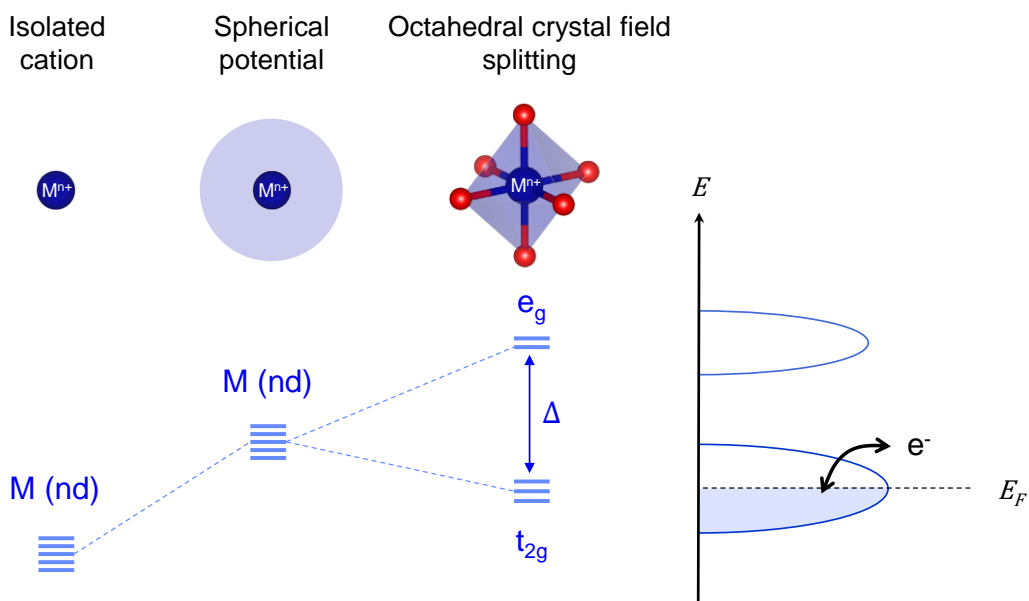


Figure I.9 : Ionic model of the electronic structure in transition metal oxides. In an octahedral crystal field, the d orbitals are splitted between  $t_{2g}$  and  $e_g$  orbitals by a value  $\Delta$ .

However, this ionic picture does not always stand. When increasing the electronegativity of the transition metal (i.e. to the right of the periodic table or by increasing its oxidation state), increasing the size of d orbitals (i.e. moving from 3d metals to 4d and 5d metals) or using less electronegative anions (i.e. S or Se instead of O), the M-X bond (M = transition metal, X = ligand) becomes more covalent due to the larger overlap and lower energy difference between M(d) and X(p) orbitals. In that case, M(d) and X(p) orbitals form bonding M-X and antibonding M-X\* orbitals according to the ligand field theory (Figure I.10a), the latter being situated at the Fermi level and responsible for the electrochemical activity of the material. This situation has led Ceder *et al.* to suggest, in 1997, that charge compensation in  $\text{LiCoO}_2$  was due to both Co and O.<sup>26,27</sup> Tarascon *et al.*, as mentioned earlier, observed that the oxidation of O was concomitant with a shortening of the O-O distance, and linked this observation to the pioneering work of Jean Rouxel on anionic redox in chalcogenides. Because of the lower electronegativity of X = S, Se or Te compared to O, it is not uncommon that the X(p) orbitals stand at the Fermi level instead of M(d) orbitals, resulting in a transfer of electrons from the X(p) orbitals to the M(d) orbitals and forming dimers ( $X_2^{2-}$ ), trimers ( $X_3^{2-}$ ) or even “polymeric chains” of oxidized anions.<sup>66</sup>

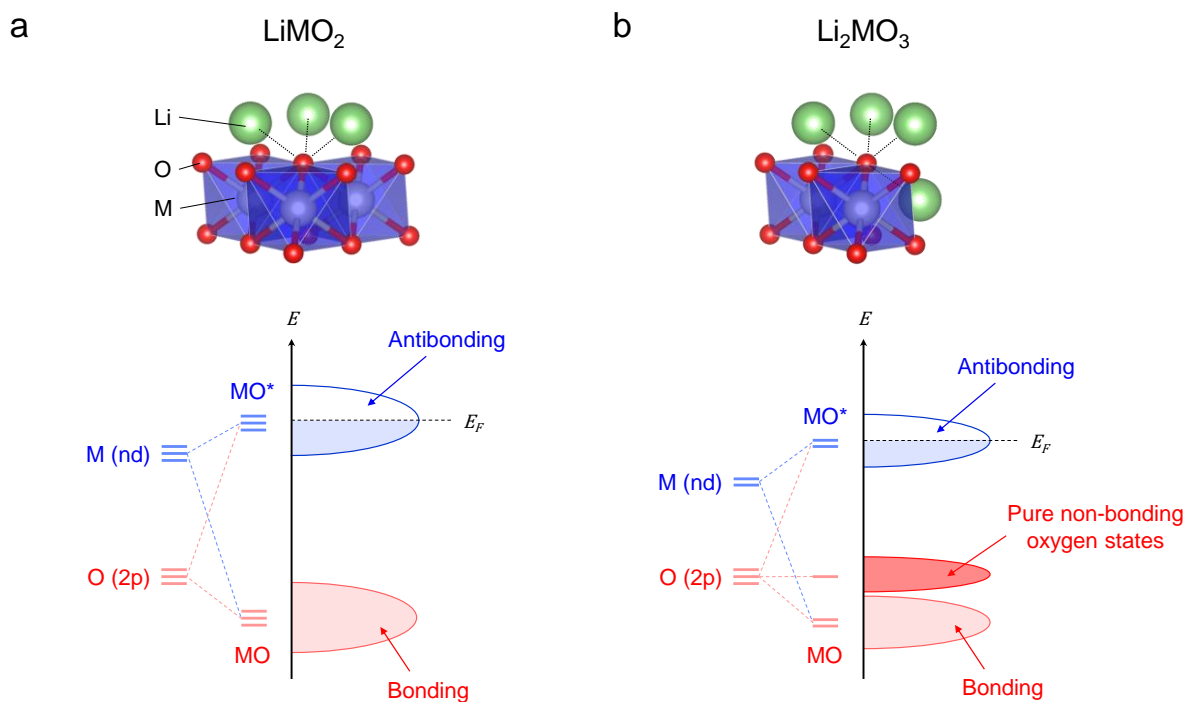


Figure I.10 : Molecular orbital diagram of transition metal oxides. (a) In  $\text{LiMO}_2$ , the  $\text{M}(\text{np})$  and  $\text{O}(2\text{p})$  orbitals form bonding  $\text{MO}$  and antibonding  $\text{MO}^*$  orbitals with a dominant oxygen and metallic character, respectively. (b) In  $\text{Li}_2\text{MO}_3$ , oxygens atoms are coordinated by only two metals, so that part of the  $\text{O}(2\text{p})$  orbitals do not have the good symmetry to participate in  $\text{MO}$  bonds and remain as pure  $\text{O}$  non-bonding states.

In classical layered oxides with formula  $\text{LiMO}_2$ , all  $\text{O}(2\text{p})$  orbitals participate in antibonding and bonding orbitals (Figure I.10a), suggesting that participation of anions to the redox is limited to the oxidation/reduction of antibonding  $\text{M-O}^*$  levels, which remains mostly cationic by nature.  $\text{MO}$  bonding levels, which are mostly anionic, stand too low in energy to be reached. When moving to Li-rich  $\text{Li}_2\text{MO}_3$  compounds, the replacement of  $\text{M}$  by  $\text{Li}$  in the metallic layers leaves some  $\text{O}(2\text{p})$  orbitals that are unable to participate in  $\text{M-O}$  bonds (Figure I.10b). These non-bonding  $\text{O}$  levels, called “unhybridized”, “orphans” or “lone-pairs” in the literature, are now commonly accepted to be at the origin of pure anionic redox,<sup>67–69</sup> although the question of whether the oxidation of these levels creates localized holes on the oxygen<sup>70</sup> or leads to the formation of  $(\text{O}_2)^{n-}$  dimers as in  $4\text{d}/5\text{d}$  model compounds<sup>54,58</sup> is difficult to answer and requires the use of sophisticated experimental techniques for each new material. Furthermore, questions regarding the reversibility of anionic redox, the reactivity of surface oxygen with the electrolyte, or the stability of the material upon oxygen oxidation, remain mostly unanswered. It is therefore crucial to bring solid fundamental understanding on oxygen redox in order to design viable high energy density materials for Li-ion batteries.

## I.4. Conclusion

This first chapter described the principal aspects of the development of Li-ion batteries, from the beginning of intercalation chemistry in layered materials to the recent paradigm shift represented by anionic redox in the design of high capacity cathode materials. This is clearly a long journey, and the energy density achieved by commercial systems has slowly increased over the past years. But each step forward opens a large array of new applications, from portable electronics to electric vehicles, which strongly impacts society.

High capacity cathode materials relying on anionic redox could represent the next large step forward, provided that the numerous issues preventing their application are addressed and solved. Identifying the redox properties of oxygen and the origin of its activity opened the door to new materials with high capacity. Understanding the parameters controlling this new chemistry will help in solving the issues mentioned above. In this context, the stability of Ir-based oxides makes them excellent model materials to explore the redox properties of oxygen.

In this work, we investigate the electrochemical properties of several iridate materials with different intercalation cations ( $\text{H}^+/\text{Li}^+/\text{Na}^+$ ) and different ratios between alkali and transition metal ions, in order to understand how the electronic properties of the material are affected by the oxygen environment.



## Chapter II. Anionic redox in Na-rich layered oxides: study of Na<sub>2</sub>IrO<sub>3</sub>

### II.1. Introduction

Na-ion batteries, as mentioned in the first chapter, benefit from a renewed interest as a potential storage system for large scale applications, due to the lower cost of Na compared to Li, and the possibility to replace the expensive Cu current collector of Li-ion cells with a cheaper one made of Al, since Al does not alloy with Na at low potential. However, in order to reach the market, the performances of Na-ion cells need to get closer to those of Li-ion batteries. This will rely on the development of cathode materials with both high energy density and long cyclability. Na-based layered oxides, with Na<sub>x</sub>MO<sub>2</sub> formula (M = transition metal), provide a great versatility of compositions and structures, offering an opportunity to tune their electrochemical properties. However, most of these layered oxides present a limited energy density because of their low Na content together with their low redox voltage. The P2-Na<sub>2/3</sub>[Fe<sub>1/2</sub>Mn<sub>1/2</sub>]O<sub>2</sub> phase, which contains ~0.7 Na per formula unit and shows a redox voltage of ~2.8 V vs Na<sup>+</sup>/Na, has achieved the best performance (140 mAh/g) up to now<sup>71</sup>. To alleviate this energy density issue, research is presently parted between searching for i) new polyanionic compounds besides Na<sub>3</sub>V<sub>2</sub>(PO<sub>4</sub>)<sub>2</sub>F<sub>3</sub>, which shows a higher redox voltage (~3.6 V vs Na<sup>+</sup>/Na) for a capacity of 120 mAh/g and ii) new layered phases having larger capacities.

Following this second approach, and in light of the knowledge acquired on anionic redox from Li-rich layered oxides, Rozier *et al.* investigated the solid-solution Na<sub>2</sub>Ru<sub>1-y</sub>Sn<sub>y</sub>O<sub>3</sub> and found that high capacity (up to 1.3 Na<sup>+</sup>) could be obtained at 2.8 and 3.8 V vs Na<sup>+</sup>/Na, based on the Ru<sup>4+</sup>/Ru<sup>5+</sup> and O<sup>2-</sup>/(O<sub>2</sub>)<sup>n-</sup> redox couples.<sup>72</sup> Mortemard de Boisse *et al.* compared two polymorphs of Na<sub>2</sub>RuO<sub>3</sub>, with and without honeycomb ordering of Ru and Li in the (Na<sub>1/3</sub>Ru<sub>2/3</sub>) layers, and found that extra capacity due to anionic redox only arises in the ordered material, thus proposing that honeycomb order is required to trigger anionic redox. The origin of such difference however remains unclear as Li-rich disordered materials have been reported to undergo anionic redox. Furthermore, as with Li-rich materials, voltage fade from cationic migration or oxygen loss upon cycling hinder the careful analysis of Na-rich materials, leaving some questions unanswered.

How does the insertion/deinsertion of large and highly polarizable ions ( $\text{Na}^+$ ) into these rocksalt oxide structures affect the anionic redox mechanism, the massive cation migration and capture in interstitial tetrahedral sites, and the stability of the reactive  $(\text{O}_2)^{n-}$  oxygenated species towards the release of  $\text{O}_2$  during electrode charging? To address the first question, we decided, for the sake of simplicity, to study the Na-based iridium phase  $\text{Na}_2\text{IrO}_3$  with the hope to bypass  $\text{O}_2$  release and cation migration.<sup>73</sup>

## II.2. Synthesis and structure

The  $\text{Na}_2\text{IrO}_3$  compound was first identified in the  $\text{Na}_2\text{O}$ - $\text{IrO}_2$  phase diagram by McDaniel in 1974 (Figure 2.1).<sup>74</sup> The phase is formed by heating at  $800^\circ\text{C}$ , in air, stoichiometric amounts of  $\text{Na}_2\text{CO}_3$  and  $\text{IrO}_2$  or Ir. This report already signals the instability of the material formed in contact with air at room temperature, an issue clarified by Krizan *et al.* showing that  $\text{Na}_2\text{IrO}_3$  reacts with moisture and  $\text{CO}_2$  to form hydrated sodium carbonates and a Na-poor  $\text{Na}_x\text{IrO}_3$  phase.<sup>75</sup> For this study, the material was therefore prepared by mixing  $\text{Na}_2\text{CO}_3$  and Ir using a mortar and pestle, heating the precursors in a covered alumina crucible a first time at  $800^\circ\text{C}$  for 48h, reground, and heated a second time at  $900^\circ\text{C}$  for 24h. After each step, the furnace was slowly cooled to  $600^\circ\text{C}$  and the sample was quickly transferred to an Ar-filled glovebox to avoid reaction with air.

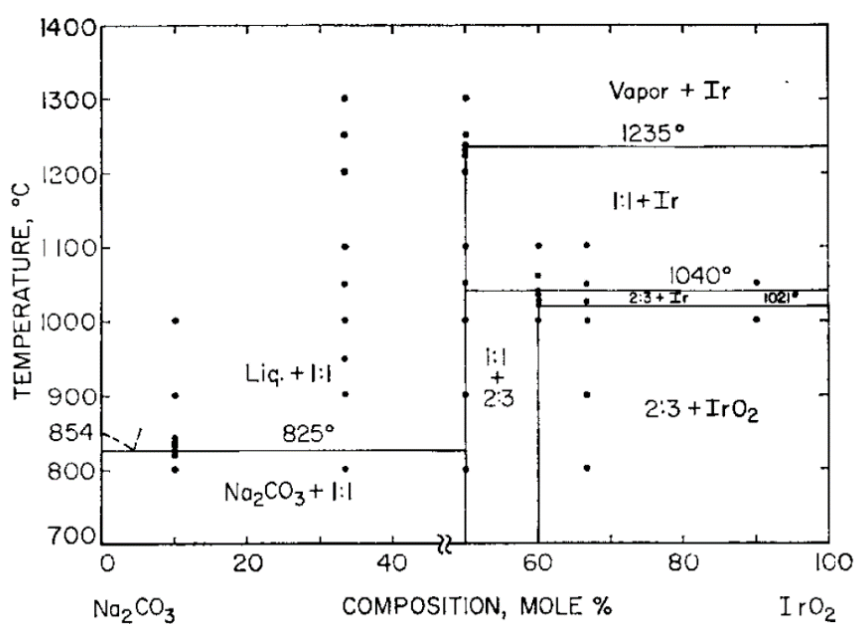


Figure II.1: Phase diagram of the  $\text{Na}_2\text{O}$ - $\text{IrO}_2$  system from McDaniel<sup>74</sup>

The structure of the as-prepared Na<sub>2</sub>IrO<sub>3</sub>, which can also be written as Na[Na<sub>1/3</sub>Ir<sub>2/3</sub>]O<sub>2</sub>, is derived from the rocksalt structure, with a framework of cubic close-packed oxygens and cations occupying the octahedral sites. Segregation of Na<sup>+</sup> and Ir<sup>4+</sup> cations leads to a layered structure, with pure Na layers alternating with mixed Na<sub>1/3</sub>Ir<sub>2/3</sub> layers, in which Ir<sup>4+</sup> and Na<sup>+</sup> are distributed in a honeycomb pattern. Using the notation introduced by Delmas *et al.*<sup>4</sup>, Na<sub>2</sub>IrO<sub>3</sub> has an O3 structure, where O stands for the octahedral coordination of Na in the Na layers, and 3 for the number of [Na<sub>1/3</sub>Ir<sub>2/3</sub>]O<sub>2</sub> layers needed to describe the oxygen stacking (ABCABC).

The synchrotron X-ray powder diffraction (SXRD, see A.1.b for details) pattern (Figure II.2a) was refined using the Rietveld method and fitted with a monoclinic *C2/m* unit cell ( $a = 5.43004(3)$  Å,  $b = 9.40163(5)$  Å,  $c = 5.61095(2)$  Å and  $\beta = 108.9660(4)^\circ$ ). In order to obtain a good fit, it was necessary to introduce some site mixing between Ir and Na in the Na<sub>1/3</sub>Ir<sub>2/3</sub> layers. However, this is an artificial way to reduce the intensity of the superstructure peaks in the 5-8° 2 $\theta$  region (see inset), and does not represent the real structure of the material. The asymmetric broadening of these superstructure peaks arises from the presence of stacking faults, as is commonly observed in Li-rich materials with honeycomb ordering such as Li<sub>2</sub>MnO<sub>3</sub>.<sup>76</sup>

To confirm the perfect ordering of Ir atoms, transmission electron microscopy (TEM) data were collected by D. Batuk and A. Abakumov at EMAT, Belgium (see A.4.a for details). The samples were measured without exposure to air using a special vacuum transfer holder. The long-range ordered sequence of close-packed oxygen layers, corresponding to the O3-type structure was confirmed (see [010] HAADF-STEM image in Figure II.3a). The [100] HAADF-STEM image of this sample (Figure II.3b) indicates perfect honeycomb cation ordering in the Na<sub>1/3</sub>Ir<sub>2/3</sub> layers, which can be seen by the rows of double closely projected Ir columns. However, numerous stacking faults are present, violating the perfect arrangement of the honeycomb layers.

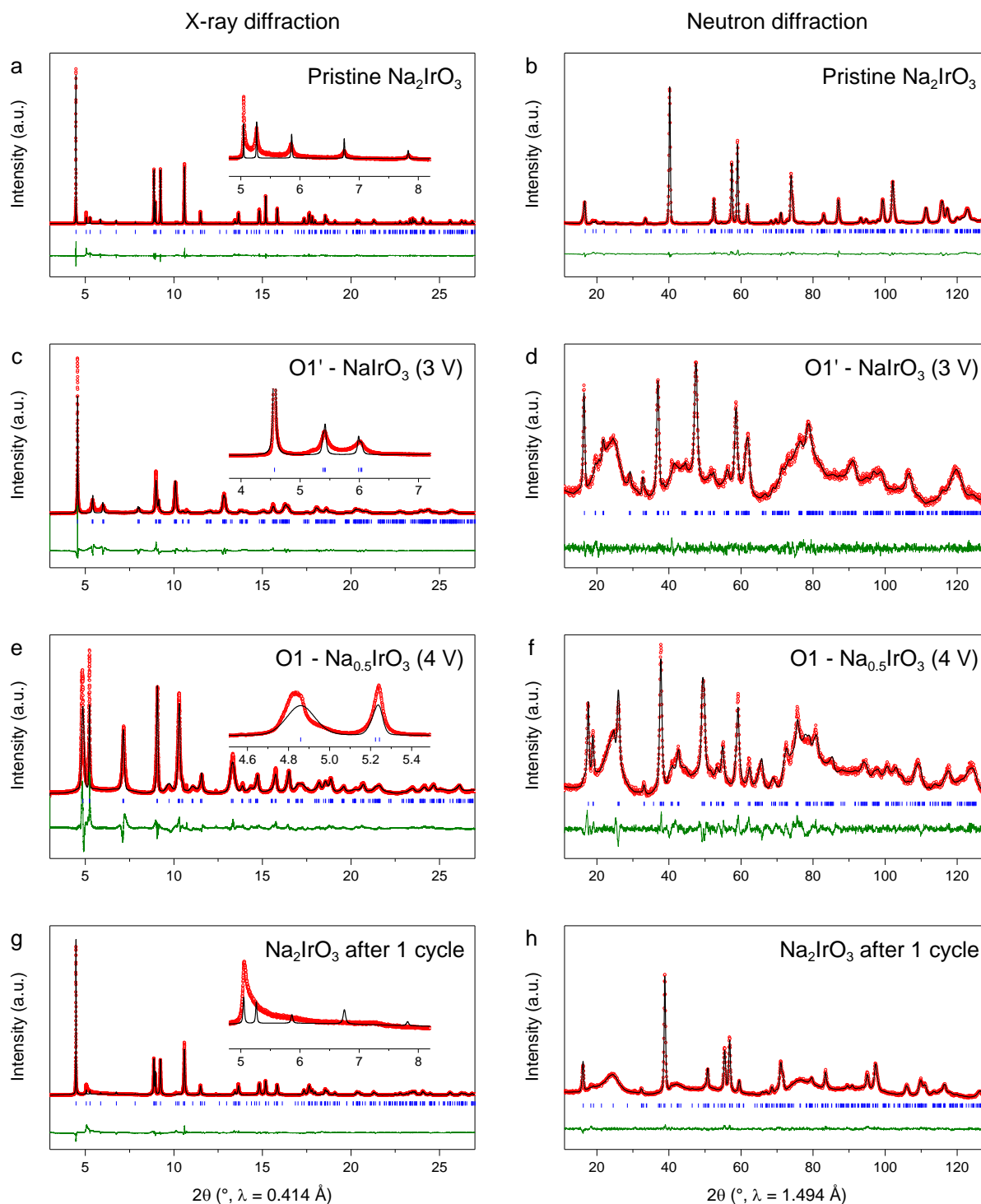


Figure II.2 : Rietveld refinement of diffraction data. Synchrotron X-ray (left) and neutron (right) diffraction data for the pristine  $\text{Na}_2\text{IrO}_3$  (a,b), charged  $\text{NaIrO}_3$  (c,d), fully charged  $\text{Na}_{0.5}\text{IrO}_3$  (e,f) and after a complete charge/discharge cycle (g,h). The experimental points, calculated pattern, difference pattern and Bragg positions are represented by red markers, black line, green line and blue ticks, respectively. The insets highlight specific peaks presenting broadening unaccounted for by the Rietveld method. Large broad peaks in the neutron diffraction pattern of the cycled samples are from the conductive carbon additive.

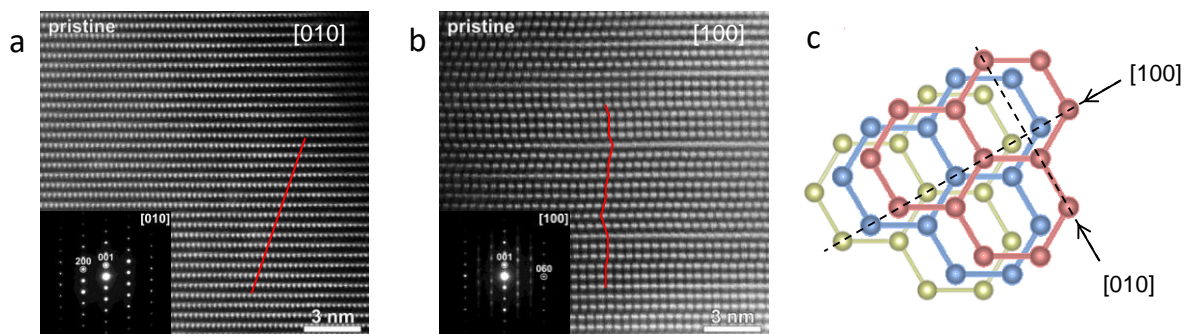


Figure II.3 : High resolution HAADF-STEM images and corresponding ED patterns for the pristine  $\text{Na}_2\text{IrO}_3$  indexed on the monoclinic lattice corresponding to the O3 structure. Red lines were added to highlight the perfect cubic close-packing ABCABC sequence (a) and the stacking faults in the honeycomb staking (b). A schematic of the ideal Ir honeycomb stacking is shown (c).

Refinement of the broadened superstructure peaks from the SXRD pattern can be done using the FAULTS software<sup>77</sup>, by adjusting the relative probabilities of different possible stacking vectors (Figure II.4). For the pristine material, neither a small amount of stacking fault (A) nor a completely faulted model (B) reproduce properly the shape of the peaks. A mixed model with 70% A and 30% B gives a better result. The shape of the superstructure peaks is best represented with a model using a combination of 30% of random stacking sequences and 70% of alternating short-range ordered stacking sequences.

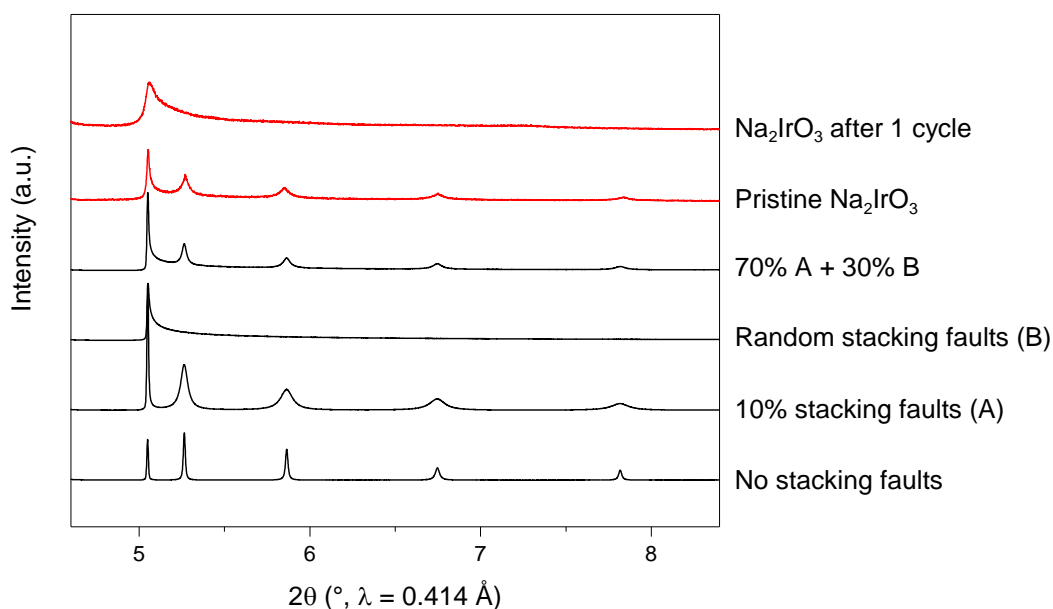


Figure II.4 : Broadening of the superstructure peaks can be modeled by the FAULTS program. Simulated curves with different stacking models (in black) are compared to the experimental data (in red).

Finally, as the X-ray diffraction pattern is dominated by the Ir contribution because of its high electron density, complementary neutron powder diffraction was used to obtain the accurate O and Na positions (see A.1.c for details). The final Rietveld refinement is shown in Figure II.2b and Table II.1 gathers the deduced structural information.

Table II.1 : Structural parameters of Na<sub>2</sub>IrO<sub>3</sub> obtained from Rietveld refinement of SXRD and neutron diffraction data.

<b>O3 - Na<sub>2</sub>IrO<sub>3</sub> pristine</b>						
Space group : C2/m						
		<i>a</i> (Å)	<i>b</i> (Å)	<i>c</i> (Å)	$\beta$ (°)	
SXRD		5.42810(3)	9.40318(3)	5.61056(3)	108.9611(5)	
ND		5.42698(14)	9.3969(2)	5.60614(10)	108.6371(18)	
Atom	Site	<i>x</i>	<i>y</i>	<i>z</i>	Occupancy	B (Å <sup>2</sup> )
O1	8 <i>j</i>	0.2572(6)	0.3190(3)	0.7944(4)	1	0.13(7)
O2	4 <i>i</i>	0.2916(9)	0	0.7934(10)	1	0.78(15)
Ir1	4 <i>g</i>	0	0.3339(2)	0	0.878(2)	0.292(8)
Na1	4 <i>g</i>	0	0.3339(2)	0	0.122(2)	0.292(8)
Na2	2 <i>a</i>	0	0	0	0.756(2)	0.61(3)
Ir2	2 <i>a</i>	0	0	0	0.244(2)	0.61(3)
Na3	4 <i>h</i>	0	0.8416(7)	0.5	1	0.85(7)
Na4	2 <i>d</i>	0	0.5	0.5	1	1.79(15)

Reliability parameters :  $\chi^2 = 6.60$ , Bragg R-factor = 12.1 % (SXRD)  
 $\chi^2 = 18.9$ , Bragg R-factor = 5.84 % (ND)

### II.3. Electrochemical properties

The electrochemical properties of Na<sub>2</sub>IrO<sub>3</sub> were investigated in Swagelok or 2032 coin cells (see A.2.b). The active material was used as a powder mixed with 20% conducting carbon or as a self-standing electrode using PTFE as a binder (A.2.a) and Na was used as an anode. At first, 1M NaPF<sub>6</sub> or NaClO<sub>4</sub> in ethylene carbonate (EC)/dimethyl carbonate (DMC) (1:1) were used as electrolytes, but a strong irreversible capacity and a rapid capacity decay were observed. The instability of linear carbonate in contact with metallic Na has been largely observed in the literature and complicates the use of Na as a stable reference electrode. To alleviate this issue, 1% of fluoroethylene carbonate (FEC) was used as an additive in NaClO<sub>4</sub>:EC:DMC since it enables high coulombic efficiency in Na half-cells, as reported by several groups.<sup>22,78</sup> The first two charge-discharge cycles are shown in Figure II.5.

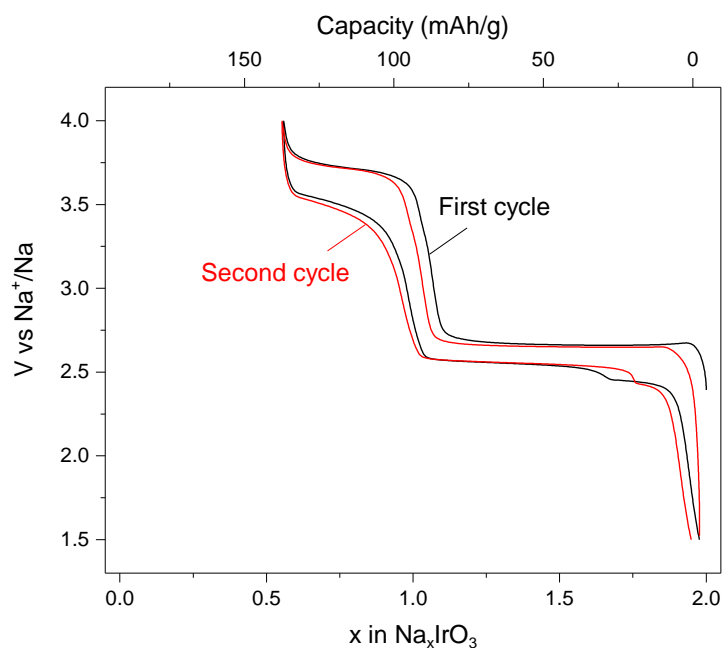


Figure II.5 : First and second galvanostatic cycles of  $\text{Na}_2\text{IrO}_3$  in a Na cell. The cell was cycled between 1.5 and 4 V at a rate of  $C/10$  (1  $\text{Na}^+$  exchanged in 10h).

During the first charge, the  $\text{Na}^+$  deintercalation proceeds through two plateaus at 2.7 V ( $2.0 > x > 1.0$ ) and 3.7 V ( $1.0 > x > 0.5$ ), respectively. They correspond to a cumulative removal of 1.5  $\text{Na}^+$ , which are fully reinserted on the subsequent discharge, leading to a reversible capacity of  $130 \text{ mAh.g}^{-1}$ . At the end of discharge, an extra polarization is observed, which has been explained by additional impedance when Na is stripped from below the resistive SEI layer formed by FEC.<sup>79</sup> This polarization can clearly be attributed to the anode side by using a three-electrode cell (A.2.b.iii) with a reference electrode to measure the potential of the cathode and anode independently (Figure II.6).

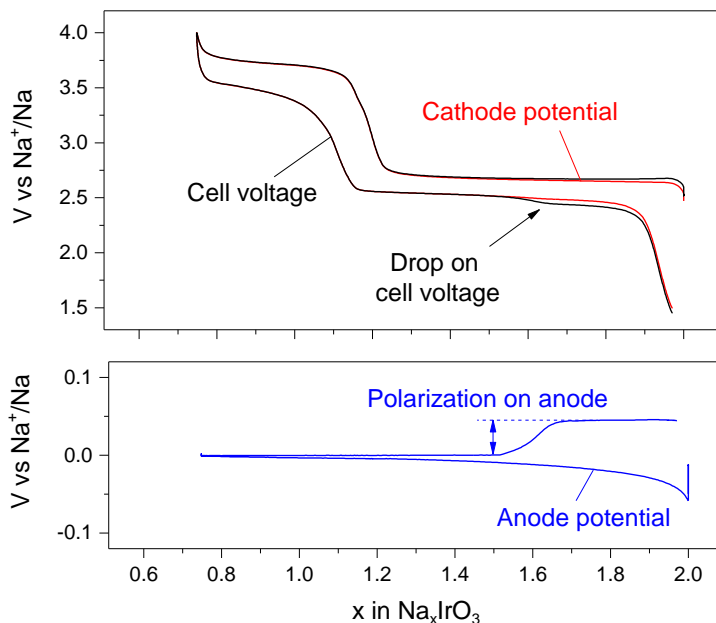


Figure II.6 : Electrochemical data obtained with a 3-electrode cell using Na as a reference electrode. The drop of cell voltage (black curve) at the end of the discharge is not observed on the potential of the cathode alone (red curve) but instead comes from extra polarization at the anode side (blue curve).

Unlike most Li-rich materials, the two plateaus are well preserved through the discharge on subsequent cycles. Such a behavior might indicate that, alike to  $\text{Li}_2\text{IrO}_3$ , the  $\text{Na}_2\text{IrO}_3$  material does not demonstrate pronounced Ir migration upon cycling. To check for the possible release of oxygen upon cycling, an Online Electrochemical Mass Spectrometry experiment was performed by E. J. Berg at PSI (Villigen, Switzerland). It resulted in a very small  $\text{O}_2$  release on the first and second cycles (Figure II.7) at the very end of charge ( $> 3.8$  V). This small quantity would correspond to only 0.06 % of the total oxygen content in the material if it was solely attributed to oxygen release from  $\text{Na}_2\text{IrO}_3$ . A release of  $\text{CO}_2$  is also observed, that probably comes from electrolyte decomposition on the Na anode. The possibility of electrolyte reacting with surface oxygen on  $\text{Na}_2\text{IrO}_3$  cannot be ruled out, but this is quite unlikely here as the material shows a good reversibility and no surface reconstruction is observed after cycling, unlike for Li-rich NMC.

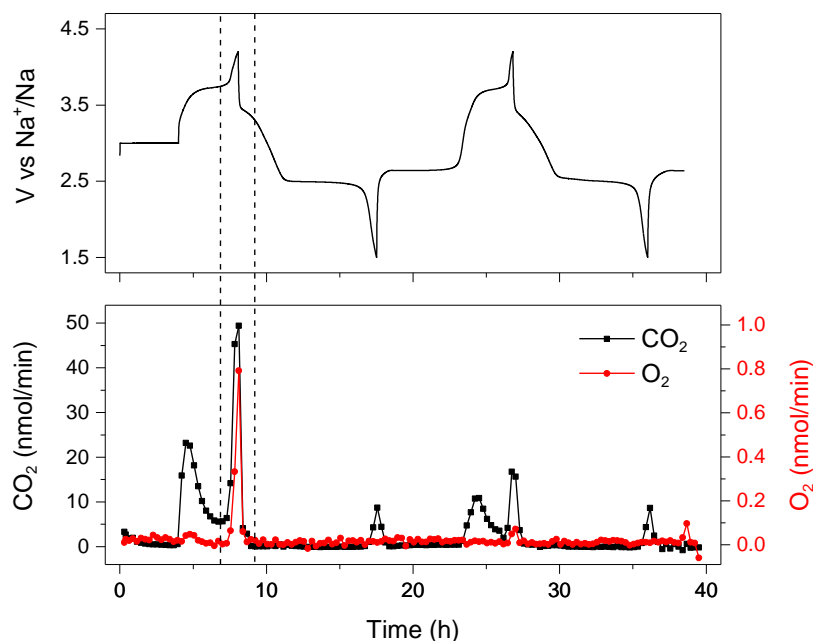


Figure II.7: Online Electrochemical Mass Spectrometry data for the first and second cycles, with the voltage curve (top) and the evolution rate of  $\text{CO}_2$  and  $\text{O}_2$  indicated in black and red respectively (bottom). The cycling started from the material precharged at 3 V to limit degradation in air while preparing the electrode. A small amount of  $\text{O}_2$  is detected at the very end of charge (between dashed lines).

## II.4. Structural evolution upon cycling

### II.4.a. *In situ* XRD study

*In situ* XRD was used to probe the structural evolution of  $\text{Na}_2\text{IrO}_3$  during the first cycle (Figure II.8). For this experiment, a Swagelok-modified electrochemical cell equipped with a Be window was used (A.2.b.v).<sup>80</sup> The cell was charged and discharged at C/20, and one hour diffraction patterns were continuously measured, giving a diffraction pattern every 0.05  $\text{Na}^+$  exchanged. The first plateau appears to be composed of two distinct processes: first a solid solution with a continuous modification of the lattice cell parameters, followed by a two-phase process, with the pristine phase disappearing at the expense of a new phase. The latter becomes pure at the end of the first plateau and has a composition close to  $\text{NaIrO}_3$ . The second plateau also corresponds to a two-phase process, leading to another phase with low Na content, close to  $\text{Na}_{0.5}\text{IrO}_3$  ( $\text{Na}/\text{Ir} = 0.50(8)$  according to the EDX analysis). These new intermediate and final phases were further characterized by TEM, synchrotron XRD and ND.

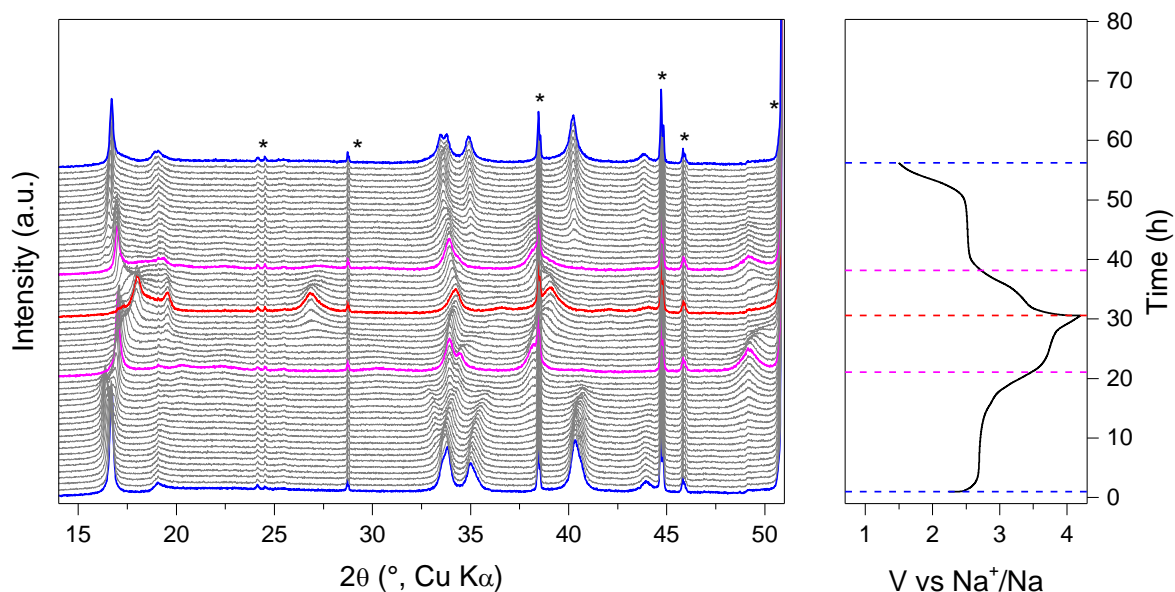


Figure II.8 : *In situ* XRD study of  $\text{Na}_2\text{IrO}_3$  cycled at C/20 between 1.5 V and 4 V (cycling curve shown on the right). The stacking of Ir layers changes reversibly from O3 (blue) to O1' (pink) and O1 (red). The peaks marked by an asterisk are from the *in situ* cell and are not affected by the cycling.

#### II.4.b. O1'- $\text{NaIrO}_3$

To isolate the intermediate structure appearing at the end of the first plateau, a cell was charged up to 3.2 V vs.  $\text{Na}^+/\text{Na}$ , hold at this voltage until the reaction completed and the cycled powder was recovered after washing with dimethylcarbonate (DMC) to remove traces of electrolyte. At the time of this study, Wallace and McQueen reported the synthesis of the same  $\text{NaIrO}_3$  phase using  $\text{Br}_2$  as a chemical oxidizing agent.<sup>81</sup> The structure they reported was used successfully to refine X-ray and neutron powder diffraction (Figure II.2cd). X-ray and neutron diffraction data for this structure can be indexed using a  $P\bar{1}$  space group with the cell parameters  $a = 5.28226(14) \text{ \AA}$ ,  $b = 5.27079(14) \text{ \AA}$ ,  $c = 5.99680(17) \text{ \AA}$ ,  $\alpha = 115.564(2)^\circ$ ,  $\beta = 90.121(3)^\circ$  and  $\gamma = 119.761(2)^\circ$  (Table II.2).

Table II.2 : Structural parameters of O1'-NaIrO<sub>3</sub> obtained from Rietveld refinement of SXRD and neutron diffraction data.

<b>O1' - NaIrO<sub>3</sub> (3V)</b>							
Space group : $P\bar{1}$							
		$a$ (Å)	$b$ (Å)	$c$ (Å)	$\alpha$ (°)	$\beta$ (°)	$\gamma$ (°)
SXRD		5.2887(3)	5.2809(2)	6.0323(3)	115.662(7)	90.597(8)	119.935(3)
ND		5.2912(7)	5.2841(7)	6.0468(8)	115.840(15)	90.479(12)	120.068(14)
Atom	Site	$x$	$y$	$z$	Occupancy	B (Å <sup>2</sup> )	
O1	2i	0.132(4)	0.521(6)	0.212(4)	1	0.37(14)	
O2	2i	0.700(3)	0.722(3)	0.182(3)	1	0.37(14)	
O3	2i	0.430(4)	0.159(5)	0.216(4)	1	0.37(14)	
Na1	1a	0	0	0	0	0.115(14)	
Ir1	1a	0	0	0	0.322(1)	0.115(14)	
Ir2	2i	0.349(3)	0.677(3)	-0.011(2)	0.839(1)	0.115(14)	
Na2	2i	0.868(3)	0.733(6)	0.5944(16)	1	2.33(17)	
Na3	1f	0.5	0	0.5	0	N/A	

Reliability parameters :  $\chi^2 = 36.1$ , Bragg R-factor = 16.8 % (SXRD)  
 $\chi^2 = 1.50$ , Bragg R-factor = 1.50 % (ND)

During charging from Na<sub>2</sub>IrO<sub>3</sub> to NaIrO<sub>3</sub>, the stacking of the oxygen sublattice changes from the cubic close-packed ABCABC arrangement, characteristic of the O3 structure, to the hexagonal close-packed ABAB arrangement referred to as O1 (Figure II.9a). In this structure, the Ir/Na sites are aligned on top of each other but the center of the honeycomb formed by Ir atoms is systematically shifted with respect to the center of the honeycomb below and above. As the classification introduced by Delmas *et al.*<sup>4</sup> does not take into account the different possible stackings of honeycomb ordered compounds, we refer to this compound as O1', to differentiate it from the O1 phase obtained upon delithiation of Li<sub>2</sub>IrO<sub>3</sub>.

Furthermore, HAADF-STEM images show that high concentration of stacking faults remains in the stacking sequence of the honeycomb layers, which is evident in Figure II.9b and the corresponding electron diffraction pattern. This issue, similar to the pristine Na<sub>2</sub>IrO<sub>3</sub> prevents a proper description of the peak shape by Rietveld refinement, as shown in the inset of Figure II.2a.

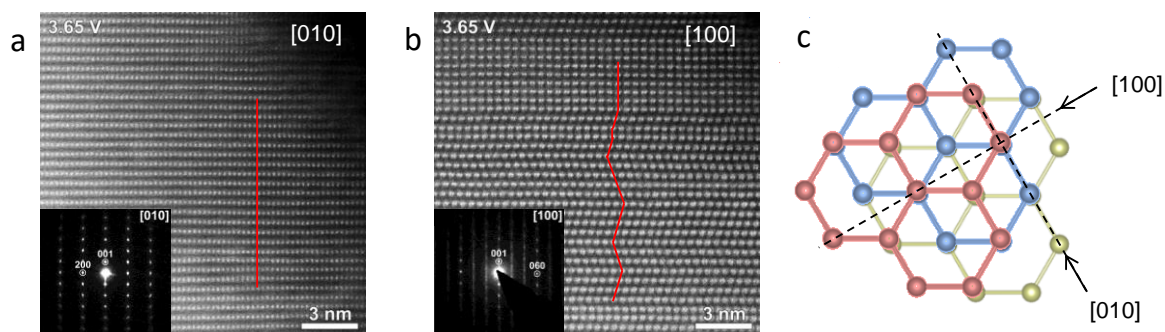


Figure II.9 : High resolution HAADF-STEM images and corresponding ED patterns for the charged O1'-NaIrO<sub>3</sub> indexed on the O1 lattice,  $a \approx 5.2 \text{ \AA}$ ,  $b \approx 9.1 \text{ \AA}$ ,  $c \approx 4.9 \text{ \AA}$  and  $\beta \approx 90^\circ$ . The perfect alignment of cations in the [010] projection reflects the hexagonal close-packed oxygen network (a) whereas some stacking faults remain in the honeycomb organization (b). The new stacking sequence of Ir honeycomb is represented in the schematic (c).

#### II.4.c. O1-Na<sub>0.5</sub>IrO<sub>3</sub>

The material was similarly charged to 4 V to isolate the final structure with chemical composition Na<sub>0.5</sub>IrO<sub>3</sub>. This structure is similar to that obtained on full charge for Li<sub>2</sub>IrO<sub>3</sub>. The corresponding X-ray and neutron diffraction profiles can be indexed using a  $C2/m$  space group with cell parameters  $a = 5.2534(2) \text{ \AA}$ ,  $b = 9.0633(2) \text{ \AA}$ ,  $c = 4.88271(19) \text{ \AA}$  and  $\beta = 89.482(17)^\circ$  (Figure II.2e-f and Table II.3). Removal of extra 0.5 Na<sup>+</sup> from O1'-NaIrO<sub>3</sub> results in a reorganization of the metallic layers but with the same ABAB oxygen stacking sequence (Figure II.10a). The O1 structure obtained differs from the previous O1' by a complete suppression of the lateral shifts of the honeycomb layers (Figure II.10b), so that the transition metal layers are stacked exactly on top of each other (Figure II.10c). However, complete and satisfying Rietveld refinements of the O1 and O1' diffraction patterns are hindered because of the presence of very broad and asymmetric peaks, probably related to anisotropic strain and stacking faults in the crystals. This can be viewed in the inset of Figure II.2e, which highlights the peculiar and asymmetric broadening of the (001) peak, pointing to a non-uniform distribution of interlayer distances in the O1 structure.

Table II.3 : Structural parameters of O1-Na<sub>0.5</sub>IrO<sub>3</sub> obtained from Rietveld refinement of SXRD and neutron diffraction data.

<b>O1 - Na<sub>0.5</sub>IrO<sub>3</sub> (4V)</b>						
Space group : <i>C2/m</i>						
		<i>a</i> (Å)	<i>b</i> (Å)	<i>c</i> (Å)	$\beta$ (°)	
SXRD		5.2534(2)	9.0633(2)	4.88271(19)	89.482(17)	
ND		5.2457(5)	9.0657(9)	4.8707(4)	89.249(6)	
Atom	Site	<i>x</i>	<i>y</i>	<i>z</i>	Occupancy	B (Å <sup>2</sup> )
O1	8 <i>j</i>	0.318(2)	0.3082(8)	0.7533(14)	1	3.72(19)
O2	4 <i>i</i>	0.346(2)	0	0.8122(18)	1	2.3(2)
Ir1	4 <i>g</i>	0	0.3339(13)	0	1	3.16(11)
Na1	2 <i>a</i>	0	0	0	0	N/A
Na3	4 <i>h</i>	0	0.33798	0.5	0	N/A
Na2	2 <i>c</i>	0	0	0.5	1	0.77(19)

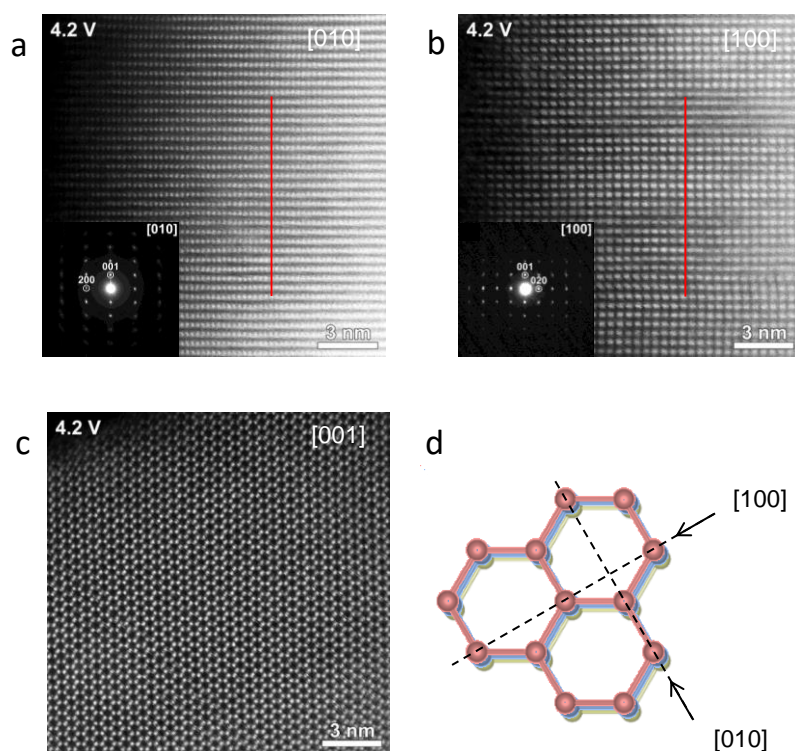
Reliability parameters :  $\chi^2 = 6.45$ , Bragg R-factor = 4.39 % (SXRD) $\chi^2 = 3.38$ , Bragg R-factor = 3.48 % (ND)

Figure II.10 : High resolution HAADF-STEM images and corresponding ED patterns for the fully charged O1-Na<sub>0.5</sub>IrO<sub>3</sub> indexed on the O1 lattice. The hexagonal close-packed oxygen network is preserved as seen on the [010] projection (a) and the Ir honeycombs are now perfectly aligned on top of each other (b). This situation allows one to observe the projection of Ir columns (c) perpendicular to the honeycomb planes as depicted in (d).

#### II.4.d. Reversibility after a complete cycle

The good reversibility of the voltage curve (Figure II.5) and the *in situ* experiment (Figure II.8) suggest that the structural transformations undergone by the material are reversible. To better assess this supposition, a sample was charged to 4 V and discharged to 1.5 V before analysis. The diffraction pattern is very similar to that of the pristine Na<sub>2</sub>IrO<sub>3</sub> material. X-ray and neutron diffraction data were indexed using the same monoclinic *C2/m* unit cell ( $a = 5.43086(5)$  Å,  $b = 9.40476(16)$  Å,  $c = 5.605504(5)$  Å and  $\beta = 108.8291(8)^\circ$ ). (Figure II.2g-h and Table II.4). The main difference with the pristine material is the broadening of the superstructure peaks in the 5-8° 2 $\theta$  region (inset), which indicates a larger number of stacking faults in the material. Simulation of this broadening with FAULTS suggests a completely random stacking of honeycomb layers (Figure II.4).

Table II.4 : Structural parameters after a full cycle obtained from Rietveld refinement of SXRD and neutron diffraction data.

O3 - Na <sub>2</sub> IrO <sub>3</sub> after 1 cycle						
Space group : C2/m						
		$a$ (Å)	$b$ (Å)	$c$ (Å)	$\beta$ (°)	
SXRD		5.43086(5)	9.40476(16)	5.60504(5)	108.8291(8)	
ND		5.4427(2)	9.4033(5)	5.5999(2)	108.778(5)	
Atom	Site	$x$	$y$	$z$	Occupancy	B (Å <sup>2</sup> )
O1	8j	0.256(2)	0.3349(9)	0.7926(15)	1	2.81(13)
O2	4i	0.279(3)	0	0.803(3)	1	4.0(2)
Ir1	4g	0	0.3202(6)	0	0.874(8)	2.61(13)
Na1	4g	0	0.3202(6)	0	0.126(8)	2.61(13)
Na2	2a	0	0	0	0.748(8)	0.6(2)
Ir2	2a	0	0	0	0.252(8)	0.6(2)
Na3	4h	0	0.830(2)	0.5	1	3.1(4)
Na4	2d	0	0.5	0.5	1	3.7(5)

Reliability parameters :  $\chi^2 = 10.4$ , Bragg R-factor = 11.8 % (SXRD)  
 $\chi^2 = 1.47$ , Bragg R-factor = 4.89 % (ND)

#### II.4.e. Minimization of cationic repulsions in the structure

The changes in stacking sequence observed upon removal of 1 and 1.5 Na<sup>+</sup> can be rationalized by looking at the positions occupied by Na<sup>+</sup> ions in the different structures, as deduced from neutron diffraction.

In the  $\text{O1}'\text{-NaIrO}_3$  structure, three different sites can be occupied (Figure II.11): the center of the Ir honeycomb (Na1), a doubly-degenerate site in the van der Waals gap between an Ir from one layer and the center of the honeycomb from the adjacent layer (Na2), and a site in the gap between two Ir atoms (Na3). Neutron diffraction suggests that the Na2 site is fully occupied, which corresponds to the site with minimum cationic repulsions. This structural evolution is similar to the one observed upon desodiation of  $\text{Na}_2\text{RuO}_3$  to  $\text{NaRuO}_3$ .<sup>59</sup>

When removing an extra  $0.5 \text{ Na}^+$  to form  $\text{Na}_{0.5}\text{IrO}_3$ , the stacking changes again, suggesting that the final O1 structure is more stable than the  $\text{O1}'$  for this stoichiometry. Looking at the Na sites (Figure II.11, right), one new site is formed with very little cationic repulsion which stands between empty sites of the honeycomb layer above and below (Na2). The sites in the center of the honeycomb layer (Na1) and between two Ir atoms (Na3) are closer to highly charged Ir atoms.

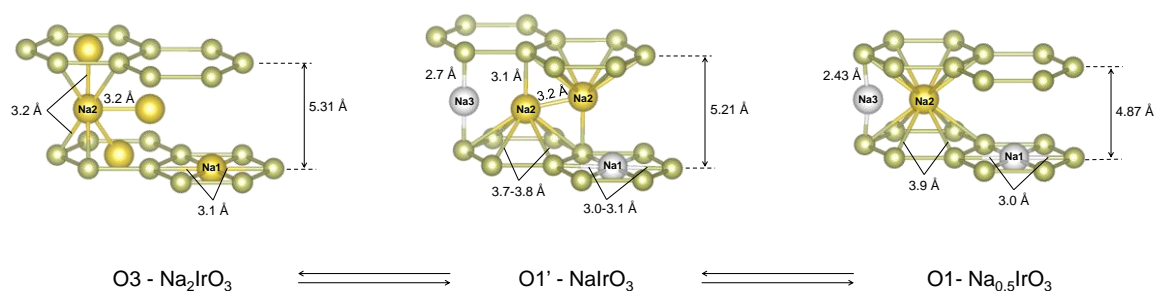


Figure II.11 : Possible Na positions for the pristine (left),  $\text{O1}'$  (center) and O1 (right) structures. Only cations are indicated for clarity, with the honeycomb formed by Ir atoms highlighted. Yellow atoms are the occupied positions and white balls represent sites left vacant with strong electrostatic repulsion from neighbouring cations.

DFT calculations performed by M. Saubanère and M.-L. Doublet at ICGM (Montpellier, France) confirmed that the structures found experimentally were the one presenting the lowest energy (Figure II.12, see A.4.c for details), and that structures with Na in the center of the honeycomb layers (Na1) were less stable than others, suggesting that this Na is removed first upon desodiation.

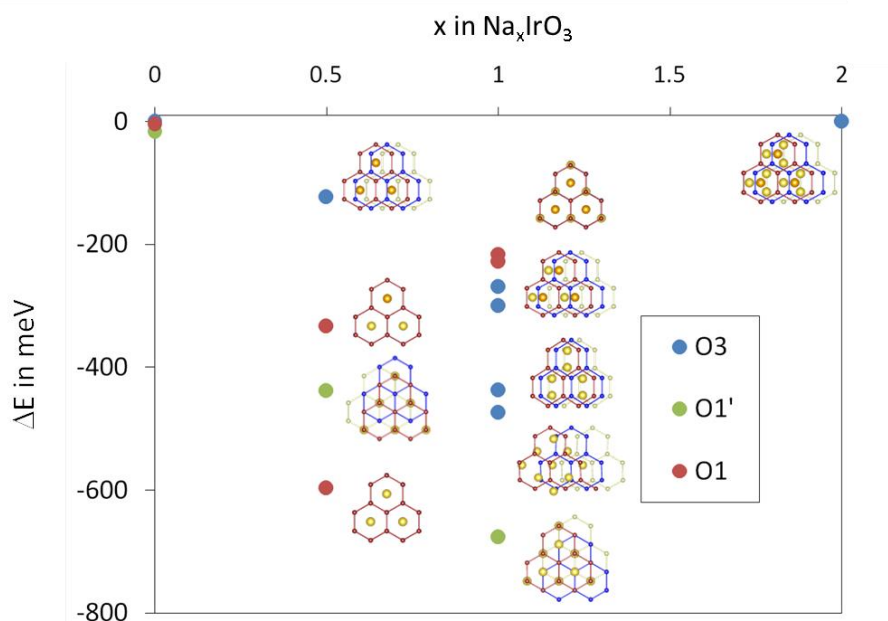


Figure II.12 : Phase stability diagrams of  $\text{Na}_2\text{IrO}_3$  computed with DFT-D3 and considering the different polymorphs O3, O1' and O1. It confirms the stability of the polymorph O1' (O1) for the  $\text{NaIrO}_3$  ( $\text{Na}_{0.5}\text{IrO}_3$ ) compositions. Selected structural organization of the different polymorph are displayed, highlighting the different stacking of the  $\text{NaIr}_2$  layer and the different positions of Na. Yellow and orange atoms refers to sodium in the Na and  $\text{NaIr}_2$  layers, respectively.

The complete alignment of the honeycombs in the O1- $\text{Na}_{0.5}\text{IrO}_3$  phase results in a very stable site for the remaining  $\text{Na}^+$  (Figure II.11). The stability of this site is most likely at the origin of our inability to electrochemically remove more than 1.5  $\text{Na}^+$  from  $\text{Na}_2\text{IrO}_3$  as it will hinder the ionic conduction in the two-dimensional planes. Alternative diffusion paths for  $\text{Na}^+$  exist and involve either i) its passage through octahedral sites sharing faces with two strongly repulsive Ir ions or ii) its 1D diffusion perpendicular to the layers, through the empty sites in the honeycombs; both of which are quite unlikely. Thus, the structural transition to O1 for Na-rich layered oxides is viewed as the origin of the practical capacity limitation of the material, and the same reasoning can be applied to Li-rich materials undergoing the same structural transition, such as in the layered  $\alpha\text{-Li}_2\text{IrO}_3$ . This conclusion was further confirmed through the study of  $\beta\text{-Li}_2\text{IrO}_3$ ,<sup>65</sup> a high temperature polymorph of  $\text{Li}_2\text{IrO}_3$  with a tridimensional framework which prevents this structural transition. As a result, all the  $\text{Li}^+$  can be removed from the  $\beta$  polymorph whereas the layered  $\alpha$  phase has a capacity limited to 1.5  $\text{Li}^+$ .

## II.5. Participation of Ir and O to the redox

Similar to the Li-rich materials, the 130 mAh·g<sup>-1</sup> reversible capacity on the first cycle cannot be explained only by a classical cationic redox mechanism with oxidation of Ir<sup>4+</sup> to Ir<sup>5+</sup>. To understand in depth the charge compensation mechanism in this material, several characterization techniques were used, including X-ray photoemission spectroscopy (XPS), X-ray absorption (XAS), TEM and neutron diffraction to follow the structural distortions corresponding to these processes.

### II.5.a. X-ray photoemission spectroscopy study

*Ex situ* samples at different states of charge were measured using XPS by D. Foix at IPREM (Pau, France), with the detail of the experiment in A.4.b. Figure II.13 shows the evolution of Ir 4f and O 1s peaks for Na<sub>x</sub>IrO<sub>3</sub> with x = 2.0 (pristine), 1.5 (pristine + O1'), 1.0 (O1') and 0.5 (O1). The Ir 4f peaks shifts towards higher binding energy during the first plateau (2.0 > x > 1.0), indicative of the oxidation of Ir<sup>4+</sup>, and broadens for x = 1.5 as this corresponds to a biphasic composition of O3-Na<sub>2</sub>IrO<sub>3</sub> and O1'-NaIrO<sub>3</sub>. At x = 1.0, the shape of the Ir 4f peak recovers its original width. The Ir peak does not shift upon further removal of Na (1.0 > x > 0.5), suggesting that iridium is not involved in the redox mechanism at high potential. Turning to the corresponding evolution of the O 1s peaks (Figure II.13b), we observe the emergence of a peak indicating oxidized oxygen species (O<sub>2</sub>)<sup>n-</sup> as soon as 0.5 Na<sup>+</sup> is removed and its relative intensity keeps increasing until full charge. The surface sensibility of XPS has to be kept in mind, especially the presence of oxygenated species deposited on the surface (in grey) which can severely reduce the intensity of the peaks from the bulk. Ideally, a similar XPS study using synchrotron radiation with higher penetration depth should be performed to reduce the parasitic contribution of these surface species.

At this point, we can conclude that both iridium and oxygen redox processes are responsible for the electrochemical activity of the material on the first plateau (2.0 > x > 1.0), whereas the second plateau (1.0 > x > 0.5) seems to be only due to oxygen redox. The coexistence of both cationic and anionic activity on the low voltage plateau was previously shown for Li<sub>2</sub>IrO<sub>3</sub>, which was also subject to a structural transition from O3 to O1 upon delithiation.<sup>58</sup>

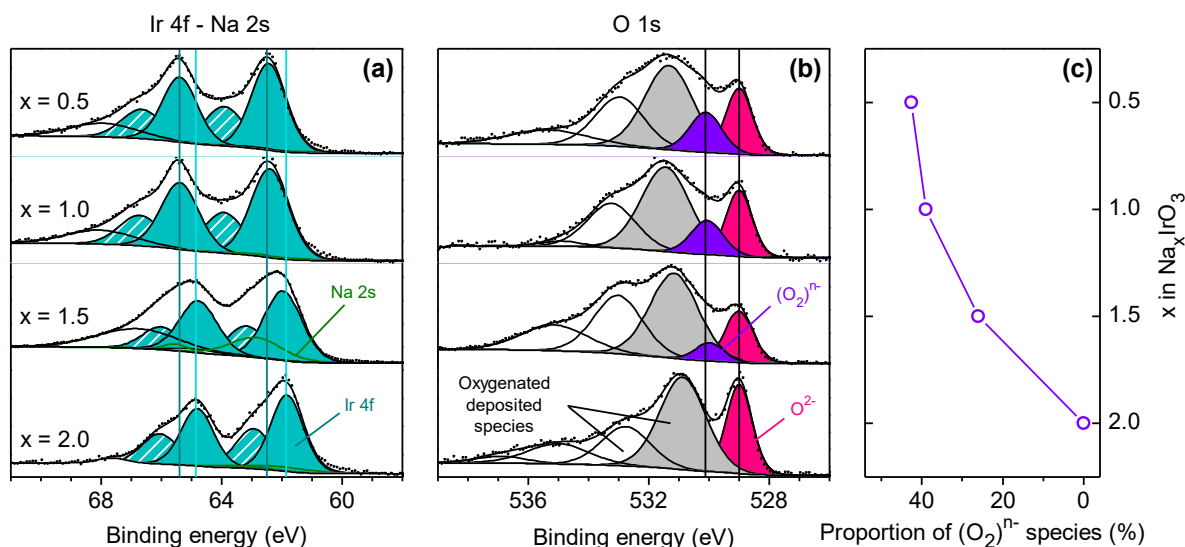


Figure II.13 : XPS analysis of Ir 4f (a) and O 1s (b) peaks show that both Ir and oxygen are oxidized on the first plateau, and oxygen only on the second plateau. The proportion of  $(O_2)^{n-}$  species depending on state of charge is shown in (c).

### II.5.b. X-ray Absorption Near-edge Spectroscopy (XANES)

In order to obtain bulk-sensitive information, X-ray absorption spectroscopy (XAS) was measured at Ir  $L_3$ -edge during cycling of  $Na_2IrO_3$  (see A.3 for experimental details and data treatment). For this purpose, an electrochemical cell derived from the cell dedicated to *in situ* XRD experiments was used, which contains a second Be window permitting to work in transmission mode (A.2.b.v). One absorption spectrum was measured every 15 min while the cell was cycled at C/5. The main feature at Ir  $L_3$ -edge is the intense white line (WL) that overlaps with the absorption edge, and corresponds to the electronic transition from Ir(2p) to unoccupied Ir(5d) orbitals. It can therefore be used to follow the changes in oxidation states of Ir. In Figure II.14, the evolution of the WL area and position in energy are compared to the charge/discharge curve. The unusually large capacity obtained on the high voltage plateau suggests that some side reactions took place at the same time as the transition from O1' to O1, but this does not impede us to comment the data. During the first plateau, from  $Na_2IrO_3$  to  $Na_1IrO_3$ , the WL shifts to higher energy by approximately 1 eV, which is in line with the difference reported by Choy *et al.* for a series of Ir-based perovskites with 4+ and 5+ oxidation states.<sup>82</sup> The intensity of the WL is also found to increase by 18%, a number close to the expected 20 % increase in hole population in 5d levels when going from Ir<sup>4+</sup> ( $5d^5$ ) to Ir<sup>5+</sup> ( $5d^4$ ). Further oxidation from  $Na_1IrO_3$  to  $Na_{0.5}IrO_3$  results in a much smaller shift in energy (0.34 eV) and no variation in the WL intensity. Here again, it seems that the low voltage process is marked by a large participation of Ir to the redox, whereas the high voltage

process does not correspond to clear variations in the Ir electronic states and could therefore be explained by an anionic process. The subsequent discharge does not display such clear features, and is not completely reversible, showing that a better set of data could probably be obtained after further optimization of the electrochemical setup.

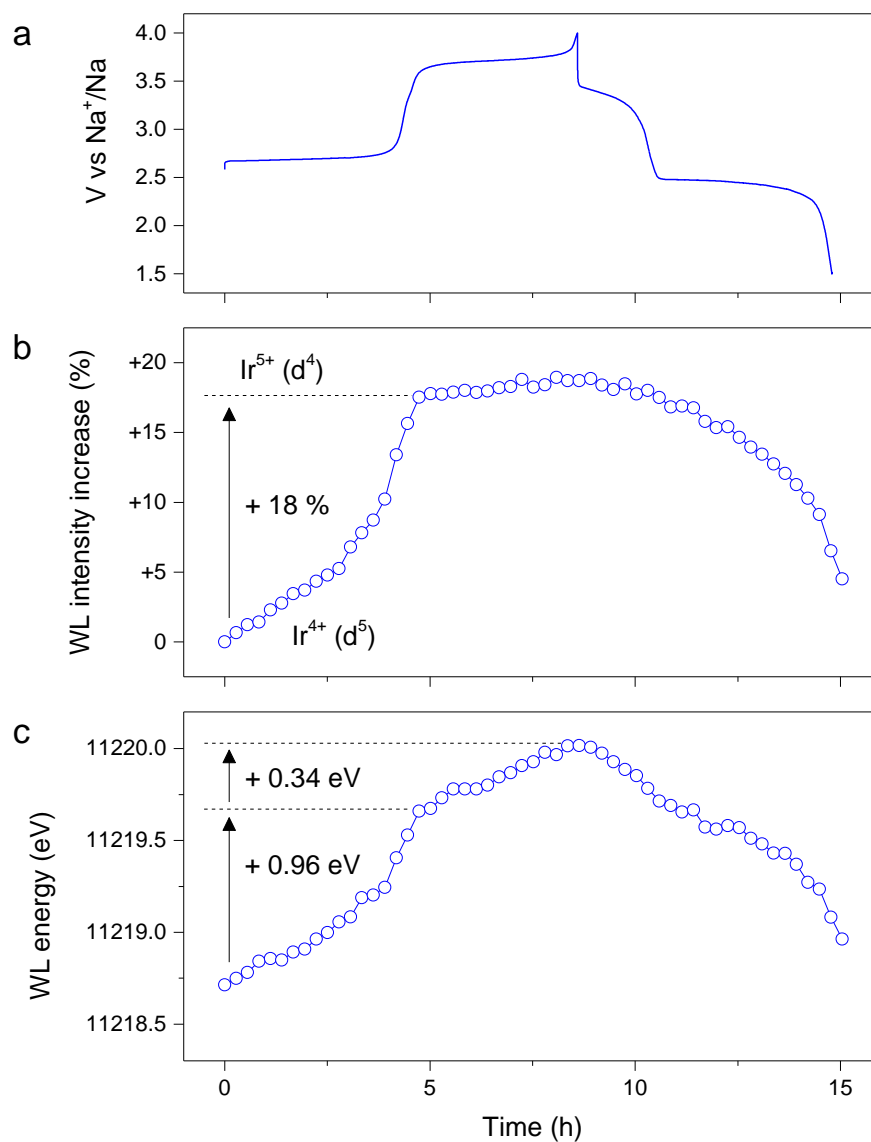


Figure II.14 : Analysis of XANES data at Ir  $L_3$ -edge collected *in situ*. Electrochemical curve of  $\text{Na}_2\text{IrO}_3$  cycled in the *in situ* transmission cell (a). Evolution of the white line intensity (b) and energy (c) are compared.

### II.5.c. Distortion of the IrO<sub>6</sub> octahedra

One of the hypotheses concerning the stabilization of oxidized oxygen in the crystal structure is the reorganization of orbitals from two neighbouring oxygens to form quasi-molecular (O<sub>2</sub>)<sup>n-</sup> species, resulting in the shortening of some O-O distances. This distortion was characterized by TEM and neutron diffraction .

#### II.5.c.i Projected O-O distance observed by TEM

The specific ordering of the fully charged O1 structure, with the honeycomb layers aligned on top of each other, provides a clear projection of both the oxygen and cation sublattices along the [001] axis (Figure II.15), where the cation and oxygen columns can be viewed separately. This opportunity was used to visualize O atomic columns using the ABF-STEM imaging technique as reported for the Li<sub>0.5</sub>IrO<sub>3</sub> structure.<sup>58</sup> In the [001] ABF-STEM image (Figure II.15c), the Ir columns appear as the darkest dots forming a hexagonal honeycomb pattern (red). Each Ir column is surrounded by 6 faint dots corresponding to the IrO<sub>6</sub> octahedra projected along their 3-fold symmetry axis (yellow). The dots centering the Ir hexagons can be attributed to the residual Na atoms (blue). Absence of Ir and ordered location of Na in the hexagonal tunnels is evident from the comparison of [100] HAADF-STEM and ABF-STEM images (Figure II.16): the Na atomic columns are visible in the ABF-STEM image and do not show up in the HAADF-STEM image due to relatively low atomic number of Na. ABF intensity profiles (Figure II.15d) clearly demonstrate two different sets of the projected O-O separations, with a formation of three longer and three shorter distances. The average projected O-O distances were measured at 2.07(4) Å and 1.33(3) Å for longer and shorter separations, respectively.

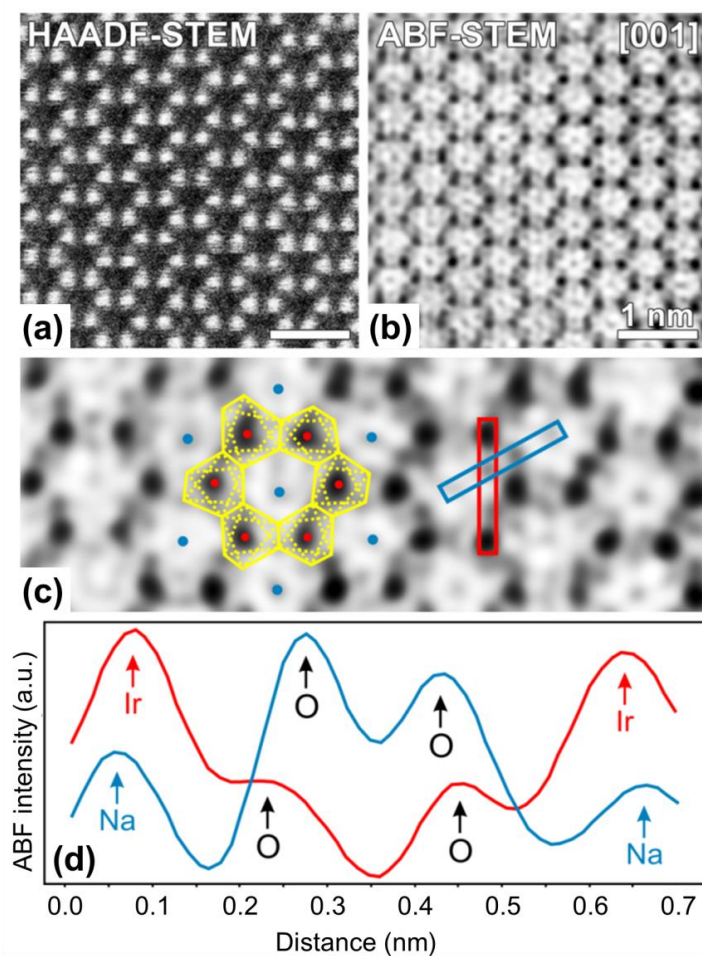


Figure II.15 : Projection of O-O short distances visualized by TEM. Complementary [001] HAADF-STEM (a) and ABF-STEM (b) images of the fully charged  $\text{Na}_{0.5}\text{IrO}_3$  sample. Magnified fragment of the ABF-STEM image with marked projections of the  $\text{IrO}_6$  octahedra (c) and intensity profiles highlighting short and long projected O-O distances (d).

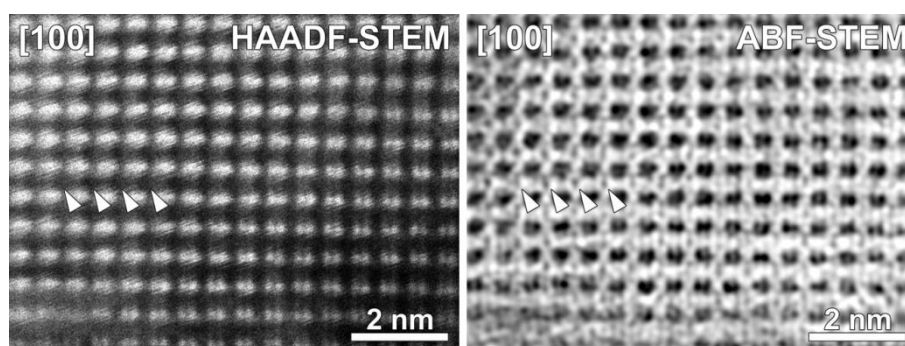


Figure II.16 : Position of the Na left in  $\text{Na}_{0.5}\text{IrO}_3$ . Complementary [100] HAADF-STEM and ABF-STEM images of the fully charged  $\text{Na}_{0.5}\text{IrO}_3$  sample demonstrating that Na atoms in the structure primarily occupy positions between the empty octahedra of the honeycomb layers. Some Na columns are marked with arrowheads in the ABF-STEM image. They are not visible in the HAADF-STEM image, ruling out the possibility of Ir migration in the Na layers.

### II.5.c.ii Neutron diffraction

As TEM only gives information on the projected distances, we compared the different O-O distances obtained from refinement of neutron diffraction data in the O3 and O1 structures (Figure II.17). In the pristine material, short and long O-O distances already exist to a lesser extent, with the shortest bonds (2.668 Å) having a relative deviation of -8.3 % from the average O-O distance in the structure (2.909 Å). For the O1-Na<sub>0.5</sub>IrO<sub>3</sub> charged sample, the average O-O distance is decreased to 2.837 Å as a result of Ir oxidation, and the shortest O-O bond is found to be 2.456 Å, which represents an increased deviation from the average distance of -13.4 %. This short O-O distance is very close to the one found in Li<sub>0.5</sub>IrO<sub>3</sub> (2.45 Å).<sup>58</sup> Drawing similar conclusions from the intermediate phase Na<sub>1</sub>IrO<sub>3</sub> is more difficult because of a strongly distorted octahedra. However, it is interesting to note that the average Ir-O distance does not change much from Na<sub>1</sub>IrO<sub>3</sub> to Na<sub>0.5</sub>IrO<sub>3</sub>, further supporting the negligible contribution of Ir to the redox on the high voltage process.

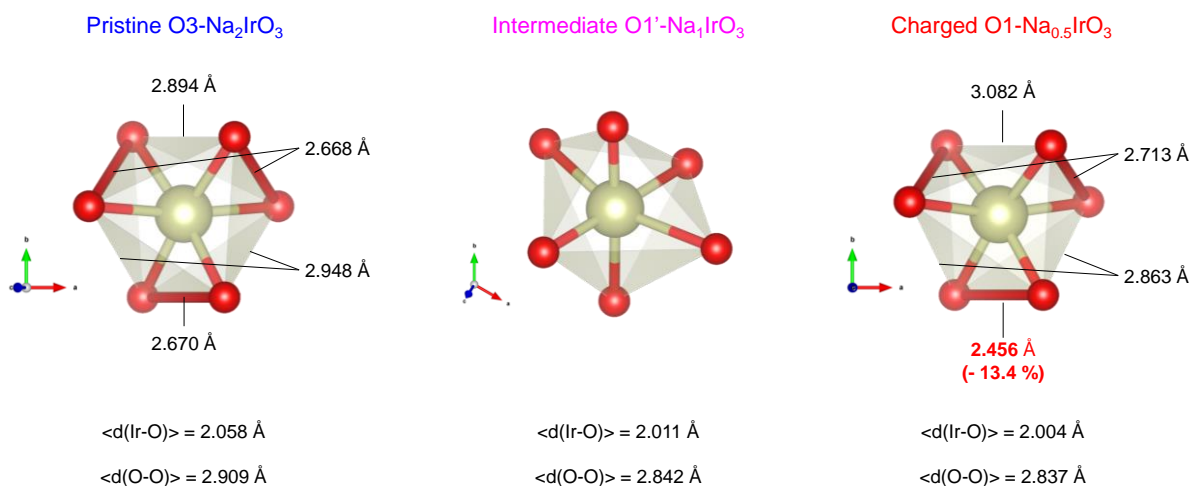


Figure II.17 : Distortion of the IrO<sub>6</sub> octahedra in Na<sub>x</sub>IrO<sub>3</sub> for the pristine (x = 2, left) and fully charged (x = 0.5, right) samples from refinement of neutron diffraction data. The shortest O-O distances are highlighted in red.

## II.6. Stability issues and long-term cycling

### II.6.a. Capacity decrease in Na half-cells

The long-term cycling performances of Na<sub>2</sub>IrO<sub>3</sub> in Na half cells are shown in Figure II.18. When cycling on the full voltage range (1.5 V to 4 V, Figure II.18a), the discharge capacity steadily decreases (Figure II.18c), indicating a slow degradation process. To verify

whether this decay arises from a low or high voltage process, the cycling was repeated on the lower plateau only with an upper cutoff of 3 V (Figure II.18b). The reversibility of the low plateau is good, indicating that the process hindering the reversibility of  $\text{Na}_2\text{IrO}_3$  is a high voltage process. On the other hand, cycling on the high voltage plateau, between 2.6 and 4 V, was found to be poor with a rapid capacity decay and a gradual polarization on discharge.

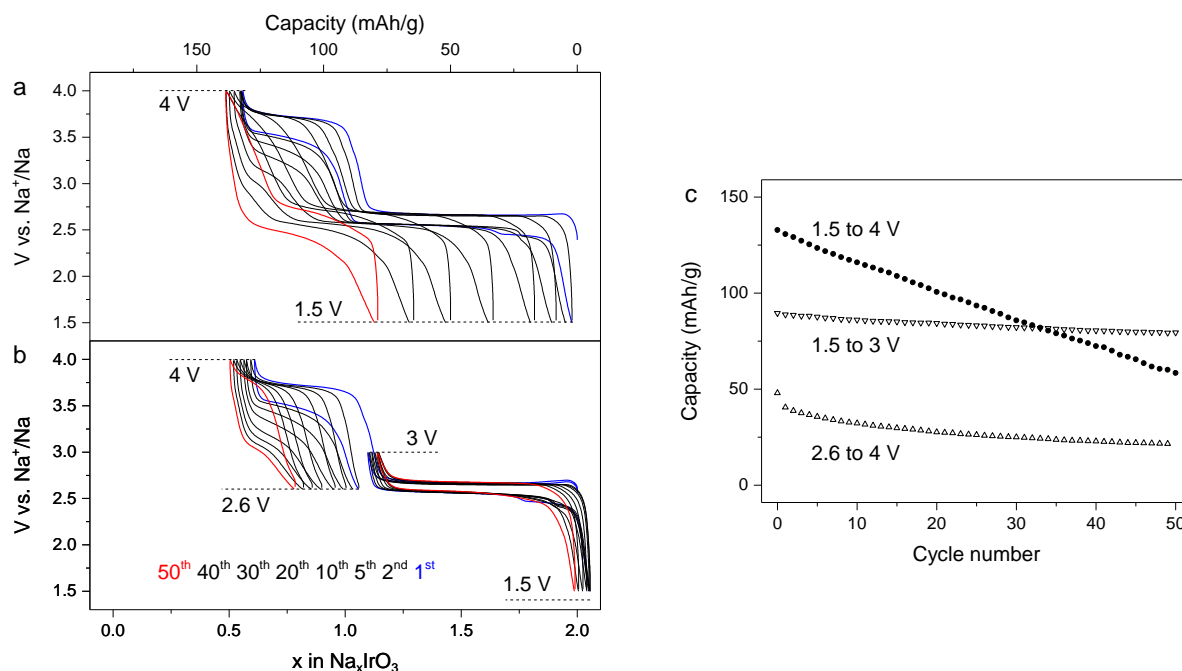


Figure II.18 : Cycling performances of  $\text{Na}_2\text{IrO}_3$  vs. Na. Rapid capacity decay is observed when cycling on the full voltage window (1.5 to 4 V) (a). Limiting the cycling to the low voltage region (1.5 to 3 V) gives a much better cyclability, whereas cycling on the high voltage region (2.6 to 4 V) shows poor capacity retention (b). Selected cycles are shown in the figure, with the 1<sup>st</sup> and 50<sup>th</sup> cycles highlighted in blue and red, respectively. The discharge capacity on the different voltage windows is compared for the first 50 cycles in (c).

XRD analysis of the sample discharged after 50 cycles between 1.5 V and 4 V indicates the presence of both O3 phase and a new phase as shown in Figure II.19. This new phase is very similar to the fully charged O1 phase, i.e. with hexagonal close packing of the O atoms and the honeycomb layers stacked perfectly on top of each other (see TEM data in Figure II.20). However, the unit cell parameters are very different, with  $a = 5.42839(11)$  Å and  $b = 9.3664(2)$  Å, close to those of the pristine structure, and  $c = 4.56187(7)$  Å, approximately 0.3 Å smaller than in the O1 structure (Table II.5). This new phase will be referred to as O1\* and corresponds to a collapsed O1 phase, with a smaller interlayer distance. This result indicates that part of the sample undergoes an irreversible transition from O1 to O1\* and remains blocked in the O1\* structure, while the intact part of the material reversibly

reinserts  $\text{Na}^+$  through the O1-O1'-O3 structural transitions. This gradual transformation of O1 to O1\* results in a steady capacity decrease, as shown in Figure II.18c. On the other hand, a low cutoff voltage at 3 V limits the structural transition to O3-O1' and the cycling is not hindered by the formation of the blocked O1\* phase.

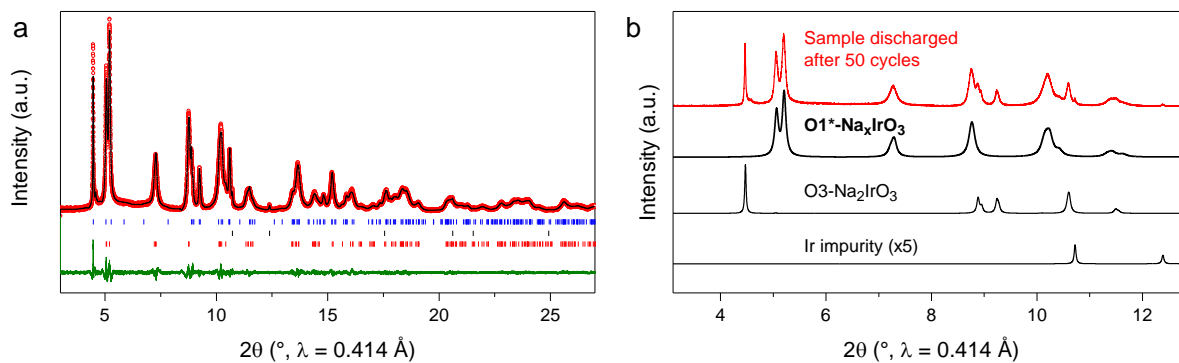


Figure II.19 : Structure of  $\text{Na}_2\text{IrO}_3$  after 50 cycles of charge/discharge in a Na half-cell. The synchrotron XRD pattern (a) was fitted using the pristine O3- $\text{Na}_2\text{IrO}_3$  structure without honeycomb ordering, a new phase with an O1 stacking (named O1\*- $\text{Na}_x\text{IrO}_3$ ) and a small amount of metallic Ir impurity. The individual contribution of each phase is shown in (b).

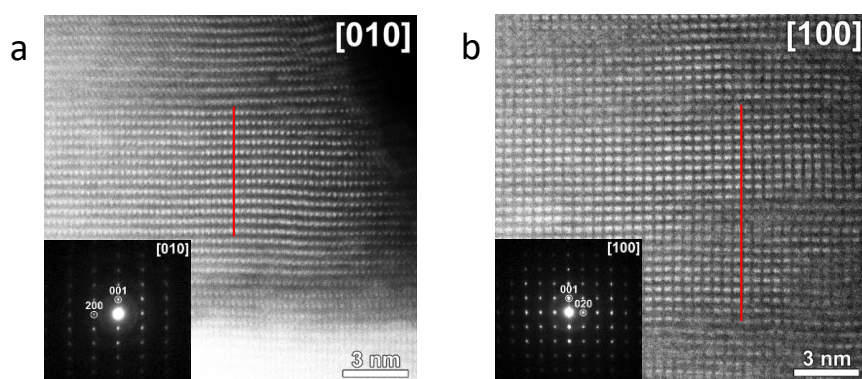


Figure II.20 : High resolution HAADF-STEM images and corresponding ED patterns for the discharged sample after 50 cycles, demonstrating stabilization of the O1 structure even in the discharged state (a-b). Cation composition of the sample measured with EDX is  $\text{Na}/\text{Ir} = 0.55(11)$ .

Table II.5 : Structural parameters for the sample discharged after 50 cycles. 3 phases are present.

Phase 1 was refined using the structural parameters of O3-Na<sub>2</sub>IrO<sub>3</sub> after 1 cycle (Table II.4) and complete mixing of Ir and Na sites in the honeycomb layer. Phase 2 corresponds to an Ir impurity. The remaining contribution of the pattern was fitted in pattern matching (Le Bail refinement) with a *C2/m* space group similar to that of the O1 structure.

---

#### Phase 1 : O3 - Na<sub>2</sub>IrO<sub>3</sub> Rietveld refinement

---

Space group : *C2/m*

		<i>a</i> (Å)	<i>b</i> (Å)	<i>c</i> (Å)	$\alpha$ (°)	$\beta$ (°)	$\gamma$ (°)
SXRD		5.42063(11)	9.40694(18)	5.61671(10)	90	108.8291(8)	90
Atom	Site	<i>x</i>	<i>y</i>	<i>z</i>	Occupancy	B (Å <sup>2</sup> )	
O1	8 <i>j</i>	0.256(2)	0.3349(9)	0.7926(15)	1	1.0	
O2	4 <i>i</i>	0.279(3)	0	0.803(3)	1	1.0	
Ir1	4 <i>g</i>	0	0.3202(6)	0	2/3	1.0	
Na1	4 <i>g</i>	0	0.3202(6)	0	1/3	1.0	
Na2	2 <i>a</i>	0	0	0	1/3	1.0	
Ir2	2 <i>a</i>	0	0	0	2/3	1.0	
Na3	4 <i>h</i>	0	0.830(2)	0.5	1	1.0	
Na4	2 <i>d</i>	0	0.5	0.5	1	1.0	

---

#### Phase 2 : Ir impurity - Rietveld refinement

---

Space group : *Fm $\bar{3}$ m*

		<i>a</i> (Å)	<i>b</i> (Å)	<i>c</i> (Å)	$\alpha$ (°)	$\beta$ (°)	$\gamma$ (°)
		3.839	3.839	3.839	90	90	90
Atom	Site	<i>x</i>	<i>y</i>	<i>z</i>	Occupancy	B (Å <sup>2</sup> )	
Ir	4 <i>a</i>	0	0	0	1	1.0	

---

#### Phase 3 : O1\*-Na<sub>x</sub>IrO<sub>3</sub> - Pattern matching

---

Space group : *C2/m*

<i>a</i> (Å)	<i>b</i> (Å)	<i>c</i> (Å)	$\alpha$ (°)	$\beta$ (°)	$\gamma$ (°)
5.42839(11)	9.3664(2)	4.56187(7)	90	90.7332(17)	90

---

Reliability parameters :  $\chi^2 = 1.11$ , Bragg R-factor = 1.63 % (Phase 1), 1.97 % (Phase 2), 0.224 % (Phase 3)

### II.6.b. Long-term cycling in full cells

As mentioned previously, cycling without FEC led to a poor coulombic efficiency accompanied by fast capacity decay. The predominance of the O1\* phase after most of the capacity was lost suggests a possible relation between electrolyte decomposition in the cell and degradation of the material. In order to avoid any electrolyte decomposition in contact with metallic Na, Na<sub>2</sub>IrO<sub>3</sub> was cycled in a full cell configuration using hard carbon instead of Na as an anode and NaPF<sub>6</sub> in EC:DMC as an electrolyte (Figure II.21a). No FEC additive was

used here as it has negative effects on the cycling of hard carbon.<sup>83</sup> This full Na-ion cell delivers a reversible capacity of  $96 \text{ mAh}\cdot\text{g}^{-1}$ , with a coulombic efficiency of 75.3 % on the first cycle, due to the formation of a SEI on the hard carbon anode, and around 99.5 % on the next 150 cycles (Figure II.21b). The cell could cycle more than 150 cycles with barely any capacity decay.

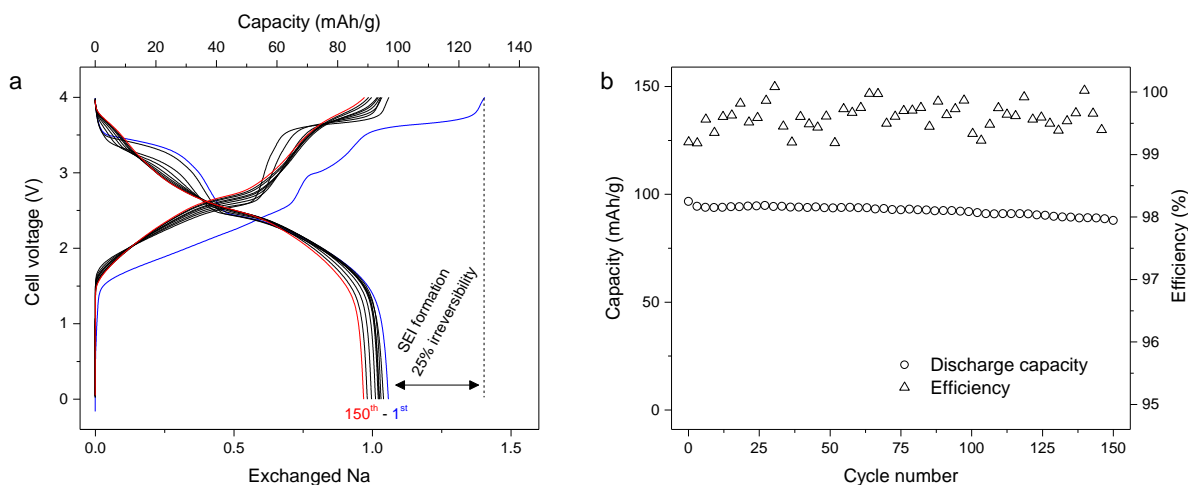


Figure II.21 : Cycling performances of  $\text{Na}_2\text{IrO}_3$  in a full cell configuration (a) with hard carbon as an anode (C/5, 0 V to 4 V) and using  $\text{NaPF}_6$  in EC:DMC as an electrolyte. 1<sup>st</sup> and 150<sup>th</sup> cycles are highlighted in blue and red, respectively. Capacity retention and efficiency upon over 150 cycles (c).

It is important to address the issue of capacity decay in  $\text{Na}_2\text{IrO}_3/\text{Na}$  cells. This decay is mitigated by the use of FEC in Na half-cells and by replacing the Na anode by hard carbon in a full Na-ion cell configuration. The best performances (150 cycles with less than 9 % lost) were obtained by replacing  $\text{NaClO}_4$  with  $\text{NaPF}_6$  in EC:DMC. The precise degradation mechanism of the material in Na-half cells remains unclear. FEC is known to form an elastomeric layer at the surface of Na metal,<sup>79</sup> hence minimizing electrolyte decomposition at the Na electrode without completely preventing it. Therefore, in absence of FEC, the large amount of degradation products coming from the electrolyte decomposition could migrate to the positive electrode and react with  $\text{Na}_2\text{IrO}_3$ .

Overall, these results stress that the choice of electrolyte is critical for achieving long-term performance and highlight the full reversibility of the cumulative cationic and anionic process if the proper electrolyte formulation is selected. This validates the possibility to use Na-rich layered oxides with anionic redox activity as cathode materials for Na-ion batteries.

## II.7. Conclusion

In this chapter, the electrochemical properties of  $\text{Na}_2\text{IrO}_3$  were investigated and the material was found to be a good model material to study the electrochemical performances of Na-rich layered oxides as it eliminates the structural complexity associated to cationic migration and  $\text{O}_2$  release encountered for the Li-rich phases. Due to the strong overlap of Ir and O orbitals, the integrity of transition metal layers is preserved upon cycling. This situation leads to a very good reversibility of the anionic redox process, which confirms the use of Na-rich layered oxides as a valid strategy to increase the potential and capacity of Na-ion cathode materials.

However, several limits of Na-rich layered oxides were identified. Upon desodiation, the stacking of Ir honeycomb layers changes to minimize the cationic repulsions ( $\text{Na}^+\text{-Na}^+$ ,  $\text{Na}^+\text{-Ir}^{5+}$ ) in the material. The resulting O1 structure limits, through a stabilization of the  $\text{Na}^+$  sites, the deintercalation to  $\sim 1.5 \text{ Na}^+$ . This intrinsic structural limitation, which can be extended from Na-rich to Li-rich layered oxides, stands as a warning for the design of high capacity cathode materials. The second limitation is related to the high reactivity of Na-based layered oxides with electrolyte decomposition products, highlighting that a proper choice of electrolyte is critical to the performances of a given material. A possible explanation for the degradation mechanism involves the generation of protons in the electrolyte, and will be discussed more in the last chapter.

Finally, even though the structural changes and the redox of Ir and O seem to be similar in  $\text{Na}_2\text{IrO}_3$  and  $\text{Li}_2\text{IrO}_3$ , the effect of changing from  $\text{Li}^+$  to a more polarizable ion such as  $\text{Na}^+$  results in much lower potentials ( $\sim 0.5 \text{ V}$  lower on the first plateau and  $\sim 0.2 \text{ V}$  on the second plateau). In an attempt to bring more understanding on this difference,  $\text{Na}(\text{Li}_{1/3}\text{Ir}_{2/3})\text{O}_2$ , a material with an intermediate composition between  $\text{Na}_2\text{IrO}_3$  and  $\text{Li}_2\text{IrO}_3$  was studied and is the focus of the third chapter.



## Chapter III. Metastability of the Li-substituted $\text{Na}(\text{Li}_{1/3}\text{Ir}_{2/3})\text{O}_2$

### III.1. Introduction

In the previous chapter, similar electrochemical properties were found for  $\text{Na}_2\text{IrO}_3$  and  $\text{Li}_2\text{IrO}_3$ , with the main difference lying in a lower potential for the Na compound compared to the Li one. This potential difference between  $\text{Na}^+$  and  $\text{Li}^+$  insertion is commonly observed in cathode materials, and is usually ascribed to the lower energy gain of inserting  $\text{Na}^+$  in a structure compared to  $\text{Li}^+$ .<sup>84</sup> This comparison needs however to be made carefully and case by case as  $\text{Li}^+/\text{Na}^+$  insertion can lead to different structural evolutions. Apart from the voltage, no clear differences were observed in terms of cationic/anionic redox activity when going from  $\text{Li}^+$  to  $\text{Na}^+$ . The influence of the alkali ion nature on the activation of anionic redox remains unclear, but should nevertheless act on the electrostatic stabilization/destabilization of the non-bonding O(2p) orbitals. To get better insight on the role of the alkali ion on the voltage of cationic/anionic redox, we decided to prepare intermediate compositions  $(\text{Na}_{1-x}\text{Li}_x)_2\text{IrO}_3$  ( $0 < x < 1$ ) between  $\text{Na}_2\text{IrO}_3$  and  $\text{Li}_2\text{IrO}_3$ .

### III.2. Synthesis and structure

#### III.2.a. Phase diagram: solid-solution or not ?

The interesting magnetic properties of iridates provide us with a large literature on these materials. In 2013, Cao *et al.* reported the synthesis of single crystals of  $(\text{Na}_{1-x}\text{Li}_x)_2\text{IrO}_3$  ( $0 < x < 0.9$ ) with a monotonous evolution of cell parameters from Na to Li, suggesting a solid-solution between  $\text{Na}_2\text{IrO}_3$  and  $\text{Li}_2\text{IrO}_3$ . In a later report, Manni *et al.* disproved the existence of the solid-solution by failing in their attempt to reproduce the results and by showing, through DFT calculations, that only the  $x = 0.25$  composition is stable ( $\text{Na}/\text{Li} = 3$ ).<sup>85</sup> However, these conclusions need to be considered carefully, as the samples in this work were probably exposed to air. This is suggested by the XRD pattern of the  $\text{Na}_2\text{IrO}_3$  compound, which shows signs of decomposition.

With this information, we tried to prepare compounds with different Na/Li ratios and without exposure to air, following the same procedure as described previously for  $\text{Na}_2\text{IrO}_3$ .

$\text{Na}_2\text{CO}_3$ ,  $\text{Li}_2\text{CO}_3$  and metallic Ir were mixed in different proportions, heated in air at  $800^\circ\text{C}$  for 48 h, cooled to  $500^\circ\text{C}$  and directly transferred in a glovebox to avoid decomposition in air. A second heating for 24 h at  $900^\circ\text{C}$  was performed in the same conditions to improve the crystallinity of the samples. All the compositions we tried gave mixtures of  $\text{Na}_2\text{IrO}_3$ ,  $\text{Li}_2\text{IrO}_3$  and  $\text{IrO}_2$ , except for the phase with  $\text{Na}/\text{Li} = 3$  ratio. This result supports the theoretical calculation by Manni *et al.* on the stability of the  $\text{Na}_{1.5}\text{Li}_{0.5}\text{IrO}_3$  phase against the solid-solution proposed by Cao *et al.* The laboratory XRD pattern of the material was first refined using the same  $C2/m$  space group as for the parent compounds, with cell parameters intermediate between  $\text{Na}_2\text{IrO}_3$  and  $\text{Li}_2\text{IrO}_3$ . However, some small peaks were not indexed by this structural model, suggesting that the  $C2/m$  space group was not adapted to this material. To get more precise information on the structure, synchrotron X-ray diffraction and neutron diffraction were used on this compound.

### III.2.b. Synchrotron X-ray diffraction: honeycomb stacking

Synchrotron X-ray diffraction was measured on the sample to precisely determine the space group and cell parameters. The synchrotron data clearly shows a larger number of Bragg reflections (Figure III.1) which were not seen at first on the data collected in the laboratory. These peaks arise from a higher order superstructure compared to the ideal 3 honeycomb layers stacking sequence of the O3 structure. Similar superstructure peaks were observed and very well described in  $\text{Na}_3\text{Ni}_2\text{BiO}_6$  by Liu *et al.* with,<sup>86</sup> in that case, 6 layers (6L), 9 layers (9L) and 12 layers (12L) stacking periods. McCalla *et al.* also found a 4 layer (4L) stacking sequence for  $\text{Li}_4\text{FeSbO}_6$ .<sup>87</sup> According to Liu *et al.* this high-order stacking sequence is a consequence of long-range strain present in the material.<sup>86</sup> During synthesis, layered materials with honeycomb ordering gradually transform from a random stacking sequence to the ideal 3L stacking sequence (O3). High order stacking sequences (4L, 6L, 9L, 12L...) correspond to intermediate energy minima, and their existence should be largely dependent on the synthesis conditions.

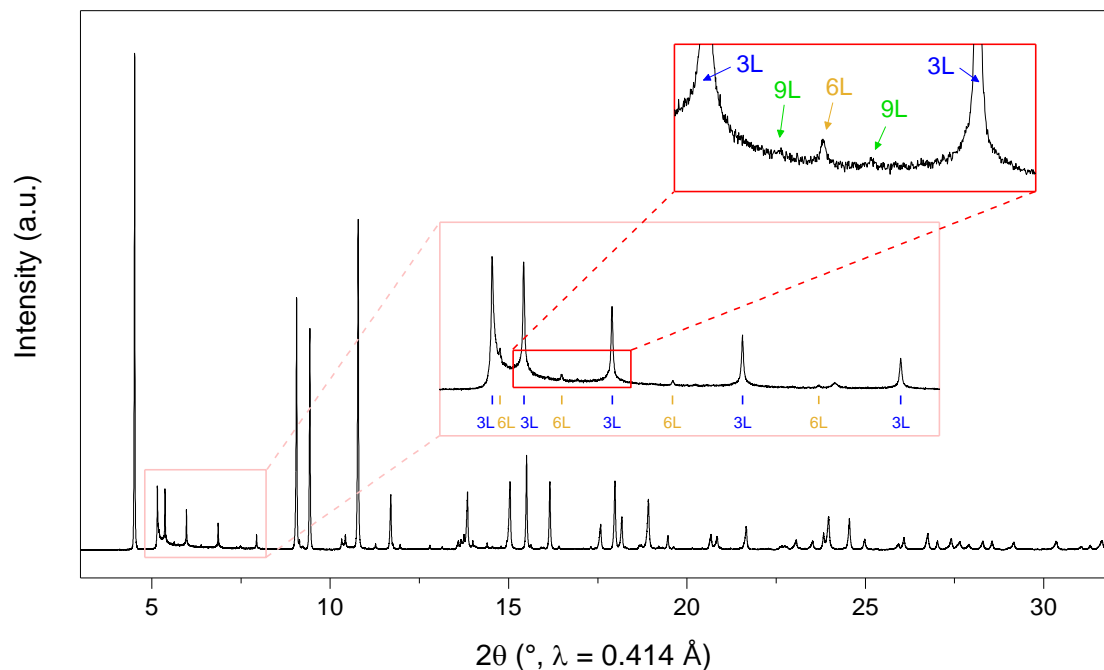


Figure III.1 : High order superstructure peaks observed in the synchrotron X-ray diffraction pattern of  $\text{Na}(\text{Li}_{1/3}\text{Ir}_{2/3})\text{O}_2$ . 3L, 6L and 9L indexed peaks arise from the 3, 6 and 9 layers periodicity of the stacking sequence, respectively.

In the case of  $\text{Na}(\text{Li}_{1/3}\text{Ir}_{2/3})\text{O}_2$ , the 6L peaks are clearly observed (Figure III.1), whereas higher order stacking sequences (9L, 12L) can only be guessed. This situation is more common in Li-rich layered oxides with honeycomb ordering, such as  $\text{Li}_2\text{SnO}_3$ , and can be taken into account by Rietveld refinement using the  $C2/c$  space group. The unit cell is twice as large as the usual  $C2/m$  unit cell, permitting a description of honeycomb stacking with a 6 layer periodicity. We used this space group to refine our experimental data, and introduced some site mixing in the metallic layer, as previously described for  $\text{Na}_2\text{IrO}_3$ , in order to artificially reduce the intensity of superstructure peaks. As X-ray scattering of Li is too small compared to Na and Ir, the data was first refined using mixed occupancy of Li/Na sites according to the stoichiometry of the material, giving a satisfactory fit of the experimental data. Neutron diffraction data was then used to improve the model with accurate positions of atoms in the unit cell.

### III.2.c. Neutron diffraction: position of Li and Na

The theoretical calculation done by Manni *et al.* suggested that  $\text{Li}^+$  ions would preferentially sit in the center of the Ir honeycomb,<sup>85</sup> resulting in pure Na planes and mixed  $\text{Li}_{1/3}\text{Ir}_{2/3}$  planes. To verify this result, we performed neutron diffraction on the D1B

diffractometer of ILL (Grenoble, France) to determine the position of Li in the material. As Li and Na have negative and positive coherent scattering lengths, respectively, it is straightforward to differentiate the sites they occupy in the crystal structure. Rietveld refinement of the neutron data was performed with different positions for  $\text{Li}^+$  and the best fit was indeed found for  $\text{Li}^+$  in the center of Ir honeycombs, whereas the  $\text{Na}^+$  ions occupy all the octahedral sites in the interlayer space, giving  $\text{Na}(\text{Li}_{1/3}\text{Ir}_{2/3})\text{O}_2$  (see Figure III.2). The positions of all atoms in the unit cell were refined using the neutron data, and used to improve the refinement of synchrotron XRD data. The final result of neutron and synchrotron X-ray diffraction Rietveld refinement is shown in Figure III.3 and the structural parameters obtained are listed in Table III.1.

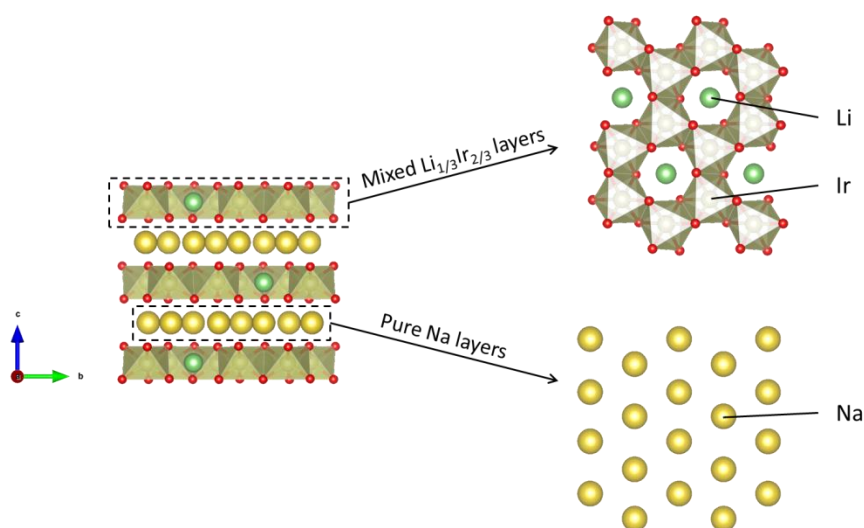


Figure III.2 : Crystal structure of  $\text{Na}(\text{Li}_{1/3}\text{Ir}_{2/3})\text{O}_2$ . This schematic corresponds to the ideal stacking sequence, without stacking faults in the material.

Table III.1 : Structural parameters for  $\text{Na}(\text{Li}_{1/3}\text{Ir}_{2/3})\text{O}_2$  obtained from Rietveld refinement of synchrotron X-ray and neutron diffraction data. Site mixing between Li and Ir in the  $8f$  and  $4d$  sites was introduced to artificially reduce the intensity of superstructure peaks.

<b><math>\text{Na}(\text{Li}_{1/3}\text{Ir}_{2/3})\text{O}_2</math></b>						
Space group : $C2/c$						
		$a$ (Å)	$b$ (Å)	$c$ (Å)	$\beta$ (°)	
SXRD		5.33150(5)	9.23324(8)	10.67604(5)	99.5400(8)	
ND		5.3303(5)	9.2257(9)	10.6802(5)	99.664(10)	
Atom	Site	$x$	$y$	$z$	Occupancy	$B$ (Å <sup>2</sup> )
O1	$8f$	0.593(2)	0.0697(14)	0.1034(11)	1	1.09(5)
O2	$8f$	0.617(3)	0.4225(13)	0.0993(10)	1	1.09(5)
O3	$8f$	0.631(2)	0.754(2)	0.1025(6)	1	1.09(5)
Ir1	$8f$	0.2520(19)	0.0812(5)	0.0045(8)	0.863(4)	1.06(5)
Li1	$8f$	0.2520(19)	0.0812(5)	0.0045(8)	0.137(4)	1.06(5)
Li2	$4d$	0.75	0.25	0	0.726(4)	1.06(5)
Ir2	$4d$	0.75	0.25	0	0.274(4)	1.06(5)
Na3	$4e$	0	0.092(3)	0.25	1	1.80(13)
Na4	$4e$	0	0.429(3)	0.25	1	1.80(13)
Na5	$4e$	0	0.741(5)	0.25	1	1.80(13)

Reliability parameters :  $\chi^2 = 17.0$ , Bragg R-factor = 12.8 % (SXRD)  
 $\chi^2 = 135$ , Bragg R-factor = 5.92 % (ND)

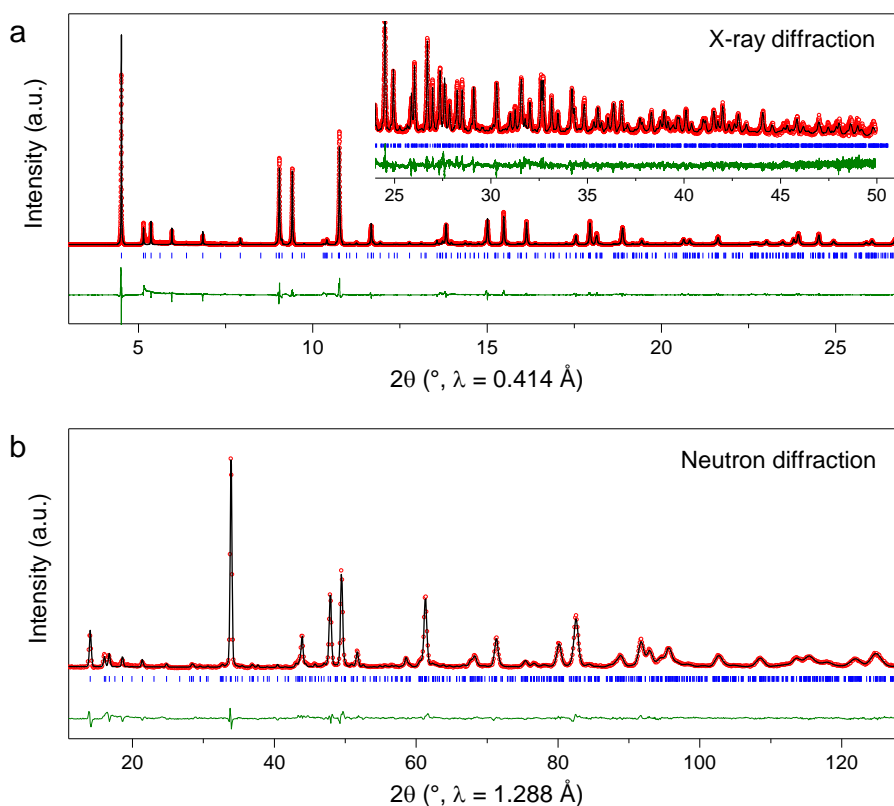


Figure III.3 : Rietveld refinement of diffraction data for  $\text{Na}(\text{Li}_{1/3}\text{Ir}_{2/3})\text{O}_2$ , using synchrotron X-ray (a) and neutron (b) data.

### III.3. Electrochemical properties

#### III.3.a. $\text{Na}(\text{Li}_{1/2}\text{Ir}_{2/3})\text{O}_2$ vs. Li

The electrochemical properties of  $\text{Na}(\text{Li}_{1/3}\text{Ir}_{2/3})\text{O}_2$  were first measured in Li cells using metallic Li as an anode and LP30 as an electrolyte (1M  $\text{LiPF}_6$  in 1:1 mix of ethylcarbonate (EC) and dimethylcarbonate (DMC)). The cell was cycled at C/10 between 1.3 and 4.5 V and the cycling curve is shown in Figure III.4. Before knowing more on the mechanism, the composition of the material during cycling will be written as  $(\text{Na/Li})_x\text{IrO}_3$  with  $x$  corresponding to the number of charge measured by the potentiostat. Up to 1.5  $\text{Li}^+/\text{Na}^+$  can be removed on oxidation to 4.5 V, a maximum capacity similar to that of  $\text{Na}_2\text{IrO}_3$  and  $\text{Li}_2\text{IrO}_3$ , most likely because of the formation of a stable O1 phase for the composition  $(\text{Na/Li})_{0.5}\text{IrO}_3$ . The charge occurs through 4 plateaus at 3.1, 3.5, 4 and 4.2 V. On discharge, the plateaus are preserved, with a very large polarization for  $1.7 < x < 2.0$  in  $(\text{Na/Li})_x\text{IrO}_3$  and, surprisingly, an extra capacity on discharge around 1.4 V, with up to 0.7 extra ions inserted in the material. To make sure that this extra capacity did not come from an error in the stoichiometry of the material, a second cell was assembled and started directly on discharge down to 1.3 V (red dashed line in Figure III.4). No capacity was obtained, showing that the starting stoichiometry is correct and that the extra capacity is only available after the first cycle.

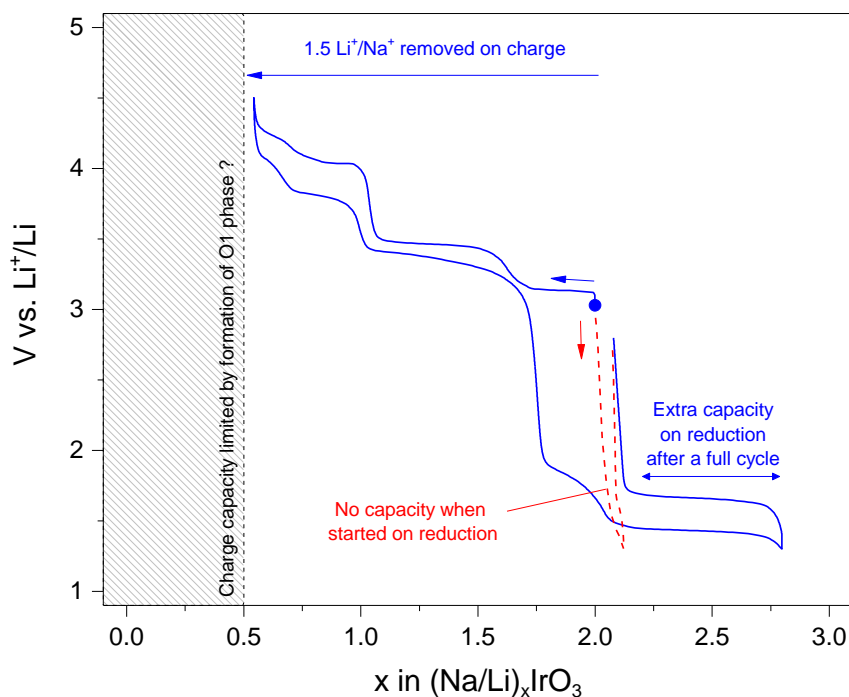


Figure III.4 : Galvanostatic cycling of  $\text{Na}(\text{Li}_{1/3}\text{Ir}_{2/3})\text{O}_2$  vs. Li. The first charge/discharge cycle between 1.3 and 4.5 V is shown in blue. An identical cell was started on reduction down to 1.3 V (red dashed line) but no  $\text{Li}^+$  was inserted, in contrast with the extra insertion observed after a complete cycle. The diagonal-filled rectangle represents the capacity limitation to  $x = 0.5$  if an O1 phase is formed.

The multiple plateaus in the voltage curve suggest a complex structural evolution of the material upon removal of  $\text{Na}^+/\text{Li}^+$ . To assign each voltage step with the deinsertion of Li or Na, it was tempting to compare the derivative curve  $dx/dV$  of  $\text{Na}(\text{Li}_{1/3}\text{Ir}_{2/3})\text{O}_2$  to those of  $\text{Li}_2\text{IrO}_3$  and  $\text{Na}_2\text{IrO}_3$  (Figure III.5). At the exception of the first plateau (3.1 V) which is  $\sim 100$  mV higher than that of  $\text{Na}_2\text{IrO}_3$ , each process correlates very well with either Na or Li extraction from  $\text{Na}_2\text{IrO}_3$  and  $\text{Li}_2\text{IrO}_3$ , respectively. Overall, it seems that  $\text{Na}^+$  is removed first on oxidation at 3.1 V, followed by  $\text{Li}^+$  at 3.5 V,  $\text{Na}^+$  again at 4 V and finally  $\text{Li}^+$  at 4.2 V. The discharge process is more difficult to discuss as it is possible that  $\text{Na}^+$  ions get diluted in the  $\text{Li}^+$ -based electrolyte and do not reinsert in the material. At this point, to understand better the mechanism, some structural characterization is needed.

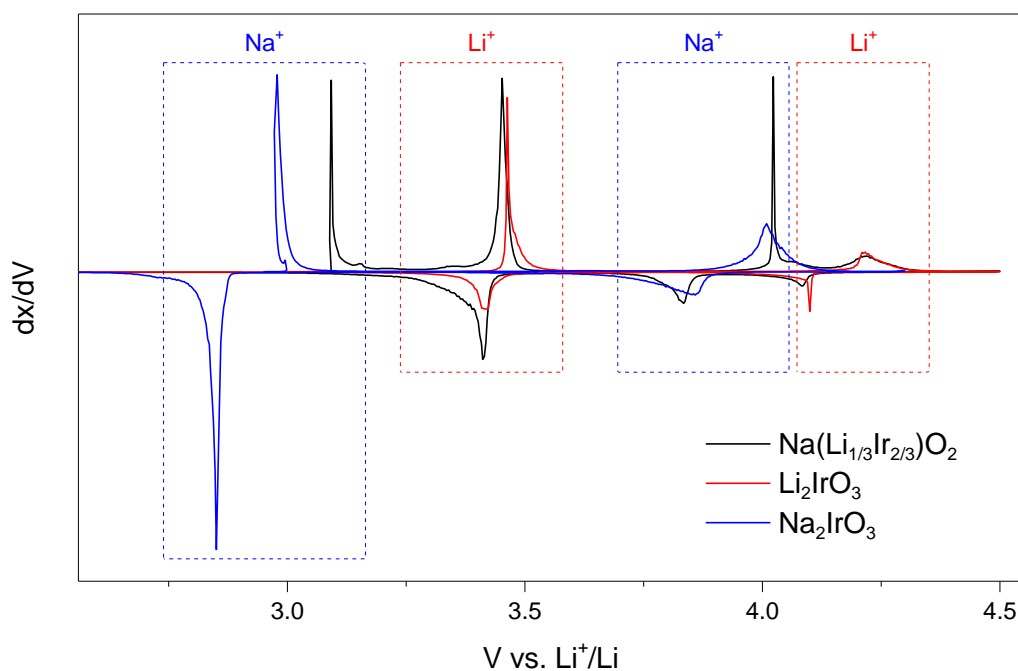


Figure III.5 : Derivative curves of  $\text{Na}(\text{Li}_{1/3}\text{Ir}_{2/3})\text{O}_2$ ,  $\text{Li}_2\text{IrO}_3$  and  $\text{Na}_2\text{IrO}_3$ . To help the comparison, the potential for  $\text{Na}_2\text{IrO}_3$ , which was measured in a Na cell, was shifted by 0.33 V to take into account the thermodynamical potential difference between  $\text{Na}^+/\text{Na}$  ( $E^0 = -2.71$  V vs. SHE) and  $\text{Li}^+/\text{Li}$  ( $E^0 = -3.04$  V vs. SHE). The blue and red boxes highlight the potential correspondence between the different samples, suggesting exchange of  $\text{Na}^+$  and  $\text{Li}^+$ , respectively.

### III.3.b. *In situ* and *ex situ* XRD study

*In situ* XRD was performed during a complete charge/discharge cycle vs. Li at C/10. One XRD pattern was measured every 30 min, giving one pattern for every change in  $x$  of 0.05 in  $(\text{Na}/\text{Li})_x\text{IrO}_3$ . Figure III.6 shows the changes of the XRD pattern upon cycling. Complex structural change can be seen upon cycling, corresponding to each plateau in the voltage curve. One striking point is that the pristine structure (highlighted in black) is never recovered at any time during the cycling. More generally, we observe an asymmetric evolution of Bragg peaks during charge and discharge. Overall, this shows an irreversible evolution of the material upon cycling.

To understand precisely the structural changes on cycling, *ex situ* samples of the material after each plateau were prepared and measured using synchrotron X-ray diffraction. The result was very surprising: except for the pristine material, none of the XRD patterns could be indexed with a single phase. Instead, all patterns can be reasonably well indexed with mixtures of  $\text{Na}_x\text{IrO}_3$  and  $\text{Li}_x\text{IrO}_3$  ( $x = 1, 0.5$ ), suggesting that the starting material separates into two phases, one being Li-rich, and the other Na-rich. This is quite clear when

the sample is charged to 3.2 V, i.e. after the first plateau, for which the refinement of the XRD pattern with O1- $\text{Na}_1\text{IrO}_3$  and O3- $\text{Li}_2\text{IrO}_3$  gives a good result (Figure III.7).

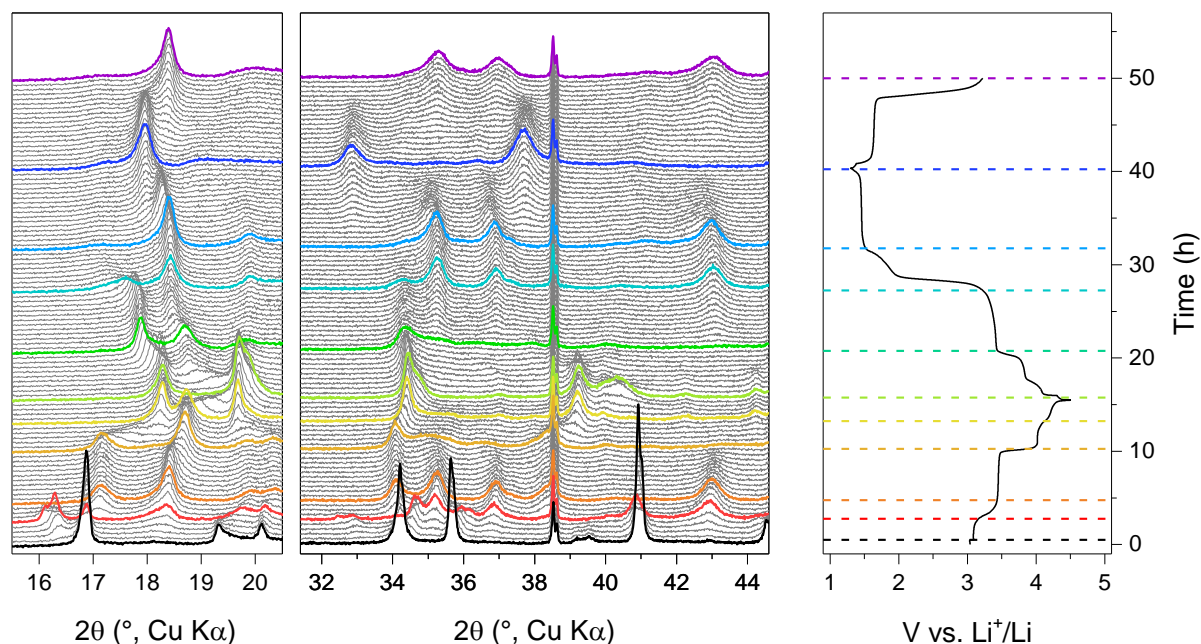


Figure III.6 : *In situ* XRD study of  $\text{Na}(\text{Li}_{1/3}\text{Ir}_{2/3})\text{O}_2$  vs. Li. The cell was charged to 4.5 V, discharged to 1.3 V and finally recharged to  $x = 2$ . Colored lines highlight the different phases observed during cycling.

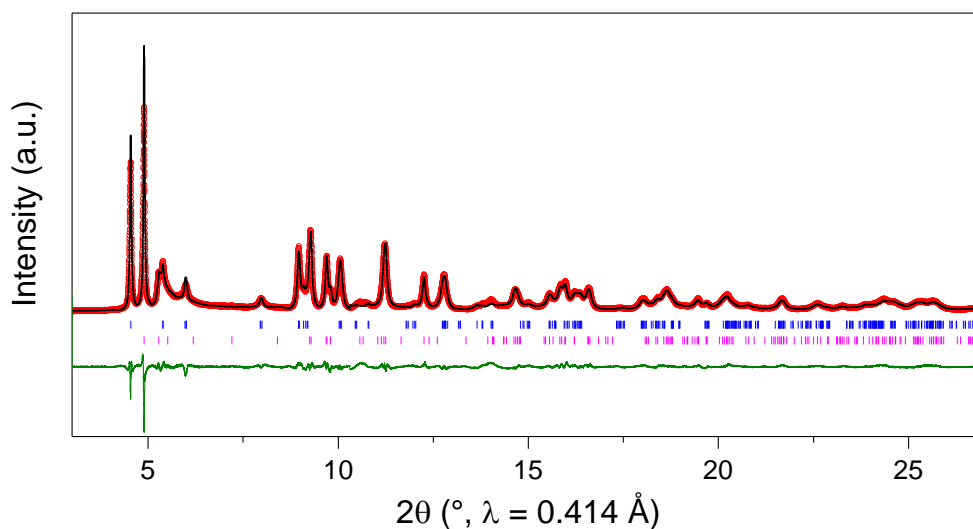


Figure III.7 : Rietveld refinement of XRD data for an *ex situ* sample charged to 3.2 V. The blue and pink ticks correspond to O1- $\text{NaIrO}_3$  and O3- $\text{Li}_2\text{IrO}_3$ , respectively. For simplicity, the asymmetric superstructure peaks were taken into account in the background.

This result explains why the voltage of each plateau can be correlated so well with the voltage curves of  $\text{Na}_2\text{IrO}_3$  and  $\text{Li}_2\text{IrO}_3$ , as shown in Figure III.5. Apart from the first plateau,

which starts from the pristine  $\text{Na}(\text{Li}_{1/3}\text{Ir}_{2/3})\text{O}_2$  material, the following plateaus simply correspond to the superposition of the voltage curves of the  $\text{Na}_x\text{IrO}_3$  and  $\text{Li}_x\text{IrO}_3$  phases formed.

### III.3.c. Decomposition of the material

To explain the decomposition reaction of the material into  $\text{Na}_x\text{IrO}_3$  and  $\text{Li}_x\text{IrO}_3$ , several mechanisms can be imagined: the first one enlists the segregation of  $\text{Li}^+$  and  $\text{Na}^+$  in the sample to form  $\text{Na}_x\text{IrO}_3$  and  $\text{Li}_x\text{IrO}_3$  domains. A second mechanism corresponds to the exchange of  $\text{Na}^+$  in the material with  $\text{Li}^+$  in the electrolyte and would result in a pure  $\text{Li}_x\text{IrO}_3$  phase with longer reaction time.

These two mechanisms are actually simple chemical reactions, which do not require exchange of electrons. They can easily be tested by repeating the previous *in situ* XRD experiment while leaving the cell at open circuit voltage (OCV). In that case, XRD patterns were measured as a function of time, together with the cell voltage. The cycling curve and selected XRD patterns are shown in Figure III.8. For the first 48h, no change was observed, indicating that the material is stable when simply left in the Li-based electrolyte. In the meantime, the cell voltage slightly decreased, a common feature for resting cells. After 48 h, the cell was charged during 2h at C/20 in order to remove 0.1  $\text{Na}^+/\text{Li}^+$  from the material and left to rest again. Following this event, the electrode potential started to increase well above the 3.1 V of the first plateau in the material. After stabilization of the potential, XRD shows a phase very close to  $\text{Li}_2\text{IrO}_3$ , with broad and asymmetric peaks indicative of the poor crystallinity of the sample. Small impurity peaks could indicate the presence of some  $\text{Na}_x\text{IrO}_3$ , but in a very small amount. This experiment shows that indeed  $\text{Na}^+$  in the material can be exchanged with  $\text{Li}^+$  in the electrolyte if the material is partially oxidized to decrease the kinetic barrier for ion diffusion in and out of the material. The increase of material potential can most likely be correlated to the stabilization energy of the material upon cation exchange and would deserve more in-depth study.

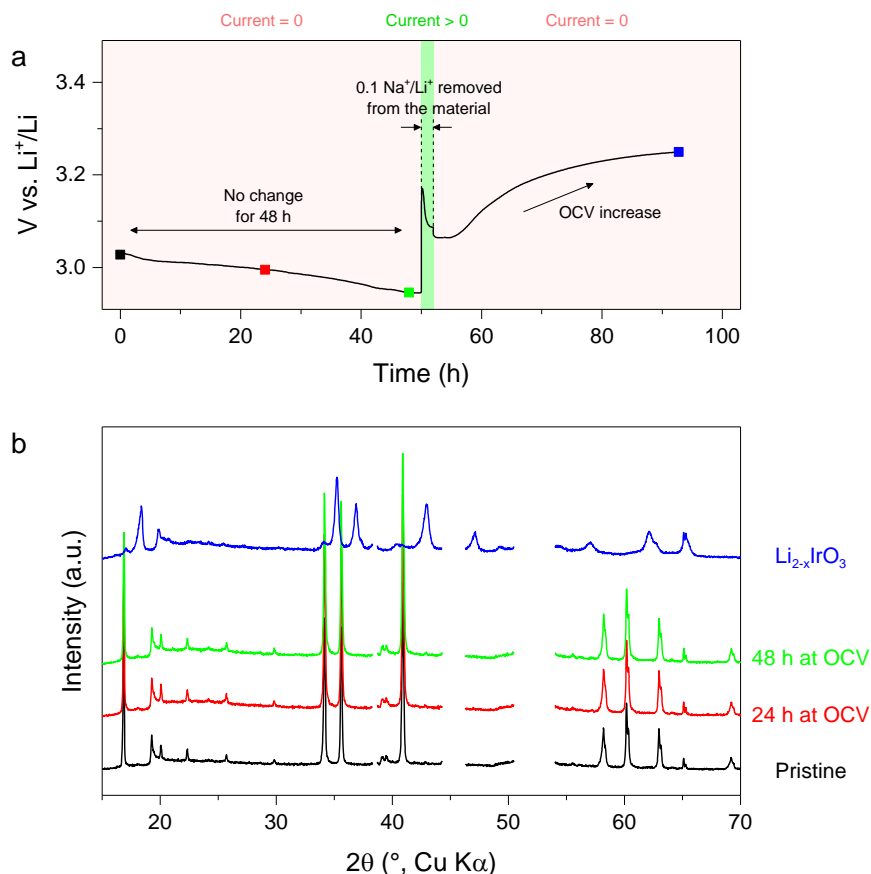


Figure III.8 : XRD study of the  $\text{Na}^+/\text{Li}^+$  exchange reaction in a Li cell. (a) The voltage of the cell is measured as a function of time. The cell is first left at OCV for 48h, then charged at C/20 for 2h (0.1  $\text{Na}^+/\text{Li}^+$  removed) and finally left at OCV. (b) Selected XRD patterns obtained at different times of the experiment, indicated by square markers on the voltage curve.  $2\theta$  regions corresponding to peaks of the *in situ* cell are not plotted for clarity.

### III.3.d. $\text{Na}(\text{Li}_{1/2}\text{Ir}_{2/3})\text{O}_2$ vs. Na

At this point, it seems that  $\text{Na}^+/\text{Li}^+$  exchange is the main mechanism to explain the behavior of this material. Cycling in a Na cell using a Na-based electrolyte should therefore prevent the formation of the  $\text{Li}_x\text{IrO}_3$  phase. A cell was assembled using the material mixed with 10% Csp, a similar electrolyte as the one used for  $\text{Na}_2\text{IrO}_3$  (1M  $\text{NaPF}_6$  in EC:DMC with 1% FEC) and Na as an anode. The cell was cycled between 2 and 4.2 V vs.  $\text{Na}^+/\text{Na}$  at C/10. In that case, the voltage curve on oxidation partially differs from that of the Li cells (Figure III.9). The same capacity ( $\sim 1.5 \text{ Na}^+/\text{Li}^+$ ) can be obtained, but the following reduction curve shows a lower voltage compared to the Li cell.

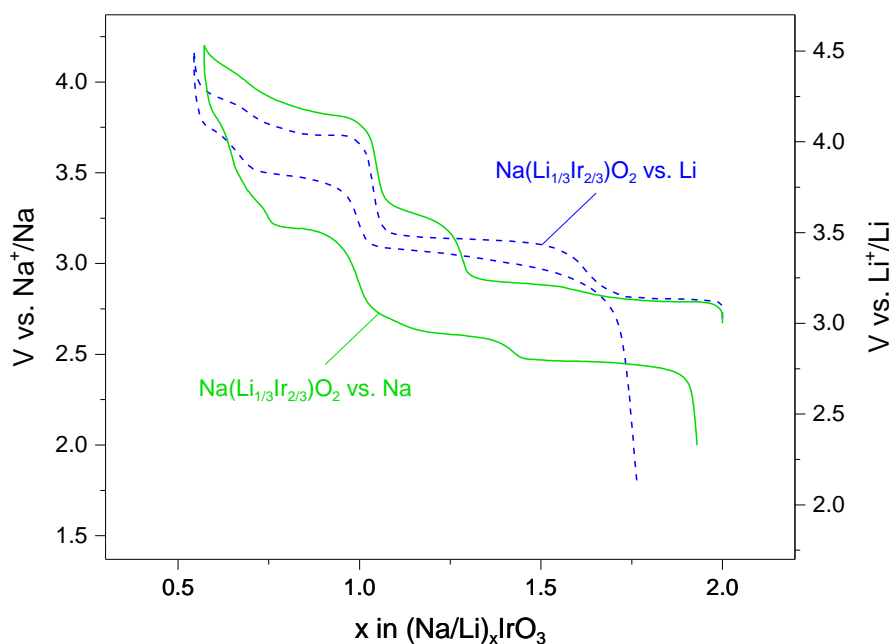


Figure III.9 : Galvanostatic cycling of  $\text{Na}(\text{Li}_{1/3}\text{Ir}_{2/3})\text{O}_2$  vs. Na (green curve, left axis). The curve in a Li cell is shown for comparison (blue dashed line, right axis). The two y-axis were shifted to take into account the potential difference between  $\text{Na}^+/\text{Na}$  and  $\text{Li}^+/\text{Li}$ .

For  $x$  between 2 and 1 in  $(\text{Na}/\text{Li})_x\text{IrO}_3$ , there are now three plateaus instead of two at 2.8, 2.9 and 3.3 V vs.  $\text{Na}^+/\text{Na}$ . For  $x < 1$ , two processes are still visible, while the following discharge is more complex. Going to lower voltages did not result in extra  $\text{Na}^+$  insertion, as was the case for the Li cell. To understand the difference between the two cycling conditions, an *in situ* XRD experiment was performed during the first charge/discharge cycle vs. Na (Figure III.10). The structural changes are notably different compared to the previous experiment vs. Li. The first striking difference is the solid-solution between  $x = 2$  and  $x = 1.6$  in  $(\text{Na}/\text{Li})_x\text{IrO}_3$ , corresponding to the formation of a new phase with a structure similar to the pristine material and an increased interlayer distance, consistent with desodiation (highlighted in red in Figure III.10). This structural transition was barely observed during the cycling vs. Li due to the concurrent  $\text{Na}^+/\text{Li}^+$  exchange reaction. On the next plateau, it is possible to observe intense peaks pertaining to a  $\text{Na}_x\text{IrO}_3$  phase and smaller peaks from a  $\text{Li}_x\text{IrO}_3$  phase (signaled with arrows in Figure III.10), showing that the  $\text{Na}^+/\text{Li}^+$  exchange reaction cannot explain by itself the decomposition of  $\text{Na}(\text{Li}_{1/3}\text{Ir}_{2/3})\text{O}_3$  upon cycling, which is also associated to a segregation of Li and Na in the structure. The  $\text{Li}_x\text{IrO}_3$  phase is however less intense here compared to the Li cell as the exchange reaction is prevented. The fully charged material, after removing 1.5 Na/Li, is very similar to that obtained in the Li cell, again with a lower contribution of the  $\text{Li}_x\text{IrO}_3$  phase. On the next discharge,  $\text{Na}^+$  is intercalated back in the

material, giving two phases at 1.5 V (Figure III.11): the first one corresponding to  $\text{Na}_2\text{IrO}_3$  and the second one closer to the pristine  $\text{Na}(\text{Li}_{1/3}\text{Ir}_{2/3})\text{O}_2$  phase.

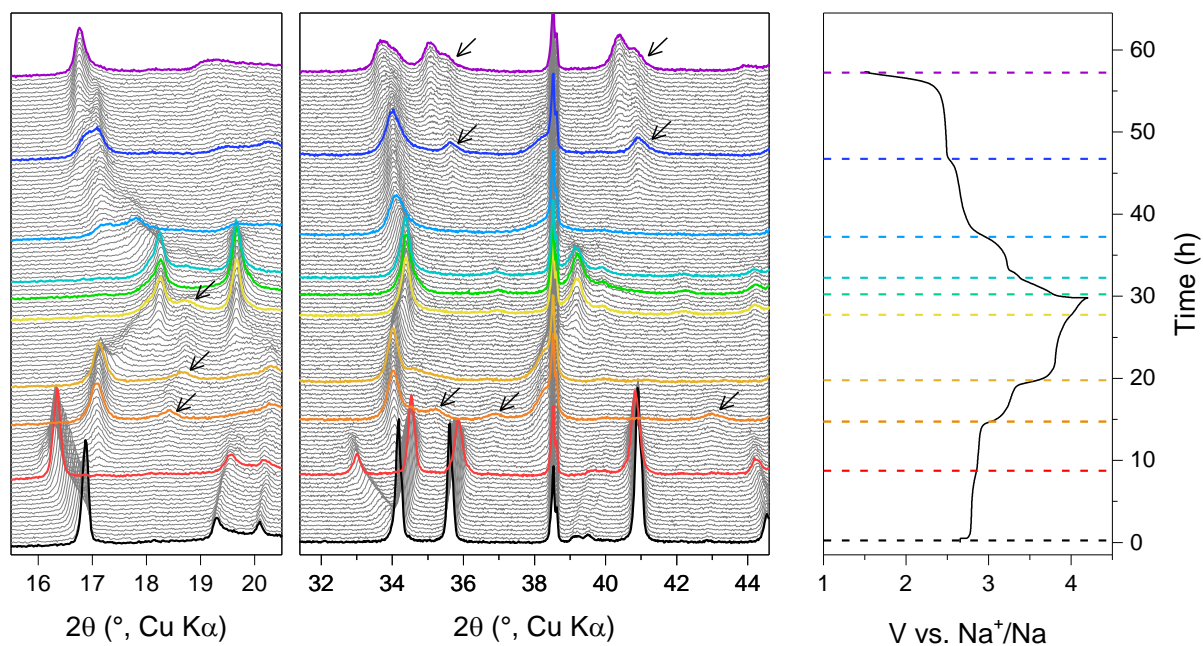


Figure III.10 : *In situ* XRD study of  $\text{Na}(\text{Li}_{1/3}\text{Ir}_{2/3})\text{O}_2$  vs. Na. The cell was charged to 4.2 V and discharged to 1.5 V at C/20. Colored lines highlight the different phases observed during cycling. Arrows point at representative peaks of the  $\text{Li}_x\text{IrO}_3$  phase present in small amount in the electrode.

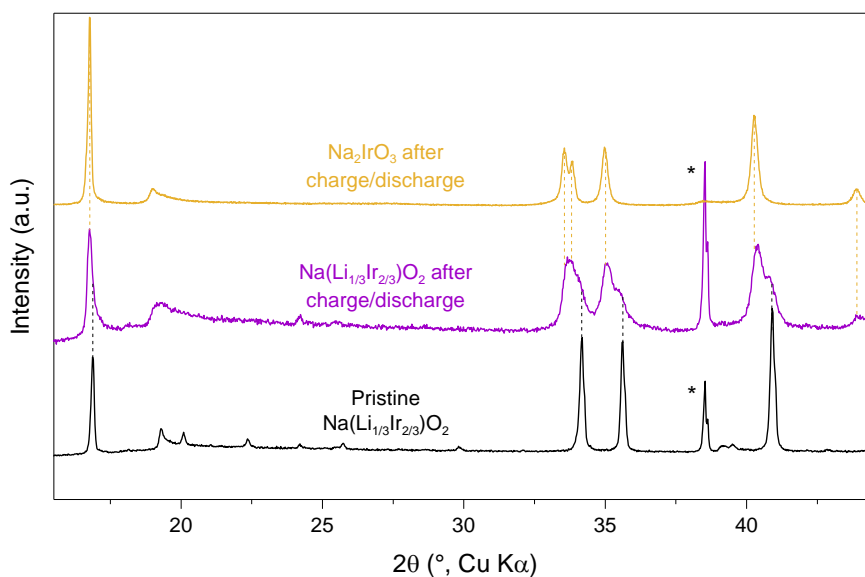


Figure III.11 : Structure of  $\text{Na}(\text{Li}_{1/3}\text{Ir}_{2/3})\text{O}_2$  after a complete charge/discharge cycle vs. Na (middle, purple), compared to the pattern of the pristine material (bottom, black) and that of  $\text{Na}_2\text{IrO}_3$  cycled in the same conditions (top, yellow). The dashed lines highlight the contribution of each phase to the cycled  $\text{Na}(\text{Li}_{1/3}\text{Ir}_{2/3})\text{O}_2$ . Asterisks mark peaks belonging to the *in situ* cell.

The overall electrochemical processes observed when cycling against Li and Na are summarized for clarity in Figure III.12a and b, respectively.

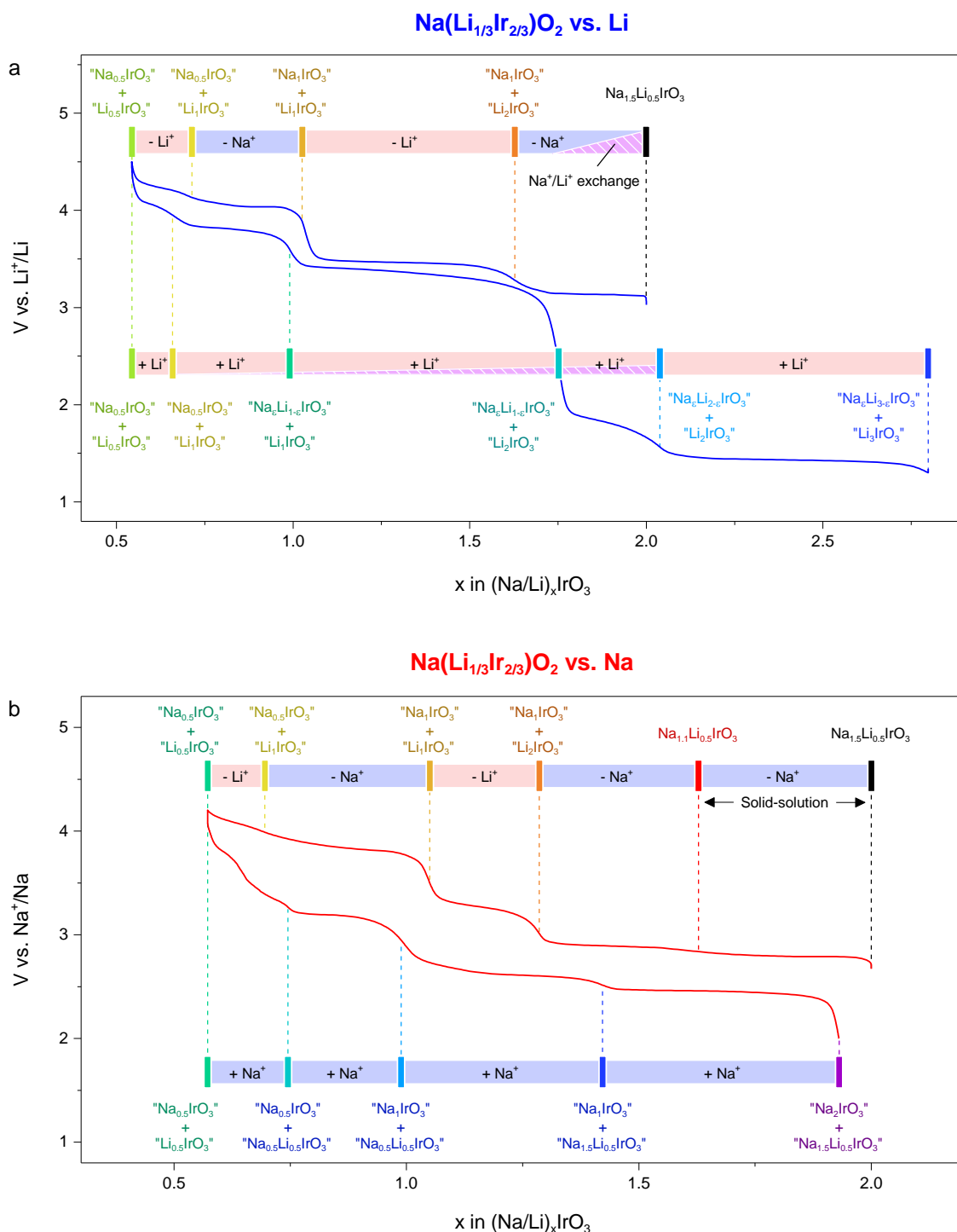


Figure III.12 : Overall electrochemical mechanism of Na(Li<sub>1/3</sub>Ir<sub>2/3</sub>)O<sub>2</sub> in Li and Na batteries. (a) Cycling vs. Li results in exchange between Na in the material and Li from the electrolyte. Part of the material still contains some Na<sup>+</sup> after 1 cycle, whereas most material turns to Li<sub>2</sub>IrO<sub>3</sub>. (b) Cycling vs. Na prevents the exchange reaction, but also results in the segregation of Na and Li, so that after one cycle the material is split between Na<sub>2</sub>IrO<sub>3</sub> and a phase close to the pristine Na(Li<sub>1/3</sub>Ir<sub>2/3</sub>)O<sub>2</sub>. The composition of the phases is not known precisely, therefore it is indicated between quote marks.

### III.4. Conclusion

In this chapter, we prepared  $\text{Na}(\text{Li}_{1/3}\text{Ir}_{2/3})\text{O}_2$  in an attempt to observe an intermediate electrochemical behavior between the pure  $\text{Na}_2\text{IrO}_3$  and  $\text{Li}_2\text{IrO}_3$  phases. We found, in agreement with a theoretical study of Manni *et al.*,<sup>85</sup> that this phase is the only stable member of the  $(\text{Na}_{1-x}\text{Li}_x)_2\text{IrO}_3$  system. The material was characterized by synchrotron X-ray and neutron diffraction and we confirmed the position of  $\text{Li}^+$  ions in the Ir layers, whereas  $\text{Na}^+$  ions remain in the interlayer space. Furthermore, the stacking sequence of honeycomb layers in the material shows a high order periodicity, which could arise from long-range strain in the material due to imperfect ordering.

To study the influence of the alkali ion substitution on the stabilization/destabilization of oxygen 2p levels in the material, and therefore the activation of anionic redox in the material, we investigated the electrochemical properties of the material in Li and Na cells. However, we found that this material undergoes a complex decomposition mechanism upon charge, which results in the formation of  $\text{Na}_x\text{IrO}_3$  and  $\text{Li}_x\text{IrO}_3$  phases. This decomposition is nested in competing exchange and segregation of  $\text{Na}^+/\text{Li}^+$  ions, and will require further experimental characterization with, among others, electron microscopy to obtain some insight on the segregation of  $\text{Li}^+$  and  $\text{Na}^+$  inside or between particles. Theoretical calculations could also give some clarification on this decomposition reaction by extending the phase diagram of the  $(\text{Na}_{1-x}\text{Li}_x)_{2-y}\text{IrO}_3$  system with different  $y$  value. It is possible that the specific  $\text{Na}(\text{Li}_{1/3}\text{Ir}_{2/3})\text{O}_2$  composition is a highly metastable phase and any change in composition results in the formation of the stable  $\text{Na}_2\text{IrO}_3$  and  $\text{Li}_2\text{IrO}_3$  parent compounds.

The result from this work should be taken as a warning when using Li-substitution as a strategy to activate anionic redox in Na-based layered oxides by preparing  $\text{Na}(\text{Li}_{1/3}\text{M}_{2/3})\text{O}_2$  phases. It could also explain the difficulty to prepare the  $\text{Na}(\text{Li}_{1/3}\text{Mn}_{2/3})\text{O}_2$  phase so far, despite several attempts and theoretical calculations suggesting that this material is stable.<sup>88,89</sup>

To study further the effect of alkali ions on the activation of anionic redox, the next chapter will introduce a different approach which, instead of changing the nature of the alkali, relies on modifying the Li/Ir ratio in the material.



## Chapter IV. Pushing to the limits of anionic redox with a new $\text{Li}_3\text{IrO}_4$ phase

### IV.1. Introduction

As presented in the first chapter, fundamental understanding of anionic redox in Li-rich layered oxides is presently backed-up by theoretical calculations, and literature is becoming rich in papers aiming at defining guidelines or indicators to conceptually identify materials showing a Li-driven anionic activity.<sup>67–69</sup> They all agree on the fact that pure oxygen 2p states are required at the Fermi level to reach extra-capacities, a situation that can be triggered from the Li/M stoichiometry (Figure IV.1). In 2016, Saubanère *et al.* proposed that increasing the Li/M ratio to form  $\text{Li}_3\text{MO}_4$  phases could lead to even higher capacities while keeping some alkali in the structure to avoid migration of the transition metal in the structure.<sup>68</sup> This suggestion stemmed from the work of Yabuuchi and coworkers on the  $\text{Li}_3\text{NbO}_4$ - $\text{LiMO}_2$  and  $\text{Li}_4\text{MoO}_5$ - $\text{NiO}$  solid-solutions,<sup>60,90</sup> in which the amount of electrochemically active transition metal was reduced on purpose to activate anionic redox. Large capacities exceeding 300 mAh/g were achieved, with good cyclability at 50°C for  $\text{Li}_{1.2}\text{Nb}_{0.4}\text{Mn}_{0.4}\text{O}_2$ . However, all the prepared compositions in these studies had the same stoichiometry as  $\text{Li}_2\text{MnO}_3$ , with  $\text{Li}/\text{M} = 2$  and  $\text{O}/\text{M} = 3$ . No electrochemical activity was reported for  $\text{Li}_3\text{NbO}_4$  and  $\text{Li}_4\text{MoO}_5$ , which are electronic insulators free of d-electrons ( $\text{Nb}^{5+}$ ,  $\text{Mo}^{6+}$ ).

To probe the effect of increasing the Li/M ratio to reach higher anionic extra-capacities, we searched for  $\text{Li}_3\text{MO}_4$  compounds relying on transition metal M having a partially filled d-band.  $\text{Li}_3\text{MO}_4$  compounds exhibit various structural forms depending on the M cation and nature of the alkali,<sup>91</sup> but the challenge of stabilizing the +5 oxidation state has limited the number of compounds reported. No such composition has been reported with Ir, but we decided to explore its synthesis, encouraged by the fact that several compounds with  $\text{Ir}^{5+}$  have been prepared before.<sup>81,82,92,93</sup>

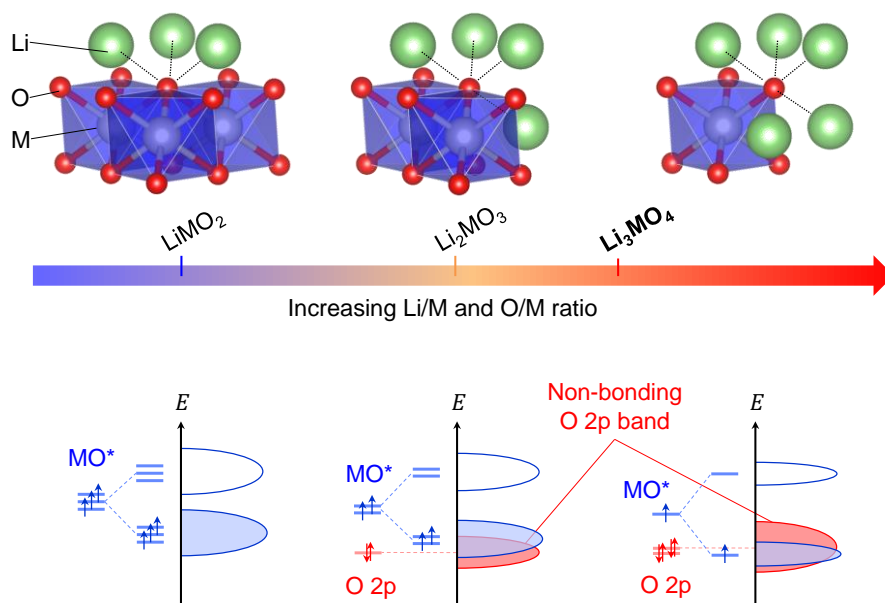


Figure IV.1 : Increasing the Li/M ratio in rocksalt oxides as a strategy to activate oxygen redox. With less metal cations coordinating oxygen, the oxygen orbitals do not form bonding MO and antibonding MO\* states, leaving pure oxygen states which are close enough to the Fermi level to be oxidized. The Mott-Hubbard splitting of the MO\* bands between filled and empty states helps in promoting the non-bonding O(2p) bands close to the Fermi level.<sup>69</sup>

## IV.2. Synthesis and structure

To prepare the material,  $\text{Li}_2\text{CO}_3$  (Sigma Aldrich, 99%) and Ir (Alfa Aesar, 325 mesh, 99.9%) were mixed in stoichiometric proportions using a mortar and pestle, and heated in air at  $950^\circ\text{C}$  for 24h in a covered alumina crucible. The synchrotron XRD data was successfully refined by the Rietveld method using the hexagonal  $R-3m$  description of layered  $\text{LiMO}_2$  phases (Figure IV.2a and Table IV.1). Among the  $\text{Li}_3\text{MO}_4$  family, this new compound adopts a specific layered rocksalt structure with oxygen atoms in a cubic close-packed arrangement, and Li/Ir occupying all octahedral sites (O3 structure). The cations are organized into pure Li layers alternating with mixed Ir/Li layers, in which Ir and Li appear to be randomly distributed (Figure IV.3), an arrangement also confirmed by HAADF-STEM imaging (Figure IV.2b).

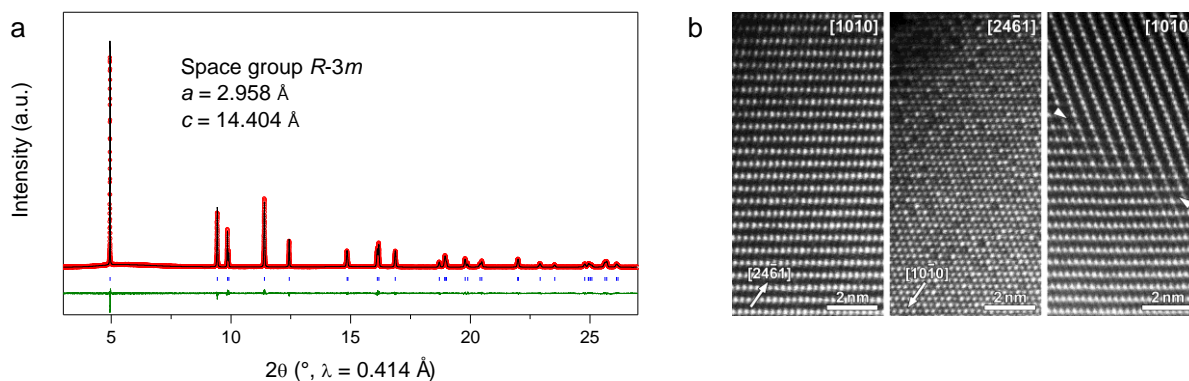


Figure IV.2 : Structural characterization of  $\text{Li}_3\text{IrO}_4$ . (a) Rietveld refinement of synchrotron X-ray diffraction for  $\text{Li}_3\text{IrO}_4$  suggests a layered structure with no long-range ordering of Li and Ir in the metallic layers. (b) Typical HAADF-STEM images of  $\text{Li}_3\text{IrO}_4$  acquired along the  $\langle 110 \rangle_{\text{NaCl}}$  directions of the rock-salt sublattice. The indexes of the directions are given with respect to the hexagonal  $R\bar{3}m$  lattice. The images on the left and in the middle confirm layered organization of the structure with random cation distribution in the Li/Ir layers. Image on the right demonstrates coherent intergrowth of structure domains with different orientations (marked with arrowheads).

Table IV.1 : Structural parameters for the pristine  $\text{Li}_3\text{IrO}_4$  sample obtained from Rietveld refinement of synchrotron XRD pattern. The mixed occupancy of site  $3a$  by Ir and Li shows that there is no long-range ordering of Ir and Li in the metallic layer.

### $\text{Li}_3\text{IrO}_4$

Space group :  $R\bar{3}m$

SXR		$a$ (Å)			$c$ (Å)	
		2.957789(4)			14.40429(5)	
Atom	Site	x	y	z	Occupancy	B (Å <sup>2</sup> )
O1	6c	0	0	0.25426(8)	1	0.931(18)
Ir1	3a	0	0	0	0.5	0.451(3)
Li1	3a	0	0	0	0.5	0.451(3)
Li2	3b	0	0	0.5	1	0.451(3)

Reliability parameters:  $\chi^2 = 1.68$ , Bragg R-factor = 4.24 %

Following the stoichiometry of the compound, which can also be written  $\text{Li}(\text{Li}_{1/2}\text{Ir}_{1/2})\text{O}_2$ , and its layered structure, we could have expected a chain-like arrangement of Li and Ir in the plane, similar to  $\text{Li}_3\text{RuO}_4$ .<sup>94</sup> The reason why Li and Ir do not have a long range order remains unclear. Several attempts to heat the sample at higher temperature, in air or under oxygen, resulted in a loss of Li and O from the material and the formation of  $\text{Li}_2\text{IrO}_3$ , but no ordering was observed so far. DFT calculations were performed on two polymorphs with chain structures: the zig-zag chain model of  $\text{Li}_3\text{RuO}_4$  and a straight chain model (Figure IV.3). The small energy difference between the two structures suggests that both chain arrangements probably exist at the local scale, but without long range order in the plane. This local arrangement therefore cannot be observed by XRD or by STEM.

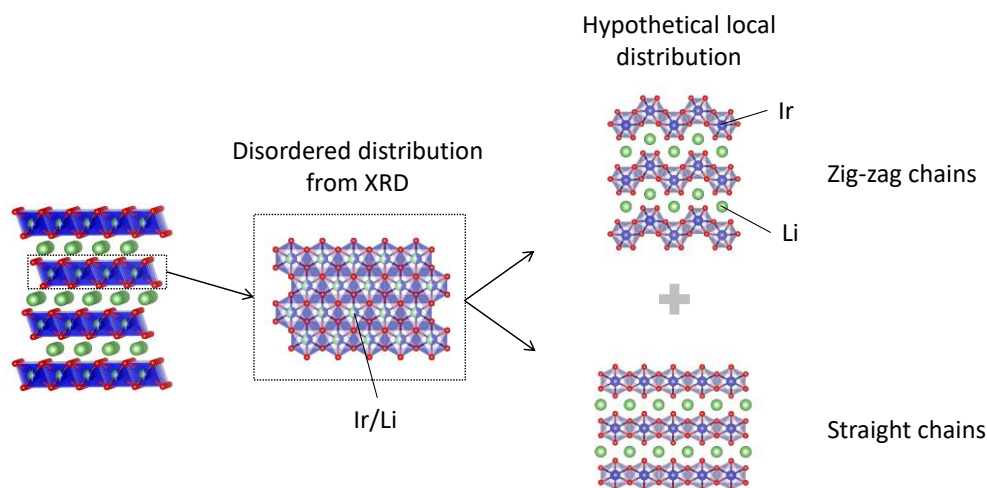


Figure IV.3 : Structural model for  $\text{Li}_3\text{IrO}_4$ . The local arrangement of Ir and Li in the mixed layers is probably composed of straight and zig-zag chains, but the lack of long-range order prevent us to use diffraction or electronic microscopy to characterize it.

### IV.3. Electrochemical properties

#### IV.3.a. Galvanostatic cycling in Li cells

The electrochemical performances of  $\text{Li}_3\text{IrO}_4$  were tested vs. Li in Swagelok cells using laminated electrodes containing 85 wt% of active material, 10 wt% Csp and 5 wt% PTFE (A.2.a). Metallic lithium was used as the negative electrode and LP100 as the electrolyte (1M  $\text{LiPF}_6$  in ethylene carbonate (EC) : propylene carbonate (PC) : dimethylcarbonate (DMC) = 1:1:3). Starting on oxidation, the delithiation occurs through a voltage plateau at an average potential of 3.9-4.0 V vs.  $\text{Li}^+/\text{Li}$  (Figure IV.4). Strikingly, all  $\text{Li}^+$  can be removed from  $\text{Li}_3\text{IrO}_4$ . Bearing in mind that, in both polymorphs of the parent material  $\text{Li}_2\text{IrO}_3$ , the electrochemical oxidation of Ir is limited to  $\text{Ir}^{5+}$ ,<sup>58,65</sup> this suggests a large participation of oxygen in the redox activity. On the subsequent discharge, the voltage profile becomes sloping, with almost 3  $\text{Li}^+$  reinserted down to a lower cutoff of 2.0 V, and remains as such on the next charge/discharge cycles with a fair reversibility. By lowering the voltage down to 0 V (Figure IV.5a), we observe a continuous voltage decrease till 0.7 V corresponding to the conversion reaction  $\text{Li}_x\text{IrO}_y + (2y-x) \text{Li}^+ + (2y-x) \text{e}^- \rightarrow \text{Ir} + y \text{Li}_2\text{O}$ , followed by electrolyte decomposition to form a polymeric gel around the Ir particles.<sup>95</sup>

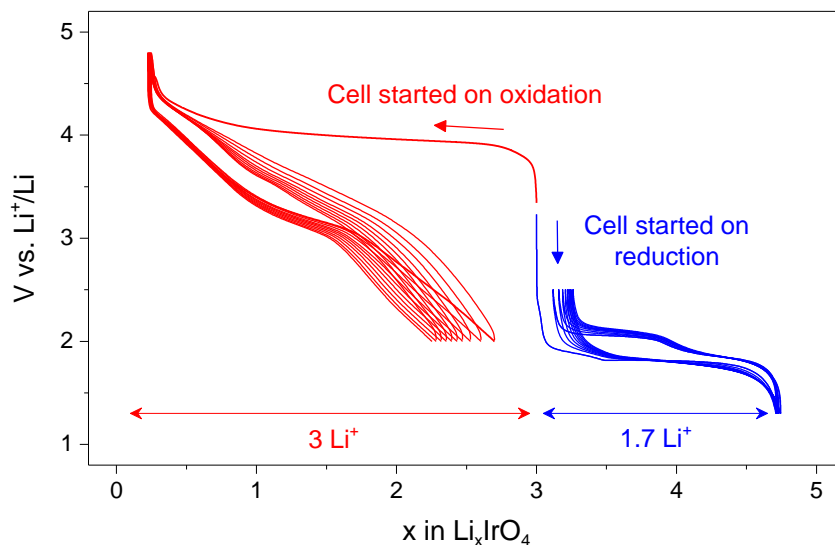


Figure IV.4 : Electrochemical properties of  $\text{Li}_3\text{IrO}_4$ . Galvanostatic curves for two cells started on oxidation and reduction are shown in red and blue, respectively. The electrochemical activity of the material spans over almost 5 electrons.

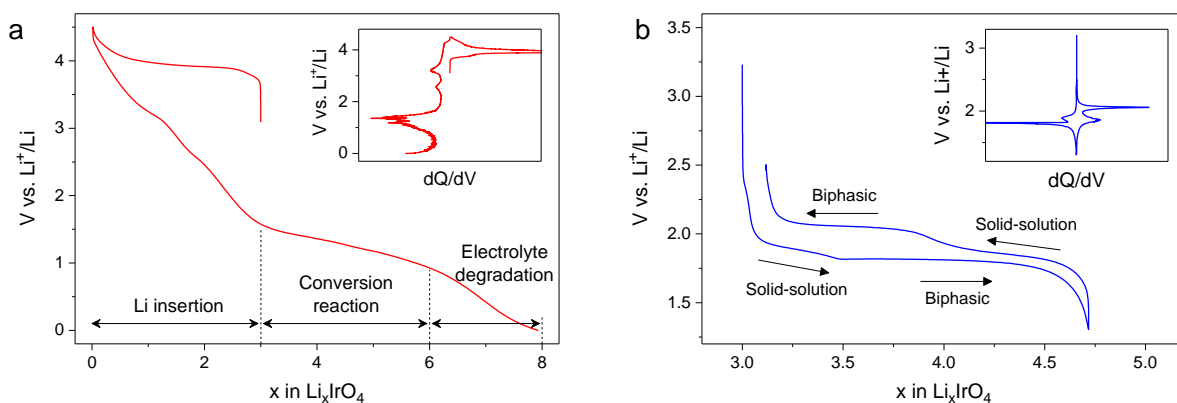


Figure IV.5 : Detailed electrochemical curves. (a) Reduction curve after full oxidation to 4.5 V showing that lowering the voltage below 2 V results in the conversion of the material and electrolyte decomposition. (b) First cycle of the reversible reduction process with a voltage profile characteristic of a classical intercalation mechanism. The corresponding derivative curves are shown in the insets.

Owing to the presence of  $\text{Ir}^{5+}$  in the pristine material, we also tested our electrode on reduction and found that  $\text{Li}_3\text{IrO}_4$  can reversibly intercalate up to 1.7 extra Li (Figure IV.4). This occurs through two well-defined processes at 1.9 V and 1.8 V in the dQ/dV derivative curve (Figure IV.5b) which are indicative of classical insertion/deinsertion mechanisms, with low polarization between charge/discharge and an excellent cyclability. We can note from the successive slopes and plateaus that the intercalation and deintercalation of  $\text{Li}^+$  is not simply reversed when the current is changed but follow the same succession of events: solid-solution followed by a biphasic process on discharge and again solid-solution followed by a biphasic process on charge.

Overall the redox activity of  $\text{Li}_3\text{IrO}_4$  spans over almost 5 electrons, but it seems impossible to take advantage of the whole capacity as the oxidation process is partially irreversible due to a large structural modification. To understand this issue and push to its maximum the reversible capacity in the material, the structural evolution upon cycling was studied in detail.

### IV.3.b. Reversible $\text{Li}^+$ intercalation on reduction

The lithiation-delithiation mechanism in  $\text{Li}_3\text{IrO}_4$  was examined by *in situ* X-ray diffraction. The cell was cycled at C/15 and XRD patterns were collected every 30 min. Rietveld refinement of the patterns was used to obtain the change in cell parameters during cycling. Upon the cell discharge, all the peaks shift to lower angle (Figure IV.6a), indicating an increase of cell parameters upon lithiation (Figure IV.6b), consistent with a solid-solution mechanism till  $\text{Li}_{3.5}\text{IrO}_4$ . For  $x$  between 3.5 and 4 in  $\text{Li}_x\text{IrO}_4$ , the peaks intensity decreases at the expense of a new phase which becomes pure after  $x = 4$ . Finally, the Bragg peaks shift continuously up to  $x = 4.7$ , at the exception of the (00l) peaks, showing that the interlayer distance is preserved.

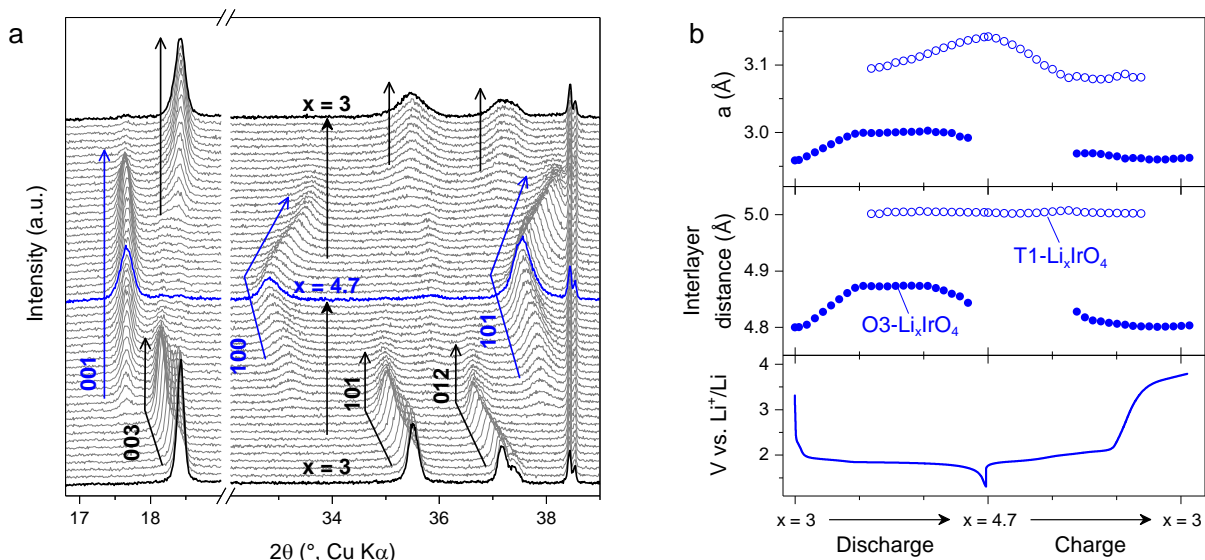


Figure IV.6 : *In situ* XRD study of the reduction process. (a) Evolution of the XRD patterns and (b) of the cell parameters during cycling.

The structure of the fully reduced  $\text{Li}_{4.7}\text{IrO}_4$  phase was deduced from XRD and neutron diffraction (Figure IV.7a,b) using the structural model of  $\text{Li}_2\text{NiO}_2$ <sup>96</sup> (Table IV.2) with the extra Li lying in tetrahedral sites (T1 structure, Figure IV.7c). These sites arise from the shift

of the  $(\text{Li}_{1/2}\text{Ir}_{1/2})\text{O}_2$  layers, which transforms the cubic close-packed (ABCABC) into an hexagonal close-packed (ABAB) oxygen stacking. This structural transition doubles the number of available sites in the pure Li layers and should theoretically lead to  $\text{T1-Li}_5\text{IrO}_4$ . Our inability to reach this value experimentally (4.7 instead of 5) is most likely nested in the limited  $\text{Li}^+$  diffusion as we are approaching the full occupancy of the Li sites.

When the cell is subsequently charged, the solid solution process is reversed with a shift of all peaks except (00l) to higher angles at a potential of 1.85 V vs.  $\text{Li}^+/\text{Li}$ , consistent with the oxidation of Ir. It is followed by a biphasic process at 2.05 V which directly leads to the original O3 structure without going through the solid solution observed at the beginning of reduction. Overall, the structural transition is reversible, but proceeds via different paths on reduction and oxidation.

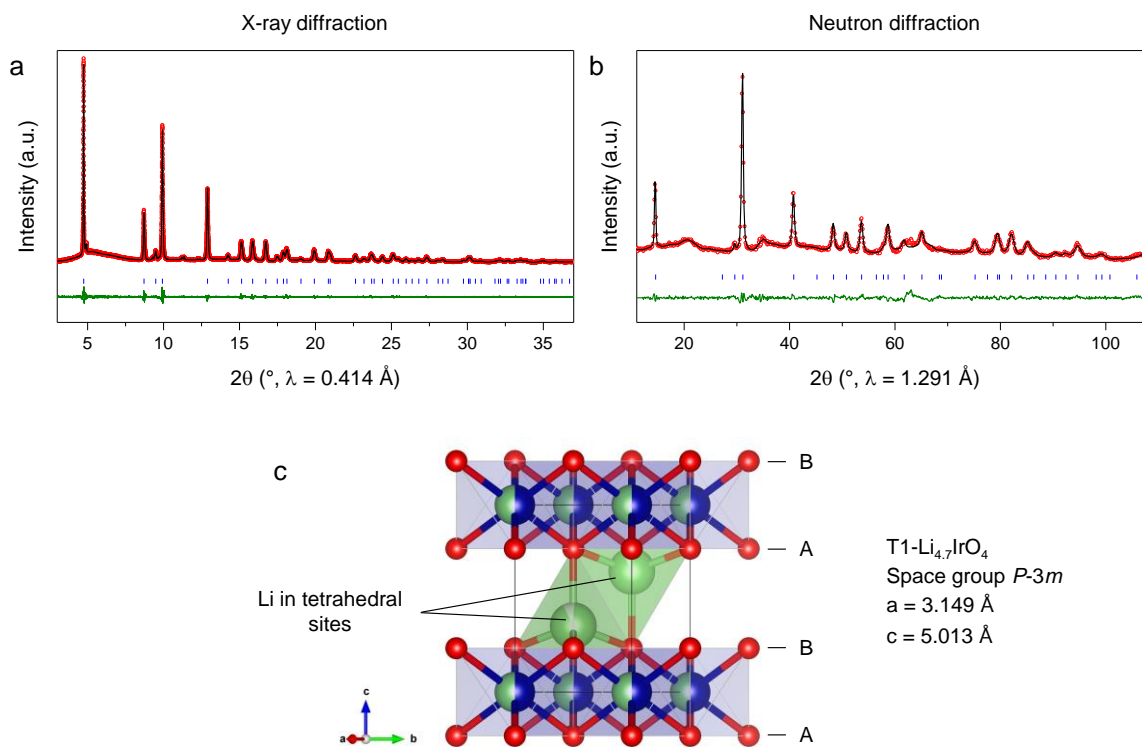


Figure IV.7 : Structure of  $\text{Li}_{4.7}\text{IrO}_4$ . Rietveld refinement of synchrotron XRD (a) and neutron diffraction (b) patterns were refined using a structural model with T1 stacking of  $(\text{Li}_{1/2}\text{Ir}_{1/2})\text{O}_2$  layers and extra Li in tetrahedral sites in the interlayer space (c).

Table IV.2 : Structural parameters for the reduced  $\text{Li}_{4.7}\text{IrO}_4$  sample obtained from combined Rietveld refinement of synchrotron XRD and neutron diffraction patterns. The mixed occupancy of site  $1a$  is kept similar to that of the site  $3a$  in the pristine material. Occupancy of the  $2d$  sites is fixed with respect to the electrochemical lithiation value. Atomic positions were refined from ND data and used as such for the refinement of SXR data. B values are indicated for SXR (first line) and ND (second line) data, respectively.

<b>T1-Li<sub>4.7</sub>IrO<sub>4</sub></b>						
Space group : $P\bar{3}m$						
		$a$ (Å)			$c$ (Å)	
SXR		3.148969(8)			5.013252(18)	
ND		3.13993(18)			5.0180(4)	
Atom	Site	$x$	$y$	$z$	Occupancy	B (Å <sup>2</sup> )
O1	$2d$	1/3	2/3	0.2340(8)	1	1.38(3) 2.69(10)
Ir1	$1a$	0	0	0	0.5	0.531(3) 0.85(13)
Li1	$1a$	0	0	0	0.5	0.531(3) 0.85(13)
Li2	$2d$	1/3	2/3	0.6455(19)	0.925	1.74(8) 2.8(2)

Reliability parameters : SXR :  $\chi^2 = 1.21$ , Bragg R-factor = 1.51 %  
 ND :  $\chi^2 = 2.41$ , Bragg R-factor = 46.9 %

### IV.3.c. Amorphisation and oxygen loss on full oxidation

*In situ* XRD diffraction patterns were similarly collected on a  $\text{Li}_3\text{IrO}_4/\text{Li}$  cell which was started on oxidation (Figure IV.8a). We initially observe a slight shift of all Bragg reflections towards lower angles up to  $x = 1$ , caused by the delithiation of the material, followed by a sudden shift toward larger angles and a drastic loss of peak intensity. After removal of 3 Li, the X-ray powder pattern of the fully delithiated phase “ $\text{IrO}_4$ ” is featureless, indicative of its amorphous nature. The large decrease of the interlayer distance at the end of charge (Figure IV.8b) indicates that the complete delithiation of the material leads to its structural collapse. Electron diffraction pattern confirms the amorphization of the material, so that only short-range interatomic correlations survive (Figure IV.9), hence explaining the drastic change in voltage curve of the material when delithiated deeper than  $x = 1$ .

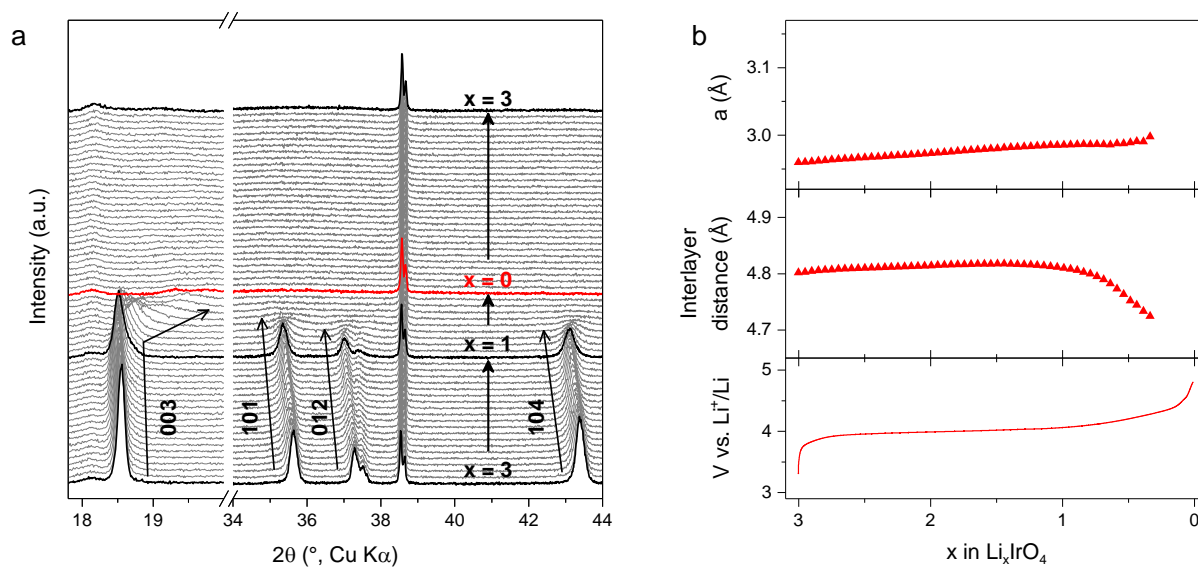


Figure IV.8 : *In situ* XRD study of the oxidation process. (a) Evolution of the XRD patterns and (b) of the cell parameters during cycling.

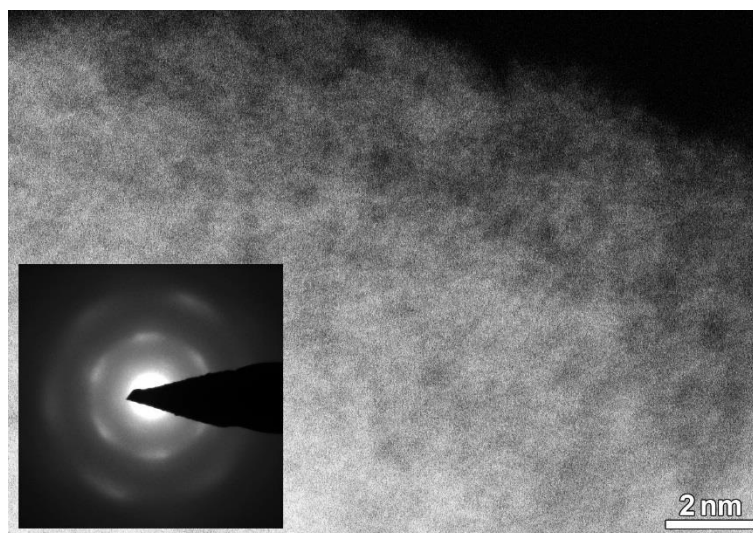


Figure IV.9 : TEM data of  $\text{Li}_3\text{IrO}_4$  charged to 4.5 V, demonstrating severe amorphization of the material. The HAADF-STEM image is shown at the same magnification as the images of the pristine structure (Figure IV.2b). Note significant random intensity variations characteristic for amorphous materials. The ED pattern (inset) contains very broad reflections, suggesting that only short-range interatomic correlations are preserved in the compound.

In light of previous works, oxygen loss may occur on charge in these high capacity electrodes. To check this point, gas pressure analysis was carried out over the first two charge/discharge cycles using a dedicated cell (A.2.b.iv).<sup>97</sup> As  $\text{Li}_x\text{IrO}_4$  is initially charged up to  $x = 1$ , the pressure remains constant, but increases rapidly as more Li is removed (Figure IV.10a). Once the first charge is achieved, the pressure does not change any longer upon cycling. From the pressure increase, we can deduce that approximately 0.35 gas molecules are released per  $\text{Li}_3\text{IrO}_4$  unit formula. The nature of the gases was assessed by DEMS analysis

which clearly shows (Figure IV.10b) that the released gas at  $x = 1$  is mainly  $O_2$  ( $m/z = 32$ ) with however the detection of minor amounts of  $CO_2$  ( $m/z = 44$ ) towards the end of the oxidation process. If we consider the formation of  $O_2$  from  $O^{2-}$ , this process enlists  $4 e^-$  /molecule of gas and would lead to an irreversible loss of  $1.4 e^-$ . The final stoichiometry of the sample after complete delithiation would therefore be closer to  $IrO_3$  than  $IrO_4$ . Obviously, this calculation is a simple estimation and does not consider other reaction pathways for oxygen release and the possible reaction of the generated  $O_2$  gas with the electrolyte or the Csp carbon additive.

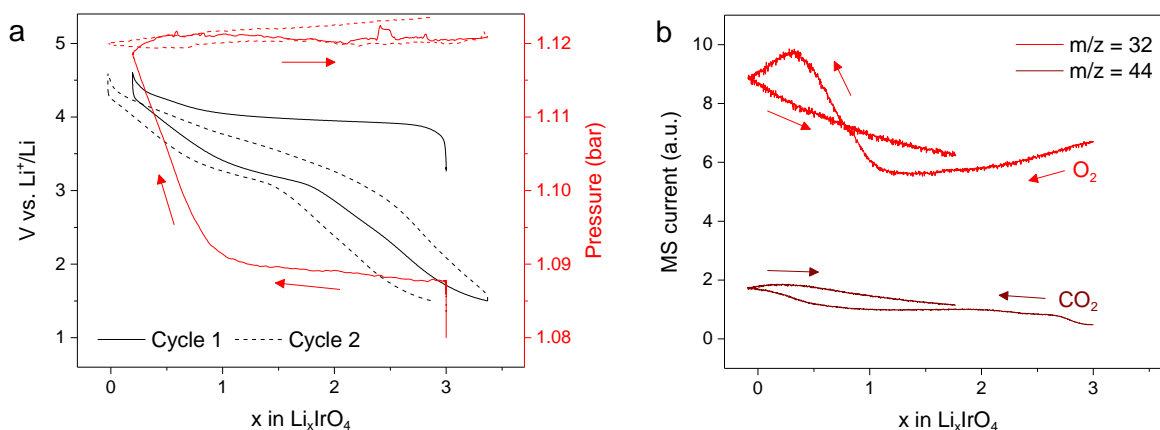


Figure IV.10 :  $O_2$  release upon complete oxidation of  $Li_3IrO_4$ . (a) *In situ* pressure measurement during the first two cycles of  $Li_3IrO_4$  between 1.5 and 4.5 V. (b) DEMS analysis of the gas formed during the first cycle.

Another indirect way to measure the oxygen loss for this highly oxidized sample consists in further exploiting the discharge-driven conversion reaction down to 0 V, with the number of uptaken Li ( $u$ ) in  $Li_xIrO_y$  being related to the amount of oxygen  $y$  by  $u = 2y - x$ . This is possible because we can assume similar 0 V end-products, i.e. Ir nanoparticles embedded into an amorphous Li-based matrix, as confirmed by HAADF-STEM (Figure IV.11). The discharge capacities of the pristine, ( $x = 3$ ) the partially charged ( $x = 2$  and 1) and fully charged ( $x = 0$ )  $Li_xIrO_y$  materials are shown in Figure IV.12. No difference can be observed between the pristine,  $x = 1$  and  $x = 2$  samples, as no oxygen is released upon oxidation. In contrast, the capacity of the fully charged sample is 2 Li lower than that of the pristine material, implying that, upon oxidation, the amorphization of the material proceeds with the release of one oxygen atom per formula unit. To confirm the stoichiometry, the discharge capacity down to 0 V of the amorphous  $IrO_3$  and the crystalline  $\beta$ - $IrO_3$  obtained by delithiating  $\beta$ - $Li_2IrO_3$  were compared (Figure IV.12).<sup>65</sup> Both samples show exactly the same capacity, confirming our hypothesis. This material will be designated from now on as a- $IrO_3$ .

for “amorphous  $\text{IrO}_3$ ”. By using the difference between integrated area of the two voltage curves on conversion collected at nearly equilibrium conditions (Figure IV.13a), we can also deduce the difference in Gibbs free energy and show that the  $\beta\text{-IrO}_3$  polymorph is more stable than the  $\alpha\text{-IrO}_3$  polymorph by 57 kJ/mol (Figure IV.13b), a value comparable to that found by Delmer *et al.* between crystalline and amorphous  $\text{RuO}_2$ .<sup>98</sup> Finally, the lower number of oxygen released obtained by gas measurement (0.35  $\text{O}_2$ ) as compared to 0.5  $\text{O}_2$  from electrochemistry is most likely due to partial reactivity of  $\text{O}_2$  with the electrolyte and/or Csp.

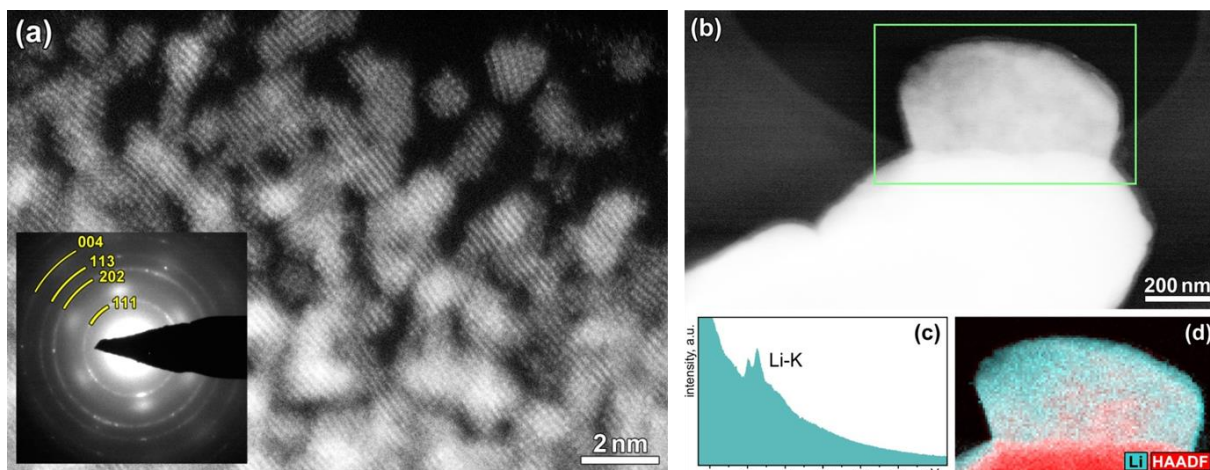


Figure IV.11 : TEM data of  $\text{Li}_3\text{IrO}_4$  discharged to 0 V. (a) High magnification HAADF-STEM image showing the formation of crystalline Ir nanoparticles of just a few nm in size. The ED pattern (inset) demonstrates sharp rings that can be indexed on the Ir structure ( $S.G. Fm\bar{3}m, a \approx 3.9 \text{ \AA}$ ); and some broad reflections, suggesting that a fraction of the material preserves short-range correlated structure of the oxide. (b) Low magnification HAADF-STEM image of a particle. The contrast is adjusted in such a way that one can identify a thin ( $\sim 5\text{-}10 \text{ nm}$ ) Li/ $\text{Li}_2\text{O}$ -based layer on the surface. (c) EELS spectrum confirming presence of Li in the coating, and (d) the corresponding Li distribution map.

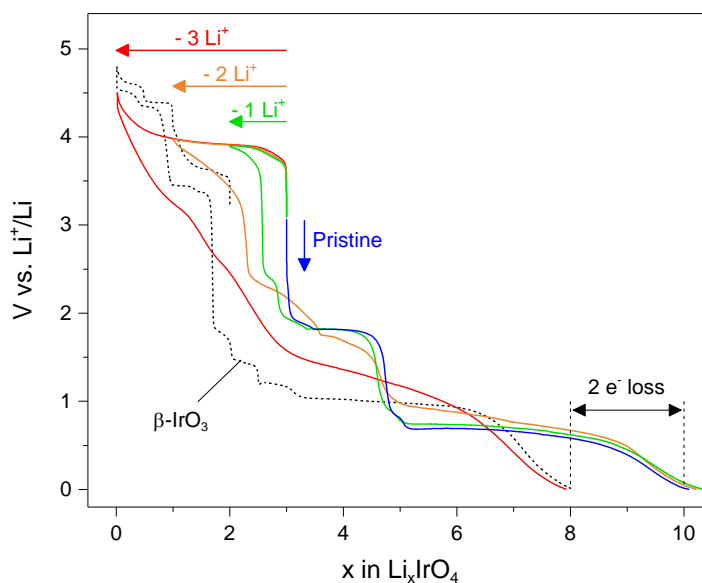


Figure IV.12 : Change in conversion capacity of  $\text{Li}_3\text{IrO}_4$ . The capacity upon complete conversion of the material does not change after charging to  $x = 2$  (green) or 1 (orange) compared to the pristine material (blue). However, almost  $2 e^-$  are lost on reduction when all 3  $\text{Li}^+$  are removed from the material (red). The reduction capacity of the amorphous phase after losing gas is similar to that of  $\beta\text{-IrO}_3$  (dashed line). The Al current collector was replaced by stainless steel to avoid Li alloying at low potentials.

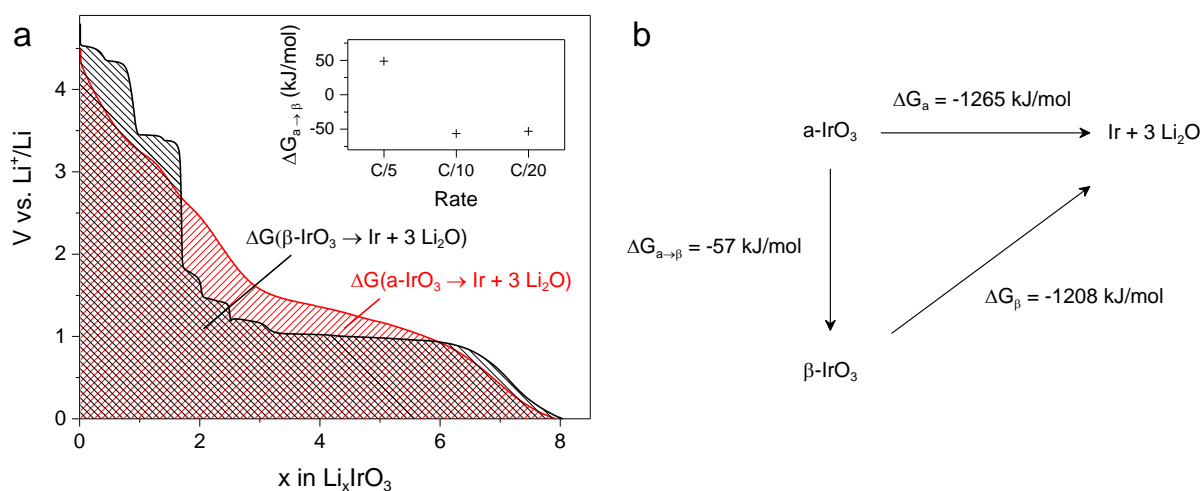


Figure IV.13 : Energy difference between the two polymorphs  $\text{a-IrO}_3$  and  $\beta\text{-IrO}_3$ . (a) The difference of area below the voltage curves gives the difference in Gibbs free energy according to (b). The inset shows that the difference in Gibbs energy converges to 57 kJ/mol when the cycling rate is decreased to C/20, approaching equilibrium conditions.

To rationalize the abundant amorphization of the material upon removal of the last  $\text{Li}^+$ , the decomposition enthalpies of  $\text{Li}_x\text{IrO}_4$  into  $\text{Li}_x\text{IrO}_3 + \frac{1}{2} \text{O}_2$  were computed for different Li contents ( $x$ ), showing that  $\text{Li}_x\text{IrO}_4$  starts to be unstable with respect to  $\text{O}_2$  release for values of  $x \leq 1$ . Interestingly, the resulting  $\text{a-IrO}_3$  material has the same stoichiometry as the crystalline  $\beta\text{-IrO}_3$ , which is perfectly stable versus oxygen release. Although  $\text{IrO}_4$  has been claimed to be

stabilized under complex matrix isolation conditions at low temperature,<sup>99</sup> it is clearly unstable in electrochemical conditions. Interestingly,  $\text{RuO}_4$  and  $\text{OsO}_4$  tetrahedral species are stable at room temperature due to their  $d^0$  configurations, opening new perspectives to stabilize delithiated  $\text{Li}_x\text{MO}_4$  structures, provided that their strong oxidative properties can be controlled.

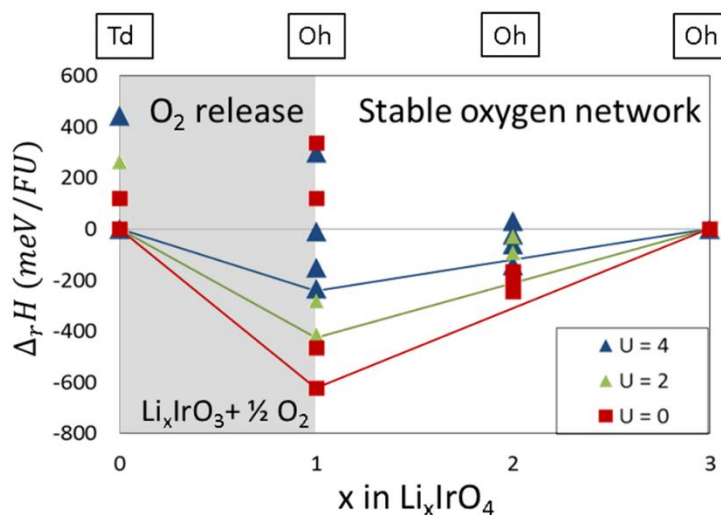


Figure IV.14 : Phase stability diagram of  $\text{Li}_x\text{IrO}_4$  computed by DFT+U ( $T = 0$  K) at different  $U$  values (in eV), in which the formation energy of  $\text{Li}_x\text{IrO}_4$  is compared to the energy of the direct  $\text{Li}_3\text{IrO}_4$  to  $\text{IrO}_4 + 3\text{Li}$  transformation, taken as the reference energy (horizontal line). The oxygen vacancy formation as well as the decomposition enthalpies of  $\text{Li}_x\text{IrO}_4$  into  $\text{Li}_x\text{IrO}_3 + \frac{1}{2}\text{O}_2$  were also computed for each Li composition. The results presented in this figure show that intermediate  $\text{Li}_x\text{IrO}_4$  phases can be electrochemically stabilized and that phase decomposition into  $\text{Li}_x\text{IrO}_3 + \frac{1}{2}\text{O}_2$  occurs between  $x = 0$  and 1.

#### IV.3.d. Reversible cycling

The oxidation mechanism proceeds via an irreversible gas release and a complete amorphization of the material when delithiated below  $x = 1$ . Based on this knowledge, we tried to improve the cyclability of the material by limiting the first charge to  $x = 1$ , and cycling between 1.3 and 4 V on the next cycles. In these conditions, the cell shows a reversible capacity of nearly  $3.5\text{Li}^+$  per transition metal (Figure IV.15), which stands as a record among all the transition metal oxides reported so far as insertion cathode materials.

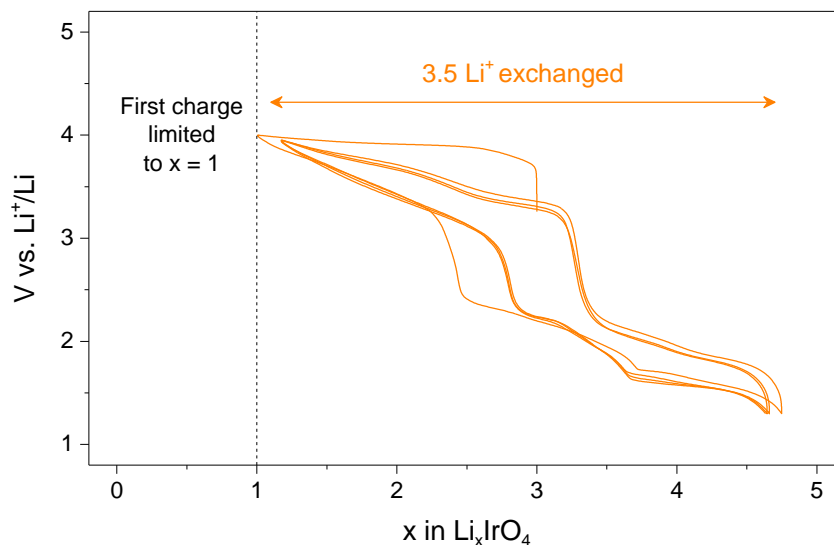


Figure IV.15 : Reversibility of intercalation over 3.5 Li<sup>+</sup> when the initial charge is limited to x = 1.

To confirm the reversibility of the intercalation process, we performed X-ray diffraction in these cycling conditions and compared the evolution of the cell parameters with the previous experiments (Figure IV.16). The first part of the charge process is similar to that observed in the cell started on oxidation, but when the current is reversed at x = 1, all Bragg peaks shift back to their initial positions, without undergoing the amorphization process. Continuing on discharge, the O3 → T1 transformation is observed, although the transition is not so well defined as for the cell started directly on reduction. After one cycle, the structure of the pristine material is recovered, unambiguously proving the reversibility of the insertion mechanism over 3.5 Li<sup>+</sup>. This process was found to be reversible upon long-term cycling, with limited capacity decay over 25 cycles at C/5 (1 cycle in 35h) as shown in Figure IV.17a. To verify the structural stability of the material upon longer cycling, the material was recovered after 25 cycles and XRD pattern of the recovered sample was found similar to the pristine material (Figure IV.17b) with the exception of peak broadening which reflects a small loss of crystallinity commonly observed for cathode materials.

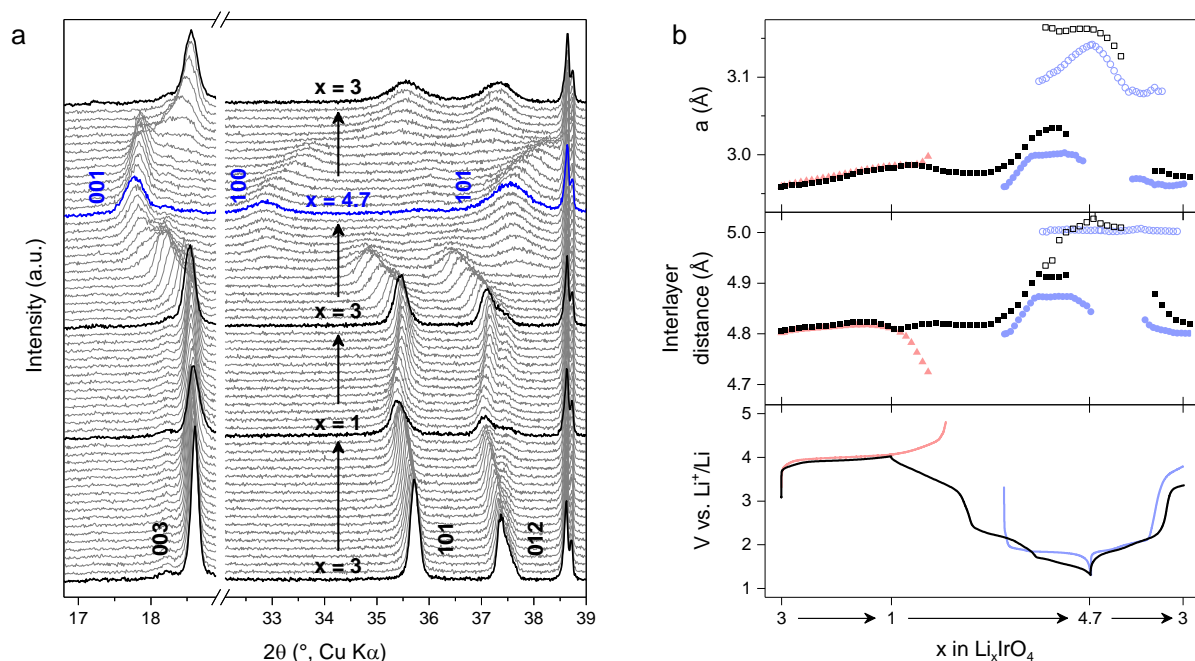


Figure IV.16 : *In situ* XRD study of the reversible cycle. Evolution of the XRD patterns (a) and cell parameters (b, black squares) during cycling. The cell parameters collected from the two other *in situ* cells (Figure IV.6 and Figure IV.8) are superimposed to help the comparison. Full and empty markers correspond to the O3 and T1 phases, respectively.

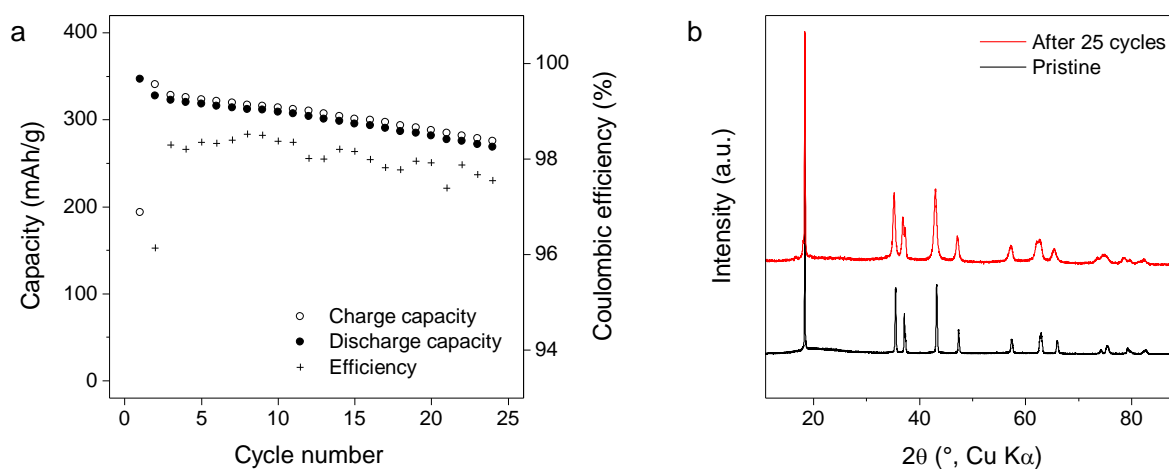


Figure IV.17 : Cycling performances. (a) Charge/discharge capacity and coulombic efficiency of the cell cycled between 1.3 and 4 V for 25 cycles. (b) XRD pattern after 25 cycles compared to the pristine electrode.

#### IV.4. Participation of oxygen and iridium to the redox

Due to the peculiar structure of  $\text{Li}_3\text{IrO}_4$ , with no long-range order of Li and Ir in the planes, we cannot rely on diffraction or electron microscopy techniques to get information on the distortion of  $\text{IrO}_6$  octahedra depending on the Li content. To circumvent this issue, we used X-ray absorption spectroscopy to probe the local environment of Ir. Both the EXAFS

and XANES parts of the signal were analyzed to get an insight on the oxidation/reduction of iridium, and indirectly of oxygen. We also used Electron Paramagnetic Resonance (EPR) spectroscopy to detect the signal of  $(\text{O}_2)^{\text{n-}}$  paramagnetic species.

#### IV.4.a. Extended X-ray Absorption Fine Structure at Ir L<sub>III</sub>-edge

*Operando* XAS measurements were carried out on the ROCK beamline of SOLEIL synchrotron (see Figure A.8),<sup>100</sup> using electrochemical cells designed for transmission experiments (Figure A.7).<sup>80</sup> Self standing PTFE films of the active material were used and cycled vs. Li at C/4. One cell was started on reduction to 1.4 V and charged again (cell A, see Figure IV.18a, left). Another was started on oxidation to 4.8 V and discharged (cell B, see Figure IV.18a, center). For the last measurement, an electrode was precharged in a swagelok cell until  $x = 1$  and discharge to  $x = 2$ , before being transferred to the *in situ* cell and cycled reversibly between 1.3 and 4 V (cell C, see Figure IV.18a, right). For each cell, one spectrum was obtained every 15 min, i.e. every  $\Delta x \approx 0.06$ .

The spectra obtained by X-ray absorption spectroscopy are the sum of the signal from all Ir species present in the material, following Beer-Lambert's law. When the different species present in the sample are known *a priori*, the signal can simply be reconstructed using a linear combination of the spectra of the individual species. Here, we do not have information about the different Ir environments which can participate to the spectra during cycling. Using the Principal Component Analysis (PCA) method, we can find the minimum number of mathematical components necessary to describe all the spectral dataset. We then used this information in the Multivariate Curve Resolution (MCR) method<sup>101,102</sup> to find chemically meaningful components and their relative concentrations in each experimental spectrum. To find a correct solution, constraints based on our knowledge of the system are implemented, such as the non-negativity of both the absorption spectra and the concentration, and the sum of concentrations of the different species being equal to the total concentration of the absorbing atom.

Only 3 components (Figure IV.18b) are needed to describe the reduction cycle for cell A, each of them corresponding to well-defined Ir local environments that were characterized by fitting the EXAFS oscillations (Table IV.3 and Figure A.10 in annex). We could then deduce the distortion of the IrO<sub>6</sub> octahedra during the Li insertion process by monitoring Ir-O and Ir-Ir distances (Figure IV.18c): both distances increase from the pristine (A1) to the

intermediate (A2) and the reduced (A3) components in agreement with the expected reduction of  $\text{Ir}^{5+}$  to  $\text{Ir}^{4+}$  and  $\text{Ir}^{3+}$ . It is important to mention the observed symmetry in the discharge/charge insertion process deduced from XAS data which contrasts with the asymmetric one obtained from XRD data. This difference is most likely nested in the sensitivity of the XAS technique to detect the oxidation state of Ir that governs local structural changes, in contrast to XRD which detects long range structural modifications, hence enabling to spot the  $\text{O3} \rightarrow \text{T1}$  transition which is not reflected on the XAS data.

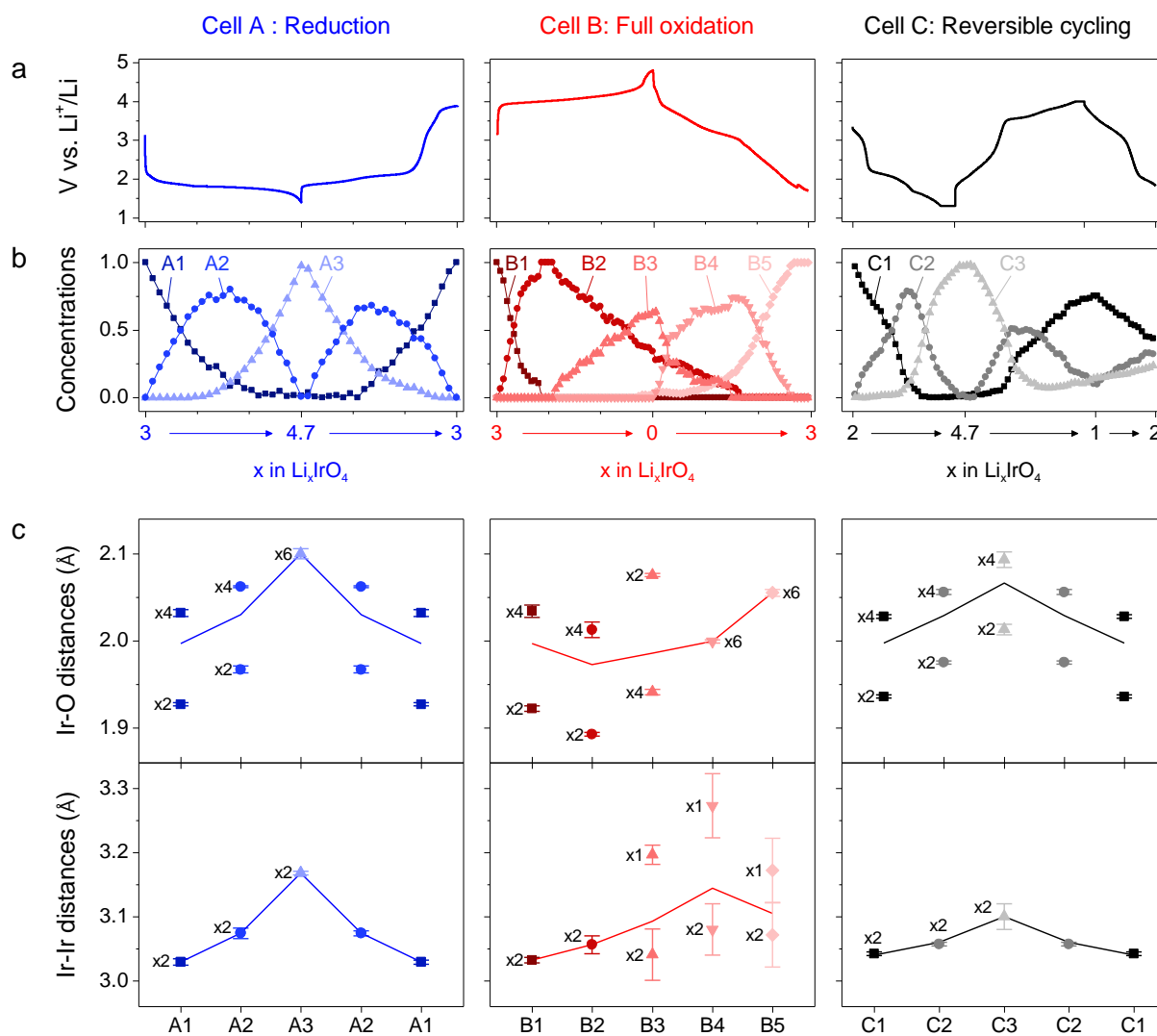


Figure IV.18 : Local structural evolution from *operando* EXAFS analysis at Ir  $L_{\text{III}}$  edge. (a) Galvanostatic curves of the three cells measured during the experiment (b) Relative concentrations during cycling of the principal components extracted using PCA and MCR-ALS analysis. Each component is described by a specific marker and color. (c) Ir-O and Ir-Ir distances obtained from fitting the EXAFS oscillations (Figure A.10 to A.12). The multiplicity of each distance is indicated next to the corresponding data point (x1, x2, x4 and x6, as reported in Table IV.3). Full lines are connecting the average Ir-O and Ir-Ir distances to highlight the distortion of  $\text{IrO}_6$  octahedra associated with Ir oxidation/reduction. Error bars were estimated from the distribution of values found for the different models tried during the fitting process.

Table IV.3 : Structural parameters obtained by fitting the EXAFS oscillations of the components extracted from PCA and MCR-ALS analysis on cells A, B and C. The difference in threshold energy ( $\Delta E_0$ ) and amplitude reduction factor ( $S_0^2$ ) were determined from reference samples and fixed at the same value for all the fits. The coordination number (N) was kept constant and only the radial distance (R) and the Debye-Waller factor ( $\sigma^2$ ) were allowed to vary. Several structural models were tried for each datasets, with the most satisfactory ones reported here. The errors were estimated from the variation of the parameters between different structural models.

		Ir-O (first shell)			Ir-Ir (second shell)			Ir-O (third shell)			Ir-O-O-Ir (multiple scattering)		
		N	R (Å)	$\sigma^2 (10^{-3} \text{Å}^2)$	N	R (Å)	$\sigma^2 (10^{-3} \text{Å}^2)$	N	R (Å)	$\sigma^2 (10^{-3} \text{Å}^2)$	N	R (Å)	$\sigma^2 (10^{-3} \text{Å}^2)$
Cell A	A1	2	1.927(2)	2.2(6)	2	3.029(5)	2.6(2)	6	3.68(3)	9.1(3)	24	3.41(6)	2
		4	2.032(4)	2.7(2)									
	<i>R-factor = 9.6 x 10<sup>-3</sup></i>												
Cell A	A2	2	1.967(4)	1.0(3)	2	3.074(8)	3.4(2)	6	3.74(3)	7(2)	24	3.47(5)	2
		4	2.062(1)	1.0(3)									
	<i>R-factor = 6.9 x 10<sup>-3</sup></i>												
Cell A	A3	6	2.101(6)	4(1)	2	3.168(3)	4.0(3)	6	3.87(3)	6(2)	24	3.59(8)	2
		<i>R-factor = 19.2 x 10<sup>-3</sup></i>											
	Cell B	B1	2	1.922(3)	1.7(7)	2	3.032(4)	2.5(2)	6	3.66(2)	7(1)	24	3.41(2)
4			2.033(7)	1.7(7)	2								
<i>R-factor = 11.9 x 10<sup>-3</sup></i>													
Cell B	B2	2	1.892(2)	4(2)	2	3.06(2)	3.4(2)	6	3.71(2)	13(3)	24	3.34(3)	2
		4	2.012(9)	4(2)									
	<i>R-factor = 23.9 x 10<sup>-3</sup></i>												
Cell B	B3	4	1.941(3)	3(2)	2	3.04(4)	7(1)	6	3.74(2)	19(3)	24	3.31(2)	2
		2	2.075(2)	3(2)									
	<i>R-factor = 21.4 x 10<sup>-3</sup></i>												
Cell B	B4	6	1.999(2)	4.7(3)	2	3.07(4)	6(2)	6	3.73(6)	10(3)	24	3.33(4)	2
		1	3.27(5)	6(2)									
	<i>R-factor = 11.0 x 10<sup>-3</sup></i>												
Cell B	B5	6	2.055(4)	4.8(3)	2	3.07(5)	5(2)	6	3.81(4)	12(3)	24	3.45(9)	2
		1	3.17(5)	5(2)									
	<i>R-factor = 11.0 x 10<sup>-3</sup></i>												
Cell C	C1	2	1.936(2)	2.7(5)	2	3.042(3)	3.5(2)	6	3.69(2)	8(2)	24	3.37(2)	4
		4	2.028(2)	2.7(5)									
	<i>R-factor = 6.4 x 10<sup>-3</sup></i>												
Cell C	C2	2	1.975(2)	2.2(5)	2	3.057(3)	3.8(2)	6	3.73(2)	8(2)	24	3.48(5)	9
		4	2.056(3)	2.2(5)									
	<i>R-factor = 5.9 x 10<sup>-3</sup></i>												
Cell C	C3	2	2.013(6)	4.9(2)	2	3.10(2)	7(2)	4	3.76(2)	4(2)	24	3.43(3)	5
		4	2.093(9)	4.9(2)									
	<i>R-factor = 7.8 x 10<sup>-3</sup></i>												
$\Delta E_0 = 3.5 \text{ eV}$				$S_0^2 = 0.8$									

For the cell started on oxidation (cell B), 5 components are needed (Figure IV.18b, center) to satisfactorily describe the data because of the irreversibility of the oxidation process. EXAFS analysis for B1 (pristine) and B2 (intermediate on charge) is very straightforward since the same structural model as for components A1 can be used (Table IV.3). In contrast, for the B3 (fully charged), B4 (intermediate on discharge) and B5 (discharged) components, new models that consider both the loss of oxygen and the amorphous nature of the material were necessary. On that basis, satisfactory fits were

obtained with the presence of  $\text{IrO}_6$  octahedra having a connectivity increasing from 2 to 3 (see Figure A.11 annex) as expected considering the new stoichiometry of  $\alpha\text{-IrO}_3$ . Interestingly, by comparing the B1 to B2 components, we observe a slight decrease of the Ir-O distances (Figure IV.18c) but an increase of the Ir-Ir distances implying that Ir is not oxidized. Such variations instead correspond to an increased distortion of the  $\text{IrO}_6$  octahedra. The average Ir-O distance eventually increases up to 2.06 Å for B5, consistent with a significant reduction of Ir upon discharge.

Lastly, 3 components were satisfactorily used both on charge and discharge to describe the cycling of cell C, indicating the reversibility of the process (Figure IV.18b, right). The imperfect symmetry of the concentration profile deduced from MCR analysis might be a consequence of the fast cycling rate (C/4) used during the experiment, and could be better understood by duplicating the experiment with different kinetics. The most oxidized component (C1) is relatively close to the pristine spectra of the other cells (A1 and B1), whereas the intermediate (C2) and reduced (C3) components show an increase of both Ir-O and Ir-Ir distances, consistent with the reduction of Ir.

#### IV.4.b. X-ray Absorption Near Edge Spectroscopy

The *operando* XANES data from the same cells was used to get information on the oxidation state of Ir during cycling via careful monitoring of the intense white line (WL) that overlaps with the Ir  $L_{\text{III}}$ -edge (Figure A.9 in annex). This WL results from dipole-allowed  $2p\text{-}5d$  transitions and its intensity is proportional to the number of unoccupied  $d$  orbitals for  $nd$  materials, as previously reported by Qi *et al.*<sup>103</sup> Thus the WL intensity (Figure IV.19a) is a better parameter to follow the oxidation or reduction of Ir, than the energy of the WL (Figure IV.19b) which is more sensitive to local distortion of the  $\text{IrO}_6$  octahedra. When starting on reduction (cell A, blue), both the WL energy and intensity decrease linearly with composition ( $\sim 0.84$  eV/ $e^-$  and  $\sim 0.15$  %/ $e^-$  respectively) and vice versa on the following oxidation, with both curves having similar slopes, indicative of a reversible process. More quantitatively, the area of the WL varies by approximately 24%, which is in good agreement with the 25% decrease in hole population expected from a classical cationic process from  $\text{Ir}^{5+}$  ( $d^4$ ) to  $\text{Ir}^{3.5+}$  ( $d^{5.5}$ ).

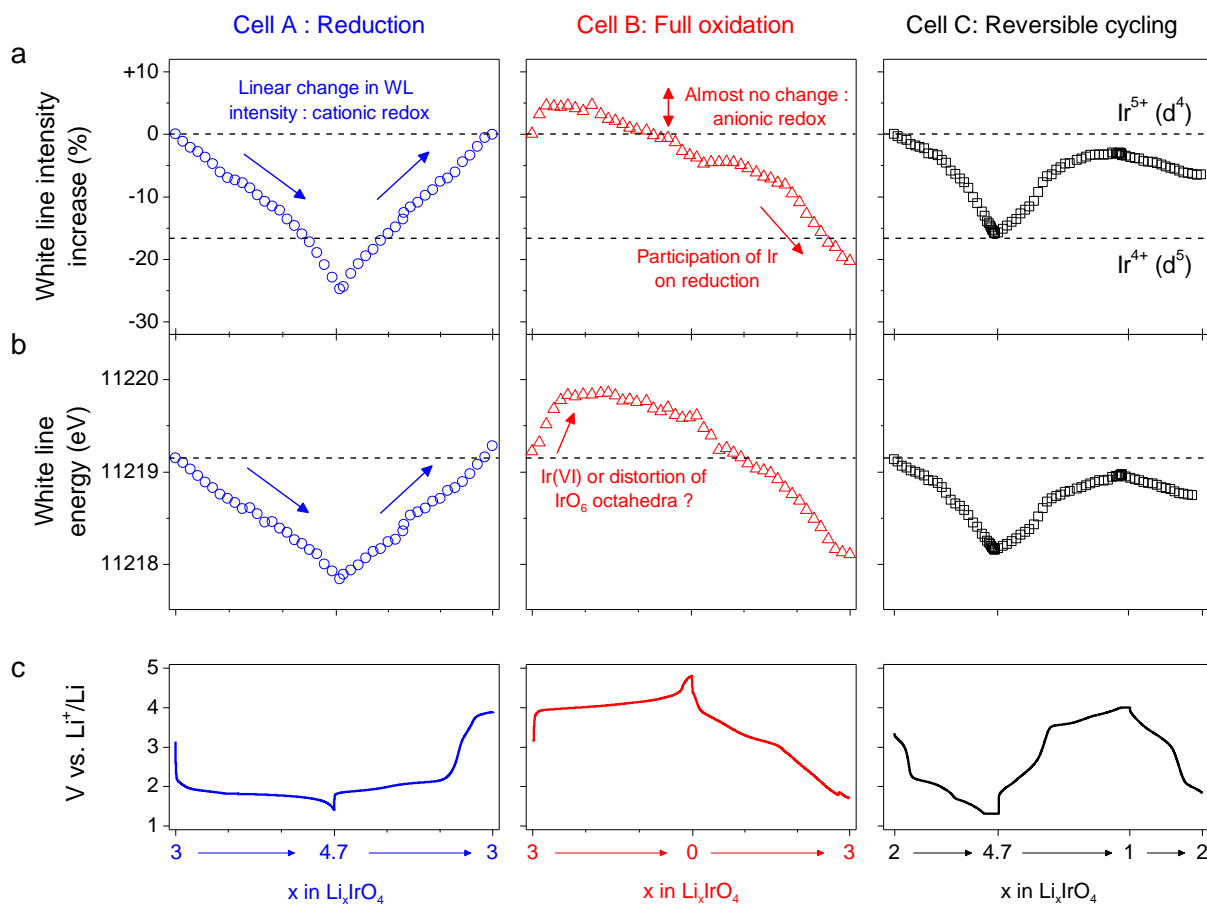


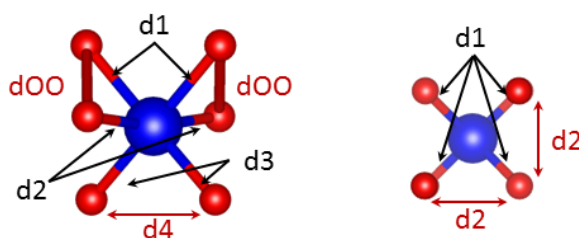
Figure IV.19 : Participation of cationic redox during cycling studied by operando XANES. (a) Changes in white line intensity during cycling for the three cells: A (blue circles), B (red triangles) and C (black squares). Dashed lines highlight the change from  $\text{Ir}^{5+}$  to  $\text{Ir}^{4+}$  according to their respective hole population. (b) Changes in energy of the white line are also reported for comparison with the energy of the pristine material indicated by a dashed line and (c) the corresponding voltage curves for each cell.

We now focus on the cell started on oxidation (cell B, red) which shows that both the intensity (Figure IV.19a) and position in energy (Figure IV.19b) of the WL slightly increase, prior to stabilize and slowly decrease once  $\sim 0.5$  Li is removed. Overall this suggests that oxygen is primarily oxidized instead of iridium during the charging process, although the shift observed at the very early stage of charge cannot discard a hint of  $\text{Ir}^{6+}$ . Indeed, while such a high oxidation state has never been achieved in the Ir-based rocksalt oxides reported so far,<sup>58,65,73</sup> it has already been stabilized in more ionic perovskites.<sup>82,92</sup> To address this question, electronic structure DFT calculations, including full structural relaxations were performed at  $x = 3, 2$  and  $1$  by M. Saubanère and M.-L. Doublet at ICGM (Montpellier, France). Results show (i) a major contribution of the oxygen states below the Fermi level in the electronic structure of  $\text{Li}_3\text{IrO}_4$  that confirms the dominant oxygen participation to the redox process below  $x = 3$  and (ii) a limited oxidation of  $\text{Ir}^{5+}$  accompanied with a significant  $\text{IrO}_6$  local distortions below  $x = 3$  that may explain the WL shift in energy (Table IV.4). This

is also consistent with the evolution of Ir-O and Ir-Ir distances obtained from EXAFS analysis. Turning to the subsequent discharge, it shows a non-linear decrease of both the WL position and intensity, indicating that both iridium and oxygen participate in the reduction process while their effects cannot be easily disentangled.

During the reversible cycling (cell C, black), both the WL intensity and its position in energy show a non-monotonous evolution, suggesting a larger degree of participation of Ir and O in the lower and higher voltage region, respectively. The extent of Ir oxidation/reduction is lower than observed in cell A in agreement with the evolution of Ir-O distances in the EXAFS analysis.

Table IV.4 : Distortion of the Ir coordination environment. Ir-O and shortest O-O distances were obtained from structural relaxations using the DFT+U formalism ( $U_{\text{eff}} = 0, 2$  or  $4$  eV for Ir) for different value of delithiation from  $x=3$  to  $x=1$ . At  $x=0$ , the most stable configuration for Ir is a tetrahedral environment, but is not observed experimentally due to the concomitant release of  $\text{O}_2$ .



		$\text{Li}_3\text{Ir}^{\text{Oh}}\text{O}_4$	$\text{Li}_2\text{Ir}^{\text{Oh}}\text{O}_4$	$\text{LiIr}^{\text{Oh}}\text{O}_4$	$\text{Ir}^{\text{Td}}\text{O}_4$
U = 4 eV	d1 (Å)	2.03	2.04	2.01	1.72
	d2 (Å)	2.02	1.97	1.95	2.77
	d3 (Å)	1.93	1.85	1.78	
	d4 (Å)	2.80	2.69	2.79	
	dOO (Å)	2.66	2.60	2.44	
U = 2 eV	d1 (Å)	2.05	2.04	2.01	1.74
	d2 (Å)	2.02	1.97	1.95	2.84
	d3 (Å)	1.93	1.86	1.79	
	d4 (Å)	2.82	2.70	2.78	
	dOO (Å)	2.67	2.60	2.45	
U = 0 eV	d1 (Å)	2.04	1.99	2.01	1.75
	d2 (Å)	2.00	1.95	1.93	2.85
	d3 (Å)	1.94	1.95	1.93	
	d4 (Å)	2.82	2.75	2.75	
	dOO (Å)	2.62	2.50	2.42	

#### IV.4.c. Electron paramagnetic resonance

EPR measurements were then carried out on *ex situ* samples to probe unpaired spins regardless of whether they belong to cationic or anionic species. The measurements were done in collaboration with H. Vezin at LASIR (Lille, France). We should recall here that  $\text{Ir}^{5+}$  ( $d^4$ ),  $\text{Ir}^{3+}$  ( $d^6$ ) and  $(\text{O}_2)^{2-}$  are EPR silent species at X band in contrast to  $\text{Ir}^{4+}$  ( $d^5$ ),  $\text{Ir}^{6+}$  ( $d^3$ ) or  $(\text{O}_2)^{3-}$  and  $(\text{O}_2)^-$  species. *Ex situ* samples were measured for different states of charge/discharge (Figure IV.20a). As expected, the pristine material, which contains  $\text{Ir}^{5+}$  (EPR silent) and  $\text{O}^{2-}$  (diamagnetic), gives no signal (see (i) in Figure IV.20b). In contrast, the EPR spectrum of the fully reduced sample ( $\text{Li}_{4.7}\text{IrO}_4$ ) shows a broad and anisotropic signal (ii) associated with  $\text{Ir}^{4+}$ , which can better be visualized by plotting the data over the full (0 to 800 mT) scale (Figure IV.20c). From integration of the EPR signal, we could calculate a density of ca. 0.2 spin/Ir. This would correspond to 20%  $\text{Ir}^{4+}$  and 80% EPR-silent Ir, most likely  $\text{Ir}^{3+}$ , a ratio close to that expected from the electrochemical composition  $\text{Li}_{4.7}\text{IrO}_4$ .

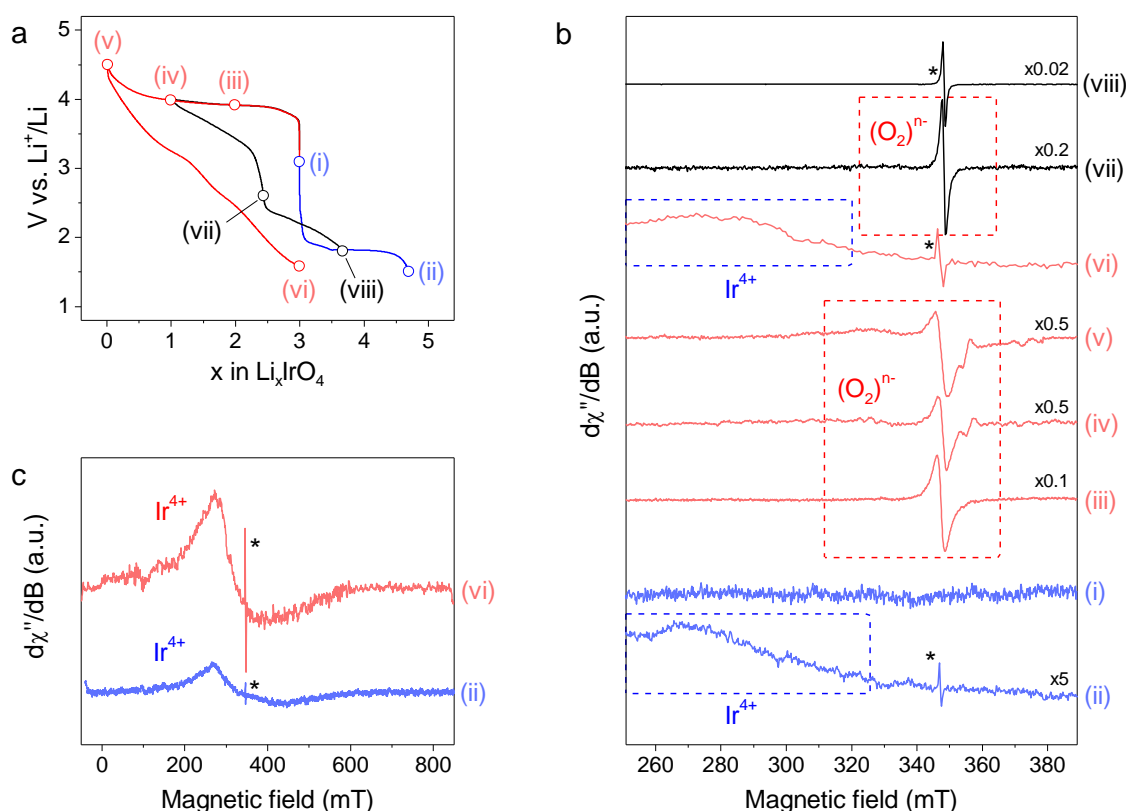


Figure IV.20 : *Ex situ* EPR spectroscopy study of paramagnetic species at different states of charge.

(a) *Ex situ* samples were measured after cycling in different conditions. The EPR spectra of the different samples are shown in (b). The signatures of  $\text{Ir}^{4+}$  and  $(\text{O}_2)^n$  species are indicated on the figure and the sharp signal of  $\text{Csp}$  is marked by an asterisk. Some spectra were resized for clarity with the scaling factors specified near the corresponding spectrum. (c) Full scale view of the spectra containing the large  $\text{Ir}^{4+}$  signal.

On oxidation, upon removal of 1 Li ( $x = 2$ ), an intense isotropic signal appears that can be attributed to oxidized  $(\text{O}_2)^{3-}$  species (iii). This signal becomes approximately 5 times less intense and more anisotropic (axial symmetry with  $g_{\parallel} = 2.012$  and  $g_{\perp} = 2.006$ ) upon removal of 2 Li (iv), suggesting an increasing proportion of more oxidized EPR silent  $(\text{O}_2)^{2-}$  peroxo species that are known to be highly unstable<sup>68,69</sup> and may recombine into  $\text{O}_2$  gas, hence explaining why the EPR spectrum remains alike for a- $\text{IrO}_3$  (v) as oxygen is released. The EPR spectra for a  $\text{Li}_3\text{IrO}_4$  sample fully charged and discharged (vi) having the composition “a- $\text{Li}_3\text{IrO}_3$ ” shows an intense  $\text{Ir}^{4+}$  signal, with an integrated spin density around 0.5 spin/Ir, corresponding to 50%  $\text{Ir}^{4+}$  and 50% EPR silent Ir. The signal shape reveals an isotropic character more important than for the sample initially reduced suggesting a more disordered Ir coordination sphere, which is in line with the amorphization and the increased connectivity of  $\text{IrO}_6$  octahedra deduced from EXAFS measurement. Lastly, for the sample charged to  $x = 1$  and then discharged to 2.6 and 1.8 V, we note the disappearance of the isotropic  $(\text{O}_2)^{n-}$  signal (vii) to the expense of a sharp signal characteristic of the carbon (viii), hence indicating the full reduction of peroxo-like species as expected. The presence or absence of the sharp carbon signal from sample to sample remains unclear, and is probably related to the cycling history of the electrode. Carbon black materials are considered as potential oximetry probes as their EPR signal appears to be very sensitive to the blood oxygen content.<sup>104</sup> It would be interesting to verify whether the signal of carbon black also depends on the oxygen content in the electrolyte of Li-ion batteries.

## IV.5. Conclusion

In this chapter, we reported the synthesis of a new  $\text{Li}_3\text{IrO}_4$  material based on theoretical predictions suggesting that an increased Li/M ratio in rocksalt oxides would lead to an enhanced participation of oxygen to the redox activity of the material, and therefore an increased capacity. This new phase was shown to reversibly uptake and release 3.5  $\text{Li}^+$  per transition metal, a capacity which stands as a record among cathode materials based on intercalation chemistry. This large capacity was shown, from XAS and EPR data, to originate from the combination of  $\text{Ir}^{3+}/\text{Ir}^{4+}/\text{Ir}^{5+}$  cationic redox processes, as well as  $\text{O}^{2-}/(\text{O}_2)^{n-}$  anionic ones.

Increasing the number of non-bonding oxygen states is therefore an interesting strategy to improve the capacity of cathode materials. The large oxygen release and structural

collapse upon complete delithiation of  $\text{Li}_3\text{IrO}_4$  clearly emphasize that following this direction comes with the risk of increasing the instability of these materials against oxygen recombination/release, hence requiring a careful selection of the transition metal. The vast array of structures existing for the  $\text{Li}_3\text{MO}_4$  family, exemplified by the  $y \text{Li}_3\text{RuO}_4 - (1-y) \text{Li}_3\text{NbO}_4$  system,<sup>105</sup> opens a large playground for designing new materials with complex structures. As it was observed for the  $\text{Li}_2\text{IrO}_3$  system,<sup>65</sup> it can also be interesting to search for tridimensional frameworks in order to improve the structural stability upon cycling. Thus, an inspiration from this work is rooted in the investigation of ordered rocksalt  $\text{Li}_3\text{MO}_4$  structures with large capacities and based on well-defined combination of 3d/4d/5d transition metals, a search which could largely benefit from high-throughput theoretical approaches similar to the one recently published on  $\text{Li}_2\text{MO}_3$  compounds.<sup>106</sup> Extending this strategy to other storage systems could also lead to interesting results, for example in Na-ion batteries or pseudocapacitive materials, the latter being explored in the final chapter of this work.

## Chapter V. Preparation of proton-based iridates and energy storage in $H_{3+x}IrO_4$

### V.1. Introduction

The interesting electrochemical properties of Ir-based oxides for  $Li^+/Na^+$  intercalation have been established through the study of a large variety of compounds,<sup>58,65,73</sup> with the aim to clarify the structural parameters controlling the activation of anionic redox in this family of materials. We extended this Ir oxide family by reporting a new member  $Li_3IrO_4$ , thus pushing the limits of insertion reactions to a new record of 3.5  $e^-$  per transition metal. In addition to their fundamental interest for battery materials, these materials are also studied for other energy applications, such as pseudocapacitors and electrocatalysis. In both fields, Ir oxides have generated a long-lasting interest as they offer excellent properties with very good stability. However, the mechanisms explaining their high performances remain unclear due to the use in most studies of amorphous  $IrO_x$  phases, prepared by electrodeposition or oxidation of metallic Ir in aqueous media. The complexity to characterize such starting material has slowed down their understanding.

Based on our knowledge on the redox activity of several Ir-based oxides with well-defined structure and stoichiometry, namely  $Na_2IrO_3$ ,  $\alpha/\beta-Li_2IrO_3$  and  $Li_3IrO_4$ , it became tempting to further extend their rich electrochemical properties to proton-based phases. Here, we present results on the proton-exchange reactions of  $Na_2IrO_3$ ,  $\alpha/\beta-Li_2IrO_3$  and  $Li_3IrO_4$  in acidic conditions, prior to studying the electrochemical properties of the acid-exchanged  $Li_3IrO_4$  material in organic and aqueous electrolytes.

### V.2. Preparation and characterization of proton-based iridates

#### V.2.a. Synthesis of the Li/Na-based precursor materials

The starting materials were prepared following the procedures described in Chapter 2 and 4 for  $Na_2IrO_3$  and  $Li_3IrO_4$ , respectively.

In the case of  $\alpha-Li_2IrO_3$ , metallic Ir and  $Li_2CO_3$  precursors were mixed in a 1:1.05 ratio, and two batches were prepared with different heating conditions. The first one was

heated in air at 1000°C for 24h, and the second batch was prepared at 900°C in air for 24h, to reduce the crystallinity and particle size.

Finally, the  $\beta$ -Li<sub>2</sub>IrO<sub>3</sub> sample was prepared by P. Pearce at Collège de France (Paris) with stoichiometric amounts of Ir and Li<sub>2</sub>CO<sub>3</sub>, and heated at 1000°C for 4 days in a covered alumina crucible, yielding large particles (5-10  $\mu$ m) with good crystallinity.

### V.2.b. Proton-exchange reaction in acidic media

The proton exchange was performed by stirring the prepared powders in 0.1 M H<sub>2</sub>SO<sub>4</sub> solutions. The volume of solution was adjusted in order to have a 5-fold excess of protons compared to the number of exchangeable Li<sup>+</sup>/Na<sup>+</sup> in the material. To assess the completeness of the reaction, X-ray diffraction on samples collected after different times was measured until a pure phase was formed for each sample. After acid-exchange, the samples were washed several times in distilled water and dried under vacuum at 55°C to remove adsorbed water.

#### v.2.b.i Na<sub>2</sub>IrO<sub>3</sub>

Na<sup>+</sup>/H<sup>+</sup> exchange reaction in Na<sub>2</sub>IrO<sub>3</sub> is very fast, with complete structural transformation happening within 1h (Figure V.1). Le Bail fit of the phase after acid-exchange of Na<sub>2</sub>IrO<sub>3</sub> was done using the same monoclinic *C2/m* space group as the one used for the O1-Na<sub>0.5</sub>IrO<sub>3</sub> phase described in Chapter 2. In fact, the cell parameters ( $a = 5.28$ ,  $b = 9.32$ ,  $c = 4.60$ ,  $\beta \approx 90^\circ$ ) are closer to those of the O1\* phase (Table V.1), which was found to appear after extended cycling of Na<sub>2</sub>IrO<sub>3</sub> and capacity loss (see Chapter 2). This result suggests that the capacity loss observed in Na half cells could be related to the insertion of protons formed upon decomposition of the electrolyte. The strong hydrogen bonds formed by protons in the structure decrease the interlayer distance and irreversibly block the structure with the O1 stacking, therefore limiting Na<sup>+</sup> diffusion. Interestingly, a similar diffraction pattern was reported by Krizan *et al.* while studying the decomposition of Na<sub>2</sub>IrO<sub>3</sub> in air.<sup>75</sup> This study nicely showed the reactivity of Na<sub>2</sub>IrO<sub>3</sub> under H<sub>2</sub>O/CO<sub>2</sub> atmosphere, but the structure of the resulting material remained unclear. Here, we propose that Na<sub>2</sub>IrO<sub>3</sub> adopts an O1 structure upon H<sup>+</sup> insertion in the material.

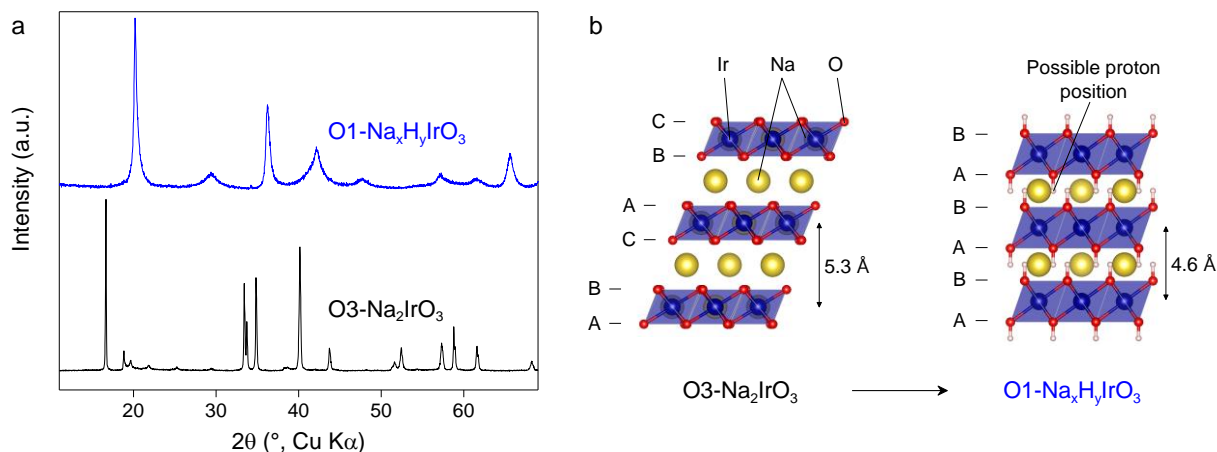
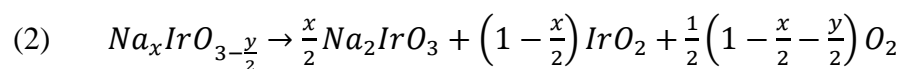
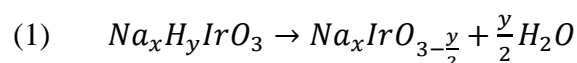


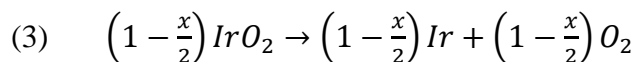
Figure V.1 : Structural modifications upon proton exchange of  $Na_2IrO_3$ . (a) XRD pattern before and after acid-leaching. (b) Schematic of the corresponding change in stacking sequence, decrease in interlayer distance and possible proton positions.

Table V.1 : Unit cell parameters for different phases derived from  $Na_2IrO_3$  with the O1 structure, using the  $C2/m$  space group.

	$a$ (Å)	$b$ (Å)	$c$ (Å)	$\beta$ (°)
O1- $Na_{0.5}IrO_3$	5.25	9.06	4.88	~ 90
O1*- $Na_xIrO_3$ after extensive cycling	5.28	9.32	4.60	~ 90
O1- $Na_xH_yIrO_3$	5.43	9.37	4.56	~ 90

The extent of  $Na^+/H^+$  exchange was indirectly obtained via analysis of the reaction supernatant by complementary Inductively Coupled Plasma Mass Spectrometry (ICP-MS) for released sodium, and acid-base titration to determine the number of remaining protons in solution. A more direct measurement of the material's composition was done by thermogravimetric analysis coupled with mass spectrometry (TGA-MS), which was performed under Ar atmosphere on the pristine and exchanged powders to measure the weight loss and nature of gas formed upon thermal decomposition. The pristine material is stable up to  $1000^\circ C$  (Figure V.2a), with no significant weight loss, whereas the exchanged material shows a large release of  $H_2O$  around  $360^\circ C$  (-5.8% weight loss), a small loss at  $530^\circ C$  (-1%) and an important release of  $O_2$  at  $880^\circ C$  (-10.7%). The overall decomposition process can be explained by the three following steps:





This last decomposition step was confirmed by measuring TGA-MS in the same conditions for commercial  $\text{IrO}_2$ . The composition of the material is approximately  $\text{Na}_{0.2}\text{H}_{1.8}\text{IrO}_{3.1}$ , showing that  $\text{Na}^+/\text{H}^+$  exchange reaction happens to a large extent, with however some  $\text{Na}^+$  left in the structure. The XRD pattern of the sample after thermal decomposition shows intense peaks of metallic Ir together with a small amount of  $\text{Na}_2\text{IrO}_3$ , consistent with the composition.

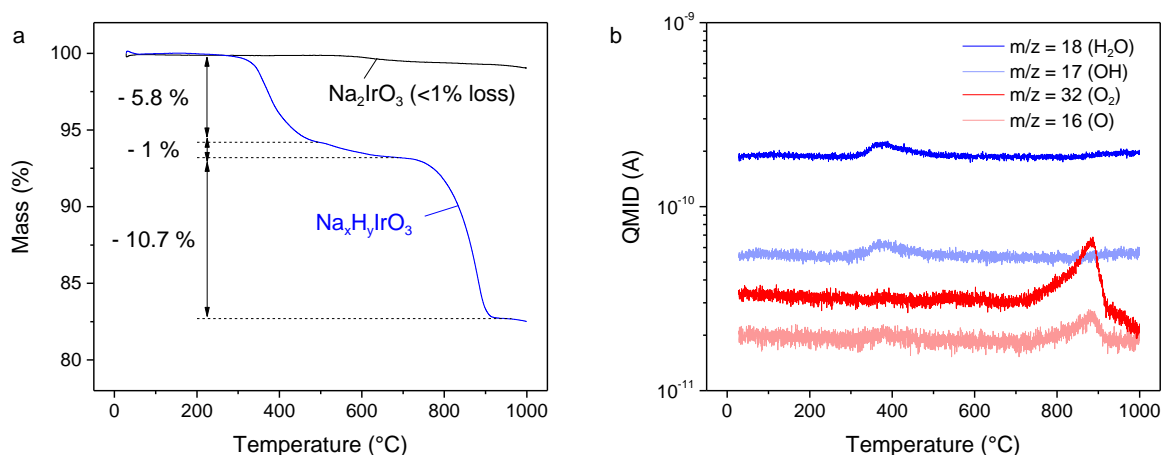


Figure V.2 : Thermal decomposition of  $\text{Na}_x\text{H}_y\text{IrO}_3$ . (a) TGA profile before and after acid-leaching. (b) MS data obtained during the measurement.

### v.2.b.ii $\alpha\text{-Li}_2\text{IrO}_3$

The proton exchange reaction of  $\alpha\text{-Li}_2\text{IrO}_3$  was more complex. Our first attempt performed with a sample prepared at  $1000^\circ\text{C}$  for 24h ( $\text{HT-Li}_2\text{IrO}_3$ ) failed as no structural change was observed (Figure V.3a). This issue was first signaled by O'Malley *et al.*,<sup>107</sup> finding that samples with a larger amount of stacking faults were reacting more easily. We therefore prepared a second sample at  $900^\circ\text{C}$  for 24h ( $\text{LT-Li}_2\text{IrO}_3$ ) in order to keep stacking faults in the structure, and we found that the proton exchange reaction was completed within 24h for this sample. However, the results recently reported by Bette *et al.*<sup>108</sup> show that, using 4 M  $\text{H}_2\text{SO}_4$  in hydrothermal conditions ( $120^\circ\text{C}$  for 96h), it is possible to complete the exchange reaction with samples prepared at high temperature ( $1000^\circ\text{C}$  for 24h). Most likely, our inability to perform the exchange at room temperature is simply due to a kinetical limitation, as the particle size of the  $\text{HT-Li}_2\text{IrO}_3$  is about 10 times larger than for the  $\text{LT-Li}_2\text{IrO}_3$  (Figure V.3cd). TGA was used to measure the composition of the sample, with similar decomposition steps as described earlier for  $\text{Na}_x\text{H}_y\text{IrO}_3$ . Three mass losses

corresponding to  $H_2O$  ( $400^\circ C$ ) and  $O_2$  release ( $630^\circ C$  and  $900^\circ C$ ) were measured (Figure V.4), and the XRD pattern of the sample after TGA showed intense Ir reflections and a small amount of  $Li_2IrO_3$ , giving a starting composition of  $Li_{0.5}H_{1.4}IrO_{3.0}$ .

The structure of the resulting  $Li_{0.5}H_{1.4}IrO_3$  is similar to the P3-CrOOH structure (Figure V.3b), with the oxygen sublattice forming an ABCCA stacking sequence. However, because of the honeycomb ordering of Ir atoms, a more complex description was proposed by Bette *et al.* for  $Li_xH_yIrO_3$  to take into account the peak broadening caused by stacking faults.<sup>108</sup> Finally, it is curious that the stacking of the exchanged material (P3) differs from that of  $Na_{2-x}H_xIrO_3$  (O1), showing that we can control the final structure by simply changing the size of the alkali ion.

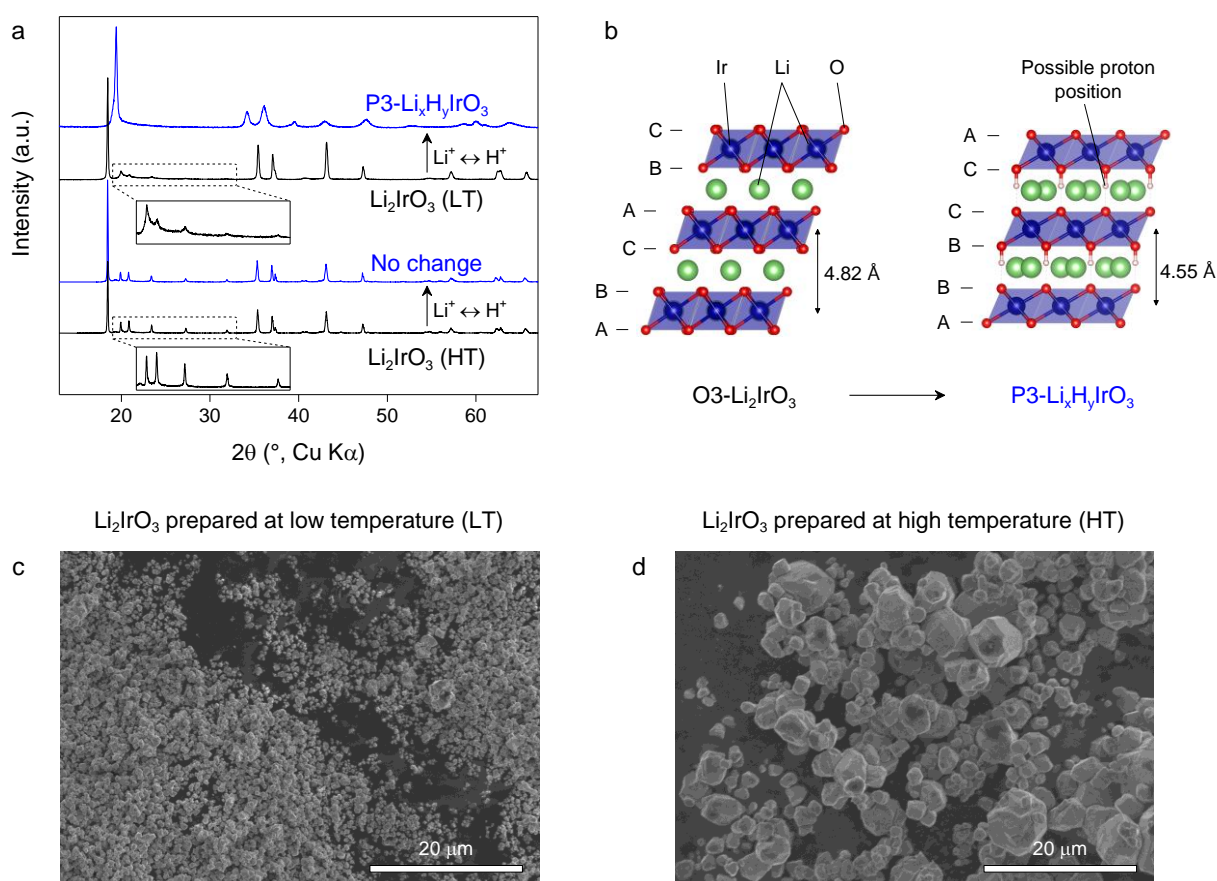


Figure V.3 : Acid-exchange properties of  $\alpha$ - $Li_2IrO_3$ . (a) Evolution of the XRD pattern after 24h reaction in  $H_2SO_4$ . The sample prepared at  $1000^\circ C$  for 24h (HT) does not change, even after longer reaction times, whereas the sample prepared at  $900^\circ C$  for 24h (LT) undergoes an O3  $\rightarrow$  P3 structural transition as shown in (b). This different behavior could be nested in the larger amount of stacking faults in LT- $Li_2IrO_3$  (see inset in a) or the smaller particle size (c) compared to HT- $Li_2IrO_3$  (d).

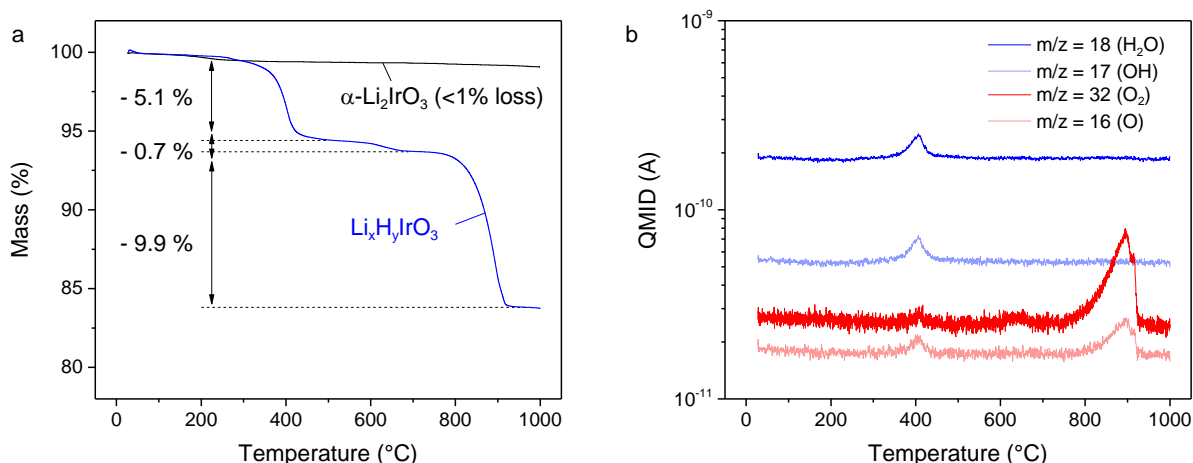


Figure V.4 : Thermal decomposition of  $\alpha\text{-Li}_x\text{H}_y\text{IrO}_3$ . (a) TGA profile before and after acid-leaching. (b) MS data obtained during the measurement.

### v.2.b.iii $\beta\text{-Li}_2\text{IrO}_3$

No change in structure was observed upon acid-leaching of  $\beta\text{-Li}_2\text{IrO}_3$  for more than a week. Because this polymorph has a rigid tridimensional framework of connected  $\text{IrO}_6$  octahedra, we do not expect drastic changes as in the case of layered phases. Nevertheless, the replacement of  $\text{Li}^+$  by  $\text{H}^+$  should affect the cell parameters. To confirm whether or not protons were inserted, we performed TGA-MS analysis on the powder after a week of acid-leaching, but less than 4 % weight loss was measured, and no  $\text{H}_2\text{O}$  was released from the material, suggesting that the exchange did not proceed significantly. Once again, the high synthesis temperature of the  $\beta\text{-Li}_2\text{IrO}_3$  polymorph results in large particle size, which could be a limiting factor. Using hydrothermal conditions, as was done for the  $\alpha$  polymorph,<sup>108</sup> could maybe help the reaction to proceed. We should however keep in mind that proton insertion in different cathode materials was investigated in the past and found to be more favorable in layered phases compared to materials with tridimensional structures, facilitated by the easy shift of  $\text{MO}_2$  layers to accommodate protons.<sup>109,110</sup>

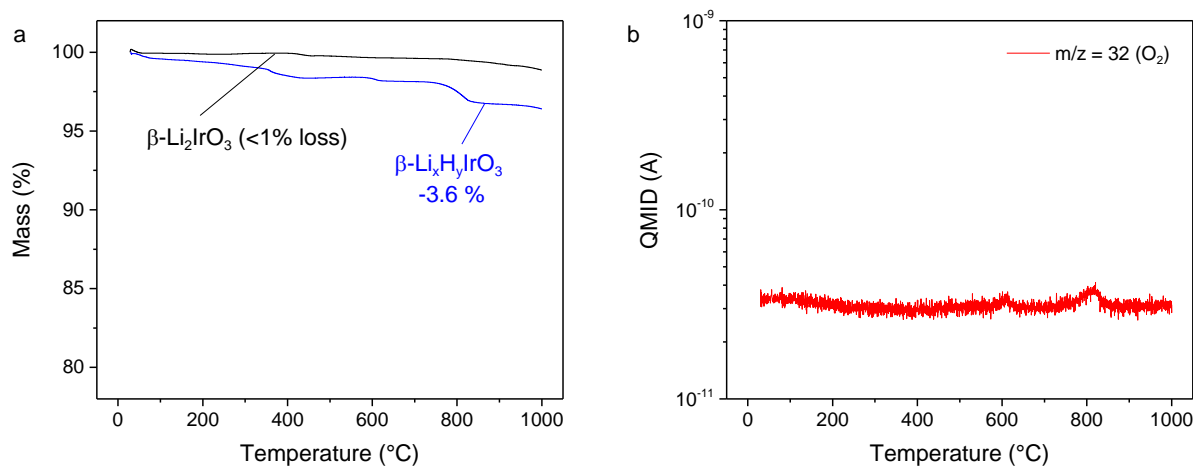


Figure V.5 : Thermal decomposition of  $\beta\text{-Li}_x\text{H}_y\text{IrO}_3$ . (a) TGA profile before and after acid-leaching. (b) MS data obtained during the measurement. Only oxygen is released from the structure.

#### V.2.b.iv $\text{Li}_3\text{IrO}_4$

Now turning to the new  $\text{Li}_3\text{IrO}_4$  phase, we found that the  $\text{Li}^+/\text{H}^+$  exchange reaction was completed within an hour. Comparative SEM pictures of the pristine and recovered powders (Figure V.6, inset) indicate the dislocation of the initial 10-20  $\mu\text{m}$  aggregates, leaving the primary particles intact with sizes around 1-2  $\mu\text{m}$  for the acid leached sample. Rietveld refinement of the phase obtained (Figure V.6b) was done using the  $\text{HCrO}_2$  structural model, with an hexagonal  $R\bar{3}m$  unit cell. In this regard,  $\text{Li}_3\text{IrO}_4$  behaves similarly to  $\alpha\text{-Li}_2\text{IrO}_3$  with an  $\text{O}3 \rightarrow \text{P}3$  transition upon acid-leaching (Figure V.6cd). The  $a$  lattice parameter slightly increases from 2.96  $\text{\AA}$  for  $\text{Li}_3\text{IrO}_4$  to 3.04  $\text{\AA}$  for the acid-exchanged phase, while the  $c$  parameter shows a greater decrease from 14.40 to 14.07  $\text{\AA}$  as expected since  $\text{H}^+$  is smaller than  $\text{Li}^+$ . Combined ICPMS and acid-base titration of the supernatant solution after the exchange suggest that all the  $\text{Li}^+$  has been replaced by  $\text{H}^+$  ions, giving  $\text{H}_{3+x}\text{IrO}_4$ . The TGA profile for  $\text{H}_{3+x}\text{IrO}_4$  (Figure V.7a) shows three consecutive steps at 190 $^\circ\text{C}$ , 700 $^\circ\text{C}$  and 900 $^\circ\text{C}$ , corresponding to the release of  $\text{H}_2\text{O}$  for the first step and of  $\text{O}_2$  for the two remaining ones (Figure V.7b). XRD of the intermediate and final products obtained at 500 $^\circ\text{C}$  and 1000 $^\circ\text{C}$  show  $\text{IrO}_2$  and  $\text{Ir}$ , respectively (Figure V.7c), confirming the absence of  $\text{Li}^+$  ions in the material. From the weight loss, and knowing the final products, we could deduce that the formula of the sample is  $\text{H}_{3.4}\text{IrO}_4$ . The  $\text{H}^+$  content higher than 3 suggests some reduction of  $\text{Ir}$  during the acid-leaching or washing process. As will be shown later, the high potential of  $\text{H}_3\text{IrO}_4$  could lead to the oxidation of water, resulting in a reduced  $\text{H}_{3+x}\text{IrO}_4$  phase with  $x$  depending on the pH.

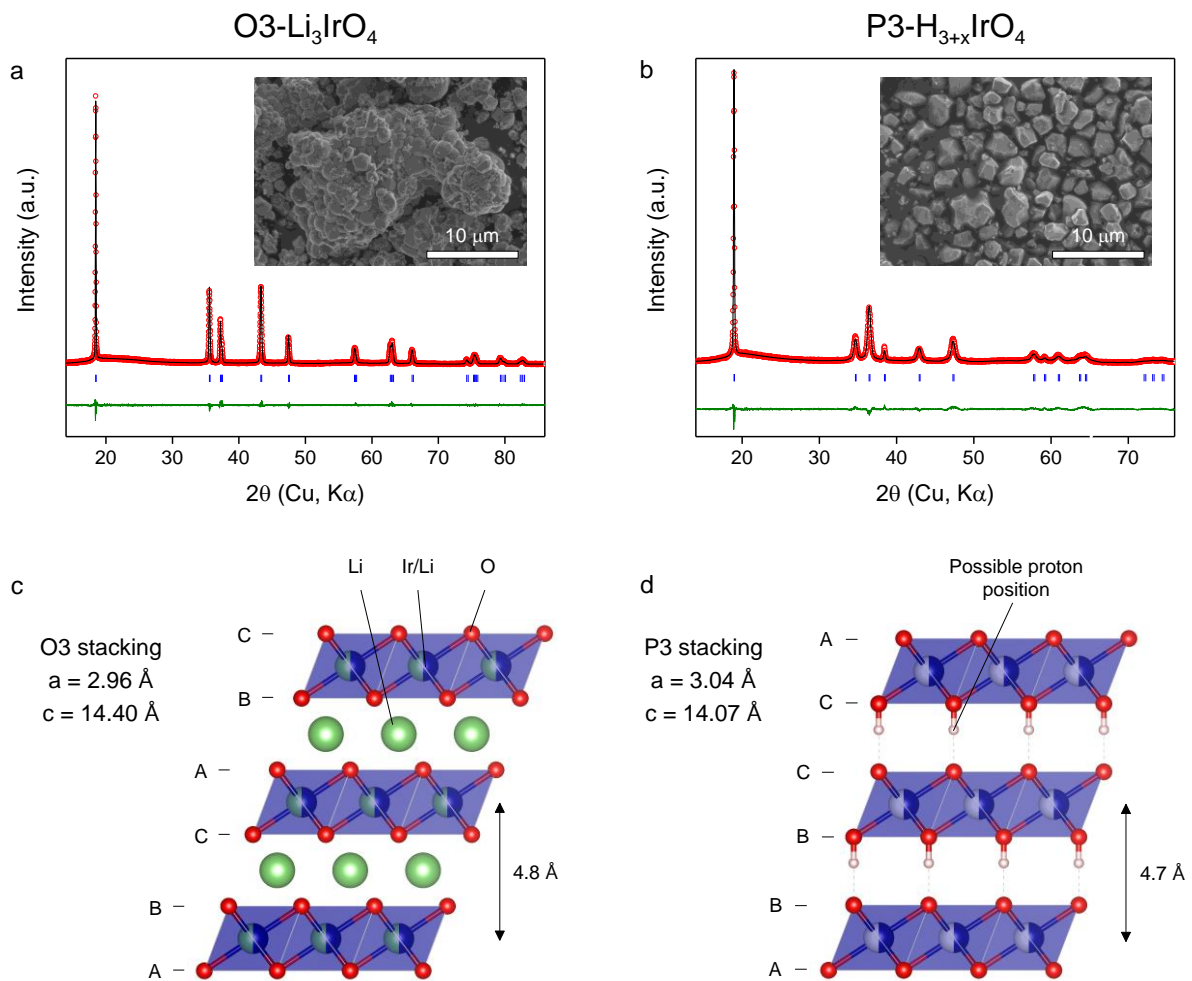


Figure V.6 : Structural modifications upon proton exchange of  $\text{Li}_3\text{IrO}_4$ . Rietveld refinement of XRD patterns before (a) and after (b) acid-leaching. Insets show SEM images of the corresponding particles. Crystal structures of the pristine (c) and proton-exchanged (d) phases.

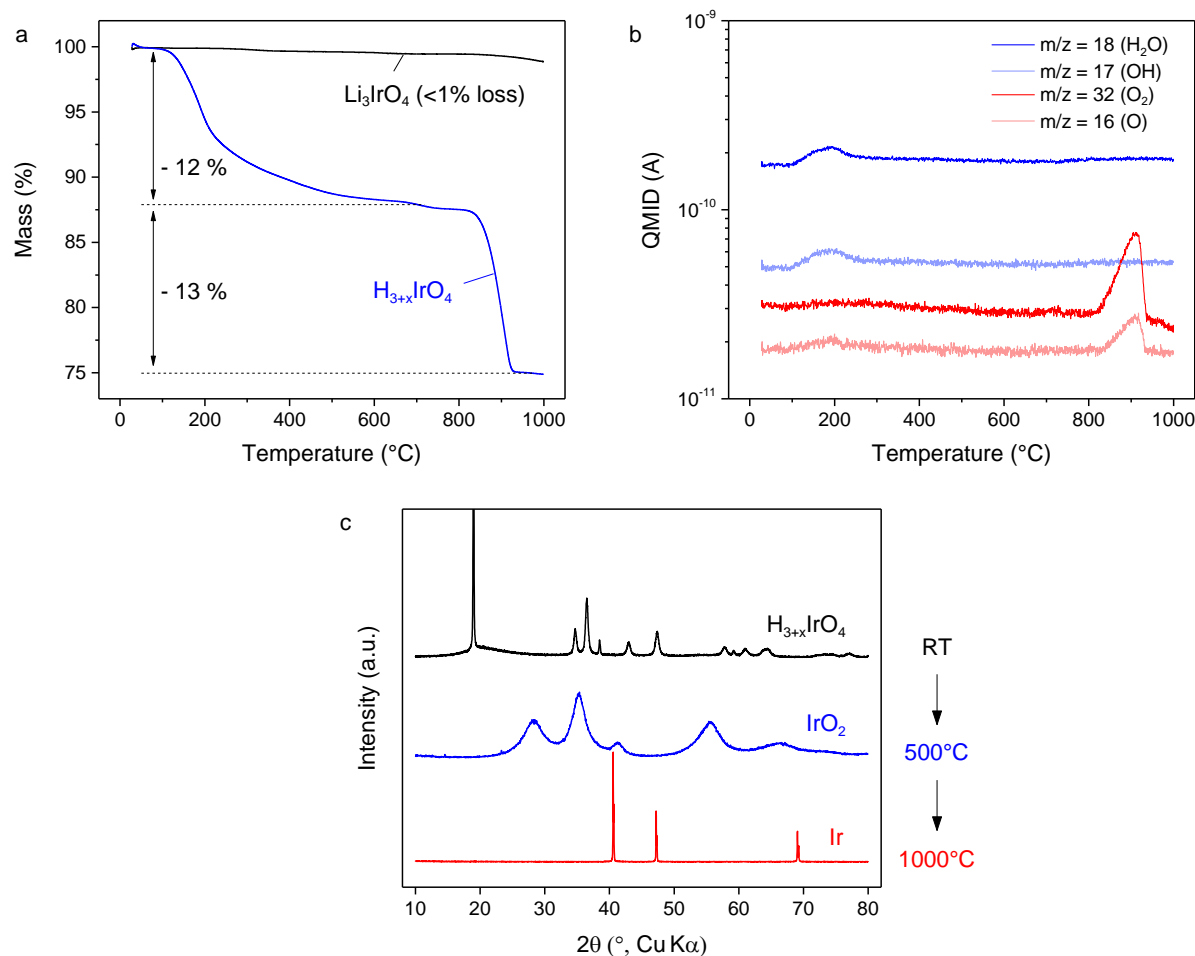


Figure V.7 : Thermal decomposition of  $Li_3IrO_4$ . (a) TGA profile before and after acid-leaching. (b) MS data obtained during the measurement showing  $H_2O$  and  $O_2$  loss at low and high temperature, respectively. (c) Evolution of XRD patterns after  $H_2O$  loss (500°C) and  $O_2$  loss (1000°C). No phase containing Li is observed.

To further characterize the protons within the sample and their existence as either -OH groups or  $H_2O$ , Fourier-transform infrared (FTIR) spectroscopy measurements were done. We note the presence of bands associated to Li carbonate impurities in  $Li_3IrO_4$  which disappear after acid-leaching (Figure V.8), however no vibration bands appear around 1600 and  $3600\text{ cm}^{-1}$ ; the wavelength domains over which the OH groups are IR-active. The absence of these bands could simply be nested in the small bandgap semiconductor character of  $H_{3.4}IrO_4$  which prevents, for absorption reasons, the detection of OH group. This was previously put forward to explain the inability to detect OH bands in the metallic  $Li_{1-x}H_xMO_2$  phase.<sup>109</sup>

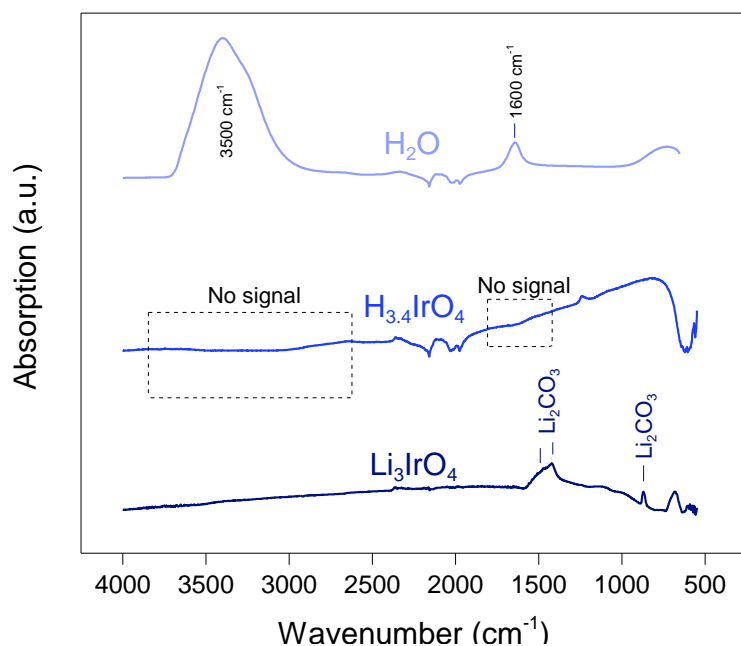


Figure V.8 : FTIR spectra of  $\text{Li}_3\text{IrO}_4$  and  $\text{H}_{3.4}\text{IrO}_4$ . The water spectrum is shown for comparison. No band characteristic of O-H or H-O-H vibrations is observed.

The extent of acid exchange reactions for all iridate compounds is summarized in Table V.2. Overall, the particle size seems to create a kinetic barrier for the reaction to proceed. The final structure and extent of acid exchange also depend on the starting material.

Table V.2 : Summary of acid exchange reactions for different Ir oxides. All exchange reactions were done in similar conditions (room temperature, 5-fold excess of protons compared to exchangeable Li/Na in the material).

Material	Structure	Annealing temperature	Particle size	Acid exchange time	Final composition	Final structure
$\text{Na}_2\text{IrO}_3$	O3	900°C	1 – 2 $\mu\text{m}$	< 1 h	$\text{Na}_{0.2}\text{H}_{1.8}\text{IrO}_3$	O1
$\alpha\text{-Li}_2\text{IrO}_3$	O3	900°C	< 1 $\mu\text{m}$	24 h	$\text{Li}_{0.5}\text{H}_{1.4}\text{IrO}_3$	P3
		1000°C	2-10 $\mu\text{m}$		No exchange	
$\beta\text{-Li}_2\text{IrO}_3$	N/A	1000°C	2-20 $\mu\text{m}$		No exchange	
$\text{Li}_3\text{IrO}_4$	O3	950°C	1 – 2 $\mu\text{m}$	< 1 h	$\text{H}_{3.4}\text{IrO}_3$	P3

### V.3. Electrochemical properties of $H_{3.4}IrO_4$

#### V.3.a. Li intercalation cathode in organic electrolyte

Electrodes of  $H_{3.4}IrO_4$  were prepared as PTFE-laminated electrode with 10 wt% Csp and 5 wt% PTFE. Swagelok cells were assembled in an Ar-filled glovebox, using Li as an anode and 1 M  $LiPF_6$  in EC/PC/DMC (1:1:3) as the electrolyte, and cycled between 1.5 and 4.2 V at a C/10 rate. Remarkably, the material reversibly uptakes 1.5  $Li^+$  with a very limited polarization (Figure V.9a) and good capacity retention, although with limited rate capability. The voltage profile varies smoothly with the removal/uptake of Li but also shows a narrow plateau at nearly 3.1 V which can nicely be visualized on the derivative curve  $dQ/dV$  (Figure V.9b) and is indicative of a phase transition.

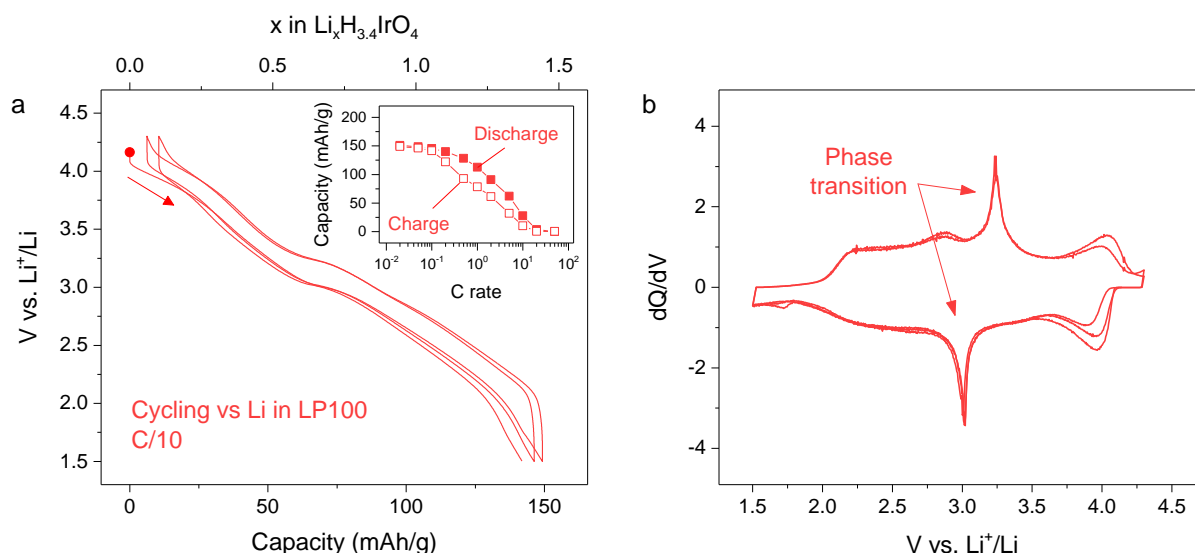


Figure V.9 : Li insertion in  $H_{3.4}IrO_4$ . (a) Galvanostatic cycling at C/10 between 1.5 and 4.3 V and (b) corresponding derivative  $dQ/dV$  curve clearly showing a phase transition around 3.1 V. The inset shows the rate capability of the material.

To understand the structural changes in  $Li_xH_{3.4}IrO_4$  on cycling, *in situ* XRD measurements were conducted at C/10 (Figure V.10, left) and patterns were collected every  $\Delta x = 0.05$ . The collected patterns are shown as 2D contour plots in Figure V.10a. As the  $Li/Li_xH_{3.4}IrO_4$  cell is discharged, we initially observe a slight shift of Bragg peaks until  $x = 0.6$ , where the peaks disappear at the expense of new ones, which continue shifting toward lower angles as more  $Li^+$  is inserted up to  $x = 1.5$  ( $Li_{1.5}H_{3.4}IrO_4$ ). Rietveld refinement of the XRD patterns demonstrate that this Li-driven structural transition is accompanied by a change in the stacking sequence from P3 to T1, with the corresponding variation of lattice

parameters shown in Figure V.10c. There is nearly a continuous increase of the  $a$  lattice parameter upon reduction, which is consistent with an increase of Ir ionic radii associated to the sequential  $\text{Ir}^{5+} \rightarrow \text{Ir}^{4+} \rightarrow \text{Ir}^{3+}$  reduction. In contrast, the interlayer distance remains nearly constant till the P3-T1 transition where it severely drops from 4.68 to 4.52 Å when the guest ions ( $\text{Li}^+$ ) shifts from prismatic to tetrahedral sites. This drop, due to the prismatic-tetrahedral contraction is fully recovered upon inserting one more  $\text{Li}^+$  into the T1 phase. The process is symmetric on the subsequent charge, indicating the full reversibility of  $\text{Li}^+$  intercalation. The formation of this T1 phase reminds us of the T1- $\text{Li}_{4.7}\text{IrO}_4$  structure obtained upon lithiation of the parent  $\text{Li}_3\text{IrO}_4$  compound. Both phases have very similar  $a$  lattice parameter (3.149 Å in  $\text{Li}_{4.7}\text{IrO}_4$  and 3.131 Å in  $\text{Li}_{1.5}\text{H}_{3.4}\text{IrO}_4$ ) which is mainly governed by the oxidation state of Ir. On the other hand, the interlayer distance in the protonated phase is much smaller (4.717 Å) than in the one containing only  $\text{Li}^+$  (5.013 Å) due to strong hydrogen bonding.

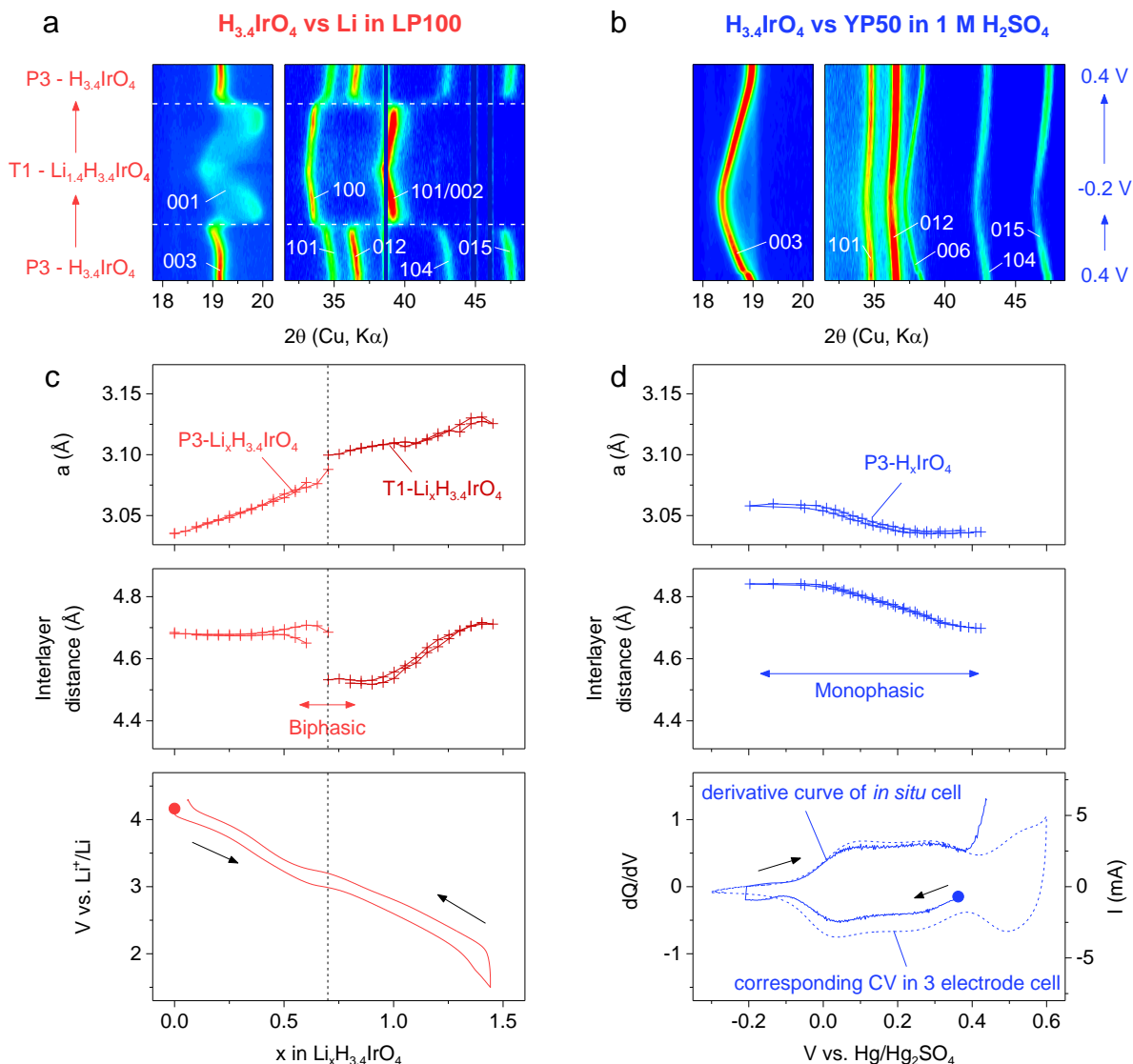


Figure V.10 : *In situ* XRD study in non-aqueous and aqueous electrolytes, on the left and right, respectively. (a) 2D contour plot of the XRD pattern evolution upon cycling in Li half-cells and (b) in acidic electrolyte vs capacitive carbon. (c) Insertion of  $Li^+$  proceeds with a phase transition from P3 to T1 stacking around  $x = 0.7$  and large changes in  $a$  parameter (3.04 to 3.13 Å) and interlayer distance ( $d = 4.5$ -4.7 Å). (d) The process in aqueous electrolyte shows a limited change in cell parameters ( $a = 3.04$ -3.06 Å,  $d = 4.7$ -4.8 Å) in the low potential region (below 0.4 V vs.  $Hg/Hg_2SO_4$ ). The high potential region cannot be reached at low current because of the concurrent water splitting reaction.

### V.3.b. Pseudocapacitive material in aqueous electrolyte

The electrochemical properties of  $H_{3.4}IrO_4$  in aqueous media were tested using three-electrode Teflon Swagelok cells with glassy carbon plungers as current collectors. Similar PTFE laminated electrodes were used as described before, with different thickness (10-150  $\mu m$ ) and density of material (4-30  $mg/cm^2$ ), out of which  $\varnothing$  6.5 mm disks were punched. The cell was assembled against a PTFE negative electrode containing capacitive carbon (YP50) in excess, with a Whatman GF/D borosilicate glass fiber membrane as the separator.

The cell was filled with 1 M  $\text{H}_2\text{SO}_4$  water solution and completed with a  $\text{Hg}/\text{Hg}_2\text{SO}_4$  reference electrode. The cells were cycled either in galvanostatic mode or by cyclic voltammetry.

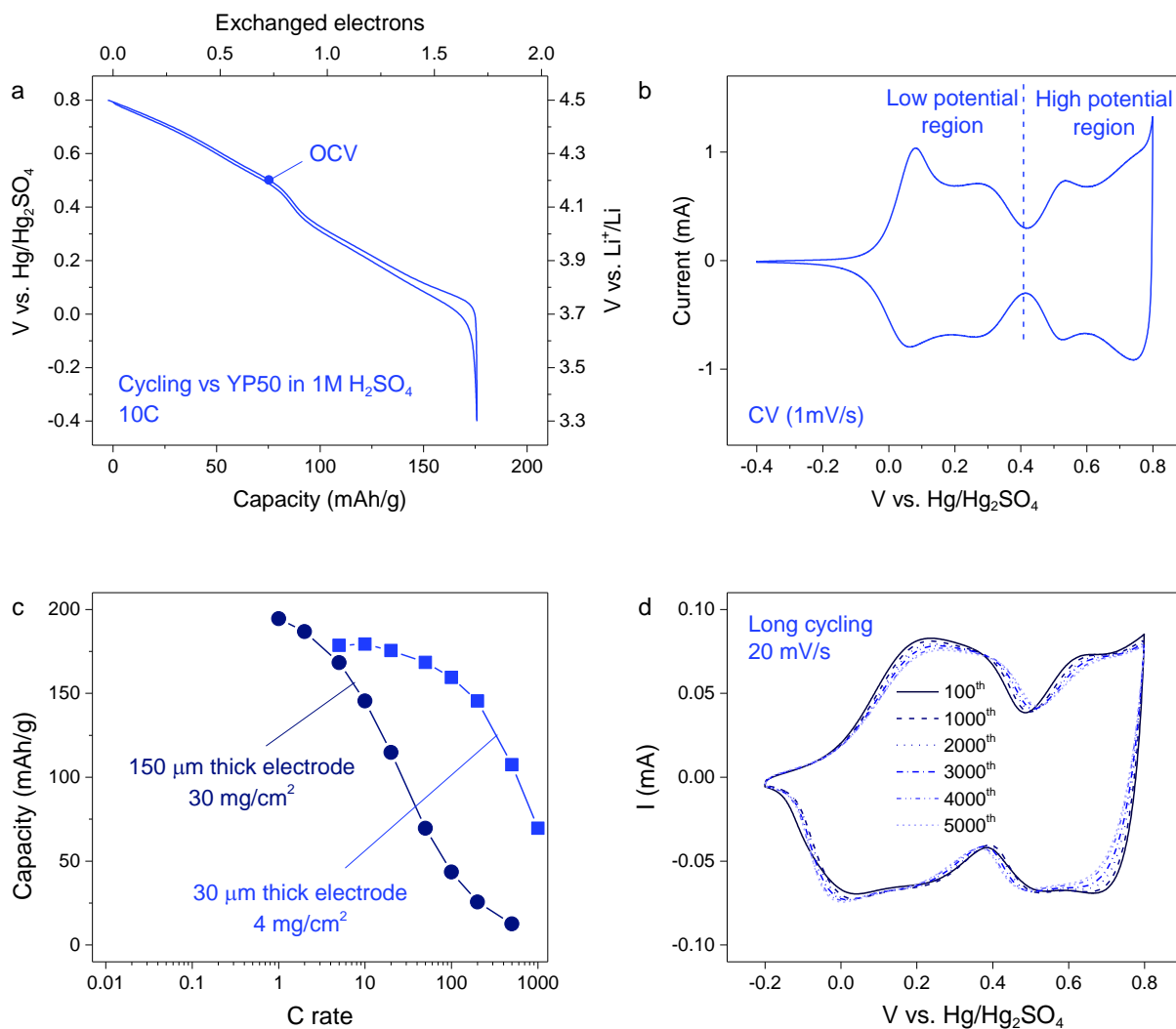


Figure V.11 : Electrochemical activity of  $\text{H}_{3.4}\text{IrO}_4$  in acidic media. (a) Galvanostatic cycling at 10C between -0.4 and 0.8 V vs.  $\text{Hg}/\text{Hg}_2\text{SO}_4$ . (b) Cyclic voltammetry at 1 mV/s in the same potential range. A dashed line separates the “low” and “high” potential regions. (c) Rate capability with electrode of different densities and thicknesses. (d) Long-term cycling stability at 20 mV/s.

Figure V.11a shows the variation of the potential, which is at 0.5 V vs.  $\text{Hg}/\text{Hg}_2\text{SO}_4$  at the OCV, as a function of  $x$ . Upon reduction to -0.4 V (3.3 V vs.  $\text{Li}^+/\text{Li}$ ) the material can uptake one  $\text{H}^+$  while, on the following charge up to 0.8 V vs  $\text{Hg}/\text{Hg}_2\text{SO}_4$  (4.5 V vs.  $\text{Li}^+/\text{Li}$ ) 1.7  $\text{H}^+$  are removed. Charging to higher potential triggers the oxygen evolution reaction (OER), for which iridium oxides are also known as excellent catalysts. Furthermore, OER activity can lead to strong reorganization/amorphisation of the material’s surface, something that we want to avoid here. Once the first cycle is achieved, the cell can reversibly cycle 1.7 protons with

minor polarization between charge and discharge curves, suggesting a rapid and reversible  $\text{H}^+$  release/uptake. By starting the cell on oxidation, we can nearly remove  $0.7 \text{ H}^+$  as well, suggesting that the electrochemical behavior is not path dependent. As an indication, from simple charge counting, this implies that on reduction  $\text{H}_{3.4}\text{Ir}_{0.6}^{5+}\text{Ir}_{0.4}^{4+}\text{O}_4$  will transform to  $\text{H}_{4.4}\text{Ir}_{0.6}^{4+}\text{Ir}_{0.4}^{3+}\text{O}_4$  which will be oxidized to  $\text{H}_{2.7}\text{Ir}_{0.7}^{5+}\text{Ir}_{0.3}^{6+}\text{O}_4$  upon full oxidation.

Cyclic voltammetry (CV) measurements collected at  $1 \text{ mV}\cdot\text{s}^{-1}$  between  $-0.1$  and  $0.8 \text{ V}$  vs.  $\text{Hg}/\text{Hg}_2\text{SO}_4$  (Figure V.11b) show several redox peaks confirming a large electrochemical activity which can be integrated to find the same reversible uptake of  $1.7$  protons as determined by galvanostatic cycling. The stability of the capacity at high rates is highlighted in Figure V.11d: the CV obtained after  $5000$  cycles at  $20 \text{ mV}\cdot\text{s}^{-1}$  neatly superimposes with the first one, indicative of a highly reversible redox process not too common at such level for intercalation chemistry. Finally, the rate capability of the material was measured from  $1\text{C}$  to  $1000\text{C}$  (Figure V.11c), revealing the high-power performances of the electrode with more than  $150 \text{ mAh/g}$  obtained up to  $10\text{C}$  using  $150 \mu\text{m}$  thick electrodes and up to  $100\text{C}$  with thinner electrodes ( $30 \mu\text{m}$ ). The rate capability of  $\text{H}_{3+x}\text{IrO}_4$  largely depends on the electrode design, similarly to what has been reported for other high rate materials, such as transition metal carbides (also known as MXene) pseudocapacitive materials.<sup>111</sup> An even more drastic consequence of the electrode design was observed by testing Swagelok cells containing  $\sim 1 \text{ mg}$  of active material powder with and without carbon additive. In the presence of carbon, both the low and high potential processes appear, whereas in the absence of carbon we can solely trigger the capacity of the high potential domain (Figure V.12).

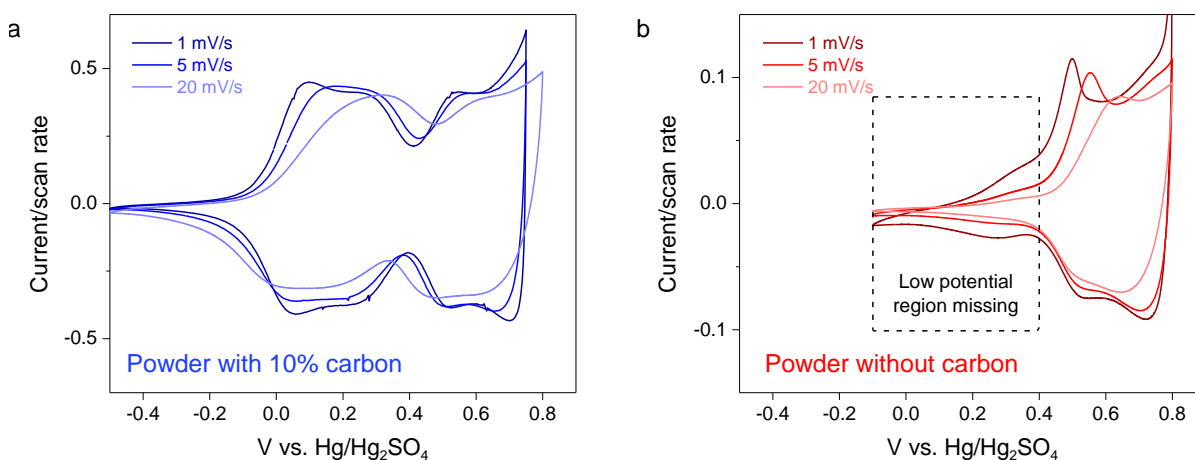


Figure V.12 : Difference in electrochemical behaviors with and without carbon additive. The low potential region observed when cycling with  $10\%$  carbon additive (a) completely disappears without carbon (b) whereas the high potential one is maintained.

To understand the kinetic differences between the low and high potential processes, we conducted deeper electrochemical analysis with the help of by Z. Lin, P.-L. Taberna and P. Simon from CIRIMAT (Toulouse, France). Swagelok cells using thin films as positive electrodes were assembled and cyclic voltammograms were collected up to scan rates of 50 mV/s over the full potential range (Figure V.13a) and then independently over the low and high potential range (Figure V.13b, c). Both the low and high potential regions show kinetic limitations as can be seen from the increasing polarization of anodic and cathodic processes (peaks moving to the right or the left in oxidation and reduction, respectively) whatever these potential ranges are swept independently or together. However, noticeable differences can be observed by focusing on the slope of the oxidation and reduction curves at various rates (Figure V.13, bottom) with greater rate polarization dependence for the lower potential domain compared to the high potential one. This observation, combined with the disappearance of the low potential domain without carbon, strongly suggests that the kinetic of the low potential process is under ohmic control. It is interesting to note the symmetry of the polarization for the high potential domain as opposed to its asymmetry for the low potential domain, with the kinetic being more sluggish on oxidation than on reduction. This is indicative of a different ohmic limitation on charge and discharge, which is most likely linked to changes in the electrode conductivity, as will be discussed later.

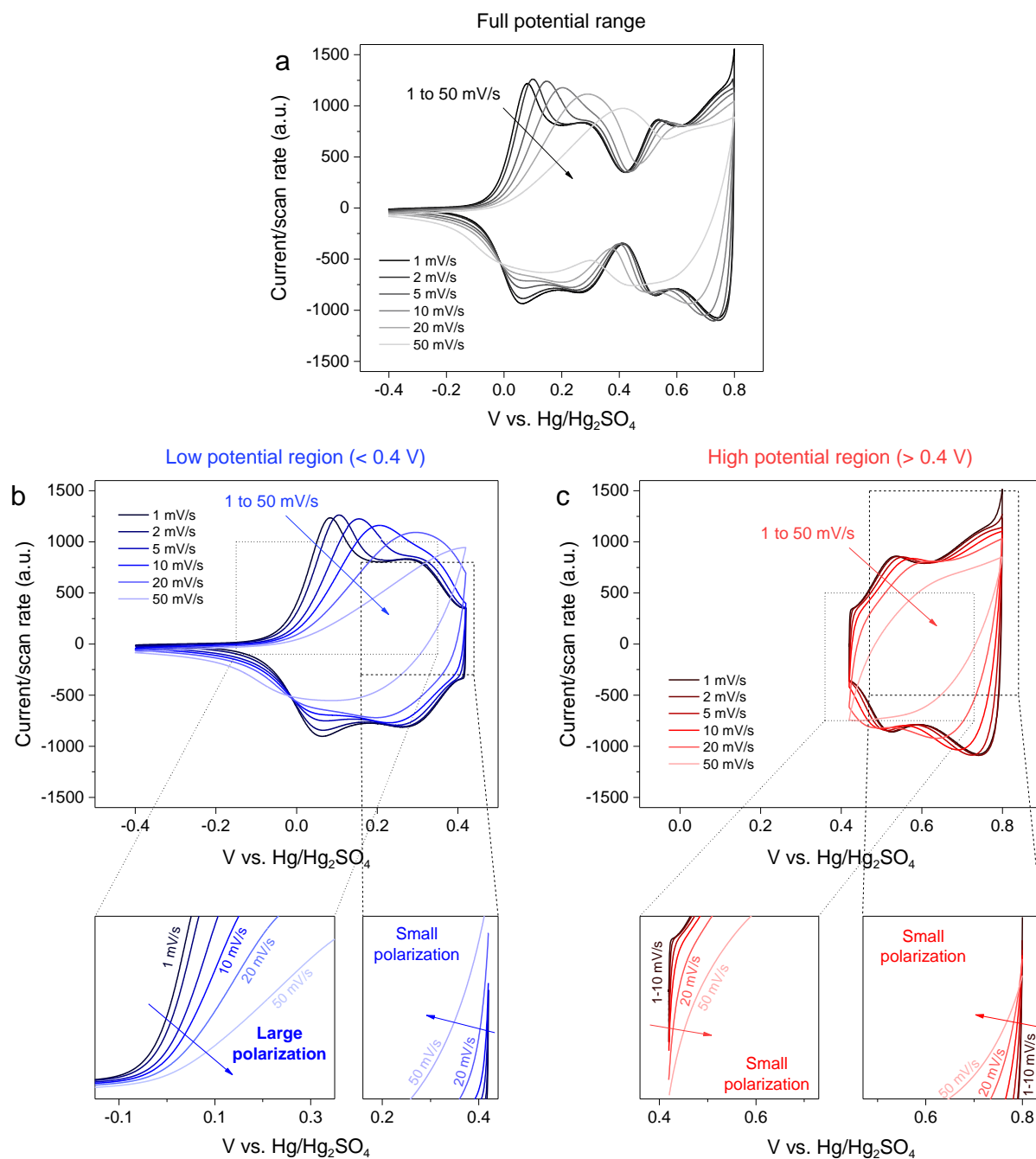


Figure V.13 : Kinetic analysis of the charge storage process. (a) CVs measured on the full potential range are compared to the low (b) and high (c) potential regions. The beginning of cathodic and anodic processes for both regions is enlarged at the bottom and show little polarization, except for the anodic process in the low potential region (left) which starts to polarize even at low scan rates.

To get rid of the ohmic limitations at high scan rates and better assess the kinetics of the material itself, this experiment was repeated by Z. Lin using a cavity microelectrode (CME) which presents several advantages compared to conventional Swagelok set-ups. First, neat active material powders can be used free from any binder. Besides, the feasibility to use only a few micrograms of active material helps to achieve high cycling rates since ohmic drop

is negligible for the low current flowing in the electrode. In these conditions, ohmic limitations were found to be negligible from 1 to 200 mV/s for all processes, except for the anodic process of the low potential region, whose kinetic seems limited by the (poor) electrical percolation inside the active material.

At this stage, it is important to understand the mechanism of the low and high potential processes which, considering the CV shape, are most likely not capacitive. To grasp further insights into this issue, *in situ* XRD measurements were done using a similar cell as before with the exception that the Be window, which cannot chemically resist acidic electrolyte, was replaced by a Kapton film, and a graphite current collector was used. This *in situ* cell cannot be used with a reference electrode, therefore we first cycled the working and counter electrodes in a 3-electrode Swagelok cell to know the relationship between cell voltage and working electrode potential. We used a similar experimental protocol as before (XRD patterns taken every  $\Delta x = 0.05$ ) and cycled at C/5. The 2D contour plot representation of the collected data (Figure V.10b) shows a smooth and continuous displacement of the Bragg peaks towards lower angles upon reduction to -0.2 V, indicative of a solid solution insertion process. This process is perfectly reversible as the Bragg peaks move back towards their initial position after switching the current. Refinement of the collected patterns indicates that the P3 stacking is preserved through the process, with however a decrease in both  $a$  and  $c$  lattice parameters when the potential is increased to 0.4 V and a flattening towards the end (Figure V.10d). Altogether, these results prove that the electrochemical activity at low potential is simply due to a classical insertion-deinsertion reaction.

The upper potential domain turns out to be more difficult to explore as we could not reach oxidation potentials greater than 0.5 V with our cell design because of water decomposition (Figure V.10d). To circumvent these difficulties, we returned to *ex situ* measurements where cells were polarized to 0.8 V in Teflon Swagelok cells, the glassy carbon current collector was recovered with the working electrode and directly measured by XRD without further processing (Figure V.14). No change in lattice parameters was detected, suggesting that the high potential storage process does not imply structural changes. To comfort the validity of this *ex situ* experiment, the electrode potential was compared before and after the XRD measurement, and was found stable. The large capacity of the high potential process seems to go in contradiction with the absence of change in XRD. At this point, we can make the supposition that in addition to the bulk intercalation process, the

material has a large pseudocapacitive activity confined to the surface, which does not affect the bulk structure as observed by XRD. Further experiments, such as electrochemical quartz crystal microbalance (EQCM) to spot the eventual adsorption of molecules, remain to be done to fully elucidate the high potential mechanism observed for the aqueous  $H^+/H_3IrO_4$  system. Lastly, it is worth mentioning that identical results were obtained using HCl or  $HNO_3$  rather than  $H_2SO_4$ , and that a very limited activity was found using  $Li_2SO_4$ , which can be understood from the voltage/composition curve for  $H_3IrO_4$  vs. Li which shows an activity of solely  $0.4 Li^+$  above 3 V (Figure V.9) in the electrochemical stability window of water.

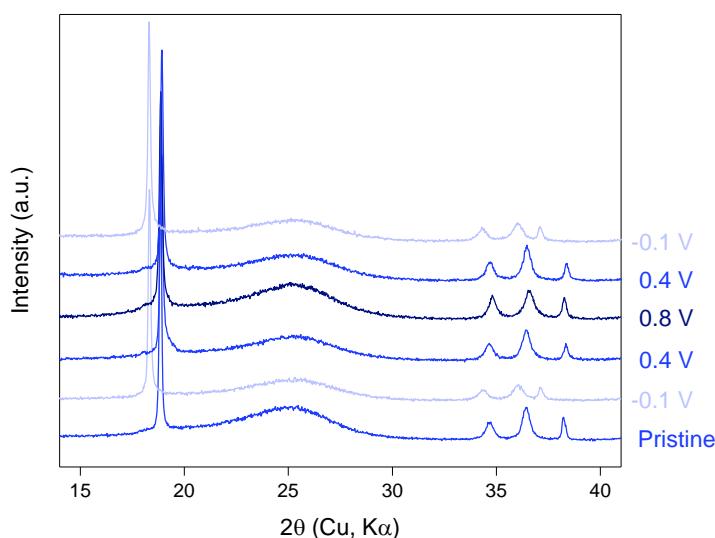


Figure V.14 : *Ex situ* XRD study of  $H_3IrO_4$  in aqueous media. The working electrode was polarized at different potentials, giving consistent results with the *in situ* study at low potential (-0.1 and 0.4 V), and did not show any cell parameter change at higher potential (0.8 V). The large and broad signal around  $25^\circ$  belongs to the glassy carbon electrode.

### V.3.c. Proton positions

The change in stacking sequence are summarize in Figure V.15. Getting insights into the local position of  $H^+$  ions is quite complex as their contribution to XRD is negligible compared to Ir. Neutron diffraction could bring more information if deuterated samples are used to overcome the large incoherent neutron scattering of protons, and provided that the disordered distribution of Ir sites in the plane does not create too many possible sites.  $^2H$  NMR spectra of samples exchanged and cycled in  $D_2SO_4$  did not allow us to discriminate different sites, and support the existence of environments with various distances and geometries relative to the paramagnetic  $Ir^{5+}$  centers, resulting in a distribution of Fermi contact shift.

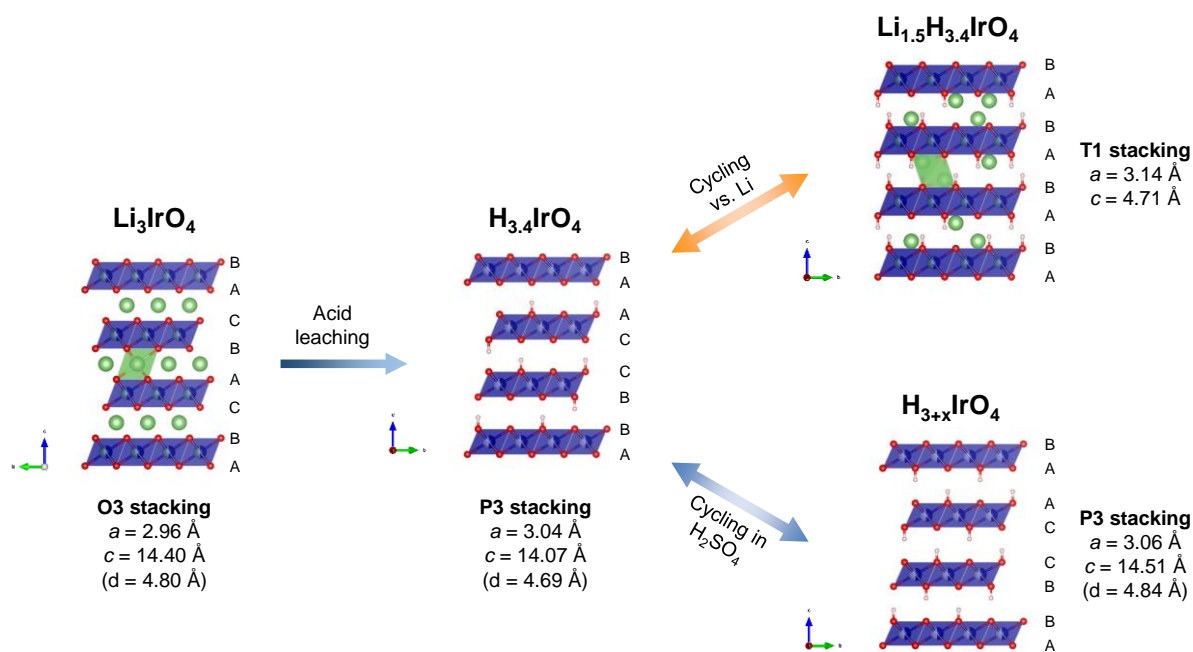


Figure V.15 : Overall structural mechanism. Acid leaching of the parent Li<sub>3</sub>IrO<sub>4</sub> phase modifies the stacking from O3 to P3 for H<sub>3.4</sub>IrO<sub>4</sub>. Cycling in aqueous media does not modify the stacking whereas insertion of Li<sup>+</sup> in organic electrolyte changes the stacking to T1. Li<sup>+</sup> and H<sup>+</sup> positions are hypothetical, as discussed in the text.

In the absence of clear structural measurements, a valuable alternative consists in looking for possible proton positions among the known structures of layered hydroxides such as CrOOH, which adopts a P3 structure (Figure V.16a). Typically, protons form strong covalent bond to one oxygen atom, with a typical length of  $\sim 0.85 - 1.0 \text{ \AA}$ , and one weaker “hydrogen” bond to another oxygen atom, which has more electrostatic nature and a length that can vary between  $1.5-2.5 \text{ \AA}$ . In CrOOH, protons occupy “out-of-plane” position between two successive (CrO<sub>2</sub>) octahedral layers being closer to one O atom ( $d(\text{O-H}) = 1.05 \text{ \AA}$ ) and more distant from the O atom from the neighbouring layer ( $d(\text{O-H}) = 1.53 \text{ \AA}$ ).<sup>112</sup> Thus a linear O-H---O fragment is formed. Turning to the protons within the metal layers, their position at the Li octahedral sites is quite unlikely. A more probable location could be deduced from the known hydroxide Al(OH)<sub>3</sub>, which has a very similar structure to Li-rich layered oxides with honeycomb ordering (Figure V.16b).<sup>113</sup> In this structure, the honeycomb ordering of the Al-filled and vacant oxygen octahedra within the (AlO<sub>3</sub>) layers provides extra “in-plane” proton positions, sitting almost within the oxygen close packed layers, with one short O-H bond of  $0.94 - 1.0 \text{ \AA}$  and another longer one of  $2.11 - 2.43 \text{ \AA}$  to the oxygen atoms of the same layer. Together, the “out-of-plane” and “in-plane” proton positions can account for the hydrogen atoms in H<sub>3.4</sub>IrO<sub>4</sub>. Finally, upon Li insertion in the material, the O3  $\rightarrow$  T1 transition creates tetrahedral sites, in a similar way as for the insertion of Li in Li<sub>3</sub>IrO<sub>4</sub>. The T1 stacking

sequence is also found in the brucite  $Mg(OH)_2$  mineral (Figure V.16c) in which protons occupy tetrahedral sites, thus doubling the number of “out-of-plane” positions compared to the  $CrOOH$  structure. In  $Li_{1.5}H_{3.4}IrO_4$ , the total number of “out-of-plane” tetrahedral positions goes up to 4, which, added to the vacant octahedral site in the Ir plane, gives a total of 5 possible positions for  $Li^+/H^+$  in the structure.

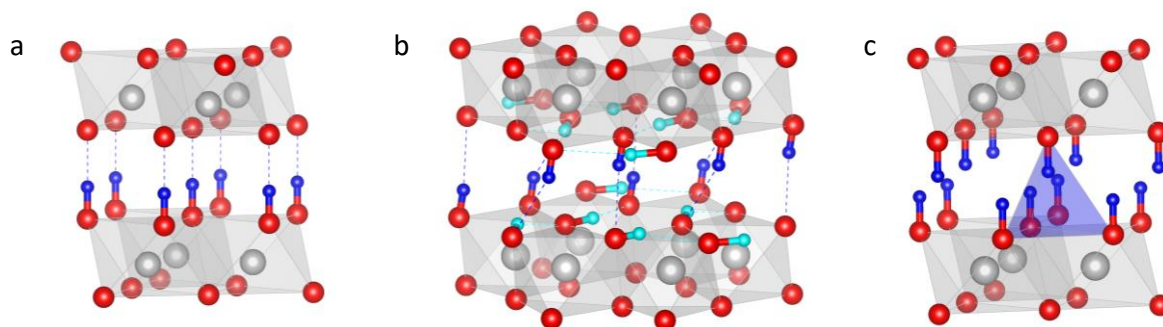


Figure V.16 : Proton positions in layered  $CrOOH$ , bayerite  $Al(OH)_3$  and brucite  $Mg(OH)_2$  structures. (a) In the  $CrOOH$  structure, protons (blue) form a strong covalent bond with oxygen atoms from one ( $CrO_2$ ) octahedral layer and a weaker hydrogen bond (represented by a dashed line) with the facing oxygen in the adjacent layer. The metal cations and oxygens are shown as grey and red spheres, respectively. (b)  $Al(OH)_3$  shows a honeycomb ordering of the  $AlO_6$  octahedra and vacant oxygen octahedra that creates free space to accommodate protons almost in the oxygen close packed planes. The “out-of-plane” and “in-plane” proton positions are colored with dark blue and cyan, respectively. (c) In  $Mg(OH)_2$ , each O atom forms a hydroxide group with the proton staying in a pseudo-tetrahedral site (shown in blue).

### V.3.d. Charge compensation by Ir

The  $Li^+$  insertion mechanism in  $H_{3.4}IrO_4$  can be reasonably well explained by the reversible  $Ir^{5+} \leftrightarrow Ir^{4+} \leftrightarrow Ir^{3+}$  redox couples. The evolution of the  $a$  parameter in  $Li_xH_{3.4}IrO_4$  is almost linear with  $Li^+$  insertion (Figure V.10c), consistent with the gradual increase in ionic radii of Ir upon reduction. The same tendency was observed for  $Li^+$  insertion in  $Li_3IrO_4$ , as described in chapter 4.

In aqueous media there is, besides a low potential process governed by cationic insertion, a high potential process associated to a reversible uptake/release of  $0.7 e^-$  for which, based on charge counting, one could propose a small amount of  $Ir^{6+}$ , which is not frequent, or some anionic redox process: “ $H_{2.7}Ir^{5+}O_{3.4}(O_2)^{3-0.3}$ ”. This is quite unlikely as anionic redox affects the structure and usually leads to slow kinetic compared to cationic redox; which is not what we found. More likely, we underestimated the amount of  $H^+$  in the material owing to the experimental uncertainty and we are again working with the  $Ir^{5+} \leftrightarrow Ir^{4+} \leftrightarrow Ir^{3+}$  redox couples.

We have shown that the two processes observed at low and high potential only differ by the existence of a greater ohmic polarization for the low potential domain process which cannot be triggered in absence of carbon additive. Its origin is most likely linked to the increasing amount of  $\text{Ir}^{3+}$  during the reduction of the  $\text{H}_x\text{IrO}_4$  phase, keeping in mind that  $\text{Ir}^{3+}$  adopts a  $d^6$  configuration so that all the  $t_{2g}$  levels are filled, thus limiting the conductivity of the material. It is the same explanation given by Conway in the 80's to explain why there is no current in  $\text{IrO}_2$  below 0.8 V vs SHE (0.15 V vs  $\text{Hg}/\text{Hg}_2\text{SO}_4$ ).<sup>114</sup> The question of the high potential process remains regarding the absence of structural change detectable by XRD. To confirm our hypothesis on the participation of Ir to the charge compensation, it would be interesting to perform *operando* X-ray Absorption Spectroscopy at Ir-L<sub>III</sub> edge to track changes in the Ir oxidation states and coordination, and fully elucidate the high potential mechanism observed for the aqueous  $\text{H}^+/\text{H}_{3+x}\text{IrO}_4$  system.

#### **V.4. Conclusion**

Several iridates phases were prepared by a simple room temperature acid leaching technique from parent compounds containing Li/Na. The electrochemical properties of the  $\text{H}_{3.4}\text{IrO}_4$  phases were explored in organic and aqueous electrolytes for the insertion of  $\text{Li}^+$  and  $\text{H}^+$ , respectively. This new phase shows large capacity storage ( $1.5 e^-$  per transition metal), and presents attractive rate capabilities in aqueous systems. The storage process was shown to mainly rely on cationic redox reactions with the possible participation of a pseudocapacitive behavior to account for the total redox process in aqueous media. The rich crystal chemistry of iridates is still largely unexplored, opening numerous opportunities for material design as exemplified by the recent preparation of a layered  $\text{K}_{0.75}\text{Na}_{0.25}\text{IrO}_2$  phase with trivalent iridium, and its acid-exchanged counterpart  $\text{IrOOH}$  with the brucite  $\text{Mg}(\text{OH})_2$  structure.<sup>115</sup>

Besides the synthesis and fundamental aspects, this work also bears importance application-wise, provided that we can implement our protonation strategy to other Li-rich phases, deviating from the use of poorly abundant and costly Ir. Finally, this rich proton chemistry of iridates opens new opportunities within the field of energy, as Ir-based materials also present a great interest for water splitting applications.

## General conclusions

In this work, fundamental aspects of anionic redox were investigated using model materials based on iridium. The versatility of structure and composition of iridium oxides, as well as their stability vs. oxygen release and cationic migrations upon oxidation make them ideal systems to understand how different structural parameters affect the competition or synergy between cationic and anionic redox. The role of the alkali ion was explored by moving from  $\text{Li}_2\text{IrO}_3$  to  $\text{Na}_2\text{IrO}_3$  and exploring an intermediate composition  $\text{Na}(\text{Li}_{1/3}\text{Ir}_{2/3})\text{O}_2$ . The importance of the ratio between alkali and transition metal was investigated through the synthesis and study of a new  $\text{Li}_3\text{IrO}_4$  phase. Finally, a protonation strategy was implemented to prepare new materials with high capacities and fast cycling performance. The synthesis and electrochemical properties of these materials were thoroughly explored using several experimental techniques.

The  $\text{Na}_2\text{IrO}_3$  phase was found to have many similarities with the previously reported  $\text{Li}_2\text{IrO}_3$  compound. The reversible change in stacking sequence  $\text{O}3 \leftrightarrow \text{O}1' \leftrightarrow \text{O}1$  during cycling was carefully characterized by diffraction and electron microscopy techniques. These structural transitions were found to intrinsically limit the deintercalation to  $1.5 \text{ Na}^+$  due to the stabilization of the remaining  $\text{Na}^+$  in the  $\text{O}1\text{-Na}_{0.5}\text{IrO}_3$  phase. This structural limitation is inherent to honeycomb ordered Li/Na-rich layered oxides with  $\text{A}_2\text{MO}_3$  stoichiometry. Possible strategies to bypass this limitation could consist in preparing a polymorph with a disordered distribution of Li/Ir in the metallic planes to avoid the stacking of honeycomb layers and keep diffusion pathways open in the material. However, this approach seems to give the opposite effect for  $\text{Na}_2\text{RuO}_3$ ,<sup>59</sup> the reason why being still unclear. A more promising solution was found by preparing the tridimensional  $\beta$  polymorph of  $\text{Li}_2\text{IrO}_3$ , which can be fully delithiated thanks to its rigid framework.<sup>65</sup> The participation of O to the redox of  $\text{Na}_2\text{IrO}_3$  results in the formation of short (2.45 Å) O-O bonds in the structure as shown by TEM and neutron diffraction studies, supporting the formation of “peroxo-like” species for 5d-based materials. This value is far from the O-O distance of true peroxo species as can be found with alkali or alkaline earth cations, but reflects the stabilization mechanism of oxygen orbitals. The formation of shorter O-O bonds has not been observed in materials with anionic redox, possibly because of the fragile equilibrium between reversible anionic redox and irreversible  $\text{O}_2$  gas formation. The use of spectroscopic techniques such as XPS and XAS brought valuable information on the oxidation state of the cations and anions in the structure.

XPS has the advantage of being relatively accessible at the laboratory scale but remains a surface sensitive technique, it is therefore important to compare with more bulk sensitive techniques such as XAS, even though it comes with more constraints. Finally, the good cycling stability of  $\text{Na}_2\text{IrO}_3$  in full cell configuration validates the strategy to search for new Na-rich materials to increase the capacity of Na-ion batteries, while keeping in mind the high sensitivity of these phases to electrolyte decomposition products.

Li substitution in the metallic layers to form  $\text{Na}(\text{Li}_{1/3}\text{Ir}_{2/3})\text{O}_2$  led to a material with a more complex stacking sequence compared to the pure Na and Li compounds. This substitution method could represent an interesting strategy to trigger anionic redox in layered oxides for Na-ion batteries.<sup>116</sup> Here we found that mixing Na and Li resulted in a highly metastable material, which decomposes upon charging due to Na/Li exchange and segregation reactions. This is to be kept in mind for the design of mixed alkali materials. However, the influence of alkali substitution on the activation of anionic redox remains an important question and deserves to be investigated further, especially with the substitution of divalent cations ( $\text{Mg}^{2+}$ ,  $\text{Ca}^{2+}$ ) in the transition metal layers which have also been shown to give access to higher capacities.<sup>117</sup>

Based on theoretical work predicting that the Li/M ratio was a key parameter for the activation of oxygen redox in rocksalt oxides,<sup>68,69</sup> we prepared a new  $\text{Li}_3\text{IrO}_4$  phase with  $\text{Li}/\text{M} = 3$ . This phase was found to stand the highest reversible capacity based on intercalation chemistry with 3.5  $\text{Li}^+$  exchanged per transition metal, thanks to the rich redox chemistry of iridium ( $\text{Ir}^{5+}/\text{Ir}^{4+}/\text{Ir}^{3+}$ ) as well as the large participation of oxygen on oxidation ( $\text{O}^{2-}/(\text{O}_2)^{n-}$ ). Complete delithiation of the material leads to large gas release and amorphization of the material. This result has two important implications for the design of new materials: the possibility to achieve high capacity by extending the Li/M ratio beyond 2 for Li-rich  $\text{Li}_2\text{MO}_3$  phases, and the risk of decomposing the material at large depth of charge. The layered structure of  $\text{Li}_3\text{IrO}_4$  with no long-range order of cations in the metallic planes makes it challenging to obtain structural information, especially on the possible formation of O-O bonds in the structure. We therefore turned to XAS and EPR spectroscopies, as well as DFT to obtain insight in the charge compensation mechanism, but local distortions remain difficult to characterize experimentally.

Finally, the rich electrochemical properties of the iridates materials investigated was extended to proton-based systems, via a simple ion exchange reaction in acid. Interesting

electrochemical properties were shown for the  $\text{H}_{3.4}\text{IrO}_4$  phase both in organic and aqueous electrolyte, with excellent rate capability for the aqueous system. Understanding electrochemical processes at high rates is highly challenging experimentally, and requires a step forward in the development of structural characterization tools. Nevertheless, the good electrochemical properties of this material are encouraging us to generalize the preparation of “proton-rich” phases from layered Li-rich materials to three-dimensional structures, or even to Li-rich disordered rocksalt phases, with the possibility to obtain pseudocapacitive materials with high capacities.

Overall, studying the electrochemical properties of these model iridate materials has delivered important insight on the possibility to use anionic redox in high capacity cathode materials. This knowledge will be beneficial to design materials based on more available elements than iridium. The preparation of new Ir-based materials will also be significant to a broader audience than the battery community as iridium oxides remain among the best materials used for water splitting applications, and attract considerable interest from solid-state physicists for their exotic magnetic properties.



## Annexes

### A.1. Structural characterization

Diffraction was used routinely to determine the purity of the samples prepared or to obtain structural parameters by performing Rietveld refinement<sup>118</sup> as implemented in the FullProf suite.<sup>119</sup> Synchrotron XRD and neutron diffraction were used to obtain more precise structural information on selected samples.

The crystal structures shown in this work were drawn with the VESTA visualization program,<sup>120</sup> using the crystallographic information obtained from Rietveld refinement or using CIF files from the ICSD database.<sup>121</sup>

#### A.1.a. Laboratory X-ray diffraction (XRD)

X-ray powder diffraction, as well as *in situ* XRD measurements were performed on a BRUKER D8 Advance diffractometer with Bragg-Brentano geometry using a Cu K $\alpha$  radiation ( $\lambda_{K\alpha 1} = 1.54056 \text{ \AA}$ ,  $\lambda_{K\alpha 2} = 1.54439 \text{ \AA}$ ) and a LynxEye detector, operating at 40 kV and 40 mA. To prevent air exposure for sensitive samples, airtight sample holders equipped with a Kapton window were used.



Figure A.1 : Air-tight XRD sample holder used for air sensitive samples.

#### A.1.b. Synchrotron XRD

Synchrotron X-ray diffraction (SXRD) was performed through the 11-BM mail-in service of the Advanced Photon Source (APS) at Argonne National Laboratory (Argonne, USA) in transmission geometry (Debye-Scherrer) with a wavelength  $\lambda \sim 0.414 \text{ \AA}$ , using

sealed quartz capillaries (0.7 mm diameter) to prevent air exposure. The capillaries were introduced in Kapton tubes and fixed to the sample holder provided by the APS service.

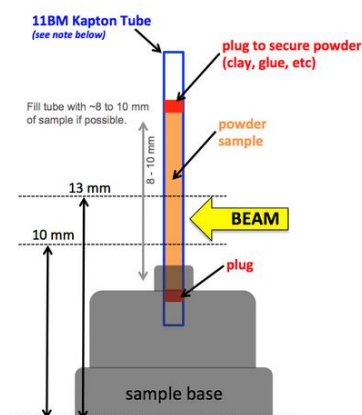


Figure A.2 : Sample holder for synchrotron XRD on the 11 BM beamline at APS.<sup>122</sup>

### A.1.c. Neutron diffraction (ND)

Neutron powder diffraction experiments were performed on three diffractometers:

- The D20 powder diffractometer at the Institut Laue-Langevin (ILL, Grenoble, France) in its high-resolution mode (take-off angle  $90^\circ$ ), with a wavelength  $\lambda = 1.5444 \text{ \AA}$ .
- The D1B powder diffractometer at Institut Laue-Langevin with a wavelength  $\lambda = 1.291 \text{ \AA}$ .
- The HRPT high-resolution neutron powder diffractometer at the Swiss Spallation Neutron Source SINQ (Paul Scherrer Institute, Villigen, Switzerland) with a wavelength  $\lambda = 1.494 \text{ \AA}$ .

For the measurement, samples were loaded in sealed  $\varnothing = 5 \text{ mm}$  vanadium cylindrical cans in an argon-filled glovebox.

## A.2. Electrochemical characterization

### A.2.a. Electrode preparation

Two methods were used to prepare the electrode from the active material. The first method consists in mixing the active material with carbon Super P used as a conductive additive, in an 80:20 weight ratio, using ball-milling in stainless steel jar for 20 min. Alternatively, self-standing laminated electrodes were prepared by adding the active material, carbon Super P and PTFE in an 85:10:5 weight ratio. Everything is mixed in a mortar with the help of a few drops of volatile solvent (dimethylcarbonate when the electrode is prepared in an Ar-filled glovebox and ethanol in air, for example). When the electrode sticks together and can be manipulated, it is alternatively rolled out and folded several times in the same way a pastry puff is prepared. Adding a few drops of solvent helps to roll out the electrode into a thin layer. The electrodes are then dried under vacuum to remove the solvent and cut for electrochemical characterization.

### A.2.b. Electrochemical cells

All the cell parts were dried for several hours at 55°C before being assembled in an Ar-filled glovebox (MBraun, O<sub>2</sub> and H<sub>2</sub>O < 0.1 ppm). The positive and negative electrodes were separated by one or more sheets of borosilicate glass fiber membranes (Whatman GF/D) soaked with electrolyte. Unless otherwise specified, metallic Li and Na were used as anodes by spreading a small chunk of metal on a stainless-steel current collector.

#### A.2.b.i. Swagelok-type cells

Routine electrochemical tests were performed using two-electrodes Swagelok-type cells (Figure A.3). All *ex situ* samples were also prepared using this cell which can be assembled and disassembled easily. To recover the electrode after cycling, the Swagelok cell was disassembled in the glovebox, the electrode washed with fresh dimethylcarbonate at least three times and then dried under vacuum. F. Lepoivre is warmly acknowledged for the cell schematics.

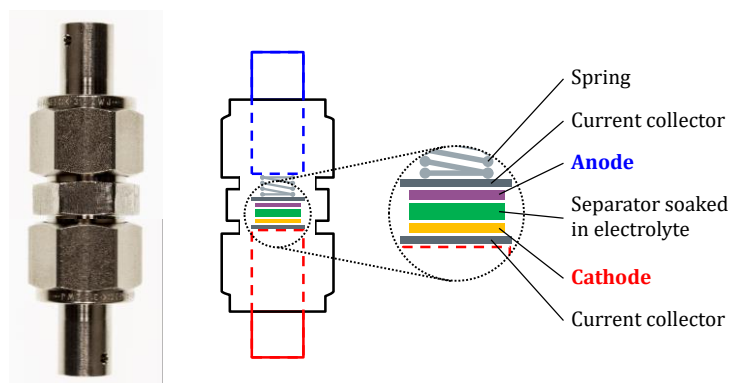


Figure A.3 : Swagelok cell

### A.2.b.ii. 2032 coin cells

For long-term cycling experiments, 2032 coin cells were used (Figure A.4), which were sealed by an automatic crimping machine applying the same pressure to all cells. To characterize the electrodes after long-term cycling tests, the coin-cell were opened with the same crimping machine to recover the electrode.

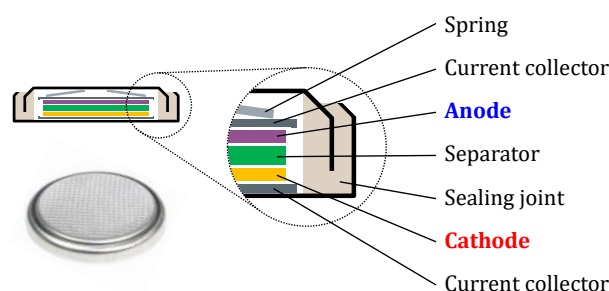


Figure A.4 : 2032 coin cell

### A.2.b.iii. Three-electrode Swagelok cell

To measure independently the potentials of the working and counter electrodes, three electrode cells were used. Using a Swagelok union tee (Figure A.5), a reference electrode can be added in the cell between two layers of separator which isolate it from the working and counter electrodes. For Li-ion (Na-ion) cells, a piece of metallic Li (Na) can be used as a reference provided that its potential remains constant. For the aqueous cells described in chapter 5, a Hg/Hg<sub>2</sub>SO<sub>4</sub> reference electrode was adapted on a perfluoroalkoxy alkane (PFA) Swagelok cell, and glassy carbon current collectors were used instead of stainless steel.

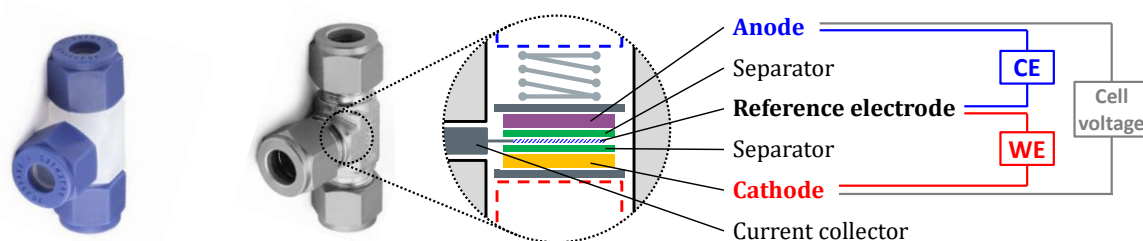


Figure A.5 : Three-electrode Swagelok cell. A stainless-steel cell can be used for organic electrolytes and a plastic PFA cell for characterization in aqueous electrolyte.

#### A.2.b.iv. Pressure cell

Gas pressure measurements during cycling were done using a cell designed by Lepoivre *et al.* in the laboratory (Figure A.6),<sup>97</sup> adapted from the Swagelok cell (bottom part). The upper part contains a gas reservoir of approximately 9 cm<sup>3</sup>, a pressure sensor and a gas inlet/outlet that can be used to fill the cell with the desired mixture of gas. In this work, the pressure cells were assembled in the glovebox and closed before taking them out so that they are slightly overpressurized with Ar. The cells are cycled at 25°C in a temperature-controlled incubator (IPP260, Memmert) and left at OCV for at least 12h prior to cycling to allow the cell temperature to equilibrate. The active material was placed on the top and a stainless-steel mesh was used as current collector to avoid the capture of the gas formed. For differential electrochemical mass spectrometry (DEMS) measurements, Ar gas was continuously flushed in the cell through the gas inlet, and a union tee Swagelok part was adapted at the bottom to connect the cell with a Hiden Analytical mass spectrometer. The current of all *m/z* fragments from 1 to 100 were measured and used to normalize individual contributions.

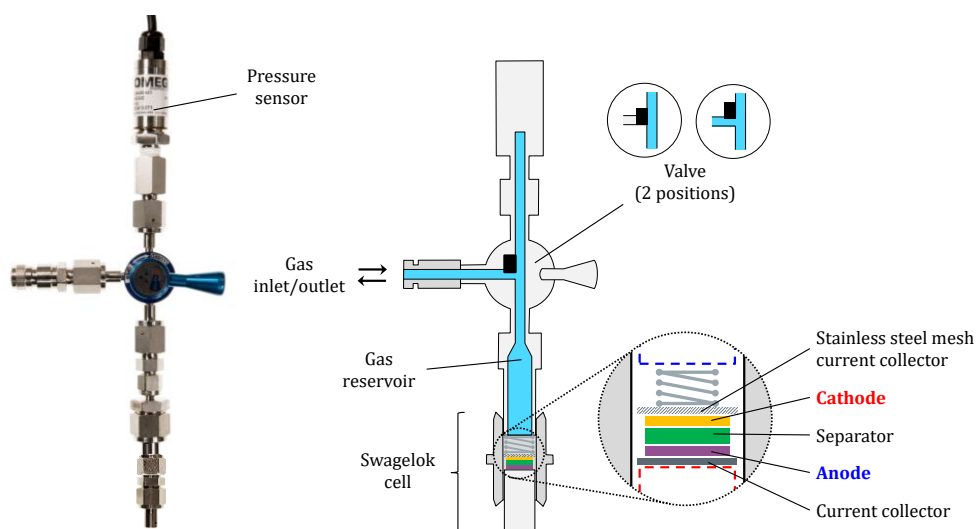


Figure A.6 : *In situ* pressure cell for gas measurements designed by Lepoivre *et al.*<sup>97</sup>

### A.2.b.v. *In situ* X-ray diffraction and absorption cells

The cell used for *in situ* X-ray diffraction studies (Figure A.7a) was developed at the Laboratoire de Réactivité et Chimie des Solides (LRCS) in Amiens, France, by Leriche *et al.*<sup>80</sup> It is equipped with a Be window which do not absorb X-ray and shows only a few diffraction peaks. The cell was used in reflection mode (Figure A.7b), adapted to XRD in Bragg-Brentano geometry, with the active material electrode placed next to the Be window. To avoid oxidation of Be above  $\sim 3.5$  V vs.  $\text{Li}^+/\text{Li}$ , a 3  $\mu\text{m}$  foil of Al was used between the Be and active material. The same cell was used for X-ray absorption (XAS) studies in transmission mode (Figure A.7c), by replacing the stainless-steel plunger with a plunger equipped of a second Be window to allow X-ray radiation to go through the cell with minimum absorption.

As this cell can contain larger amounts of active material compared to Swagelok cells, it was also used to prepare large quantities of *ex situ* samples by replacing the Be window with a stainless steel current collector and an Al foil.

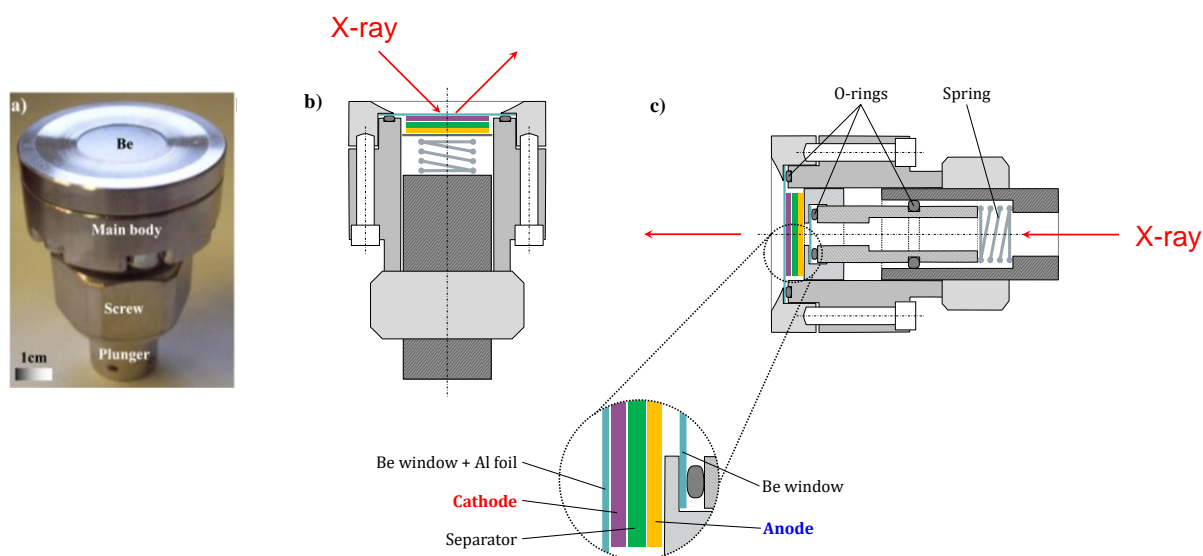


Figure A.7 : *In situ* cell for X-ray experiments. (a) Cell picture from Leriche *et al.*<sup>80</sup> (b) Schematic of the cell for XRD experiments in reflection mode. (c) Schematic of the cell for XAS experiments in transmission mode.

### A.2.c. Electrochemical cycling

All electrochemical tests were performed with VMP3 potentiostat/galvanostat (BioLogic Science Instruments).

Standard electrochemical characterization was done in a galvanostatic mode, with a constant current applied between the working and counter electrodes and the cell voltage (for two-electrode set ups) or electrode potentials (for three-electrode setups) were measured. The current was chosen to correspond to a defined cycling rate for a given material. Typically, the cells were cycled at  $C/10$ , meaning that 1  $\text{Li}^+$  is exchanged between the two electrodes in 10 hours. To evaluate the rate capability of a given electrode, the cycling rates were varied from  $C/100$  (1  $\text{Li}^+$  in 100 hours) to  $100C$  (100  $\text{Li}^+$  in 1 hour), for example. The total current passed through the cell gives the amount of  $e^-$  or  $\text{Li}^+$  exchanged, as well as the current coming from parasitic electrochemical reactions, which is negligible in normal conditions.

For the preparation of *ex situ* samples corresponding to pure phases, the cells are cycled slowly ( $C/20$  to  $C/50$ ) to a given potential and hold at this potential until the current drops to negligible values, meaning that the reaction is completed.

## A.3. X-ray absorption spectroscopy

### A.3.a. Data collection and pre-treatment

*Operando* X-ray absorption spectroscopy (XAS) measurements were performed in transmission mode at the ROCK beamline<sup>100</sup> of synchrotron SOLEIL (France) as described in Figure A.8. A Si (111) channel-cut quick-XAS monochromator with an energy resolution of 2 eV at 11 keV was used. The intensity of the monochromatic X-ray beam was measured by three consecutive ionization detectors. The *in situ* electrochemical cell<sup>80</sup> was placed between the first ( $I_0$ ) and the second ( $I_1$ ) ionization chambers. For each cell, successive spectra were collected at a rate of 2 Hz and averaged out over periods of 5 minutes. The energy calibration was established with simultaneous absorption measurements on an Ir metal foil placed between the second ( $I_1$ ) and the third ( $I_2$ ) ionization chamber. The data was treated using the Demeter package for energy calibration and normalization.<sup>123</sup>

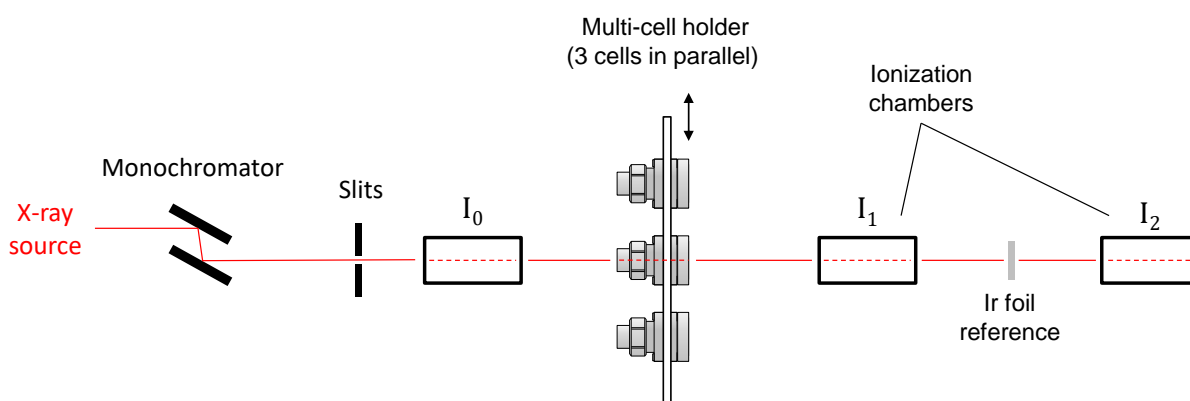


Figure A.8 : Schematic of the XAS experiment. Three *in situ* cells were cycled in parallel and were alternatively aligned with the beam to collect absorption spectra.

### A.3.b. Analysis of EXAFS data

The normalized spectra were globally analyzed with Principal Component Analysis (PCA)<sup>101</sup> in order to individuate the orthogonal components able to describe the whole evolution during cycling. The number of principal components was then used as basis for Multivariate Curve Resolution-Alternating Least Squares (MCR-ALS)<sup>102</sup> analysis. Finally, the reconstructed components were fitted using the Artemis software.<sup>123</sup> Fourier transforms of Extended X-ray Absorption Fine Structure (EXAFS) oscillations were carried out in  $k$ -range from  $3.5 \text{ \AA}^{-1}$  to 16 and  $14 \text{ \AA}^{-1}$  for crystalline and amorphous components, respectively.

Fitting was performed in R-range from 1.0 to 3.6 Å using  $k^3$  weight. EXAFS amplitudes and phase-shifts were calculated by FEFF7 with a starting model derived from Rietveld refinements of diffraction data or from CIF files of phases with the same expected structure. Except the radial distance (R) and the Debye-Waller factor ( $\sigma^2$ ), all other parameters were kept constant ( $N_i$ ,  $E_0$ ,  $S_0^2$ ) in the conventional least squares modelling using the phase and amplitude factors calculated by the FEFF7. Error bars for R and  $\sigma^2$  were estimated from the distribution of values found for the different models tried during the fitting process.

### A.3.c. Analysis of XANES data

The X-ray Absorption Near-Edge Structure region at Ir  $L_3$ -edge displays an intense white line (WL) that overlaps with the absorption edge (Figure A.9a). This WL corresponds to the absorption of X-rays for the dipole-allowed transition from core Ir(2p) levels to the partially filled Ir(5d) levels. Therefore, the WL intensity is related to the hole population in 5d levels orbitals. The XANES data was fitted with an arctangent function for the edge, and a Gaussian function to fit both the  $t_{2g}$  and  $e_g$  components of the WL. The position and area of the Gaussian were used to follow the changes in energy and intensity of the WL during cycling. The intensity was alternatively calculated by subtracting the arctangent function from the experimental data and integrating the area of the peak (Figure A.9b), as described by Clancy *et al.*,<sup>124</sup> yielding to similar results compared to those of the fitting procedure, with the advantage of being independent of the function chosen to fit the WL.

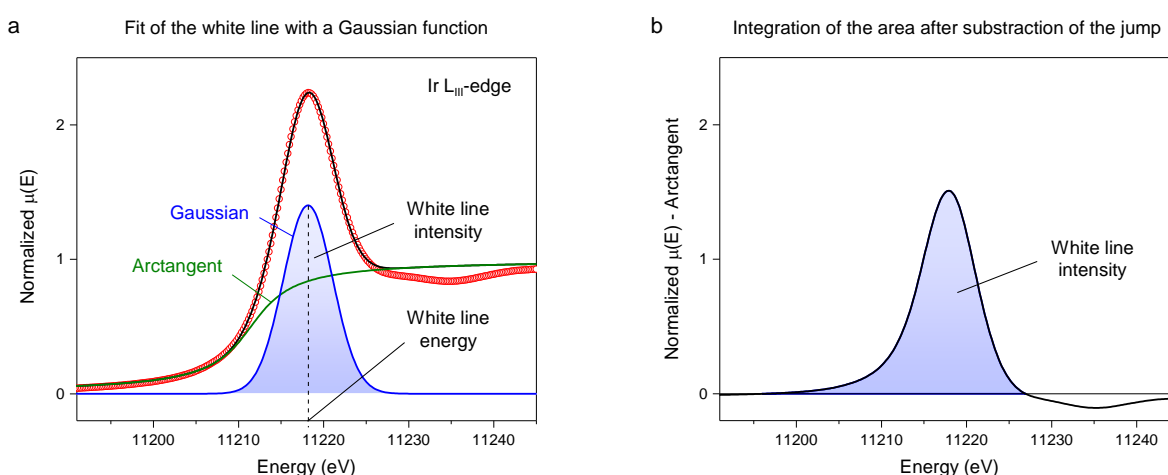


Figure A.9 : Determination of the white line intensity at Ir  $L_3$ -edge. (a) Fit with a Gaussian function for the WL and an arctangent function for the edge jump. Experimental points are shown as red marks and the result of the fit as a black line. (b) Alternatively, the area of the peak can be integrated after subtraction of the arctangent function.

## A.4. Additional experimental techniques

### A.4.a. Transmission electron microscopy (TEM)

Electron microscopy measurements were performed on pristine and *ex situ* samples by D. Batuk and A. Abakumov at EMAT (Antwerp, Belgium). Samples for the TEM investigation were prepared by grinding powdered samples in a mortar and dipping holey carbon TEM grids into the powder. To prevent exposure of the samples to air, they were stored and prepared for TEM in an Ar-filled glovebox. A special Gatan vacuum transfer holder was used for the analyses. Electron diffraction (ED) data, high-resolution high angle annular dark field scanning transmission electron microscopy (HAADF-STEM), annular bright field STEM (ABF-STEM) images and electron energy loss (EELS) spectroscopy data were acquired on a probe aberration corrected FEI Titan 80-300 electron microscope at 300 kV. Cation composition of the samples at different charge/discharge states was confirmed using energy dispersive X-ray (EDX) analysis. The data were collected on an FEI Osiris transmission electron microscope equipped with a Super-X EDX detector and operated at 200 kV.

### A.4.b. X-ray photoemission spectroscopy (XPS)

XPS measurements were carried out for Ir 4f and O 1s peaks by D. Foix in IPREM (Pau, France) with a Kratos Axis Ultra spectrometer, using focused monochromatic Al K $\alpha$  radiation ( $h\nu = 1486.6$  eV). The XPS spectrometer was directly connected through a transfer chamber to an Ar dry box to avoid exposing the samples to air. Short acquisition time spectra were recorded before and after each normal experiment to check that the samples did not suffer from degradation during the measurements. The binding energy scale was calibrated using the C 1s peak at 285.0 eV from the hydrocarbon contamination invariably present. Core peaks were analyzed using a nonlinear Shirley-type background<sup>125</sup>. The peak positions and areas were optimized by a weighted least-square fitting method using 70% Gaussian, 30% Lorentzian line shapes. Quantification was performed on the basis of Scofield's relative sensitivity factors<sup>126</sup>. The curves fit for core peaks were obtained while minimizing the number of peaks used to fit the experimental curves.

#### **A.4.c. Density Functional Theory (DFT) calculations**

Spin-polarized density functional theory (DFT) calculations were performed by M. Saubanère and M.-L. Doublet from the Institut Charles Gerhardt (Montpellier, France) to compare the relative stability of different phases formed during cycling of  $\text{Na}_2\text{IrO}_3$  and  $\text{Li}_3\text{IrO}_4$ , calculate the decomposition enthalpies of the materials to form  $\text{O}_2$  gas, determine the electronic structure of the materials and rationalize the participation of oxygen and iridium to the redox properties. DFT calculations were done using the plane-wave density functional theory VASP (Vienna ab initio simulation package) code<sup>127,128</sup> within the generalized gradient approximation of Perdew–Burke–Ernzerhof (PBE) to describe electron exchange and correlation<sup>129</sup>. The rotationally invariant Dudarev method (DFT + U)<sup>130</sup> was used to correct the self-interaction error of conventional DFT for correlated d-electrons.

#### **A.4.d. Thermogravimetric analysis - mass spectrometry (TGA-MS)**

The thermal stability of materials was investigated using thermogravimetric analysis coupled with mass spectrometry (STA449C Netzsch). Between 20-30 mg of samples were used for each measurement and heated under high purity Ar gas (5.0) at 5 °C/min. The measurements were performed by M. Courty at LRCS (Amiens, France).

## A.5. Additional experimental results

### A.5.a. EXAFS fits

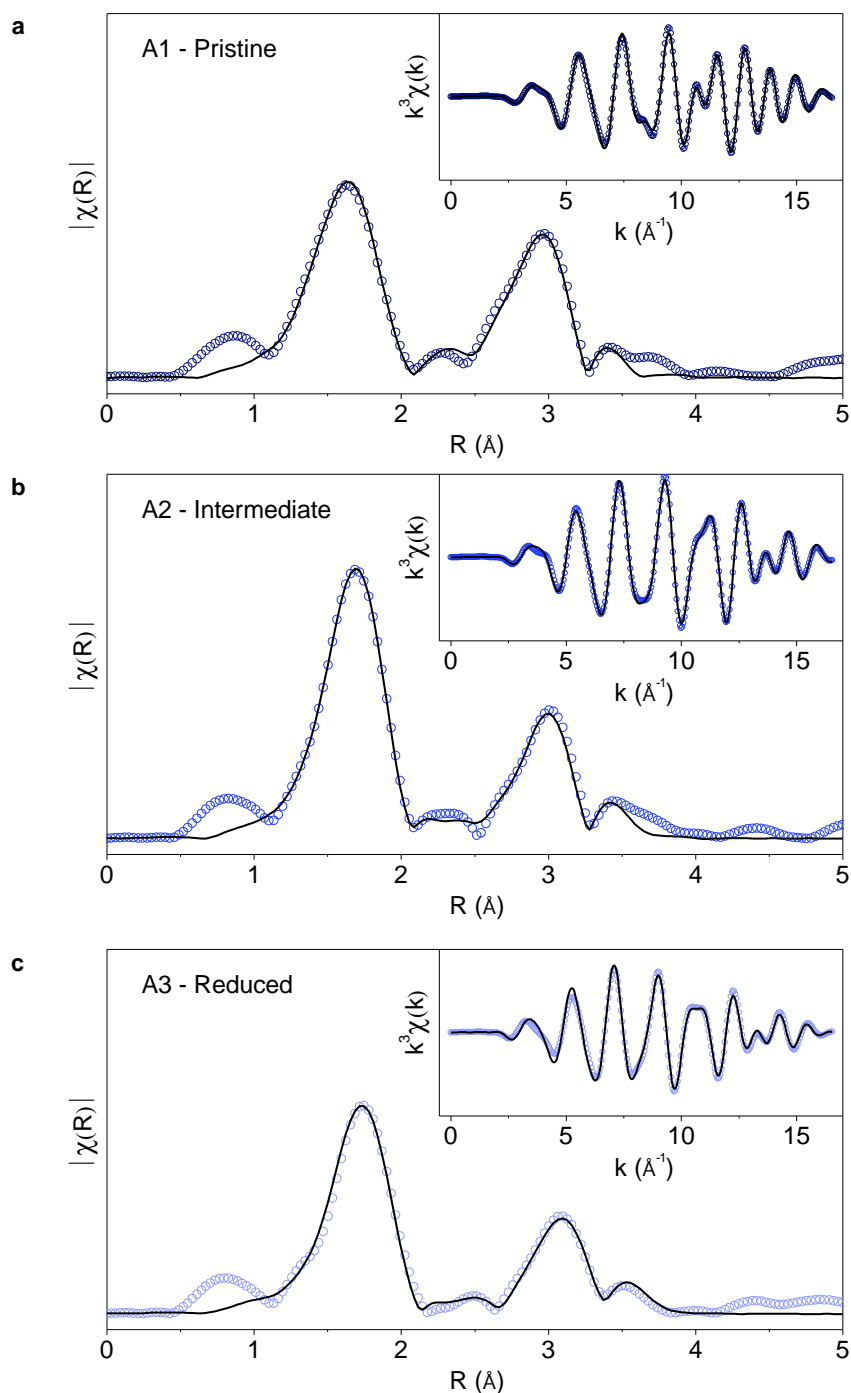


Figure A.10 : Ir L<sub>III</sub>-edge EXAFS analysis of Li<sub>3</sub>IrO<sub>4</sub> (cell A), started on reduction. The EXAFS oscillations of the three components extracted by PCA and MCR analysis were fitted to obtain structural information on the environment of Ir. Fit of the Fourier transform of the EXAFS oscillations of the pristine (a), intermediate (b) and reduced (c) components. Insets show the fit of the back Fourier transform for  $R$  ranging from 1.0 to 3.6 Å.

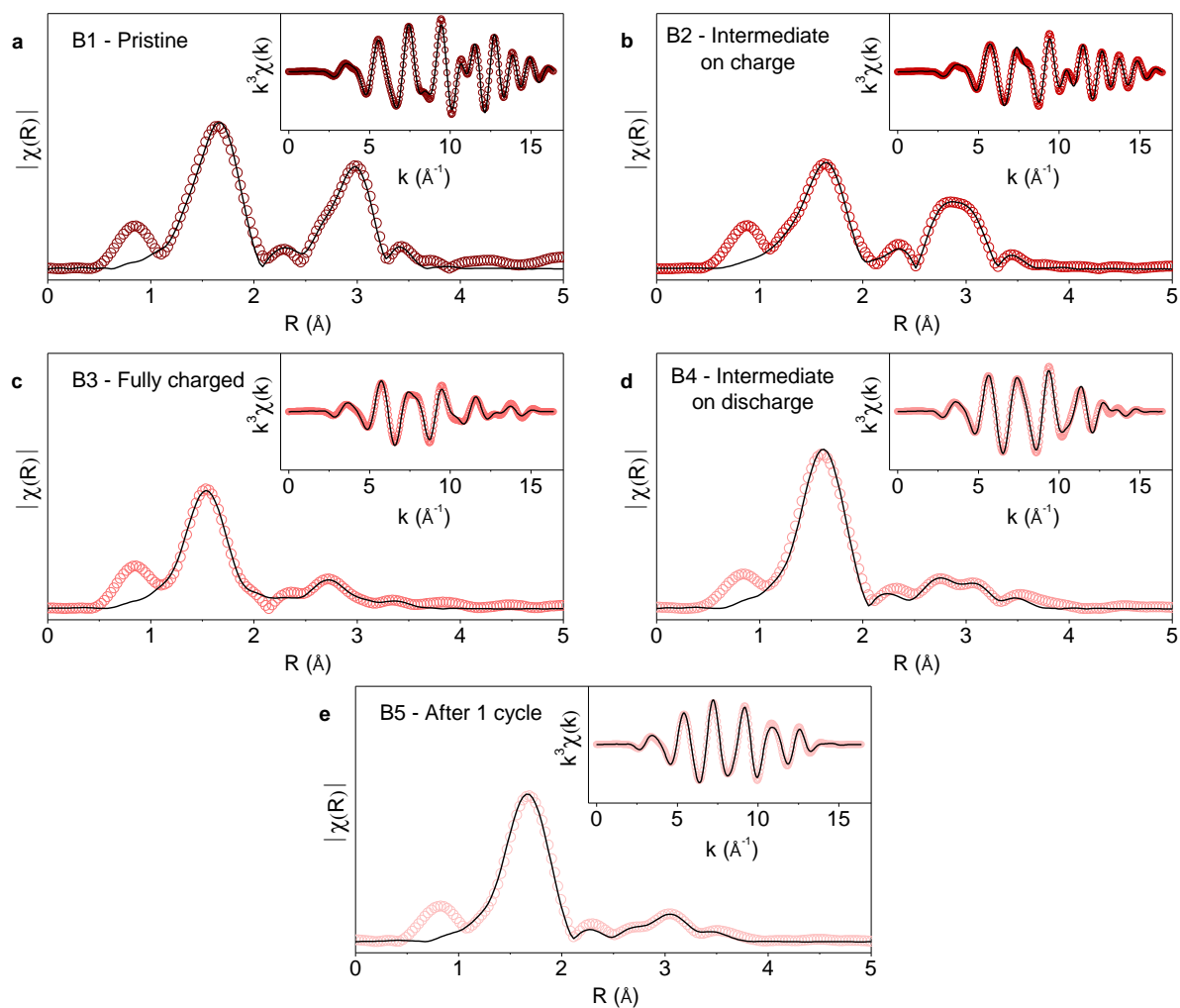


Figure A.11 : Ir L<sub>III</sub>-edge EXAFS analysis of Li<sub>3</sub>IrO<sub>4</sub> (cell B), started on oxidation. Fit of the Fourier transform of the EXAFS oscillations of the pristine (a), intermediate on charge (b), fully charged (c), intermediate on discharge (d) and after 1 cycle (e). Insets show the fit of the back Fourier transform for  $R$  ranging from 1.0 to 3.6 Å.

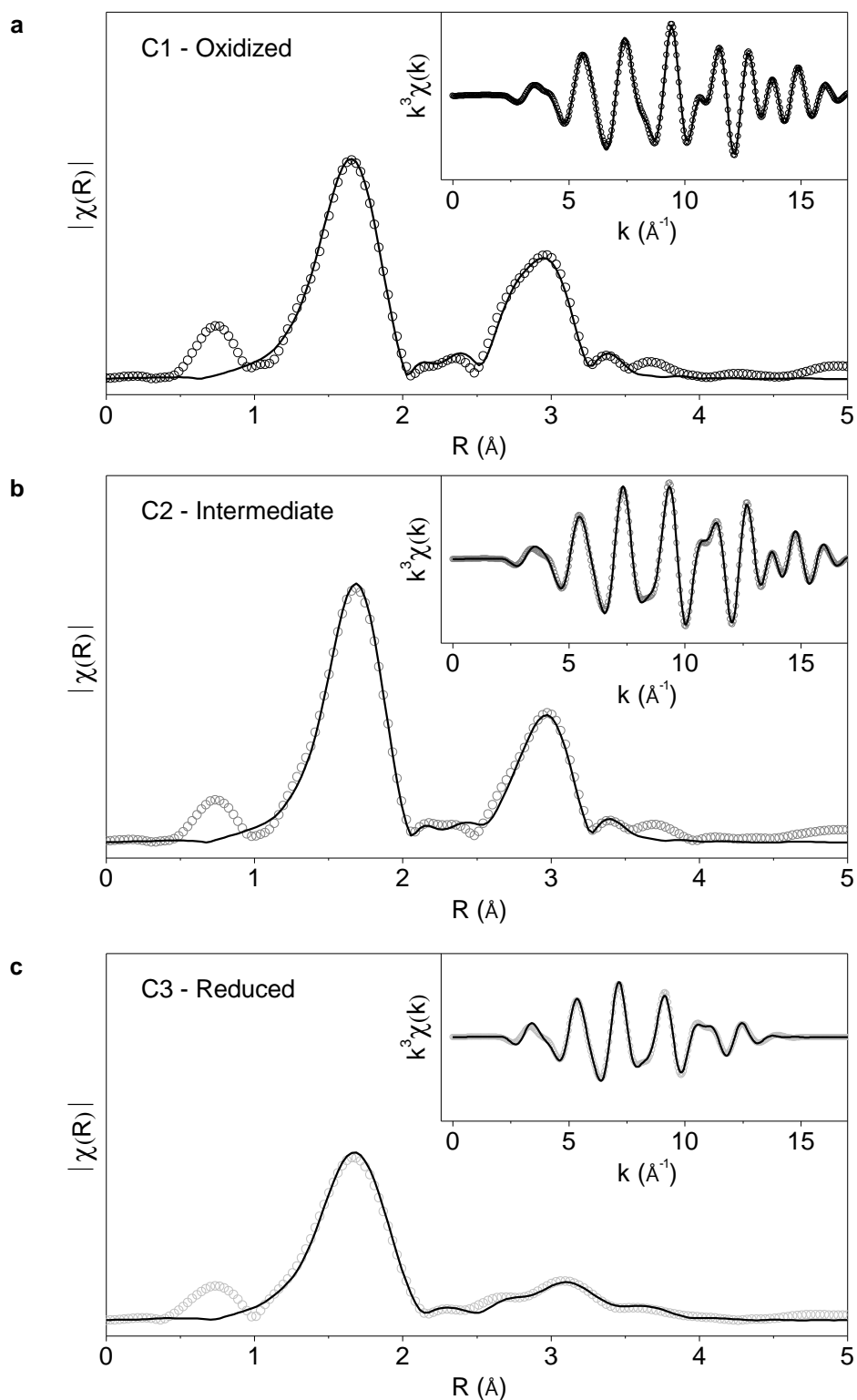


Figure A.12 : Ir  $L_{III}$ -edge EXAFS analysis of  $\text{Li}_3\text{IrO}_4$  (cell C), during the reversible cycling of  $\text{Li}_3\text{IrO}_4$ .

Fit of the Fourier transform of the EXAFS oscillations of the oxidized (a), intermediate (b) and reduced (c) components. Insets show the fit of the back Fourier transform for  $R$  ranging from 1.0 to 3.6 Å.

## References

1. Whittingham, M. S. & Gamble, F. R. **The lithium intercalates of the transition metal dichalcogenides.** *Mater. Res. Bull.* 10, 363–371 (1975). [https://dx.doi.org/10.1016/0025-5408\(75\)90006-9](https://dx.doi.org/10.1016/0025-5408(75)90006-9)
2. Whittingham, M. S. **Electrical Energy Storage and Intercalation Chemistry.** *Science* 192, 1126–1127 (1976).
3. Haering, R. R. *et al.* **United States Patent: 4224390 - Lithium molybdenum disulphide battery cathode.** (1980).
4. Delmas, C., Fouassier, C. & Hagenmuller, P. **Structural classification and properties of the layered oxides.** *Phys. BC* 99, 81–85 (1980). [https://dx.doi.org/10.1016/0378-4363\(80\)90214-4](https://dx.doi.org/10.1016/0378-4363(80)90214-4)
5. Mizushima, K., Jones, P. C., Wiseman, P. J. & Goodenough, J. B. **Li<sub>x</sub>CoO<sub>2</sub> (0 < x < -1): A new cathode material for batteries of high energy density.** *Mater. Res. Bull.* 15, 783–789 (1980). [https://dx.doi.org/10.1016/0025-5408\(80\)90012-4](https://dx.doi.org/10.1016/0025-5408(80)90012-4)
6. Braconnier, J.-J., Delmas, C., Fouassier, C. & Hagenmuller, P. **Comportement electrochimique des phases Na<sub>x</sub>CoO<sub>2</sub>.** *Mater. Res. Bull.* 15, 1797–1804 (1980). [https://dx.doi.org/10.1016/0025-5408\(80\)90199-3](https://dx.doi.org/10.1016/0025-5408(80)90199-3)
7. Braconnier, J. J., Delmas, C. & Hagenmuller, P. **Etude par desintercalation electrochimique des systemes Na<sub>x</sub>CrO<sub>2</sub> et Na<sub>x</sub>NiO<sub>2</sub>.** *Mater. Res. Bull.* 17, 993–1000 (1982). [https://dx.doi.org/10.1016/0025-5408\(82\)90124-6](https://dx.doi.org/10.1016/0025-5408(82)90124-6)
8. Delmas, C., Braconnier, J.-J. & Hagenmuller, P. **A new variety of LiCoO<sub>2</sub> with an unusual oxygen packing obtained by exchange reaction.** *Mater. Res. Bull.* 17, 117–123 (1982). [https://dx.doi.org/10.1016/0025-5408\(82\)90192-1](https://dx.doi.org/10.1016/0025-5408(82)90192-1)
9. Mendiboure, A., Delmas, C. & Hagenmuller, P. **Electrochemical intercalation and deintercalation of Na<sub>x</sub>MnO<sub>2</sub> bronzes.** *J. Solid State Chem.* 57, 323–331 (1985). [https://dx.doi.org/10.1016/0022-4596\(85\)90194-X](https://dx.doi.org/10.1016/0022-4596(85)90194-X)
10. Thackeray, M. M., Baker, S. D., Adendorff, K. T. & Goodenough, J. B. **Lithium insertion into Co<sub>3</sub>O<sub>4</sub>: A preliminary investigation.** *Solid State Ion.* 17, 175–181 (1985). [https://dx.doi.org/10.1016/0167-2738\(85\)90069-4](https://dx.doi.org/10.1016/0167-2738(85)90069-4)
11. Tarascon, J. M. & Hull, G. W. **Sodium intercalation into the layer oxides Na<sub>x</sub>Mo<sub>2</sub>O<sub>4</sub>.** *Solid State Ion.* 22, 85–96 (1986). [https://dx.doi.org/10.1016/0167-2738\(86\)90062-7](https://dx.doi.org/10.1016/0167-2738(86)90062-7)
12. James, A. C. W. P. & Goodenough, J. B. **Structure and bonding in Li<sub>2</sub>MoO<sub>3</sub> and Li<sub>2-x</sub>MoO<sub>3</sub> (0 ≤ x ≤ 1.7).** *J. Solid State Chem.* 76, 87–96 (1988). [https://dx.doi.org/10.1016/0022-4596\(88\)90194-6](https://dx.doi.org/10.1016/0022-4596(88)90194-6)

13. James, A. C. W. P. & Goodenough, J. B. **Structure and bonding in lithium ruthenate,  $\text{Li}_2\text{RuO}_3$** . *J. Solid State Chem.* 74, 287–294 (1988). [https://dx.doi.org/10.1016/0022-4596\(88\)90357-X](https://dx.doi.org/10.1016/0022-4596(88)90357-X)
14. Thackeray, M. M., Johnson, P. J., de Picciotto, L. A., Bruce, P. G. & Goodenough, J. B. **Electrochemical extraction of lithium from  $\text{LiMn}_2\text{O}_4$** . *Mater. Res. Bull.* 19, 179–187 (1984). [https://dx.doi.org/10.1016/0025-5408\(84\)90088-6](https://dx.doi.org/10.1016/0025-5408(84)90088-6)
15. Padhi, A. K., Nanjundaswamy, K. S. & Goodenough, J. B. **Phospho-olivines as Positive-Electrode Materials for Rechargeable Lithium Batteries**. *J. Electrochem. Soc.* 144, 1188–1194 (1997). <https://dx.doi.org/10.1149/1.1837571>
16. Vashishta, P., Mundy, J. N. & Shenoy, G. K. *Fast ion transport in solids: electrodes, and electrolytes : proceedings of the International Conference on Fast Ion Transport in Solids, Electrodes, and Electrolytes, Lake Geneva, Wisconsin, U.S.A., May 21-25, 1979*. (North Holland, 1979).
17. **Blue Solutions, Plastic Films - Bolloré**. Available at: <http://www.bollore.com/en-us/activities/electricity-storage-and-solutions/blue-solutions-plastic-films>. (Accessed: 24th August 2017)
18. Lazzari, M. & Scrosati, B. **A Cyclable Lithium Organic Electrolyte Cell Based on Two Intercalation Electrodes**. *J. Electrochem. Soc.* 127, 773–774 (1980). <https://dx.doi.org/10.1149/1.2129753>
19. Dahn, J. R., Sacken, U. von, Juzkow, M. W. & Al-Janaby, H. **Rechargeable  $\text{LiNiO}_2$  / Carbon Cells**. *J. Electrochem. Soc.* 138, 2207–2211 (1991). <https://dx.doi.org/10.1149/1.2085950>
20. Tarascon, J. & Guyomard, D. **Li Metal-Free Rechargeable Batteries Based on  $\text{Li}_{1+x}\text{Mn}_2\text{O}_4$  Cathodes ( $0 < x < 1$ ) and Carbon Anodes**. *J. Electrochem. Soc.* 138, 2864–2868 (1991). <https://dx.doi.org/10.1149/1.2085331>
21. Komaba, S. *et al.* **Electrochemical Na Insertion and Solid Electrolyte Interphase for Hard-Carbon Electrodes and Application to Na-Ion Batteries**. *Adv. Funct. Mater.* 21, 3859–3867 (2011). <https://dx.doi.org/10.1002/adfm.201100854>
22. Komaba, S. *et al.* **Fluorinated Ethylene Carbonate as Electrolyte Additive for Rechargeable Na Batteries**. *ACS Appl. Mater. Interfaces* 3, 4165–4168 (2011). <https://dx.doi.org/10.1021/am200973k>
23. **Batterie sodium-ion: une révolution en marche**. *CNRS Le journal* Available at: <https://lejournel.cnrs.fr/articles/batterie-sodium-ion-une-revolution-en-marche>. (Accessed: 21st August 2017)
24. Bruce, P. G., Freunberger, S. A., Hardwick, L. J. & Tarascon, J.-M. **Li- $\text{O}_2$  and Li-S batteries with high energy storage**. *Nat. Mater.* 11, 19–29 (2012). <https://dx.doi.org/10.1038/nmat3191>

25. Amatucci, G. G., Tarascon, J. M. & Klein, L. C. **CoO<sub>2</sub>, The End Member of the Li<sub>x</sub>CoO<sub>2</sub> Solid Solution.** *J. Electrochem. Soc.* 143, 1114–1123 (1996). <https://dx.doi.org/10.1149/1.1836594>
26. Ceder, G., Aydinol, M. K. & Kohan, A. F. **Application of first-principles calculations to the design of rechargeable Li-batteries.** *Comput. Mater. Sci.* 8, 161–169 (1997). [https://dx.doi.org/10.1016/S0927-0256\(97\)00029-3](https://dx.doi.org/10.1016/S0927-0256(97)00029-3)
27. Ceder, G. *et al.* **Identification of cathode materials for lithium batteries guided by first-principles calculations.** *Nature* 392, 694–696 (1998). <https://dx.doi.org/10.1038/33647>
28. Tarascon, J. M. *et al.* **In Situ Structural and Electrochemical Study of Ni<sub>1-x</sub>Co<sub>x</sub>O<sub>2</sub> Metastable Oxides Prepared by Soft Chemistry.** *J. Solid State Chem.* 147, 410–420 (1999). <https://dx.doi.org/10.1006/jssc.1999.8465>
29. Ohzuku, T., Ueda, A. & Nagayama, M. **Electrochemistry and Structural Chemistry of LiNiO<sub>2</sub> (R $\bar{3}$ m) for 4 Volt Secondary Lithium Cells.** *J. Electrochem. Soc.* 140, 1862–1870 (1993). <https://dx.doi.org/10.1149/1.2220730>
30. Armstrong, A. R. & Bruce, P. G. **Synthesis of layered LiMnO<sub>2</sub> as an electrode for rechargeable lithium batteries.** *Nature* 381, 499–500 (1996). <https://dx.doi.org/10.1038/381499a0>
31. Ohzuku, T., Ueda, A., Nagayama, M., Iwakoshi, Y. & Komori, H. **Comparative study of LiCoO<sub>2</sub>, LiNi<sub>1/2</sub>Co<sub>1/2</sub>O<sub>2</sub> and LiNiO<sub>2</sub> for 4 volt secondary lithium cells.** *Electrochimica Acta* 38, 1159–1167 (1993). [https://dx.doi.org/10.1016/0013-4686\(93\)80046-3](https://dx.doi.org/10.1016/0013-4686(93)80046-3)
32. Ammundsen, B. & Paulsen, J. **Novel Lithium-Ion Cathode Materials Based on Layered Manganese Oxides.** *Adv. Mater.* 13, 943–956 (2001). [http://onlinelibrary.wiley.com/doi/10.1002/1521-4095\(200107\)13:12/13%3C943::AID-ADMA943%3E3.0.CO;2-J/abstract](http://onlinelibrary.wiley.com/doi/10.1002/1521-4095(200107)13:12/13%3C943::AID-ADMA943%3E3.0.CO;2-J/abstract)
33. Ohzuku, T. & Makimura, Y. **Layered lithium insertion material of LiCo<sub>1/3</sub>Ni<sub>1/3</sub>Mn<sub>1/3</sub>O<sub>2</sub> for lithium-ion batteries.** *Chem. Lett.* 642–643 (2001).
34. Lu, Z., MacNeil, D. D. & Dahn, J. R. **Layered Li[Ni<sub>x</sub>Co<sub>1-2x</sub>Mn<sub>x</sub>]O<sub>2</sub> Cathode Materials for Lithium-Ion Batteries.** *Electrochem. Solid-State Lett.* 4, A200–A203 (2001). <https://dx.doi.org/10.1149/1.1413182>
35. Rozier, P. & Tarascon, J. M. **Li-Rich Layered Oxide Cathodes for Next-Generation Li-Ion Batteries: Chances and Challenges.** *J. Electrochem. Soc.* 162, A2490–A2499 (2015). <https://dx.doi.org/10.1149/2.0111514jes>
36. Kobayashi, H., Kanno, R., Kawamoto, Y., Tabuchi, M. & Nakamura, O. **Physical properties of the de-lithiated Li<sub>2-x</sub>RuO<sub>3</sub> with the layered structure.** *Solid State Ion.* 86–88, Part 2, 859–863 (1996). [https://dx.doi.org/10.1016/0167-2738\(96\)00194-4](https://dx.doi.org/10.1016/0167-2738(96)00194-4)

37. Kalyani, P., Chitra, S., Mohan, T. & Gopukumar, S. **Lithium metal rechargeable cells using  $\text{Li}_2\text{MnO}_3$  as the positive electrode.** *J. Power Sources* 80, 103–106 (1999). [https://dx.doi.org/10.1016/S0378-7753\(99\)00066-X](https://dx.doi.org/10.1016/S0378-7753(99)00066-X)
38. Shao-Horn, Y. *et al.* **Morphology modification and delithiation mechanisms of  $\text{LiMn}_2\text{O}_4$  and  $\text{Li}_2\text{MnO}_3$  by acid digestion.** *J. Electrochem. Soc.* 145, 16–23 (1998). <https://dx.doi.org/10.1149/1.1838203>
39. Johnson, C. S. *et al.* **Structural and electrochemical analysis of layered compounds from  $\text{Li}_2\text{MnO}_3$ .** *J. Power Sources* 81–82, 491–495 (1999). [https://dx.doi.org/10.1016/S0378-7753\(99\)00248-7](https://dx.doi.org/10.1016/S0378-7753(99)00248-7)
40. Robertson, A. D. & Bruce, P. G. **The origin of electrochemical activity in  $\text{Li}_2\text{MnO}_3$ .** *Chem. Commun.* 0, 2790–2791 (2002). <https://dx.doi.org/10.1039/B207945C>
41. Lu, Z. H. & Dahn, J. R. **Understanding the anomalous capacity of  $\text{Li/Li}[\text{Ni}_x\text{Li}_{(1/3-2x/3)}\text{Mn}_{(2/3-x/3)}]\text{O}_2$  cells using in situ X-ray diffraction and electrochemical studies.** *J. Electrochem. Soc.* 149, A815–A822 (2002). <https://dx.doi.org/10.1149/1.1480014>
42. Kim, J.-H., Park, C. W. & Sun, Y.-K. **Synthesis and electrochemical behavior of  $\text{Li}[\text{Li}_{0.1}\text{Ni}_{0.35-x/2}\text{Co}_x\text{Mn}_{0.55-x/2}]\text{O}_2$  cathode materials.** *Solid State Ion.* 164, 43–49 (2003). <https://dx.doi.org/10.1016/j.ssi.2003.08.003>
43. Jiang, J., Eberman, K. W., Krause, L. J. & Dahn, J. R. **Structure, Electrochemical Properties, and Thermal Stability Studies of Cathode Materials in the  $x\text{Li}[\text{Mn}_{1/2}\text{Ni}_{1/2}]\text{O}_2 \cdot y\text{LiCoO}_2 \cdot z\text{Li}[\text{Li}_{1/3}\text{Mn}_{2/3}]\text{O}_2$  Pseudoternary System ( $x + y + z = 1$ ).** *J. Electrochem. Soc.* 152, A1879–A1889 (2005). <https://dx.doi.org/10.1149/1.1995690>
44. Thackeray, M. M. *et al.*  **$\text{Li}_2\text{MnO}_3$ -stabilized  $\text{LiMO}_2$  (M = Mn, Ni, Co) electrodes for lithium-ion batteries.** *J. Mater. Chem.* 17, 3112–3125 (2007). <https://dx.doi.org/10.1039/B702425H>
45. Lu, Z., MacNeil, D. D. & Dahn, J. R. **Layered Cathode Materials  $\text{Li}[\text{Ni}_x\text{Li}_{(1/3-2x/3)}\text{Mn}_{(2/3-x/3)}]\text{O}_2$  for Lithium-Ion Batteries.** *Electrochem. Solid-State Lett.* 4, A191–A194 (2001). <https://dx.doi.org/10.1149/1.1407994>
46. Armstrong, A. R. *et al.* **Demonstrating Oxygen Loss and Associated Structural Reorganization in the Lithium Battery Cathode  $\text{Li}[\text{Ni}_{0.2}\text{Li}_{0.2}\text{Mn}_{0.6}]\text{O}_2$ .** *J. Am. Chem. Soc.* 128, 8694–8698 (2006). <https://dx.doi.org/10.1021/ja062027+>
47. Tran, N. *et al.* **Mechanisms Associated with the “Plateau” Observed at High Voltage for the Overlithiated  $\text{Li}_{1.12}(\text{Ni}_{0.425}\text{Mn}_{0.425}\text{Co}_{0.15})_{0.88}\text{O}_2$  System.** *Chem. Mater.* 20, 4815–4825 (2008). <https://dx.doi.org/10.1021/cm070435m>
48. Koga, H. *et al.* **Reversible Oxygen Participation to the Redox Processes Revealed for  $\text{Li}_{1.20}\text{Mn}_{0.54}\text{Co}_{0.13}\text{Ni}_{0.13}\text{O}_2$ .** *J. Electrochem. Soc.* 160, A786–A792 (2013). <https://dx.doi.org/10.1149/2.038306jes>

49. Koga, H. *et al.* **Different oxygen redox participation for bulk and surface: A possible global explanation for the cycling mechanism of  $\text{Li}_{1.20}\text{Mn}_{0.54}\text{Co}_{0.13}\text{Ni}_{0.13}\text{O}_2$ .** *J. Power Sources* 236, 250–258 (2013). <https://dx.doi.org/10.1016/j.jpowsour.2013.02.075>
50. Streich, D. *et al.* **Operando Monitoring of Early Ni-mediated Surface Reconstruction in Layered Lithiated Ni–Co–Mn Oxides.** *J. Phys. Chem. C* 121, 13481–13486 (2017). <https://dx.doi.org/10.1021/acs.jpcc.7b02303>
51. Croy, J. R. *et al.* **Countering the Voltage Decay in High Capacity  $x\text{Li}_2\text{MnO}_3 \cdot (1-x)\text{LiMO}_2$  Electrodes (M=Mn, Ni, Co) for  $\text{Li}^+$ -Ion Batteries.** *J. Electrochem. Soc.* 159, A781–A790 (2012). <https://dx.doi.org/10.1149/2.080206jes>
52. Croy, J. R. *et al.* **Examining Hysteresis in Composite  $x\text{Li}_2\text{MnO}_3 \cdot (1-x)\text{LiMO}_2$  Cathode Structures.** *J. Phys. Chem. C* 117, 6525–6536 (2013). <https://dx.doi.org/10.1021/jp312658q>
53. Croy, J. R., Balasubramanian, M., Gallagher, K. G. & Burrell, A. K. **Review of the U.S. Department of Energy’s “Deep Dive” Effort to Understand Voltage Fade in Li- and Mn-Rich Cathodes.** *Acc. Chem. Res.* 48, 2813–2821 (2015). <https://dx.doi.org/10.1021/acs.accounts.5b00277>
54. Sathiya, M. *et al.* **Reversible anionic redox chemistry in high-capacity layered-oxide electrodes.** *Nat. Mater.* 12, 827–835 (2013). <https://dx.doi.org/10.1038/nmat3699>
55. Sathiya, M. *et al.* **Origin of voltage decay in high-capacity layered oxide electrodes.** *Nat. Mater.* 14, 230–238 (2015). <https://dx.doi.org/10.1038/nmat4137>
56. Assat, G., Delacourt, C., Corte, D. A. D. & Tarascon, J.-M. **Practical Assessment of Anionic Redox in Li-Rich Layered Oxide Cathodes: A Mixed Blessing for High Energy Li-Ion Batteries.** *J. Electrochem. Soc.* 163, A2965–A2976 (2016). <https://dx.doi.org/10.1149/2.0531614jes>
57. Kobayashi, H., Tabuchi, M., Shikano, M., Kageyama, H. & Kanno, R. **Structure, and magnetic and electrochemical properties of layered oxides,  $\text{Li}_2\text{IrO}_3$ .** *J. Mater. Chem.* 13, 957–962 (2003). <https://dx.doi.org/10.1039/B207282C>
58. McCalla, E. *et al.* **Visualization of O-O peroxo-like dimers in high-capacity layered oxides for Li-ion batteries.** *Science* 350, 1516–1521 (2015). <https://dx.doi.org/10.1126/science.aac8260>
59. Mortemard de Boisse, B. *et al.* **Intermediate honeycomb ordering to trigger oxygen redox chemistry in layered battery electrode.** *Nat. Commun.* 7, 11397 (2016). <https://dx.doi.org/10.1038/ncomms11397>
60. Yabuuchi, N. *et al.* **High-capacity electrode materials for rechargeable lithium batteries:  $\text{Li}_3\text{NbO}_4$ -based system with cation-disordered rocksalt structure.** *Proc. Natl. Acad. Sci.* 112, 7650–7655 (2015). <https://dx.doi.org/10.1073/pnas.1504901112>

61. Lee, J. *et al.* **A new class of high capacity cation-disordered oxides for rechargeable lithium batteries: Li–Ni–Ti–Mo oxides.** *Energy Environ. Sci.* 8, 3255–3265 (2015). <https://dx.doi.org/10.1039/C5EE02329G>
62. Wang, R. *et al.* **A disordered rock-salt Li-excess cathode material with high capacity and substantial oxygen redox activity:  $\text{Li}_{1.25}\text{Nb}_{0.25}\text{Mn}_{0.5}\text{O}_2$ .** *Electrochem. Commun.* 60, 70–73 (2015). <https://dx.doi.org/10.1016/j.elecom.2015.08.003>
63. Freire, M. *et al.* **A new active Li-Mn-O compound for high energy density Li-ion batteries.** *Nat. Mater.* 15, 173–177 (2016). <https://dx.doi.org/10.1038/nmat4479>
64. Nakajima, M. & Yabuuchi, N. **Lithium-Excess Cation-Disordered Rocksalt-Type Oxide with Nanoscale Phase Segregation:  $\text{Li}_{1.25}\text{Nb}_{0.25}\text{V}_{0.5}\text{O}_2$ .** *Chem. Mater.* 29, 6927–6935 (2017). <https://dx.doi.org/10.1021/acs.chemmater.7b02343>
65. Pearce, P. E. *et al.* **Evidence for anionic redox activity in a tridimensional-ordered Li-rich positive electrode  $\beta\text{-Li}_2\text{IrO}_3$ .** *Nat. Mater.* 16, 580–586 (2017). <https://dx.doi.org/10.1038/nmat4864>
66. Rouxel, J. **Anion–Cation Redox Competition and the Formation of New Compounds in Highly Covalent Systems.** *Chem. – Eur. J.* 2, 1053–1059 (1996). <https://dx.doi.org/10.1002/chem.19960020904>
67. Seo, D.-H. *et al.* **The structural and chemical origin of the oxygen redox activity in layered and cation-disordered Li-excess cathode materials.** *Nat. Chem.* 8, 692–697 (2016). <https://dx.doi.org/10.1038/nchem.2524>
68. Saubanère, M., McCalla, E., Tarascon, J.-M. & Doublet, M.-L. **The intriguing question of anionic redox in high-energy density cathodes for Li-ion batteries.** *Energy Environ. Sci.* 9, 984–991 (2016). <https://dx.doi.org/10.1039/C5EE03048J>
69. Xie, Y., Saubanère, M. & Doublet, M.-L. **Requirements for reversible extra-capacity in Li-rich layered oxides for Li-ion batteries.** *Energy Environ. Sci.* 10, 266–274 (2017). <https://dx.doi.org/10.1039/C6EE02328B>
70. Luo, K. *et al.* **Charge-compensation in 3d-transition-metal-oxide intercalation cathodes through the generation of localized electron holes on oxygen.** *Nat. Chem.* 8, 684–691 (2016). <https://dx.doi.org/10.1038/nchem.2471>
71. Yabuuchi, N. *et al.* **P2-type  $\text{Na}_x[\text{Fe}_{1/2}\text{Mn}_{1/2}]\text{O}_2$  made from earth-abundant elements for rechargeable Na batteries.** *Nat. Mater.* 11, 512–517 (2012). <https://dx.doi.org/10.1038/nmat3309>
72. Rozier, P. *et al.* **Anionic redox chemistry in Na-rich  $\text{Na}_2\text{Ru}_{1-y}\text{Sn}_y\text{O}_3$  positive electrode material for Na-ion batteries.** *Electrochem. Commun.* 53, 29–32 (2015). <https://dx.doi.org/10.1016/j.elecom.2015.02.001>

73. Perez, A. J. *et al.* **Strong Oxygen Participation in the Redox Governing the Structural and Electrochemical Properties of Na-Rich Layered Oxide Na<sub>2</sub>IrO<sub>3</sub>.** *Chem. Mater.* 28, 8278–8288 (2016). <https://dx.doi.org/10.1021/acs.chemmater.6b03338>
74. McDaniel, C. L. **Phase relations in the systems Na<sub>2</sub>O-IrO<sub>2</sub> and Na<sub>2</sub>O-PtO<sub>2</sub> in air.** *J. Solid State Chem.* 9, 139–146 (1974). [https://dx.doi.org/10.1016/0022-4596\(74\)90065-6](https://dx.doi.org/10.1016/0022-4596(74)90065-6)
75. Krizan, J. W., Roudebush, J. H., Fox, G. M. & Cava, R. J. **The chemical instability of Na<sub>2</sub>IrO<sub>3</sub> in air.** *Mater. Res. Bull.* 52, 162–166 (2014). <https://dx.doi.org/10.1016/j.materresbull.2014.01.021>
76. Bréger, J. *et al.* **High-resolution X-ray diffraction, DIFFaX, NMR and first principles study of disorder in the Li<sub>2</sub>MnO<sub>3</sub>-Li[Ni<sub>1/2</sub>Mn<sub>1/2</sub>]O<sub>2</sub> solid solution.** *J. Solid State Chem.* 178, 2575–2585 (2005). <https://dx.doi.org/10.1016/j.jssc.2005.05.027>
77. Casas-Cabanas, M., Rodríguez-Carvajal, J. & Palacín, M. R. **FAULTS, a new program for refinement of powder diffraction patterns from layered structures.** *Z. Für Krist. Suppl* 23, 243–248 (2006).
78. Lu, H. *et al.* **Investigation of the Effect of Fluoroethylene Carbonate Additive on Electrochemical Performance of Sb-Based Anode for Sodium-Ion Batteries.** *Electrochimica Acta* 190, 402–408 (2016). <https://dx.doi.org/10.1016/j.electacta.2015.12.136>
79. Dugas, R. *et al.* **Na Reactivity toward Carbonate-Based Electrolytes: The Effect of FEC as Additive.** *J. Electrochem. Soc.* 163, A2333–A2339 (2016). <https://dx.doi.org/10.1149/2.0981610jes>
80. Leriche, J. B. *et al.* **An Electrochemical Cell for Operando Study of Lithium Batteries Using Synchrotron Radiation.** *J. Electrochem. Soc.* 157, A606–A610 (2010). <https://dx.doi.org/10.1149/1.3355977>
81. Wallace, D. C. & McQueen, T. M. **New honeycomb iridium(V) oxides: NaIrO<sub>3</sub> and Sr<sub>3</sub>CaIr<sub>2</sub>O<sub>9</sub>.** *Dalton Trans.* 44, 20344–20351 (2015). <https://dx.doi.org/10.1039/C5DT03188E>
82. Choy, J.-H., Kim, D.-K., Demazeau, G. & Jung, D.-Y. **LIII-Edge XANES Study on Unusually High Valent Iridium in a Perovskite Lattice.** *J. Phys. Chem.* 98, 6258–6262 (1994). <https://dx.doi.org/10.1021/j100076a005>
83. Dugas, R., Zhang, B., Rozier, P. & Tarascon, J. M. **Optimization of Na-Ion Battery Systems Based on Polyanionic or Layered Positive Electrodes and Carbon Anodes.** *J. Electrochem. Soc.* 163, A867–A874 (2016). <https://dx.doi.org/10.1149/2.0051605jes>
84. Ong, S. P. *et al.* **Voltage, stability and diffusion barrier differences between sodium-ion and lithium-ion intercalation materials.** *Energy Environ. Sci.* 4, 3680–3688 (2011). <https://dx.doi.org/10.1039/C1EE01782A>

85. Manni, S. *et al.* **Effect of isoelectronic doping on the honeycomb-lattice iridate  $A_2IrO_3$ .** *Phys. Rev. B* 89, 245113 (2014). <https://dx.doi.org/10.1103/PhysRevB.89.245113>
86. Liu, J. *et al.* **Quantification of Honeycomb Number-Type Stacking Faults: Application to  $Na_3Ni_2BiO_6$  Cathodes for Na-Ion Batteries.** *Inorg. Chem.* (2016). <https://dx.doi.org/10.1021/acs.inorgchem.6b01078>
87. McCalla, E. *et al.* **Novel Complex Stacking of Fully-Ordered Transition Metal Layers in  $Li_4FeSbO_6$  Materials.** *Chem. Mater.* 27, 1699–1708 (2015). <https://dx.doi.org/10.1021/cm504500a>
88. Yabuuchi, N. *et al.* **New O2/P2-type Li-Excess Layered Manganese Oxides as Promising Multi-Functional Electrode Materials for Rechargeable Li/Na Batteries.** *Adv. Energy Mater.* 4, 1301453 (2014). <https://dx.doi.org/10.1002/aenm.201301453>
89. Kim, D., Cho, M. & Cho, K. **Rational Design of  $Na(Li_{1/3}Mn_{2/3})O_2$  Operated by Anionic Redox Reactions for Advanced Sodium-Ion Batteries.** *Adv. Mater.* 29, 1701788 (2017). <https://dx.doi.org/10.1002/adma.201701788>
90. Yabuuchi, N., Tahara, Y., Komaba, S., Kitada, S. & Kajiya, Y. **Synthesis and Electrochemical Properties of  $Li_4MoO_5$ –NiO Binary System as Positive Electrode Materials for Rechargeable Lithium Batteries.** *Chem. Mater.* 28, 416–419 (2016). <https://dx.doi.org/10.1021/acs.chemmater.5b04092>
91. Mather, G. C., Dussarrat, C., Etourneau, J. & West, A. R. **A review of cation-ordered rock salt superstructureoxides.** *J. Mater. Chem.* 10, 2219–2230 (2000). <https://dx.doi.org/10.1039/B000817F>
92. Choy, J.-H., Kim, D.-K., Hwang, S.-H., Demazeau, G. & Jung, D.-Y. **XANES and EXAFS Studies on the Ir-O Bond Covalency in Ionic Iridium Perovskites.** *J. Am. Chem. Soc.* 117, 8557–8566 (1995). <https://dx.doi.org/10.1021/ja00138a010>
93. Bremholm, M., Dutton, S. E., Stephens, P. W. & Cava, R. J.  **$NaIrO_3$ —A pentavalent post-perovskite.** *J. Solid State Chem.* 184, 601–607 (2011). <https://dx.doi.org/10.1016/j.jssc.2011.01.028>
94. Alexander, A. *et al.* **Structural and magnetic properties of  $Li_3RuO_4$ .** *J. Mater. Chem.* 13, 2612–2616 (2003). <https://dx.doi.org/10.1039/B305220F>
95. Cabana, J., Monconduit, L., Larcher, D. & Palacín, M. R. **Beyond Intercalation-Based Li-Ion Batteries: The State of the Art and Challenges of Electrode Materials Reacting Through Conversion Reactions.** *Adv. Mater.* 22, E170–E192 (2010). <https://dx.doi.org/10.1002/adma.201000717>
96. Dahn, J. R., von Sacken, U. & Michal, C. A. **Structure and electrochemistry of  $Li_{1-y}NiO_2$  and a new  $Li_2NiO_2$  phase with the  $Ni(OH)_2$  structure.** *Solid State Ion.* 44, 87–97 (1990). [https://dx.doi.org/10.1016/0167-2738\(90\)90049-W](https://dx.doi.org/10.1016/0167-2738(90)90049-W)

97. Lepoivre, F., Grimaud, A., Larcher, D. & Tarascon, J.-M. **Long-Time and Reliable Gas Monitoring in Li-O<sub>2</sub> Batteries via a Swagelok Derived Electrochemical Cell.** *J. Electrochem. Soc.* 163, A923–A929 (2016). <https://dx.doi.org/10.1149/2.0421606jes>
98. Delmer, O., Balaya, P., Kienle, L. & Maier, J. **Enhanced Potential of Amorphous Electrode Materials: Case Study of RuO<sub>2</sub>.** *Adv. Mater.* 20, 501–505 (2008). <https://dx.doi.org/10.1002/adma.200701349>
99. Gong, Y., Zhou, M., Kaupp, M. & Riedel, S. **Formation and Characterization of the Iridium Tetroxide Molecule with Iridium in the Oxidation State +VIII.** *Angew. Chem. Int. Ed.* 48, 7879–7883 (2009). <https://dx.doi.org/10.1002/anie.200902733>
100. Briois, V. *et al.* **ROCK: the new Quick-EXAFS beamline at SOLEIL.** *J. Phys. Conf. Ser.* 712, 012149 (2016). <https://dx.doi.org/10.1088/1742-6596/712/1/012149>
101. Massart, B. *et al.* **Handbook of Chemometrics and Qualimetrics.** (Elsevier, 1997).
102. Juan, A. de, Jaumot, J. & Tauler, R. **Multivariate Curve Resolution (MCR). Solving the mixture analysis problem.** *Anal. Methods* 6, 4964–4976 (2014). <https://dx.doi.org/10.1039/C4AY00571F>
103. Qi, B., Perez, I., Ansari, P. H., Lu, F. & Croft, M. **L<sub>2</sub> and L<sub>3</sub> measurements of transition-metal 5d orbital occupancy, spin-orbit effects, and chemical bonding.** *Phys. Rev. B* 36, 2972–2975 (1987). <https://dx.doi.org/10.1103/PhysRevB.36.2972>
104. Lan, M., Beghein, N., Charlier, N. & Gallez, B. **Carbon blacks as EPR sensors for localized measurements of tissue oxygenation.** *Magn. Reson. Med.* 51, 1272–1278 (2004). <https://dx.doi.org/10.1002/mrm.20077>
105. Jacquet, Q. *et al.* **The Li<sub>3</sub>Ru<sub>y</sub>Nb<sub>1-y</sub>O<sub>4</sub> (0 ≤ y ≤ 1) System: Structural Diversity and Li Insertion and Extraction Capabilities.** *Chem. Mater.* 29, 5331–5343 (2017). <https://dx.doi.org/10.1021/acs.chemmater.7b01511>
106. Kim, S. *et al.* **Material design of high-capacity Li-rich layered-oxide electrodes: Li<sub>2</sub>MnO<sub>3</sub> and beyond.** *Energy Environ. Sci.* 10, 2201–2211 (2017). <https://dx.doi.org/10.1039/C7EE01782K>
107. O'Malley, M. J., Woodward, P. M. & Verweij, H. **Production and isolation of pH sensing materials by carbonate melt oxidation of iridium and platinum.** *J. Mater. Chem.* 22, 7782–7790 (2012). <https://dx.doi.org/10.1039/C2JM16791C>
108. Bette, S. *et al.* **Solution of the heavily stacking faulted crystal structure of the honeycomb iridate H<sub>3</sub>LiIr<sub>2</sub>O<sub>6</sub>.** *Dalton Trans.* 46, 15216–15227 (2017). <https://dx.doi.org/10.1039/C7DT02978K>
109. Venkatraman, S. & Manthiram, A. **Investigation of the possible incorporation of protons into oxide cathodes during chemical delithiation.** *J. Solid State Chem.* 177, 4244–4250 (2004). <https://dx.doi.org/10.1016/j.jssc.2004.08.019>

110. Benedek, R., Thackeray, M. M. & van de Walle, A. **Free Energy for Protonation Reaction in Lithium-Ion Battery Cathode Materials.** *Chem. Mater.* 20, 5485–5490 (2008). <https://dx.doi.org/10.1021/cm703042r>
111. Lukatskaya, M. R. *et al.* **Ultra-high-rate pseudocapacitive energy storage in two-dimensional transition metal carbides.** *Nat. Energy* 2, 17105 (2017). <https://dx.doi.org/10.1038/nenergy.2017.105>
112. Christensen, A. N., Hansen, P. & Lehmann, M. S. **Isotope effects in the bonds of  $\alpha$ -CrOOH and  $\alpha$ -CrOOD.** *J. Solid State Chem.* 21, 325–329 (1977). [https://dx.doi.org/10.1016/0022-4596\(77\)90130-X](https://dx.doi.org/10.1016/0022-4596(77)90130-X)
113. Zigan, F., Joswig, W. & Burger, N. **Hydrogen Positions in Bayerite, Al(OH)<sub>3</sub>.** *Z. Krist.* 148, 255–273 (1978). <https://dx.doi.org/10.1524/zkri.1978.148.3-4.255>
114. Conway, B. E. & Mozota, J. **Surface and bulk processes at oxidized iridium electrodes—II. Conductivity-switched behaviour of thick oxide films.** *Electrochimica Acta* 28, 9–16 (1983). [https://dx.doi.org/10.1016/0013-4686\(83\)85080-4](https://dx.doi.org/10.1016/0013-4686(83)85080-4)
115. Weber, D. *et al.* **Trivalent Iridium Oxides: Layered Triangular Lattice Iridate  $\text{K}_{0.75}\text{Na}_{0.25}\text{IrO}_2$  and Oxyhydroxide IrOOH.** *Chem. Mater.* 29, 8338–8345 (2017). <https://dx.doi.org/10.1021/acs.chemmater.7b02683>
116. de la Llave, E. *et al.* **Improving Energy Density and Structural Stability of Manganese Oxide Cathodes for Na-Ion Batteries by Structural Lithium Substitution.** *Chem. Mater.* 28, 9064–9076 (2016). <https://dx.doi.org/10.1021/acs.chemmater.6b04078>
117. Yabuuchi, N. *et al.* **A new electrode material for rechargeable sodium batteries: P2-type  $\text{Na}_{2/3}[\text{Mg}_{0.28}\text{Mn}_{0.72}]\text{O}_2$  with anomalously high reversible capacity.** *J. Mater. Chem. A* 2, 16851–16855 (2014). <https://dx.doi.org/10.1039/C4TA04351K>
118. Rietveld, H. M. **A profile refinement method for nuclear and magnetic structures.** *J. Appl. Crystallogr.* 2, 65–71 (1969). <https://dx.doi.org/10.1107/S0021889869006558>
119. Rodríguez-Carvajal, J. **Recent advances in magnetic structure determination by neutron powder diffraction.** *Phys. B Condens. Matter* 192, 55–69 (1993). [https://dx.doi.org/10.1016/0921-4526\(93\)90108-I](https://dx.doi.org/10.1016/0921-4526(93)90108-I)
120. Momma, K. & Izumi, F. **VESTA 3 for three-dimensional visualization of crystal, volumetric and morphology data.** *J. Appl. Crystallogr.* 44, 1272–1276 (2011). <https://dx.doi.org/10.1107/S0021889811038970>
121. Karlsruhe, F. I. Z. **ICSD.** Available at: [http://www2.fiz-karlsruhe.de/icsd\\_home.html?&L=kzejiqmpzivdud](http://www2.fiz-karlsruhe.de/icsd_home.html?&L=kzejiqmpzivdud) (Accessed: 11th October 2017)

122. **11-BM sample holder.** Available at: [https://wiki-ext.aps.anl.gov/ug11bm/images/thumb/4/4b/SampleBase\\_Diagram.png/500px-SampleBase\\_Diagram.png](https://wiki-ext.aps.anl.gov/ug11bm/images/thumb/4/4b/SampleBase_Diagram.png/500px-SampleBase_Diagram.png) (Accessed: 11th October 2017)
123. Ravel, B. & Newville, M. **ATHENA, ARTEMIS, HEPHAESTUS: data analysis for X-ray absorption spectroscopy using IFEFFIT.** *J. Synchrotron Radiat.* 12, 537–541 (2005). <https://dx.doi.org/10.1107/S0909049505012719>
124. Clancy, J. P. *et al.* **Spin-orbit coupling in iridium-based 5d compounds probed by x-ray absorption spectroscopy.** *Phys. Rev. B* 86, 195131 (2012). <https://dx.doi.org/10.1103/PhysRevB.86.195131>
125. Shirley, D. A. **High-Resolution X-Ray Photoemission Spectrum of the Valence Bands of Gold.** *Phys. Rev. B* 5, 4709–4714 (1972). <https://dx.doi.org/10.1103/PhysRevB.5.4709>
126. Scofield, J. H. **Hartree-Slater subshell photoionization cross-sections at 1254 and 1487 eV.** *J. Electron Spectrosc. Relat. Phenom.* 8, 129–137 (1976). [https://dx.doi.org/10.1016/0368-2048\(76\)80015-1](https://dx.doi.org/10.1016/0368-2048(76)80015-1)
127. Kresse, G. & Hafner, J. **Ab initio molecular dynamics for liquid metals.** *Phys. Rev. B* 47, 558–561 (1993). <https://dx.doi.org/10.1103/PhysRevB.47.558>
128. Kresse, G. & Furthmüller, J. **Efficiency of ab-initio total energy calculations for metals and semiconductors using a plane-wave basis set.** *Comput. Mater. Sci.* 6, 15–50 (1996). [https://dx.doi.org/10.1016/0927-0256\(96\)00008-0](https://dx.doi.org/10.1016/0927-0256(96)00008-0)
129. Perdew, J. P., Burke, K. & Ernzerhof, M. **Generalized Gradient Approximation Made Simple.** *Phys. Rev. Lett.* 77, 3865–3868 (1996). <https://dx.doi.org/10.1103/PhysRevLett.77.3865>
130. Dudarev, S. L., Botton, G. A., Savrasov, S. Y., Humphreys, C. J. & Sutton, A. P. **Electron-energy-loss spectra and the structural stability of nickel oxide: An LSDA+U study.** *Phys. Rev. B* 57, 1505–1509 (1998). <https://dx.doi.org/10.1103/PhysRevB.57.1505>



## List of figures

Figure I.1 : Intercalation in low dimensionality materials.....	6
Figure I.2 : Schematic representation of Li batteries.....	8
Figure I.3 : Specific energy, estimated driving range and cost of available battery technologies compared to systems under development.....	9
Figure I.4 : Schematic representations of Li-O <sub>2</sub> and Li-S batteries.....	10
Figure I.5 : Specific capacity improvement of the layered oxides cathode materials.....	11
Figure I.6 : Structural difference between the classical layered LiMO <sub>2</sub> phases and the Li-rich Li <sub>2</sub> MO <sub>3</sub> phases.....	12
Figure I.7 : Electrochemical behavior of the model compound Li <sub>2</sub> Ru <sub>0.75</sub> Sn <sub>0.25</sub> O <sub>3</sub> .....	14
Figure I.8 : Visualization of short O-O distances in Li <sub>0.5</sub> IrO <sub>3</sub> .....	15
Figure I.9 : Ionic model of the electronic structure in transition metal oxides.....	17
Figure I.10 : Molecular orbital diagram of transition metal oxides.....	18
Figure II.1: Phase diagram of the Na <sub>2</sub> O-IrO <sub>2</sub> .....	22
Figure II.2 : Rietveld refinement of diffraction data.....	24
Figure II.3 : High resolution HAADF-STEM images and corresponding ED patterns for the pristine Na <sub>2</sub> IrO <sub>3</sub> .....	25
Figure II.4 : Broadening of the superstructure peaks.....	25
Figure II.5 : First and second galvanostatic cycles of Na <sub>2</sub> IrO <sub>3</sub> in a Na cell.....	27
Figure II.6 : Electrochemical data obtained with a 3-electrode cell.....	28
Figure II.7: Online Electrochemical Mass Spectrometry data.....	29
Figure II.8 : <i>In situ</i> XRD study of Na <sub>2</sub> IrO <sub>3</sub> .....	30
Figure II.9 : High resolution HAADF-STEM images and corresponding ED patterns for the charged O1 <sup>2-</sup> -NaIrO <sub>3</sub> .....	32
Figure II.10 : High resolution HAADF-STEM images and corresponding ED patterns for the fully charged O1-Na <sub>0.5</sub> IrO <sub>3</sub> .....	33
Figure II.11 : Possible Na positions.....	35
Figure II.12 : Phase stability diagrams of Na <sub>2</sub> IrO <sub>3</sub> .....	36
Figure II.13 : XPS analysis.....	38
Figure II.14 : Analysis of XANES data at Ir L <sub>3</sub> -edge.....	39
Figure II.15 : Projection of O-O short distances visualized by TEM.....	41
Figure II.16 : Position of the Na left in Na <sub>0.5</sub> IrO <sub>3</sub> .....	41
Figure II.17 : Distortion of the IrO <sub>6</sub> octahedra in Na <sub>x</sub> IrO <sub>3</sub> .....	42
Figure II.18 : Cycling performances of Na <sub>2</sub> IrO <sub>3</sub> vs. Na.....	43

---

Figure II.19 : Structure of Na <sub>2</sub> IrO <sub>3</sub> after 50 cycles of charge/discharge in a Na half-cell .....	44
Figure II.20 : High resolution HAADF-STEM images and corresponding ED patterns for the discharged sample after 50 cycles.....	44
Figure II.21 : Cycling performances of Na <sub>2</sub> IrO <sub>3</sub> in a full cell configuration .....	46
Figure III.1 : High order superstructure peaks observed in the synchrotron X-ray diffraction pattern of Na(Li <sub>1/3</sub> Ir <sub>2/3</sub> )O <sub>2</sub> .....	51
Figure III.2 : Crystal structure of Na(Li <sub>1/3</sub> Ir <sub>2/3</sub> )O <sub>2</sub> .....	52
Figure III.3 : Rietveld refinement of diffraction data for Na(Li <sub>1/3</sub> Ir <sub>2/3</sub> )O <sub>2</sub> .....	53
Figure III.4 : Galvanostatic cycling of Na(Li <sub>1/3</sub> Ir <sub>2/3</sub> )O <sub>2</sub> vs. Li .....	55
Figure III.5 : Derivative curves of Na(Li <sub>1/3</sub> Ir <sub>2/3</sub> )O <sub>2</sub> , Li <sub>2</sub> IrO <sub>3</sub> and Na <sub>2</sub> IrO <sub>3</sub> .....	56
Figure III.6 : <i>In situ</i> XRD study of Na(Li <sub>1/3</sub> Ir <sub>2/3</sub> )O <sub>2</sub> vs. Li.....	57
Figure III.7 : Rietveld refinement of XRD data for an <i>ex situ</i> sample charged to 3.2 V .....	57
Figure III.8 : XRD study of the Na <sup>+</sup> /Li <sup>+</sup> exchange reaction in a Li cell .....	59
Figure III.9 : Galvanostatic cycling of Na(Li <sub>1/3</sub> Ir <sub>2/3</sub> )O <sub>2</sub> vs. Na .....	60
Figure III.10 : <i>In situ</i> XRD study of Na(Li <sub>1/3</sub> Ir <sub>2/3</sub> )O <sub>2</sub> vs. Na.....	61
Figure III.11 : Structure of Na(Li <sub>1/3</sub> Ir <sub>2/3</sub> )O <sub>2</sub> after a complete charge/discharge cycle vs. Na...61	
Figure III.12 : Overall electrochemical mechanism of Na(Li <sub>1/3</sub> Ir <sub>2/3</sub> )O <sub>2</sub> in Li and Na batteries	62
Figure IV.1 : Increasing the Li/M ratio in rocksalt oxides as a strategy to activate oxygen redox.....	66
Figure IV.2 : Structural characterization of Li <sub>3</sub> IrO <sub>4</sub> .....	67
Figure IV.3 : Structural model for Li <sub>3</sub> IrO <sub>4</sub> .....	68
Figure IV.4 : Electrochemical properties of Li <sub>3</sub> IrO <sub>4</sub> .....	69
Figure IV.5 : Detailed electrochemical curves.....	69
Figure IV.6 : <i>In situ</i> XRD study of the reduction process .....	70
Figure IV.7 : Structure of Li <sub>4.7</sub> IrO <sub>4</sub> .....	71
Figure IV.8 : <i>In situ</i> XRD study of the oxidation process .....	73
Figure IV.9 : TEM data of Li <sub>3</sub> IrO <sub>4</sub> charged to 4.5 V .....	73
Figure IV.10 : O <sub>2</sub> release upon complete oxidation of Li <sub>3</sub> IrO <sub>4</sub> .....	74
Figure IV.11 : TEM data of Li <sub>3</sub> IrO <sub>4</sub> discharged to 0 V .....	75
Figure IV.12 : Change in conversion capacity of Li <sub>3</sub> IrO <sub>4</sub> .....	76
Figure IV.13 : Energy difference between the two polymorphs α-IrO <sub>3</sub> and β-IrO <sub>3</sub> .....	76
Figure IV.14 : Phase stability diagram of Li <sub>x</sub> IrO <sub>4</sub> .....	77
Figure IV.15 : Reversibility of intercalation over 3.5 Li <sup>+</sup> .....	78
Figure IV.16 : <i>In situ</i> XRD study of the reversible cycle .....	79
Figure IV.17 : Cycling performances .....	79
Figure IV.18 : Local structural evolution from <i>operando</i> EXAFS analysis.....	81

Figure IV.19 : Participation of cationic redox during cycling studied by operando XANES ..	84
Figure IV.20 : <i>Ex situ</i> EPR spectroscopy study of paramagnetic species at different states of charge.....	86
Figure V.1 : Structural modifications upon proton exchange of $\text{Na}_2\text{IrO}_3$ .....	91
Figure V.2 : Thermal decomposition of $\text{Na}_x\text{H}_y\text{IrO}_3$ .....	92
Figure V.3 : Acid-exchange properties of $\alpha\text{-Li}_2\text{IrO}_3$ .....	93
Figure V.4 : Thermal decomposition of $\alpha\text{-Li}_x\text{H}_y\text{IrO}_3$ .....	94
Figure V.5 : Thermal decomposition of $\beta\text{-Li}_x\text{H}_y\text{IrO}_3$ .....	95
Figure V.6 : Structural modifications upon proton exchange of $\text{Li}_3\text{IrO}_4$ .....	96
Figure V.7 : Thermal decomposition of $\text{Li}_3\text{IrO}_4$ .....	97
Figure V.8 : FTIR spectra of $\text{Li}_3\text{IrO}_4$ and $\text{H}_{3.4}\text{IrO}_4$ .....	98
Figure V.9 : Li insertion in $\text{H}_{3.4}\text{IrO}_4$ .....	99
Figure V.10 : <i>In situ</i> XRD study in non-aqueous and aqueous electrolytes.....	101
Figure V.11 : Electrochemical activity of $\text{H}_{3.4}\text{IrO}_4$ in acidic media.....	102
Figure V.12 : Difference in electrochemical behaviors with and without carbon additive....	103
Figure V.13 : Kinetic analysis of the charge storage process.....	105
Figure V.14 : <i>Ex situ</i> XRD study of $\text{H}_3\text{IrO}_4$ in aqueous media .....	107
Figure V.15 : Overall structural mechanism .....	108
Figure V.16 : Proton positions in layered $\text{CrOOH}$ , bayerite $\text{Al}(\text{OH})_3$ and brucite $\text{Mg}(\text{OH})_2$ structures.....	109
Figure A.1 : Air-tight XRD sample holder.....	115
Figure A.2 : Sample holder for synchrotron XRD .....	116
Figure A.3 : Swagelok cell .....	118
Figure A.4 : 2032 coin cell .....	118
Figure A.5 : Three-electrode Swagelok cell.....	119
Figure A.6 : <i>In situ</i> pressure cell for gas measurements.....	119
Figure A.7 : <i>In situ</i> cell for X-ray experiments .....	120
Figure A.8 : Schematic of the XAS experiment.....	122
Figure A.9 : Determination of the white line intensity at Ir $\text{L}_{3\text{-edge}}$ .....	123
Figure A.10 : Ir $\text{L}_{\text{III-edge}}$ EXAFS analysis of $\text{Li}_3\text{IrO}_4$ (cell A) .....	126
Figure A.11 : Ir $\text{L}_{\text{III-edge}}$ EXAFS analysis of $\text{Li}_3\text{IrO}_4$ (cell B) .....	127
Figure A.12 : Ir $\text{L}_{\text{III-edge}}$ EXAFS analysis of $\text{Li}_3\text{IrO}_4$ (cell C) .....	128



## List of tables

Table II.1 : Structural parameters of $\text{Na}_2\text{IrO}_3$ .....	26
Table II.2 : Structural parameters of $\text{O1}'\text{-NaIrO}_3$ .....	31
Table II.3 : Structural parameters of $\text{O1-Na}_{0.5}\text{IrO}_3$ .....	33
Table II.4 : Structural parameters after a full cycle .....	34
Table II.5 : Structural parameters for the sample discharged after 50 cycles .....	45
Table III.1 : Structural parameters for $\text{Na}(\text{Li}_{1/3}\text{Ir}_{2/3})\text{O}_2$ .....	53
Table IV.1 : Structural parameters for the pristine $\text{Li}_3\text{IrO}_4$ .....	67
Table IV.2 : Structural parameters for the reduced $\text{Li}_{4.7}\text{IrO}_4$ .....	72
Table IV.3 : Structural parameters obtained by fitting the EXAFS oscillations .....	82
Table IV.4 : Distortion of the Ir coordination environment .....	85
Table V.1 : Unit cell parameters for different phases derived from $\text{Na}_2\text{IrO}_3$ with the O1 structure .....	91
Table V.2 : Summary of acid exchange reactions for different Ir oxides .....	98



## **Energy storage properties of iridium oxides: model materials for the study of anionic redox**

### **Abstract:**

Improving energy storage stands as a key challenge to facilitate the transition to electric vehicles and renewable energy sources in the next years. Li-ion batteries, which have already conquered the portable electronic market, will be the leading technology to achieve this goal and are therefore the focus of intense research activities to improve their performances, especially in terms of capacity. Among the most promising strategies to obtain high capacity cathode materials, the preparation of Li-rich materials combining the redox activity of cations (transition metals) and anions (oxygen) attracts considerable interest. However, activation of anionic redox in these high capacity materials comes with several issues that need to be solved prior their implementation in the energy storage market. Deep fundamental understanding of anionic redox is therefore required to go forward. Using model systems based on iridium, this work explores how the oxygen local environment can play a role on the activation of anionic redox. The electrochemical properties of  $\text{Na}_2\text{IrO}_3$  and  $\text{Na}(\text{Li}_{1/3}\text{Ir}_{2/3})\text{O}_2$  phases are studied to understand the impact of the alkali nature. The influence of the Li/M ratio in rocksalt oxides is investigated with the synthesis of a new material  $\text{Li}_3\text{IrO}_4$ , which presents the highest reversible capacity among intercalation cathode materials. The rich electrochemical properties of this family of iridate materials are finally extended by preparing proton-based materials through a simple ion-exchange reaction and the electrochemical properties of a new  $\text{H}_{3+x}\text{IrO}_4$  material are presented, with high rate capability performances.

Keywords : Li-ion, Na-ion, Cathode Materials, Layered Oxides, Anionic Redox

## **Propriétés de stockage de l'énergie dans les oxydes d'iridium : matériaux modèles pour l'étude du redox anionique**

### **Résumé:**

L'amélioration des systèmes de stockage d'énergie représente un défi majeur de la transition vers les véhicules électriques et les énergies renouvelables. Les accumulateurs Li-ion, qui ont déjà conquis le marché de l'électronique portable, constitueront la technologie dominante pour réaliser cet objectif, et sont donc l'objet d'intense recherches afin d'améliorer leurs performances, en particulier en termes de capacité. Parmi les stratégies les plus prometteuses pour augmenter la capacité des matériaux de cathodes, beaucoup d'espoir est placé dans la préparation de matériaux riches en lithium, qui combinent l'activité électrochimique des cations (métaux de transitions) et des anions (oxygène). Cependant, l'activation des propriétés redox de l'oxygène est accompagnée de plusieurs problèmes qui freinent le développement industriel de ces matériaux. Il est donc nécessaire d'obtenir de solides connaissances fondamentales sur le phénomène de redox anionique pour résoudre ces problèmes. En utilisant des matériaux modèles à base d'iridium, ce travail explore comment l'activité de l'oxygène est influencé par son environnement local. Les propriétés électrochimiques des composés  $\text{Na}_2\text{IrO}_3$  et  $\text{Na}(\text{Li}_{1/3}\text{Ir}_{2/3})\text{O}_2$  sont étudiés afin de comprendre l'impact de la nature de l'ion alcalin. L'influence du ratio Li/M dans les oxydes de structure NaCl est étudié à travers la synthèse d'un nouveau composé de formule  $\text{Li}_3\text{IrO}_4$ , qui présente la plus haute capacité réversible parmi les matériaux d'insertion utilisés comme cathode. Cette famille de matériau est finalement étendue à des phases contenant des protons par une simple méthode d'échange cationique, et les propriétés électrochimiques d'un nouveau composé  $\text{H}_{3+x}\text{IrO}_4$  sont étudiées, dévoilant de très bonnes propriétés de stockage de puissance en milieu aqueux.

Mots clés : Li-ion, Na-ion, Matériaux de Cathode, Oxydes lamellaires, Redox Anionique